

# Fabrication Process Development for High-Purity Germanium Radiation Detectors with Amorphous Semiconductor Contacts

By

Quinn Looker

A dissertation submitted in partial satisfaction of the

requirements for the degree of

Doctor of Philosophy

in

Engineering – Nuclear Engineering

in the

Graduate Division

of the

University of California, Berkeley

Committee in charge:

Professor Kai Vetter, Chair

Dr. Mark Amman

Professor Eric Norman

Professor Junqiao Wu

Spring 2014

Fabrication Process Development for High-Purity Germanium Detectors with  
Amorphous Semiconductor Contacts

© 2014 Quinn Looker

## Abstract

# Fabrication Process Development for High-Purity Germanium Radiation Detectors with Amorphous Semiconductor Contacts

by

Quinn Looker

Doctor of Philosophy in Nuclear Engineering

University of California, Berkeley

Professor Kai Vetter, Chair

High-purity germanium (HPGe) radiation detectors are well established as a valuable tool in nuclear science, astrophysics, and nuclear security applications. HPGe detectors excel in gamma-ray spectroscopy, offering excellent energy resolution with large detector sizes for high radiation detection efficiency. Although a robust fabrication process has been developed, improvement is needed, especially in developing electrical contact and surface passivation technology for position-sensitive detectors. A systematic study is needed to understand how the detector fabrication process impacts detector performance and reliability. In order to provide position sensitivity, the electrical contacts are segmented to form multiple electrodes. This segmentation creates new challenges in the fabrication process and warrants consideration of additional detector effects related to the segmentation.

A key area of development is the creation of the electrical contacts in a way that enables reliable operation, provides low electronic noise, and allows fine segmentation of electrodes, giving position sensitivity for radiation interactions in the detector. Amorphous semiconductor contacts have great potential to facilitate new HPGe detector designs by providing a thin, high-resistivity surface coating that is the basis for electrical contacts that block both electrons and holes and can easily be finely segmented. Additionally, amorphous semiconductor coatings form a suitable passivation layer to protect the HPGe crystal surface from contamination. This versatility allows a simple fabrication process for fully passivated, finely segmented detectors.

However, the fabrication process for detectors with amorphous semiconductors is not as highly developed as for conventional technologies. The amorphous semiconductor layer properties can vary widely based on how they are created and these can translate into varying performance of HPGe detectors with these contacts. Some key challenges include minimizing charge injection leakage current, increasing the long-term stability of the contacts, and achieving good charge collection properties in segmented detectors.

A systematic study of contact characteristics is presented where amorphous germanium (a-Ge) and amorphous silicon (a-Si) contacts are sputtered with varying sputter gas hydrogen content, sputter gas pressure, and amorphous film thickness. A set of about 45 detectors fabricated from 11 different crystal samples were analyzed for electron barrier height and effective Richardson constant. Most of these detectors were subjected to as many as 10 temperature cycles over a period of up to several months in order to assess their long-term stability. Additionally, 6 double-sided strip detectors were fabricated with a-Ge and a-Si

contacts in order to study their inter-electrode charge collection properties. An attempt is made to relate fabrication process parameters such as hydrogen content, sputter pressure, and film thickness to changes observed in detector performance and assess the level of reproducibility using the current methods.

Several important results and conclusions were found that enable more reliable and highly performing detectors with amorphous semiconductor contacts. Utilizing the new information should enable consistent production of finely segmented detectors with excellent energy resolution that can be operated reliably for a long period of time. The passivation process could impact planar detectors as well as other designs, such as the p-type point contact detector. It is demonstrated that the long-term stability of amorphous semiconductor contacts is primarily dependent on the time the detector is at room temperature rather than the number of temperature cycles. For a-Ge contacts, higher sputter pressure yields a more stable process that changes little with time, giving a reliable hole-blocking contact. The a-Si contacts form a good electron-blocking contact with decreasing leakage current over time. Both materials, when 7% hydrogen is included in the argon sputter gas, show acceptable levels of inter-electrode charge collection to be useful for strip electrode detectors.

# Table of Contents

<b>Table of Contents .....</b>	<b>i</b>
<b>List of Figures.....</b>	<b>iv</b>
<b>List of Tables .....</b>	<b>xi</b>
<b>Acknowledgements .....</b>	<b>xii</b>
<b>Chapter 1 Introduction.....</b>	<b>1</b>
1.1 Motivation .....	1
1.1.1 Gamma-Ray Spectroscopy.....	1
1.1.2 Gamma-Ray Imaging.....	3
1.1.3 Challenges.....	3
1.2 Dissertation Overview .....	4
<b>Chapter 2 Radiation Detectors .....</b>	<b>5</b>
2.1 Detector Systems .....	5
2.2 Radiation Interactions.....	6
2.2.1 Gamma-Ray Interactions .....	6
2.2.2 Charged Particles and Other Particles.....	7
2.3 Signal Generation .....	8
2.3.1 Information Carriers.....	8
2.3.2 Pulse processing.....	9
2.3.3 Electronic Noise.....	10
<b>Chapter 3 Germanium-Based Radiation Detectors .....</b>	<b>12</b>
3.1 Semiconductor Material Properties .....	12
3.1.1 The Fermi Level.....	12
3.1.2 Energy Bands .....	13
3.1.3 Electrically Active Impurities .....	15
3.1.4 Charge Carrier Movement .....	16
3.2 High-Purity Germanium Detectors .....	20
3.2.1 Historical Overview .....	20
3.2.2 Common Detector Geometries .....	21
3.2.3 Electrical Contact Properties.....	27
3.2.4 Surface Passivation Properties .....	29
3.2.5 Types of Electrical Contacts .....	30
<b>Chapter 4 Fabrication Challenges with High-Purity Germanium Detectors using Amorphous Semiconductor Contacts .....</b>	<b>43</b>
4.1 Leakage Current .....	43
4.2 Long-Term Stability .....	44
4.3 Inter-electrode Impedance .....	45
4.4 Surface Passivation.....	47
4.4.1 Surface Channels .....	48
4.4.2 Inter-Electrode Charge Collection .....	49
<b>Chapter 5 Leakage Current .....</b>	<b>51</b>
5.1 Background .....	51
5.1.1 Effect on Detectors .....	51

5.1.2	Previous Work .....	52
5.2	Detector Fabrication .....	53
5.3	Current-Voltage Testing .....	55
5.4	Analysis .....	57
5.5	Results .....	62
5.5.1	Reproducibility .....	62
5.5.2	Effect of Hydrogen Content .....	64
5.5.3	Effect of Sputter Pressure .....	66
5.5.4	Effect of Film Thickness .....	67
5.6	Conclusions .....	68
<b>Chapter 6</b>	<b>Long-Term Stability .....</b>	<b>70</b>
6.1	Background .....	70
6.1.1	Effect on Detectors .....	71
6.1.2	Previous Work .....	71
6.2	Current-Voltage Testing .....	71
6.3	Analysis .....	73
6.4	Results .....	75
6.4.1	Effect of Time Warm .....	75
6.4.2	Effect of Sputter Pressure .....	76
6.4.3	Effect of Hydrogen Content .....	77
6.4.4	Effect of Film Thickness .....	79
6.4.5	Reproducibility .....	80
6.5	Conclusions .....	82
<b>Chapter 7</b>	<b>Inter-Electrode Charge Collection .....</b>	<b>84</b>
7.1	Background .....	84
7.1.1	Effect on Detectors .....	84
7.1.2	Previous Work .....	86
7.2	Strip Detector Testing .....	87
7.2.1	Fabrication .....	88
7.2.2	Experiments .....	90
7.2.3	Weighting Potential Calculation .....	92
7.2.4	Data Processing .....	94
7.3	Results .....	99
7.3.1	a-Ge with no Hydrogen .....	99
7.3.2	a-Ge with Hydrogen .....	101
7.3.3	a-Si with Hydrogen .....	110
7.4	Conclusions .....	111
<b>Chapter 8</b>	<b>Conclusions .....</b>	<b>113</b>
8.1	Significant Findings .....	113
8.2	Future Work .....	114
<b>References</b>	.....	<b>116</b>
<b>Appendices</b>	.....	<b>124</b>
<b>Appendix A Detector Fabrication</b>	.....	<b>125</b>
A.1	Crystal Preparation .....	125
A.2	Sputtering .....	129
A.3	Metal Evaporation .....	132

A.4 Photolithography .....	135
A.5 Wire Bonding .....	136
<b>Appendix B Current-Voltage Testing .....</b>	<b>138</b>
B.1 Single-Detector Cryostat .....	138
B.2 Multi-Detector Cryostat .....	141
B.3 Measurement Equipment.....	144
B.4 Current-Voltage Testing Procedure.....	149
<b>Appendix C Strip Detector Testing.....</b>	<b>150</b>
C.1 Cryostat .....	150
C.2 Measurement Equipment.....	153
C.3 Miscellaneous Effects.....	154
<b>Appendix D Shockley-Ramo Theorem .....</b>	<b>158</b>

# List of Figures

Figure 1.1. Energy spectrum from $^{110m}\text{Ag}$ decay, acquired with a NaI scintillation detector and a Ge(Li) detector. [10] .....	2
Figure 2.1. Schematic of the basic components of a radiation detector system. .....	5
Figure 2.2. Energy dependence of photon interaction mechanisms in germanium for the gamma-ray energy range. [29] .....	7
Figure 2.3. Schematic of a semiconductor detector circuit.....	9
Figure 2.4. Example calculated value of equivalent noise charge as a function of shaping time. ....	11
Figure 3.1. Fermi function at various temperatures with germanium reference levels. ....	13
Figure 3.2. Classes of crystalline solids defined by energy band structure. ....	13
Figure 3.3. Impurity levels in units of eV for germanium crystal with selected elemental impurities. [42].....	15
Figure 3.4. Electron drift velocity in germanium as a function of electric field. Data are presented at 8 K (upper axis labels) and 77 K (lower axis labels), with different markers representing two crystallographic directions. [44].....	17
Figure 3.5. Hole drift velocity in germanium as a function of electric field. Data are presented at various temperatures for the $<100>$ crystallographic direction. [43] .....	17
Figure 3.6. Illustration of theoretical mobility dependence on temperature.....	18
Figure 3.7. Charge carrier mobility in germanium as a function of temperature. The left panel shows electron mobility [44] and the right panel shows hole mobility [43]. The data points indicate experimental measurements and the solid lines show theoretical dependence. ....	19
Figure 3.8. Illustration of a planar germanium detector. ....	21
Figure 3.9. Illustration of depletion layer and electric field profile of a planar detector with varying bias.....	22
Figure 3.10. Illustration of electric field strength as a function of depth in a planar detector. [55] .....	23
Figure 3.11. Schematic illustration of the double-sided strip detector geometry. Separate electrodes give two-dimensional position sensitivity. ....	24
Figure 3.12. Schematic illustration of the coaxial detector geometry. ....	25
Figure 3.13. Calculated electric field strength as a function of radius in a coaxial germanium detector. [55] .....	25
Figure 3.14. Schematic illustration of a p-type point contact detector. ....	26
Figure 3.15. Sources of current in a radiation detector.....	28
Figure 3.16. Illustration of a planar detector with a guard ring electrode configuration. ....	29
Figure 3.17. Illustration of a detector with a B-implanted contact. ....	31
Figure 3.18. Band diagram and depletion region for a p-n junction at equilibrium, forward bias, and reverse bias.....	32
Figure 3.19. Example of an ideal diode current-voltage characteristic. ....	32
Figure 3.20. Illustration of a detector with a Li-diffused contact. ....	33
Figure 3.21. Illustration of a metal Schottky contact on germanium.....	34
Figure 3.22. Band structure of a metal-semiconductor junction according to the Schottky model. The left picture shows the materials when separated and the right picture shows when the two are brought into contact and reach thermal equilibrium. ....	35

Figure 3.23. Schematic band structure and charge carrier motion in crystalline and amorphous semiconductors. ....	38
Figure 3.24. Schematic of energy vs. density of states for an amorphous-crystalline semiconductor junction. Adapted from [97]. ....	39
Figure 3.25. Band structure of an amorphous-crystalline junction with barrier lowering due to field penetration in the amorphous layer. Adapted from [97]. ....	39
Figure 3.26. Predicted behavior of an amorphous-crystalline junction compared to the ideal rectifier of Schottky theory. [97] ....	40
Figure 3.27. Illustration of a detector with amorphous semiconductor contacts and passivation. ....	41
Figure 4.1. Change in leakage current as a function of temperature cycle for two different detectors with a-Ge contacts. [110] ....	45
Figure 4.2. Equivalent circuit elements between two electrodes. ....	46
Figure 4.3. Illustration of inter-electrode resistance measurement. ....	47
Figure 4.4. Example data showing inter-electrode resistance measurement. ....	47
Figure 4.5. Illustration of electric field alteration due to a surface channel. [110] ....	48
Figure 4.6. Illustration of inter-electrode charge collection. [110] ....	49
Figure 4.7. A plot of the type used for investigating inter-electrode charge collection. The sum energy of two adjacent electrodes is plotted against the energy of one of those electrodes. [110] ....	50
Figure 5.1. Photograph of an HPGe slice as received from Ortec. ....	54
Figure 5.2. The crystal sample geometry used for the leakage current study. ....	54
Figure 5.3. Schematic illustration of the sequence of depositions used to fabricate a guard ring planar detector used in the leakage current study. ....	55
Figure 5.4. Photograph of a guard ring detector in the single-detector, variable-temperature cryostat. ....	56
Figure 5.5. Readout schematic for current-voltage testing. ....	56
Figure 5.6. Example current-voltage data. The left panel shows a set of I-V data acquired at various temperatures. The right panel illustrates one I-V curve acquired at 100 K. ....	57
Figure 5.7. Top contact current estimation by fitting the I-V curve below full depletion. ....	59
Figure 5.8. Top contact current subtraction. The left panel shows the full I-V curve before and after subtraction. The right panel is a zoom on the current below full depletion. ....	60
Figure 5.9. Example of a fit to the portion of the I-V curve above full depletion. The data have been corrected for the top contact contribution and only data above full depletion voltage are used for the fit. ....	60
Figure 5.10. Current-temperature fit to example data. The slope gives a barrier height of 0.321 eV and the offset of the line gives a pre-factor of $75 \text{ A cm}^{-2}\text{K}^{-2}$ . ....	61
Figure 5.11. Current-voltage curves for five detectors fabricated in rapid succession using the same fabrication process on the same crystal. The data acquired at 100 K are shown for all five detectors. ....	63
Figure 5.12. Current-voltage characteristic for all detectors fabricated with a-Ge in 15 mTorr Ar (7% $\text{H}_2$ ). Data were acquired at 100 K. ....	63
Figure 5.13. Current-voltage characteristic at 100 K for all detectors fabricated with a-Ge sputtered in 7 mTorr Ar (7% $\text{H}_2$ ) atmosphere. ....	64
Figure 5.14. Electron barrier as a function of hydrogen content of the sputter gas. ....	65
Figure 5.15. Pre-factor as a function of sputter gas hydrogen content. ....	65

Figure 5.16. Electron barrier as a function of sputter gas pressure for all a-Ge contacts with 7% H <sub>2</sub> sputter gas. ....	66
Figure 5.17. Pre-factor as a function of sputter gas pressure for all a-Ge contacts with 7% H <sub>2</sub> sputter gas. ....	67
Figure 5.18. Electron barrier as a function of amorphous semiconductor film thickness. ....	68
Figure 5.19. Pre-factor as a function of amorphous semiconductor film thickness. ....	68
Figure 6.1. Schematic illustration of detector temperature during a temperature cycle. ....	72
Figure 6.2. Example of I-V data at 100 K over several temperature cycles. ....	73
Figure 6.3. Plot of leakage current density vs. temperature cycle at a specific temperature and bias. ....	73
Figure 6.4. Normalized change in current as a function of time warm between cycles. The left panel shows the example data from previous plots, while the right panel shows data from another detector to clearly illustrate the role of air exposure. ....	74
Figure 6.5. Example data shown as current normalized to the initially measured current vs. cumulative time spent at room temperature. ....	75
Figure 6.6. Leakage current density ratio as a function of total time warm for a-Ge contacts sputtered in various gas pressures. All used 7% H <sub>2</sub> sputter gas and crystals were taken from the same boule. ....	76
Figure 6.7. Measured film stress in RF-magnetron sputtered a-Ge as a function of sputter pressure. [102]....	77
Figure 6.8. Leakage current density ratio as a function of total time warm for detectors with a-Ge contacts sputtered at 15 mTorr with gases of varying hydrogen content. All detectors were made using the same crystal sample. ....	78
Figure 6.9. Leakage current density ratio as a function of total time warm for detectors with a-Si contacts sputtered at 7 mTorr with gases of varying hydrogen content. All crystal samples were from the same boule. ....	78
Figure 6.10. Leakage current density ratio as a function of total time warm for detectors with a-Ge contacts sputtered at 15 mTorr gas with 7% H <sub>2</sub> content. The number of depositions was different, giving different values for estimated contact thickness. ....	79
Figure 6.11. Leakage current density ratio as a function of total time warm for detectors with a-Ge contacts sputtered in 7% H <sub>2</sub> gas. Detectors made with crystals from three different boules are pictured. ....	81
Figure 6.12. Leakage current density ratio as a function of total time warm for detectors with a-Ge contacts sputtered in 15 mTorr 7% H <sub>2</sub> gas. Detectors made with crystals from three different boules are pictured. ....	81
Figure 6.13. Leakage current density ratio as a function of total time warm for detectors with a-Si contacts sputtered in 7 mTorr 7% H <sub>2</sub> gas. Detectors made with crystals from three different boules are pictured. ....	82
Figure 7.1. Summed energy spectra of two adjacent strips from two detectors with a-Ge contacts. One had no added hydrogen in the amorphous layer, while the other had 7% H <sub>2</sub> content. ....	84
Figure 7.2. Illustration of a method for examining inter-electrode charge collection. The plot shows the sum energy of two adjacent electrodes as a function of the energy for one of those electrodes. Additional illustrations show the type of events that contribute to different regions on the graph. [110]....	85

Figure 7.3. Schematic illustration of the etched inter-electrode region strategy for eliminating charge deficit.....	86
Figure 7.4. Schematic illustration of the steering electrode approach to eliminating charge sharing deficit.....	87
Figure 7.5. Photograph of shadow masks for strip detector fabrication. The left photo shows the mask to define the strips and parallel part of the guard ring. The center photo shows the mask to define the connecting component of the guard ring, while the photo on the right shows the mask for depositing wire bonding pads.....	88
Figure 7.6. Photograph of a double-sided strip detector fabricated for this study.....	89
Figure 7.7. Illustration of inter-electrode charge collection measurement. A low-energy source creates a charge cloud that drifts across the crystal toward a series of strips. Two adjacent strips are read out and their sum is examined for a summed energy deficit.....	90
Figure 7.8. Weighting potential of one strip in the geometry used for inter-electrode charge collection measurements.....	93
Figure 7.9. Simulated estimate of signal magnitude for strips in the experimental electrode configuration. The red and blue curves show the weighting potential for two individual strips evaluated at the top surface. The green curve is the sum of the red and blue curves. The black rectangles indicate the positions of the strip electrodes along the x axis.....	94
Figure 7.10. Example raw waveforms acquired with the SIS3302 digitizer (black) with digital trapezoidal filter output (red). Note the different vertical scales for the two panels. ....	95
Figure 7.11. Example waveforms (black) overlaid with trapezoidal filter output (red). Blue lines indicate horizontal and vertical positions of the value chosen for energy determination.....	95
Figure 7.12. Plot of channel 1 energy vs. channel 2 energy for a typical Am-241 measurement. The inset shows a zoomed view of one full-energy lobe, which has a mean negative value for the non-triggered channel. ....	96
Figure 7.13. Energy of channel 1 vs. energy of channel 2 shown as in Figure 7.12. The black marks indicate raw energy values, while red markers indicate cross-talk-corrected energy values. The inset shows a zoomed image of the class of events where channel 2 has zero energy.....	97
Figure 7.14. Charge sharing plot example for Am-241 measurement. The sum of the two adjacent strip energies is on the vertical axis and one of the strip energies is on the horizontal axis. The black horizontal line indicates the incident photon energy and the black circles show the mean of a Gaussian fit to several vertical slices along the horizontal direction. ....	98
Figure 7.15. Charge sharing plot for one detector with a bottom contact created by sputtering a-Ge in 15 mTorr Ar. No hydrogen was added. The data, acquired at 1500 V, are for holes collected to the bottom contact. The thin black curve shows the estimated response as determined by the weighting potential for events collected directly to the gap. ....	99
Figure 7.16. Charge sharing plots for the detector with an a-Ge bottom contact sputtered in 15 mTorr Ar with no added hydrogen. Different data sets have varying bias. Open markers indicate data sets acquired when the detector was recently biased, while filled markers show data sets acquired when the detector was biased for more than 1 hour prior to acquisition. The data are for holes collected to the bottom contact. ....	100
Figure 7.17. Charge sharing plot for one detector with the bottom contact created by sputtering a-Ge in 15 mTorr Ar with no added hydrogen. Different data sets were acquired at 1500 V bias before and after storage in a dry box. The data are for holes collected to the bottom contact. .	101
Figure 7.18. Charge sharing plot for one detector with a bottom contact created by sputtering a-Ge in 15 mTorr 7% H <sub>2</sub> . The thin black curve shows the estimated response as determined by the	

weighting potential for events collected directly to the gap. The data, acquired at 1500 V, are for holes collected to the bottom contact.....	102
Figure 7.19. Charge sharing plot for bottom strips on one detector with an a-Ge bottom contact sputtered in 15 mTorr Ar (7% H <sub>2</sub> ). Each series is indicated by a different color and represents a separate data set, all taken at 1500 V bias. Open markers represent those data sets where the detector was recently biased, while filled markers represent data where the detector had been biased for a long time prior to data acquisition. The data are for holes collected to the bottom contact.....	103
Figure 7.20. Charge sharing plot for three detectors having the bottom contact formed by the same fabrication process. All had the bottom contact formed by sputtering a-Ge in 15 mTorr Ar (7% H <sub>2</sub> ) atmosphere with a thickness of ~480 nm. One crystal was fabricated twice in the same fashion and a different crystal was fabricated in the same way. All data were acquired at about 1000 V more than depletion voltage. All data are for holes collected to the bottom contact....	104
Figure 7.21. Charge sharing plot for one detector with an a-Ge contact sputtered in 15 mTorr Ar with 7% H <sub>2</sub> at varying positive bias. The examined strips were collecting holes. The detector fully depleted at 500 V.....	105
Figure 7.22. Charge sharing plot for one detector with an a-Ge contact sputtered in 15 mTorr Ar with 7% H <sub>2</sub> at varying negative bias. The examined strips were collecting electrons. The detector fully depleted at -500 V. ....	106
Figure 7.23. Charge sharing plot for the top electrodes of one detector. The top contact was created by sputtering a-Ge in 15 mTorr Ar (7% H <sub>2</sub> ) gas. The data are for electrons collected to the top contact. ....	107
Figure 7.24. Comparison of the top and bottom contact processes collecting both charge carrier polarities. All contacts studied were a-Ge contacts sputtered in 15 mTorr Ar with 7% H <sub>2</sub> .....	108
Figure 7.25. Data for the evaluation of the effect of photolithography on a-Ge contacts sputtered in 15 mTorr Ar with 7% H <sub>2</sub> . One detector was tested with no bake (black and magenta) and again after a 30 minute bake at 90° C (red and green). Another detector was fabricated with photolithography and tested in the same way (blue and purple). ....	109
Figure 7.26. Charge sharing plot for a detector fabricated with an a-Ge bottom contact sputtered in a-Ge 15 mTorr Ar (7% H <sub>2</sub> ) with electrodes patterned using photolithography. The data, acquired at 1000 V, are for bottom electrodes collecting holes.....	110
Figure 7.27. Charge sharing plot for a detector fabricated with an a-Ge top contact sputtered in a-Ge 15 mTorr Ar (7% H <sub>2</sub> ) with electrodes patterned using photolithography. The data, acquired at -1000 V, are for top electrodes collecting electrons. ....	110
Figure 7.28. Charge sharing plot for one detector with a bottom contact created by sputtering a-Si in 7 mTorr Ar (7% H <sub>2</sub> ). The data, acquired at 1000 V, are for bottom electrodes collecting holes. ....	111
Figure A.1. Photograph of a slice of high-purity germanium crystal purchased from Ortec. ...	125
Figure A.2. Photograph of grinding the crystal slice to the desired dimensions. A crystal slice is normally cut into multiple smaller samples. ....	126
Figure A.3. Photograph of crystals partially through the cutting procedure. A large chip defect can be seen on one of the samples near the center of the photograph. Other side surfaces show the typical texture with saw marks.....	127
Figure A.4. Photograph of a crystal lapped with 1900 grit Al <sub>2</sub> O <sub>3</sub> . The top surface shows the matte texture left by lapping, while the sides, inaccessible to lapping, have the surface left by crystal cutting and some residual wax. ....	127

Figure A.5. Photograph of germanium crystal in 4:1 HNO <sub>3</sub> :HF mixture.....	128
Figure A.6. Photograph of a chemically polished germanium crystal.....	128
Figure A.7. Photograph of germanium crystal on a stand for the first sputtering sequence. The geometry allows maximum side coating by keeping the non-winged sides well away from obstructions.....	130
Figure A.8. Photograph of full-wing crystal geometry sputter stand. The crystal can rest on a flat surface as there are no critical non-winged edges where incomplete coating is an issue. The bottom surface rests on a square of indium strips with the center cut out so the active surface area makes no contact.....	130
Figure A.9. Photograph of the inside of the main chamber of the MRC sputtering system. A crystal can be seen upper center on the rotation stage under the Ge target.....	131
Figure A.10. Photograph of HPGe crystal before and after sputtering a-Ge on the top and sides. It gains a darker color but retains the original surface texture.....	132
Figure A.11. Photograph of the bottom surface of HPGe crystal coated with a-Si.....	132
Figure A.12. Photograph of tungsten filaments pre-loaded with aluminum.....	133
Figure A.13. Photograph of a detector ready for aluminum deposition of the top center contact and guard ring structure. A shadow mask defines the outside of the guard ring and a metal ring defines the gap between the electrodes.....	133
Figure A.14. Photograph of a detector loaded in the evaporator, ready for aluminum evaporation.....	134
Figure A.15. Photograph of aluminized detector surface showing a large Al drop. A drop of this size causes significant damage and the electrode will not sustain an electric field.....	135
Figure A.16. Photographs of a detector before (left panel) and after (right panel) applying S1818 photoresist by spin-coating.....	136
Figure A.17. Crystal with developed photoresist mask to form the strip electrode pattern. ....	136
Figure A.18. Photograph of a strip detector test device in its mount with wire-bonded electrodes. ....	137
Figure B.1. Photograph of the single-detector variable-temperature cryostat for current-voltage testing.....	138
Figure B.2. Photograph of the inside the small variable-temperature cryostat. This equipment is used for current-voltage testing. ....	139
Figure B.3. Cooldown curve for the variable-temperature stage of the single-detector cryostat. ....	140
Figure B.4. CAD model of the multi-detector cryostat coldfinger. The flanged tee is made transparent to show the LN tube inside.....	141
Figure B.5. CAD model of the multi-detector cryostat in the final (as used) configuration. Outer dimensions are shown for scale. Example detectors with various mounting schemes are shown mounted inside.....	142
Figure B.6. Photograph of the multi-detector cryostat with four detectors loaded for testing. The top plate and infrared shield are removed to show the variable-temperature stage with mounted detectors. ....	144
Figure B.7. Circuit diagram of the current-voltage measurement system in the single-detector variable-temperature cryostat. The high-voltage power supply is connected through two low-pass filters to the bottom electrode of the detector. The center contact at the top has DC current readout and a pulse height measurement system, while the guard ring goes to a picoammeter. The detector is modeled as a collection of capacitors and current sources. ....	145

Figure B.8. Photograph of the center contact readout box for the single-detector variable-temperature cryostat. The box contains a circuit for both DC current measurement and pulse height measurement of signals from the center contact.....	146
Figure B.9. Photograph of the NIM bin containing external electronics modules used in guard ring detector testing.....	147
Figure B.10. Photograph of the guard ring readout box on the single-detector variable-temperature cryostat. The guard ring electrode can be switched between the ammeter input and a voltage source by the relays (red rectangular components).....	147
Figure B.11. Photograph of Keithley 6485 (left) and 6487 (right) picoammeters used for precision current measurement.....	148
Figure B.12. Photograph of LakeShore 335 temperature controllers used for temperature readout and heater control of variable-temperature cryostat stages.....	149
Figure C.1. Photograph of the outside of the strip detector testing cryostat.....	151
Figure C.2. A photograph of the baseplate inside the cryostat with a mounted and wired detector. The cryostat wall and infrared shield are removed.....	152
Figure C.3. Photograph of the VME crate with Struck Innovative Systems modules used for strip detector testing (left 2 modules).....	154
Figure C.4. Charge sharing plot for one detector bottom contact created by sputtering a-Ge in 15 mTorr Ar (7% H <sub>2</sub> ) gas. The Am-241 source provided 59.5 keV gamma-rays.....	155
Figure C.5. Charge sharing plot for one detector bottom contact created by sputtering a-Ge in 15 mTorr Ar (7% H <sub>2</sub> ) gas. The Co-57 source provided 122 keV gamma-rays.....	155
Figure C.6. Signal from one strip vs. signal from the neighboring strip for a detector that was not fully depleted. The strips examined were in undepleted material.....	156
Figure C.7. Charge sharing plot and waveforms for a detector not fully depleted, but with strips in the depletion region. The upper left panel is the charge sharing plot. Three boxes of different color show three different cuts based on the sum energy and ch. 2 energy. The stacked waveforms for each of the three data sets created by the three cuts are shown in the panels with colored outlines, with colors corresponding to the box that defines the subset on the upper left panel.....	157
Figure D.1. Electric field for a single-sided strip detector.....	159
Figure D.2. Weighting potential for one strip on a single-sided strip detector.....	159
Figure D.3. Schematic of weighting potential for selected electrodes in common detector geometries. The top row shows electrode geometries for a planar detector, orthogonal strip detector, and single-sided pixel detector. The middle row shows a cross-section view with charge drift and biasing scheme, while the bottom row shows the weighting potential for two electrodes on opposite faces of each detector.....	160

## List of Tables

Table 3.1. Material properties of selected semiconductor detector materials.....	14
Table 3.2. Charge carrier mobility and lifetime for selected radiation detector materials. ....	16
Table 3.3. Summary of key features for the different classes of electrical contacts on HPGe detectors.....	30
Table 3.4. Work function of selected metals. [89].....	36
Table 7.1. Summary of inter-electrode charge collection data for a-Ge with 0% H <sub>2</sub> .....	101
Table 7.2. Reproducibility of inter-electrode charge collection data on the same detector.....	104
Table 7.3. Effect of electric field strength on a-Ge contacts sputtered in 15 mTorr Ar with 7% H <sub>2</sub> .....	106
Table 7.4. Inter-electrode charge collection characteristics of different contacts and charge carrier polarity.....	108
Table 7.5. Summary of charge sharing results for different contacts. ....	112
Table A.1. Crystal slice specifications.....	125

## Acknowledgements

I would like to thank my wonderful wife Rebecca for all of the love and support through the years of graduate school. I couldn't have done it without her.

I would also like to thank Dr. Mark Amman for ideas and direction on a daily basis. I learned a lot from Mark, and I'm thankful he allowed me to bother him constantly through the years.

Thanks to Prof. Kai Vetter for the hard work writing the proposal that funded this work and providing support.

Thanks to the other committee members, Prof. Rick Norman and Prof. Junqiao Wu, for taking time out of their busy schedules to read this dissertation and provide comments.

This work was supported by the Department of Energy Office of Nuclear Physics.

# Chapter 1 Introduction

## 1.1 Motivation

Radiation detectors have a wide range of uses in scientific research, industry, and nuclear security applications. Gamma-rays, or energetic photons, are of particular interest because they travel on the order of many meters in air, as opposed to a few cm for charged particles like alpha and beta particles. Gamma-rays can also provide unique information about radioactive isotopes of interest based on the emitted photon energy. Among the different classes of radiation detectors, germanium detectors stand out as a technology that can provide a precise measurement of gamma-ray energy and the ability to capture a large number of gamma-ray interactions. Although operation of these detectors requires cryogenic cooling, their excellent energy resolution and large volume has made them a staple for precision gamma-ray spectroscopy since the 1960s and mature and commercialized products are available today. However, modern applications often involve gamma-ray imaging, which necessitates a measure of the interaction position of incident gamma-rays. More recent work has focused on methods of providing germanium detectors that combine excellent energy resolution with fine position resolution. Amorphous semiconductor contacts are a technology that enables these types of detectors, but this type of electrical contact is less developed than conventional impurity-based contacts. The focus of the work presented here is the development of the fabrication process using amorphous semiconductor contacts to provide a reproducible method for manufacturing germanium detectors with excellent energy and position resolution that can be operated reliably for a long period of time.

### 1.1.1 Gamma-Ray Spectroscopy

Gamma-ray spectroscopy is the practice of acquiring and analyzing the energy spectrum of gamma-rays in an environment. Their energy signature contains important information about what radioactive isotopes are present, and a precise read on gamma-ray energy is a key asset. Germanium-based detectors have represented the gold standard in energy resolution for gamma-ray spectroscopy for several decades [1]. The typical resolution in modern high-purity germanium (HPGe) detectors is about 0.2% full-width at half maximum (FWHM) at 662 keV, compared with CdZnTe detectors at 1-2% FWHM at 662 keV [2] and NaI scintillators at typically ~7% FWHM at 662 keV. Some detector technologies, such as bolometers, have significantly better resolution, but germanium-based detectors stand apart from similar detector types because of the large detector volumes available, providing high gamma-ray detection efficiency.

The appearance of the lithium-drifted germanium diode detector in the early 1960s [3] allowed much finer energy measurement of gamma-ray decays compared with the NaI detectors of the time. This spurred a frenzy of development for germanium detectors to measure gamma-ray transitions in nuclear science [4] [5]. Figure 1.1 shows an example of energy spectra from a NaI scintillation detector and a Ge(Li) detector for an isotope with multiple gamma-ray decay modes. This illustrates the additional information provided by the superior energy resolution

obtained with germanium-based detectors. High-purity germanium material was developed to overcome some of the drawbacks of Ge(Li) detectors, allowing larger detector sizes that are room temperature stable. Today, the demand for HPGe detectors in nuclear physics experiments continues. Two significant examples are the GRETA [6] and AGATA [7] HPGe detector arrays, which require good energy resolution in order to precisely identify new gamma-ray transitions and take advantage of position sensing to track all gamma-ray interactions in the detectors, thereby increasing the overall detection efficiency by 1000 times [8] [9]. HPGe detectors are one of the few technologies that can fulfill this role because of the energy and position sensing requirements.

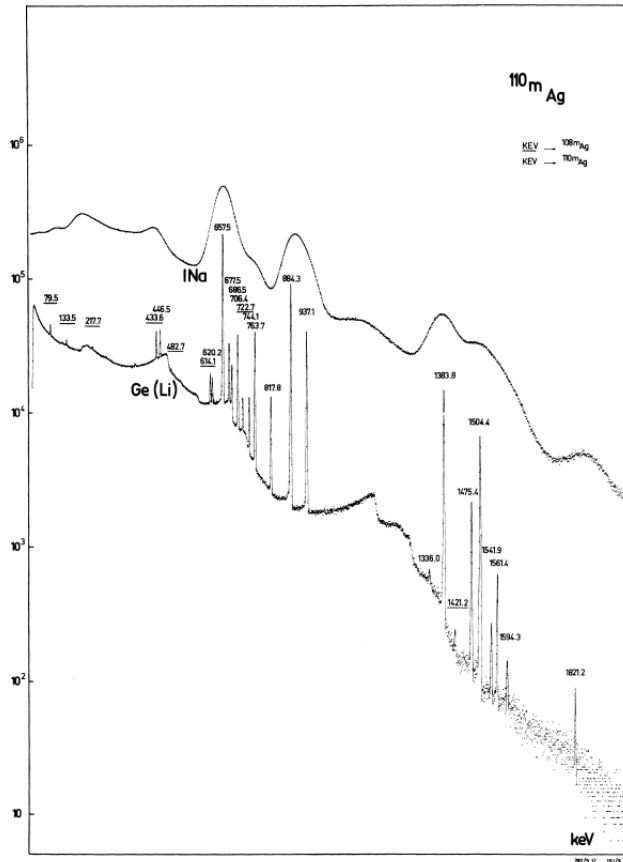


**Figure 1.1. Energy spectrum from  $^{110m}\text{Ag}$  decay, acquired with a NaI scintillation detector and a Ge(Li) detector. [10]**

In nuclear security and safety applications, energy resolution is beneficial in identifying isotopes of interest. The challenge of separating threat sources from naturally occurring radioactive material (NORM) makes HPGe detectors a good choice in situations where the cost and cooling requirements can be tolerated. The energy resolution of HPGe detectors is unsurpassed for the detector sizes available, which is helpful in increasing signal-to-background ratio for isotopic identification.

Excellent energy resolution is also a benefit to medical imaging, astrophysics, and other applications where identifying a unique gamma-ray signature can reduce background. Precise identification of energy in multiple interactions also enables Compton imaging [11].

### 1.1.2 Gamma-Ray Imaging

Conventional HPGe gamma-ray detectors can provide excellent energy resolution, but do not provide a measure of interaction position. Some measure of interaction position is necessary for gamma-ray imaging, which can provide additional benefits in a wide range of applications. A detector must have multiple sensing electrodes in order to have some position sensitivity. An image of a gamma-ray source can be formed through the use of a collimator or coded aperture or by using Compton imaging [12]. Imaging can be used as a method of improving signal-to-background ratio [13], which can aid isotope identification in situations with relatively low signal-to-background ratio. HPGe detectors offer fine position sensitivity [14] [15] in addition to excellent energy resolution, making them ideal for imaging. Forming an image is useful in medical applications, where a radioactive tracer is used to track biological processes, as in positron emission tomography (PET) or single-photon emission computed tomography (SPECT). Additionally, verification of the dose distribution in radiotherapy can be accomplished using gamma-ray imaging. Some segmented germanium detectors have been examined for medical imaging applications [16] [17] [18] [19] [20] [21] [22] because of the unique combination of good energy and position resolution.

In astrophysics, HPGe detectors have provided essential energy and position sensitivity for solar astronomy and gamma-ray bursts. The Reuven Ramaty High-Energy Solar Spectroscopic Imager (RHESSI) consists of nine HPGe detectors with two segments each [23]. The Nuclear Compton Telescope (NCT) [24] and the Gamma-Ray Imager/Polarimeter for Solar Flares (GRIPS) [25] consist of arrays of position-sensitive germanium detectors. These instruments provide precise isotope identification and utilize the Compton scattering interactions to help measure photon polarization in astrophysical sources.

### 1.1.3 Challenges

Germanium detectors for gamma-ray spectroscopy are now a mature and commercialized technology. Modern high-purity germanium detectors with excellent energy resolution and reliability can be purchased from commercial suppliers, but detectors for imaging are more difficult to produce. The conventional contacts used in state-of-the-art detectors are ion-implanted or Li-diffused contacts, which reliably provide low electronic noise. However, they can give additional difficulty in separating the electrical contact into multiple segments, as is required for position sensing. The details of the contact structure and challenges are discussed in Chapter 3.

Amorphous semiconductor contacts have been identified as a useful alternative contact technology that allows easier segmentation of electrodes for position-sensitive detectors [26]. The amorphous semiconductor is a layer of germanium (a-Ge) or silicon (a-Si) that lacks the long-range crystalline order of its single-crystal counterpart. Layers of these materials have been shown to form suitable electron-blocking and hole-blocking contacts [27] as well as passivation layers on non-contact surfaces [28]. With this versatility, a fabrication process is possible where

amorphous semiconductor material is deposited on all surfaces of a HPGe crystal to provide blocking contacts on both sides and full passivation of all surfaces.

The amorphous semiconductor contact fabrication process is not as highly developed as the process for conventional spectrometers. Some earlier work indicated that the sputter pressure used in amorphous semiconductor deposition as well as the species of amorphous material used (Ge or Si) would affect the contact properties [26]. The present work seeks to investigate the role of fabrication parameters to increase understanding of which factors are important in producing electrical contacts with amorphous semiconductor layers to give low electronic noise and are stable with time. A detailed description of the present challenges is given in Chapter 4. Understanding these challenges and developing the technology should yield an improved fabrication process that reliably produces high-performance, position-sensitive HPGe detectors. A systematic study of the amorphous layer properties that contribute to successful passivation of HPGe detectors could also yield improvements in other detectors, such as coaxial detectors or point contact detectors.

## 1.2 Dissertation Overview

This chapter has introduced the topic of germanium-based radiation detectors, which provide excellent energy resolution combined with high detection efficiency to play a unique role in gamma-ray detection applications. The following chapter provides a basic description of radiation detection. Chapter 3 covers the basic knowledge necessary to understand the present work, including the basics of semiconductors and how germanium compares to other radiation detector materials, an overview of germanium detector structure and operation, and a description of germanium detector geometries and types of electrical contacts. The introductory material concludes with Chapter 4, where the present challenges in HPGe detector development are summarized. Specific effects are discussed with characterization methods for each.

Chapters 5-7 describe the detector fabrication process development efforts the author has conducted in order to investigate the effect of the fabrication process on detector leakage current, long-term stability of contacts, and inter-electrode charge collection on segmented detectors. Each chapter is a self-contained study, with an introduction to the challenge, past research efforts in that area, experimental methods used in this study, results, and conclusions.

Chapter 8 gives overall conclusions for the entire work and future prospects. A series of appendices describe some of the experimental methods in greater detail for those interested in reproducing the results.

# Chapter 2 Radiation Detectors

This chapter describes the basic elements of a radiation detector, with an emphasis on semiconductor radiation detectors. The important concepts are described for each major component of a radiation detector system. First, radiation interactions in the absorbing material are outlined, then an overview of the signal readout electronics is given.

## 2.1 Detector Systems

Radiation detector systems are designed to gain some information about incident radiation, which may include gamma-rays, ions, electrons, neutrinos, or other energetic particles. Key goals of a measurement often include the rate of incoming particles, their energy, timing information, and interaction position information.

A radiation detector system consists of two major components: an absorber and an electronic readout system. Many types of detector systems exist that rely on different physics to provide information carriers produced by the incident radiation, but all require a particle to interact in the absorber. While other types utilize the generation of phonons or breakup of Cooper pairs, semiconductor detectors utilize ionization in the absorber due to radiation interactions to create a signal. Some detectors use the scintillation photons created in the recombination of electrons and ionized atoms to measure the properties of the incident particles. Gas ionization detectors utilize an electric field to separate the electrons and positively charged species from ionization, thereby inducing a charge on nearby electrodes. All of these detector types have an external electronic circuit that is designed to extract features of the particle interactions, such as the energy, time, or position, and maximize the precision of the measurement. Figure 2.1 shows a schematic diagram of the basic components of a radiation detector system. The absorber in this context is a piece of semiconductor material where radiation interactions cause ionization. A preamplifier is typically used to measure the magnitude of the detector response; characteristics of the rising edge of the pulse can give timing information, the pulse shape can help with position sensing, and the pulse height is related to the deposited energy. In order to maximize the signal-to-noise ratio, a shaping amplifier can be used on the preamplifier output. The energy measurements for individual events are usually placed in a histogram to form an energy spectrum for energy spectroscopy.

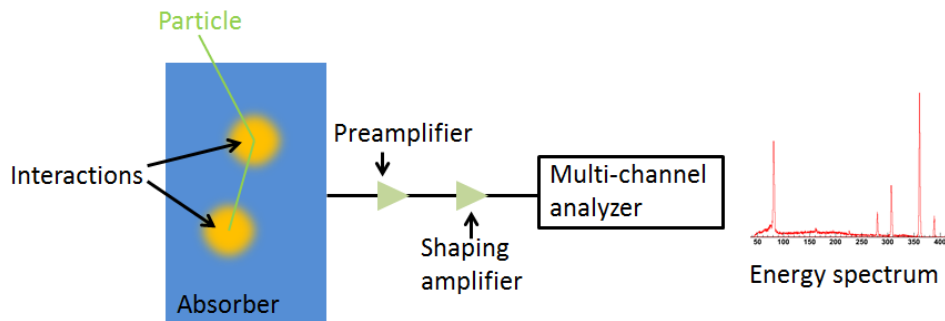


Figure 2.1. Schematic of the basic components of a radiation detector system.

## 2.2 Radiation Interactions

In order to detect the presence or measure the properties of incident particles, they must interact with the absorber. The nature of the radiation interaction dictates aspects of the detector design such as the absorber size and the packaging. For example, high-energy gamma-rays do not readily interact with matter, so detector volumes of at least several  $\text{cm}^3$  are often needed to acquire the necessary number of interactions in a reasonable time period. Neutrinos have an even smaller probability of interaction, so detector sizes are typically many  $\text{m}^3$ . By contrast, the greater challenge with charged particles is energy loss in insensitive material surrounding the detector, but the particle energy can be absorbed in a relatively small detector volume. This section gives an overview of radiation interactions, with special attention given to gamma-rays because of their ubiquity in real-world environments. Although natural isotopes often emit multiple types of radiation, the charged particles are easily absorbed in surrounding matter and gamma-rays are more readily observed at a distance.

### 2.2.1 Gamma-Ray Interactions

Gamma-rays are energetic photons with keV-MeV energies. Photon interactions are discrete and random in nature, and attenuation follows an exponential dependence on distance traveled within a material. The absorption coefficient  $\mu$  describes how quickly radiation is attenuated in matter and is a property of the intervening material and the photon energy.

A beam of radiation incident on some material, having intensity  $I_0$  before entering the material, has intensity [30] (p. 53)

$$I = I_0 e^{-\mu t} \quad (1)$$

after passing through the material some distance  $t$ .

Figure 2.2 shows the absorption coefficients in germanium due to various photon attenuation processes. The blue dotted line shows attenuation due to Compton (incoherent) scattering, the pink line shows attenuation due to photoelectric absorption, the cyan line shows attenuation due to pair production, and the green line shows the total attenuation from the three individual interactions combined. The energy dependence of each interaction type is different, and one type usually dominates attenuation at a particular energy. For example, photoelectric absorption in germanium dominates below about 100 keV, and Compton scattering is dominant between 100 and 1000 keV. The discontinuities around 1 keV and 11 keV coincide with the lower edges of atomic energy levels in germanium.

The gamma-ray interactions in ionization detectors (of which semiconductor detectors are an example) are sensed indirectly by the energy imparted to electrons in the matter by photon interactions. The electrons, being a charged particle, transfer energy to the surrounding material in a continuous and localized manner. Secondary radiation may be produced, such as x-rays or Auger electrons, that interacts with nearby absorber material or escapes the detector.

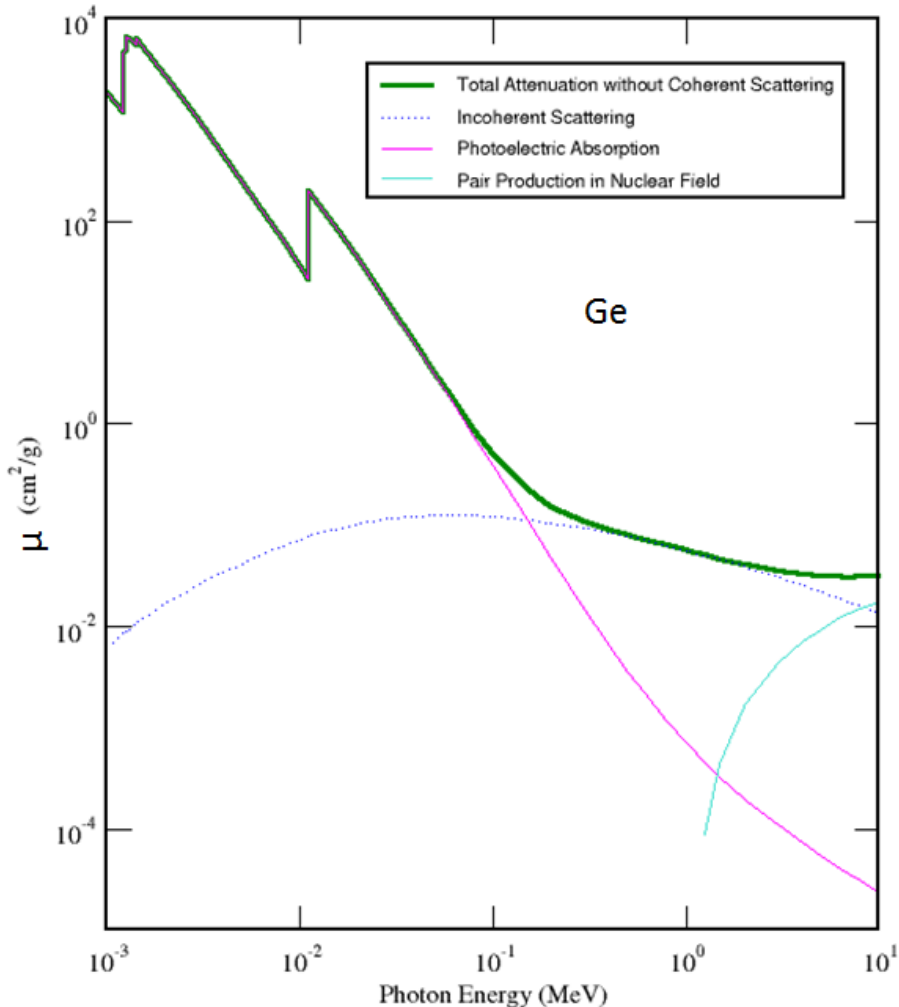


Figure 2.2. Energy dependence of photon interaction mechanisms in germanium for the gamma-ray energy range. [29]

## 2.2.2 Charged Particles and Other Particles

In contrast to gamma-rays, charged particles such as ions or electrons interact continuously via the Coulomb force as they travel through matter. Although most of the energy deposition occurs when the particle has slowed down near the end of its travel, some energy is lost as soon as it enters the absorber. Since semiconductor detectors invariably have an inactive layer, or “dead layer,” on the outside and are sometimes surrounded by an enclosure, the charged particle can lose significant energy before it enters the active region of the absorber. This property necessitates a small dead layer on the outside of the detector when it will be used for charged particles. For ions, the detector does not need to be as large to absorb the incident radiation as is needed for gamma-rays, but the dead layer thickness becomes much more important for ions than for gamma-rays. Other particles, such as neutrinos, are very difficult to detect because of the extremely small probability of interaction with any matter. Detectors for these particles tend

to be very large ( $\sim 10\text{-}100 \text{ m}^3$ ) in order to facilitate a sufficient number of interactions in a reasonable time period.

## 2.3 Signal Generation

This section covers the methods used in radiation detectors to measure the properties of radiation interactions in the absorber. The interaction generates some information carriers, specifically charge carriers in the context of semiconductor detectors. The external readout circuit is designed to measure properties of the interaction such as energy, timing, or position. The output is subject to electronic noise that increases the uncertainty on these measurements. Electronic processing of the readout pulse is normally conducted to maximize the signal-to-noise ratio. A thorough description of detector readout is given by Knoll [30] and Spieler [31].

### 2.3.1 Information Carriers

In semiconductor detectors, energy deposited by radiation interactions causes some electrons to surmount the bandgap energy into the conduction band. Band structure is discussed in more detail in Chapter 3. The information carriers in these detectors are electrons and holes (the vacancy of an electron in the valence band). Other classes of detectors utilize different physics, with a major distinction being the amount of energy required to produce an information carrier. For phonon-based detectors, this is typically a few meV, while in germanium ionization detectors it is 2.96 eV [32]. On the other end of the spectrum, gas detectors require about 30 eV per information carrier [30] (p. 130) and scintillator/photomultiplier tube detectors often need over 100 eV for one information carrier [30] (p. 330).

For energy spectroscopy, the number of information carriers is counted in order to give a measurement proportional to the energy deposited in the detector. Statistical variation in the number of information carriers creates some uncertainty in the energy measurement. The statistical variance is

$$\sigma_{\text{statistical}}^2 = FN, \quad (2)$$

where  $N$  is the number of information carriers and  $F$  is called the Fano factor. The number of information carriers is related to the measured energy by  $N = \frac{E}{W}$ , where  $W$  is the average energy required to form an information carrier. The standard deviation as a fraction of the measured energy is

$$\frac{\sigma_E}{E} = \frac{\sigma_{\text{statistical}}}{N} = \frac{\sqrt{FN}}{N} = \sqrt{\frac{FW}{E}}. \quad (3)$$

From this expression we can see that it is desirable to create more information carriers for a given energy deposited, or, put another way, a lower value of  $W$  is helpful to energy resolution.

Semiconductor detectors have less statistical variation than what would be expected from statistical variation. The peak width at a given energy is reduced by the Fano factor  $F$ , about 0.11 for germanium [33]. About 1/3 of the energy deposited by gamma-rays contributes to ionization [31], while the rest goes to phonon creation. The phonons are not observed in conventional ionization detector technology, but variation in their number must be offset by a

variation in the number of electron-hole pairs to conserve energy. The variation in ionization pairs (the observed quantity) is less than the standard variance based on the mean electron-hole pair creation energy  $W$  and the deposited energy  $E$ .

The electrons and holes created by ionization move in an applied electric field, which induces a mirror charge on the electrodes and generates the output signal. The Shockley-Ramo theorem [34] [35] describes the geometry dependence of this charge induction using the weighting potential, an imaginary quantity useful for predicting pulse characteristics. An excellent review is given by He [36] showing the utility of this method for semiconductor radiation detectors. An overview of this concept is also described in Appendix D.

### 2.3.2 Pulse processing

Gamma-ray spectroscopy is performed by measuring the amplitude of individual pulses from radiation interactions in a readout scheme known as pulse-mode readout. A schematic of this readout scheme is shown in Figure 2.3. In this example, positive bias  $V_b$  is applied to the left side of the detector and the right side is at ground potential. Holes drift toward the right and electrons drift toward the left. The electrode on the right side is instrumented with a charge-sensitive preamplifier, which produces a voltage pulse with a height proportional to the amount of induced charge on the electrode. In the example pulse shown in Figure 2.3, the fast rising edge has a voltage proportional to the amount of charge induced on the attached electrode and the output exponentially decays to the baseline level.

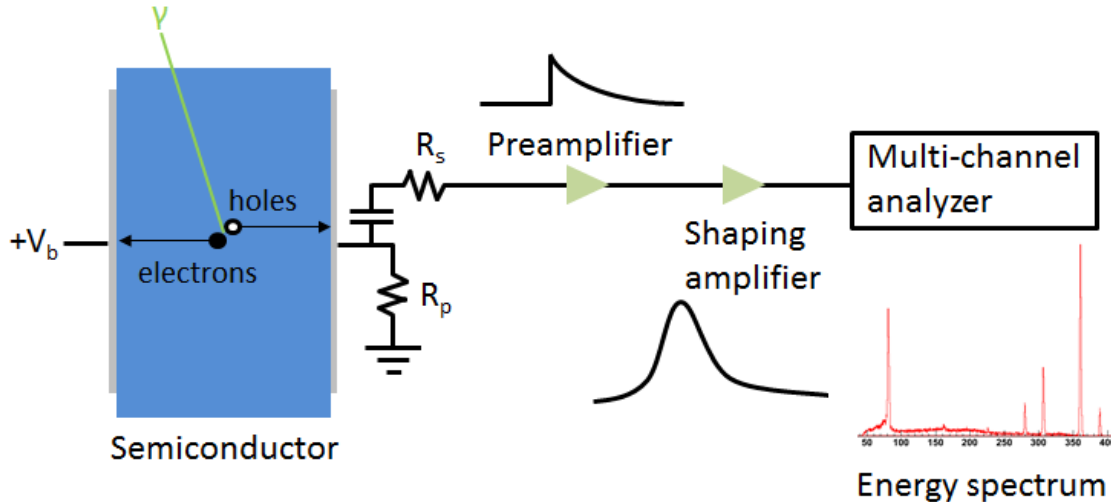


Figure 2.3. Schematic of a semiconductor detector circuit.

The preamplifier output pulse magnitude in semiconductor detectors is typically a few hundred mV in amplitude, but electronic noise often adds a significant amount of uncertainty to the pulse height. The precision of the pulse height measurement can be increased by amplifying and “shaping” the preamplifier output to increase the signal-to-noise ratio. A shaping amplifier is designed to narrow the bandwidth (thereby reducing noise) and quickly return the signal to the baseline level.

A multi-channel analyzer senses the maximum voltage of the shaped pulse and increments a histogram for each radiation event to form an energy spectrum of all events in a data run. Gamma-ray spectra have many unique features, and the reader is referred to Knoll for a complete description [30]. Here it is sufficient to say that a more precise energy measurement is preferable for analyzing spectra. The energy resolution is usually given as the full-width at half maximum (FWHM) for a full-energy gamma-ray peak. For example, HPGe detectors generally have less than 2 keV FWHM at 662 keV.

### 2.3.3 Electronic Noise

The signal induced on electrodes in semiconductor radiation detectors is subject to some uncertainty from electronic noise. The characteristics of the noise are affected by the external electronic components shown in Figure 2.3. Some resistance  $R_p$  in parallel with the detector is common, especially when a coupling capacitor is used. Some series resistance  $R_s$  may also exist between the detector and the charge-sensitive preamplifier.

The variance due to electronic noise is

$$\sigma_{electronic}^2 = [WQ_n]^2, \quad (4)$$

where  $Q_n$  is the electron equivalent noise charge, a measure of the noise excursions in terms of sensed charge. Electronic noise is not dependent on energy, as is statistical uncertainty. Equivalent noise charge is given by [31] (p. 34)

$$Q_n^2 = \left( 2qI_d + \frac{4kT}{R_p} \right) F_i \tau + 4kT R_s F_v \frac{C_d^2}{\tau} + F_f C_d^2. \quad (5)$$

The first term is current noise, or parallel noise, and increases with shaping time  $\tau$ . It consists of shot noise associated with the detector leakage current  $I_d$  and thermal noise (or Johnson noise) associated with the parallel resistance  $R_p$ . Other terms include the electronic charge  $q$ , Boltzmann constant  $k$ , device temperature  $T$ , and amplifier shape factor  $F_i$ .

The second term is voltage noise or series noise. It decreases with shaping time and depends on series resistance  $R_s$  and input capacitance  $C_d$ .  $F_v$  is the amplifier shape factor for this term. The third term is called 1/f noise, named after its noise power spectrum. This term also depends on input capacitance and a shape factor  $F_f$ . Important references for electronic noise contributions are a paper by Radeka [37] and Helmuth Spieler's book *Semiconductor Detector Systems*.

The different noise contributions have varying dependence on the shaping time, which is related to the frequencies that will be most strongly amplified. By selecting an appropriate shaping time and limiting the bandwidth of the amplifier, one can reduce the noise contribution [31] from either current noise or voltage noise and find a minimum noise value [37]. Figure 2.4 shows example calculated values of equivalent noise charge  $Q_n$  as a function of shaping time  $\tau$ . The blue and red lines show the current noise contributions from shot noise and thermal noise, respectively. The green line shows the voltage noise contribution, the magenta line shows the 1/f noise contribution, and the black curve is the total  $Q_n$  value. Example values of leakage current, parallel resistance, series resistance, and input capacitance typical for a Ge strip detector were chosen for this illustration. The shaping amplifier, either an analog device or a digital algorithm,

can be optimized to use the shaping time corresponding to a minimum noise contribution. The output of the shaping amplifier is sent to a multi-channel analyzer or analyzed using digital techniques.

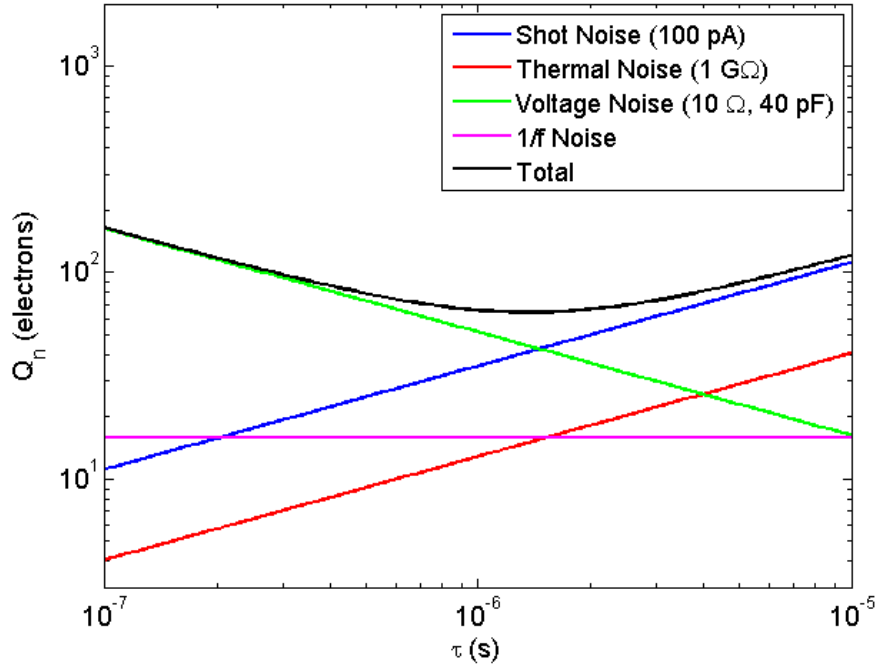


Figure 2.4. Example calculated value of equivalent noise charge as a function of shaping time.

# Chapter 3 Germanium-Based Radiation Detectors

This chapter gives an overview of the basic operation and structure of high-purity germanium (HPGe) detectors. First, a review of important semiconductor material properties is given to cover the Fermi level, energy bands, electrically active impurities, and charge carrier motion. The material properties of germanium are described in the context of other important semiconductor radiation detector materials. The next section covers the basic structure of germanium detectors with a historical overview of germanium detector development, common detector geometries, requirements for electrical contacts and surface passivation, and the types of electrical contacts used on HPGe detectors. This final section introduces amorphous semiconductor contacts in detail and motivates their use on HPGe detectors.

## 3.1 Semiconductor Material Properties

Semiconductors are a class of materials whose crystal structure gives rise to a series of energetically forbidden regions of energy for electrons in the lattice. The conductivity varies vastly with temperature and other material properties. This section describes some material properties, including the Fermi level and the bandgap along with characteristics of charge carrier motion in semiconductors. Properties of various important semiconductor detector materials are compared, highlighting the significance of germanium as a detector material.

### 3.1.1 The Fermi Level

Electrons are Fermions and therefore obey the Pauli exclusion principle, which states that two of these particles cannot occupy identical states [38]. In a system with many electrons, such as a semiconductor crystal, electrons must occupy higher energy states than they otherwise would because the lower states are filled. The energy of the highest filled state for a free electron gas at absolute zero temperature is called the Fermi level [38], represented by the symbol  $E_F$ . The electrons in a semiconductor crystal can be approximated as a free electron gas and the Fermi level gives a material-specific energy reference level. The number of filled energy states at energy  $E$  is given by the Fermi function  $f$ :

$$f = \frac{1}{e^{\frac{E-E_F}{kT}} + 1}. \quad (6)$$

The function  $f$  depends on temperature  $T$  because of thermal excitation of the particles in the uppermost energy levels. The Boltzmann constant  $k$  relates temperature to a characteristic thermal energy  $kT$ . The Fermi function is shown for various temperatures in Figure 3.1 with relevant band levels for germanium as a reference. The intrinsic Fermi level for germanium is at 0.35 eV above the valence band and 0.35 eV below the conduction band. The significance of these bands is discussed in the next subsection. At 0 K, the Fermi function has a value of one for all energies below  $E_F$ , and a value of zero for all energies above  $E_F$ . At successively higher temperatures, the step becomes less defined, giving more electrons at higher energies. Generally, electrons within about  $3kT$  of the Fermi level are the ones free to move about.

However, if the electrons are prevented from gaining a small amount of kinetic energy due to forbidden energy values, their movement may be restricted.

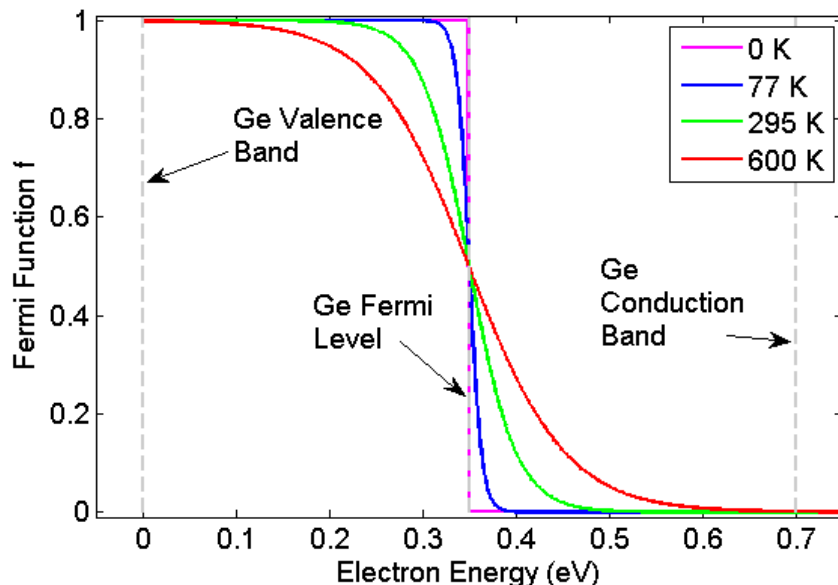


Figure 3.1. Fermi function at various temperatures with germanium reference levels.

### 3.1.2 Energy Bands

When atoms are placed in a regularly spaced lattice, electrons moving in that lattice can undergo Bragg scattering with the lattice atoms. Due to the wave nature of the electrons, constructive or destructive interference causes some energies to be allowed and others to be forbidden. This gives rise to the energy band structure of solids, where some regions of energy are occupied by electrons and others are completely empty.

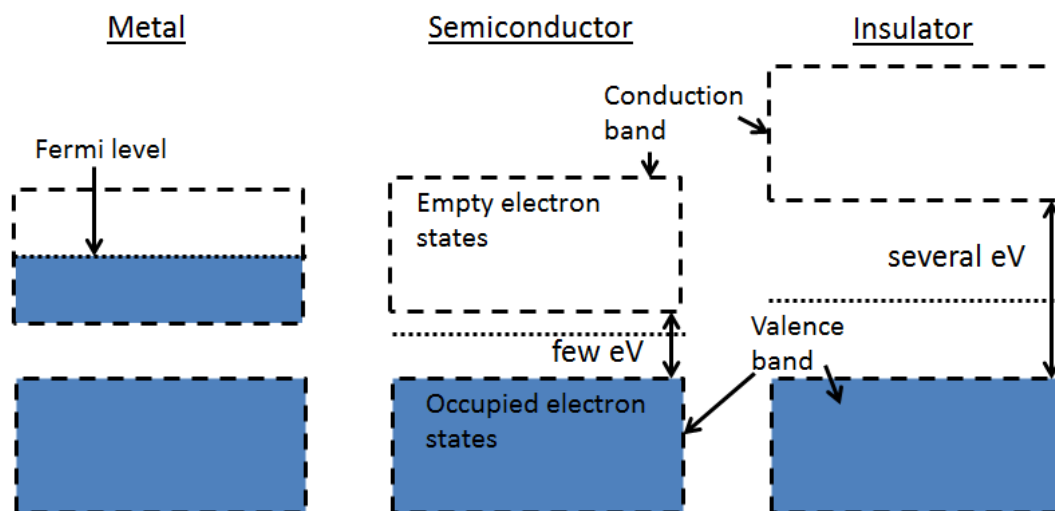


Figure 3.2. Classes of crystalline solids defined by energy band structure.

The spacing of the energy bands and relative placement of the Fermi level makes for different classes of materials, as shown in Figure 3.2. Metals have a Fermi level within an allowed energy band or an allowed band and forbidden band overlap in energy. Electrons near the Fermi level are free to gain a small amount of kinetic energy and move about the crystal. Semiconductors and insulators have their Fermi level in a forbidden band, which is called the bandgap. The allowed bands below the Fermi level are almost completely filled by electrons, which do not move. The band immediately below the bandgap is called the valence band. The band immediately above the bandgap is called the conduction band because electrons in this band can move freely and contribute to conduction.

The absence of an electron in the crowded valence band also allows conduction. The vacant state moves much like a particle, so it is convenient to treat it as a positively charged particle, called a “hole.” Holes move easily in the valence band and contribute to current in an equivalent fashion to electrons moving in the conduction band, only holes move in the opposite direction of electrons in an electric field.

Insulators have a relatively large bandgap ( $>3$  eV), while semiconductors have a relatively small bandgap. Semiconductors occupy a unique position among materials because the Fermi level is in a forbidden energy band that is small enough that the material resistivity changes dramatically over a small temperature range. The bandgap is an important parameter in detectors because it is related to the amount of energy needed to form an electron-hole pair [39]. Table 3.1 shows the bandgap, average electron-hole pair creation energy, density, and average atomic number of some common semiconductor detector materials at room temperature [31] (p. 85). Germanium has a lower bandgap and correspondingly lower electron-hole pair creation energy than other semiconductor detector materials, giving lower statistical uncertainty in the number of electron-hole pairs created by a radiation interaction.

**Table 3.1. Material properties of selected semiconductor detector materials.**

Material	Bandgap at 300 K (eV)	e-h pair creation energy (eV)	Density (g/cm <sup>3</sup> )	Mean Z
Si	1.12	3.6	2.33	14
Ge	0.67	2.96	5.33	32
Cd <sub>0.9</sub> Zn <sub>0.1</sub> Te	1.57	4.64	5.78	49.1

The smaller bandgap, however, precludes operation of germanium as a radiation detector at room temperature due to the number of thermally generated electron-hole pairs. Even in the lowest leakage current configuration possible, germanium still has excessive leakage current at room temperature on the order of  $\mu\text{A}$  [31] (p. 457) due to thermal generation of electron-hole pairs. This gives electronic noise amounting to at least 10 keV at typical shaping times, much larger than the typical  $\sim 1$  keV values in HPGe detectors operated at cryogenic temperature. By contrast, a Si p-n junction may have only a few nA of reverse-bias leakage current [31] (p. 457), which can still give acceptable performance. The thermal generation current depends on the size of the depletion region and scales linearly with the intrinsic charge carrier concentration [31]. This quantity, denoted by the symbol  $n_i$ , can be calculated by the overlap of the Fermi function and the density of states for either the conduction band (for electrons) or valence band (for holes). Using the empirical expression for the intrinsic charge carrier density by Conwell [40],

the number of free charge carriers at room temperature (300 K) for germanium is  $2.5 \times 10^{13} \text{ cm}^{-3}$  and near liquid nitrogen temperature (77 K) the intrinsic carrier concentration is  $1.9 \times 10^{-6} \text{ cm}^{-3}$ . The leakage current due to thermally generated charge carriers is reduced by over ten orders of magnitude, showing the necessity of cooling germanium detectors. However, other materials can be attractive because of their ability to operate at room temperature. For example, Si has an intrinsic carrier concentration of  $6.7 \times 10^{10} \text{ cm}^{-3}$  at 300 K [40], in line with the  $10^3$  reduction in p-n junction leakage current indicated by Spieler [31] (p. 457). CdZnTe has a room temperature intrinsic carrier concentration of  $2 \times 10^5 \text{ cm}^{-3}$  [41], potentially giving orders of magnitude further improvement over Si if ideal blocking contacts could be formed. Materials like CdZnTe are attractive because of the possibility for low-leakage room temperature operation, but the charge collection properties are not as favorable as those of germanium.

Since the semiconductor material acts as the radiation absorber, a higher atomic number and density increase detection efficiency for gamma-rays [31]. Germanium, with an atomic number of 32 and density of  $5.323 \text{ g/cm}^3$ , is more appropriate for absorbing higher energy gamma-rays than Si, but not as efficient as materials like CdZnTe that have even higher atomic numbers.

### 3.1.3 Electrically Active Impurities

Semiconductor materials contain various impurities that may form states within the bandgap. Shallow states are characterized by the relatively small energy gap ( $\sim 10 \text{ meV}$ ) between them and an allowed energy band. The impurity states themselves are spatially localized and do not form a band. Figure 3.3 shows several electrically active impurity levels in germanium. The numbers above or below each state indicate the difference in eV between that state and the nearest allowed energy band. The shallow states (B, Li, P, etc.) are virtually entirely ionized at liquid nitrogen temperature (where  $3kT$  is about 0.02 eV) and above.

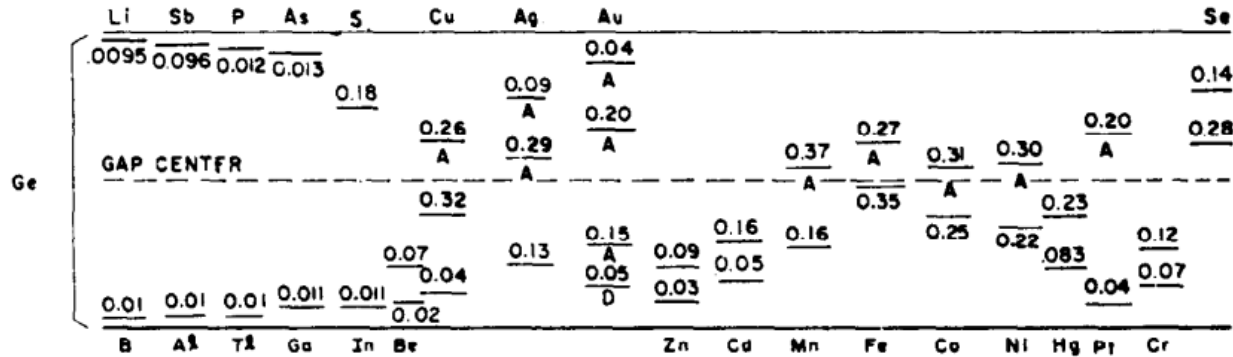


Figure 3.3. Impurity levels in units of eV for germanium crystal with selected elemental impurities. [42]

Group III elements such as boron are called p-type impurities, or “acceptors,” because they form states close to the valence band and easily contribute a hole to the valence band. Group V elements like phosphorus form states near the conduction band and easily contribute an extra electron to the conduction band. These are called n-type impurities, or “donors.” A semiconductor crystal will naturally have more of one impurity type than the other. The net electrically active impurity concentration determines whether the crystal is called “n-type” or “p-type.” The impurity states are associated with an atom in the crystal lattice, which remains fixed

even if the electron or hole moves away. HPGe typically has a net electrically active impurity concentration between  $\sim 4 \times 10^9 \text{ cm}^{-3}$  and  $\sim 2 \times 10^{10} \text{ cm}^{-3}$ .

Electrically active impurities are sometimes introduced purposefully to control the semiconductor material properties. Shallow level impurities can be added by diffusion or ion implantation to “dope” a region of the semiconductor crystal. For radiation detectors, this is done to form a p-n diode junction for charge injection blocking. When many donors are introduced to a region of semiconductor, it is called an  $n^+$  region. For acceptors, it is called a  $p^+$  region. The + superscript indicates a high level of doping above  $\sim 10^{16} \text{ cm}^{-3}$ .

### 3.1.4 Charge Carrier Movement

In order to obtain near-complete charge collection, charge carriers must move efficiently in the semiconductor crystal. The relationship between drift velocity and electric field is

$$\vec{v} = \mu \vec{E}, \quad (7)$$

where  $\vec{v}$  is the velocity vector,  $\vec{E}$  is the electric field vector, and  $\mu$  is a proportionality factor called the mobility. The mobility is generally a material property for a specific charge carrier type, but material quality and other external factors can affect the mobility and charge carrier motion. Table 3.2 shows typical mobility values for electrons and holes in selected radiation detector materials at their typical operating temperatures, which is room temperature for Si and CZT and liquid nitrogen temperature for Ge.

**Table 3.2. Charge carrier mobility and lifetime for selected radiation detector materials.**

Material	Hole mobility $\mu_h \text{ (cm}^2/\text{V}\cdot\text{s)}$	Electron mobility $\mu_e \text{ (cm}^2/\text{V}\cdot\text{s)}$	Hole lifetime $\tau_h \text{ (s)}$	Electron lifetime $\tau_e \text{ (s)}$	$\mu_h \tau_h \text{ (cm}^2/\text{V)}$	$\mu_e \tau_e \text{ (cm}^2/\text{V)}$
Ge (77 K)	42000 [43]	36000 [44]	$2 \times 10^{-4}$ [45]	$2 \times 10^{-4}$ [45]	$> 1$ [31]	$> 1$ [31]
Si (300 K)	450 [47]	1350 [47]	$2 \times 10^{-3}$ [46]	$> 10^{-3}$ [46]	$> 1$ [31]	$> 1$ [31]
CZT (300 K)	30 [48]	1100 [48]	$1 \times 10^{-6}$ [46]	$3 \times 10^{-6}$ [46]	$5 \times 10^{-5}$ [2]	$5 \times 10^{-3}$ [2]

Figure 3.4 shows experimental data for electron drift velocity in HPGe as a function of electric field for two different crystallographic directions. Charge carriers move with varying levels of efficiency, depending on the charge carrier motion with respect to the crystal orientation. The crystal direction is specified as a Miller index, a vector relative to the unit lattice. In germanium, the  $\langle 100 \rangle$  direction generally has the highest drift velocity for moving charge carriers, so HPGe detectors are normally operated so that charge carriers drift in this direction, when possible.

The drift velocity generally increases with electric field strength, although some secondary effects in HPGe can cause decreasing charge carrier velocity with increasing electric field above a few kV/cm [44]. Termed negative differential mobility, this is mainly due to population of higher bands (due to the higher carrier energy) and non-parabolicity of the bands [44]. Figure 3.4 shows experimental data for electron drift velocity in HPGe as a function of electric field and Figure 3.5 shows the corresponding data for holes. After achieving a maximum velocity around 2-3 kV/cm, the electron velocity tends to decrease with greater field strength. There is a less pronounced but similar effect for holes. For this reason, the target range for electric field

magnitude is generally around a few kV/cm throughout the active detector volume to ensure adequate charge carrier collection.

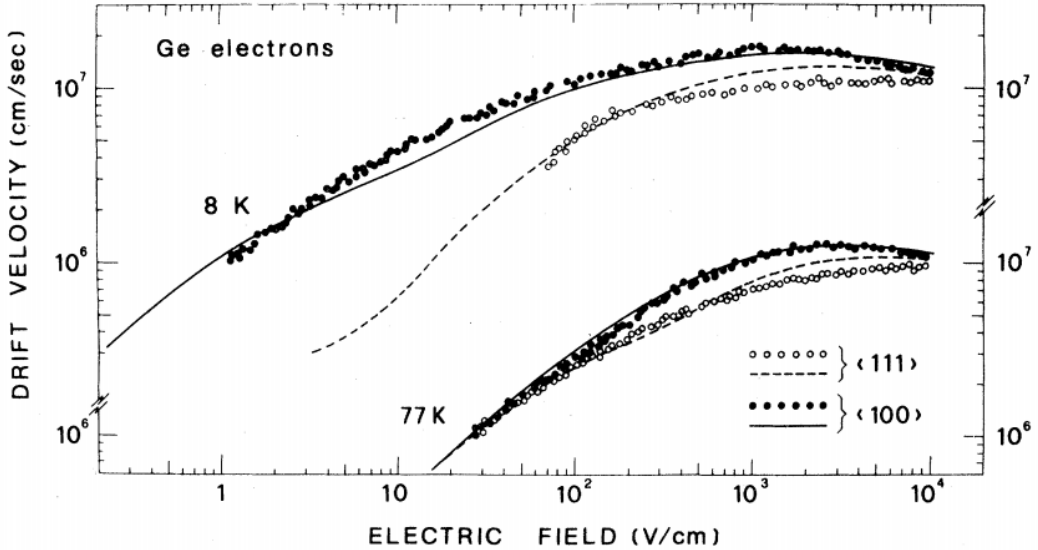


Figure 3.4. Electron drift velocity in germanium as a function of electric field. Data are presented at 8 K (upper axis labels) and 77 K (lower axis labels), with different markers representing two crystallographic directions. [44]

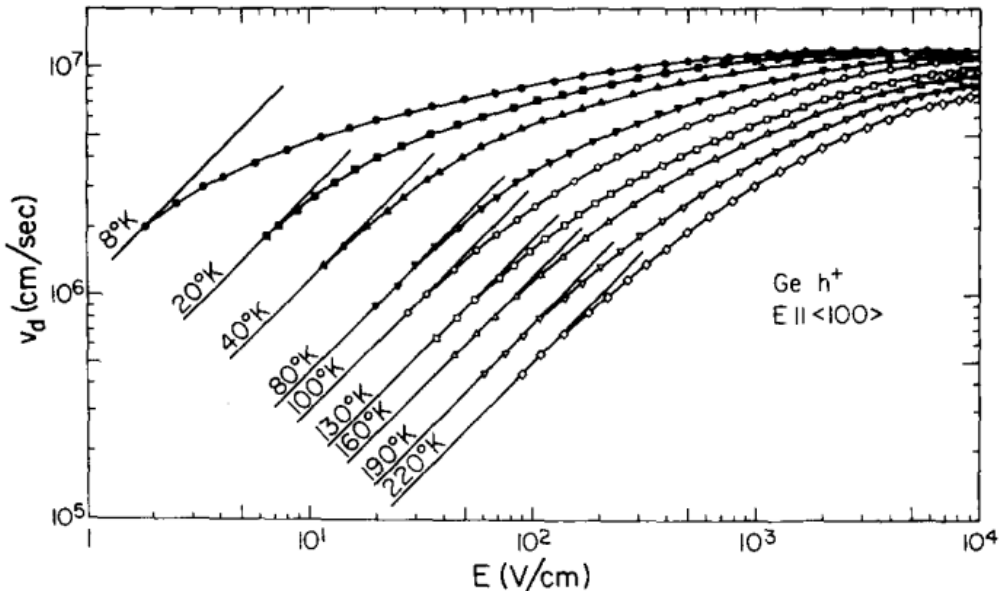


Figure 3.5. Hole drift velocity in germanium as a function of electric field. Data are presented at various temperatures for the <100> crystallographic direction. [43]

Mobility is influenced by two scattering effects [49]. The first, dominant at lower temperature, involves Coulomb scattering of charge carriers on ionized impurities. With a  $T^{3/2}$  theoretical dependence, this shows the largest effect when the thermal velocity of carriers is low,

so that more interactions occur between carriers and impurities. This type of scattering increases with impurity concentration. Lattice scattering becomes dominant at higher temperatures as lattice atom vibrations increase, giving an increased likelihood that an atom will be significantly out of place as a carrier passes, disrupting the traveling wave nature of the carrier. Lattice scattering temperature dependence is approximately  $T^{-3/2}$ , although this can depend on lattice material due to varying levels of contribution from optical and acoustic phonons. Figure 3.6 shows this dependence schematically. There is an optimum temperature for highest mobility, a balance between lattice and impurity scattering. However, HPGe has a low enough impurity concentration that the optimum mobility is reached at a colder temperature than is reasonably achievable through normal means of cooling [44], so increasing temperature generally implies lower carrier mobility for germanium. Figure 3.7 shows experimental data for the low-field electron mobility and low-field hole mobility in germanium at various temperatures. At saturation velocity ( $\sim$ kV/cm fields), the dependence of mobility on temperature is weak.

Another important quantity for semiconductor material is the carrier lifetime, a measure of the average time a carrier exists in an allowed band before occupying a non-conduction-band, immobile state. Occupying such a state means the carrier will be immobilized until it is freed by re-excitation or disappears by recombination. Very shallow states may exist only a fraction of an eV below the conduction band and carriers will quickly escape, while some states may exist deeper in the bandgap, meaning longer average time to acquire necessary thermal energy to escape. In a detector, trapped charges may not be observed within the collection time if they are significantly delayed compared to normal drift times, creating lower-amplitude signals whose magnitude depends on drift distance within the detector. This is generally an undesirable effect, and therefore longer average carrier lifetime is best for radiation detector materials.

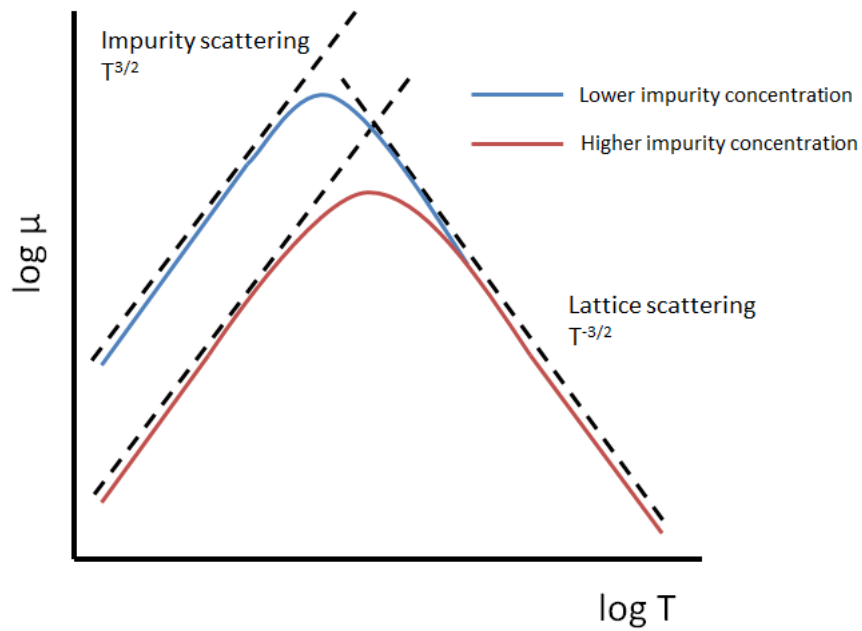


Figure 3.6. Illustration of theoretical mobility dependence on temperature.

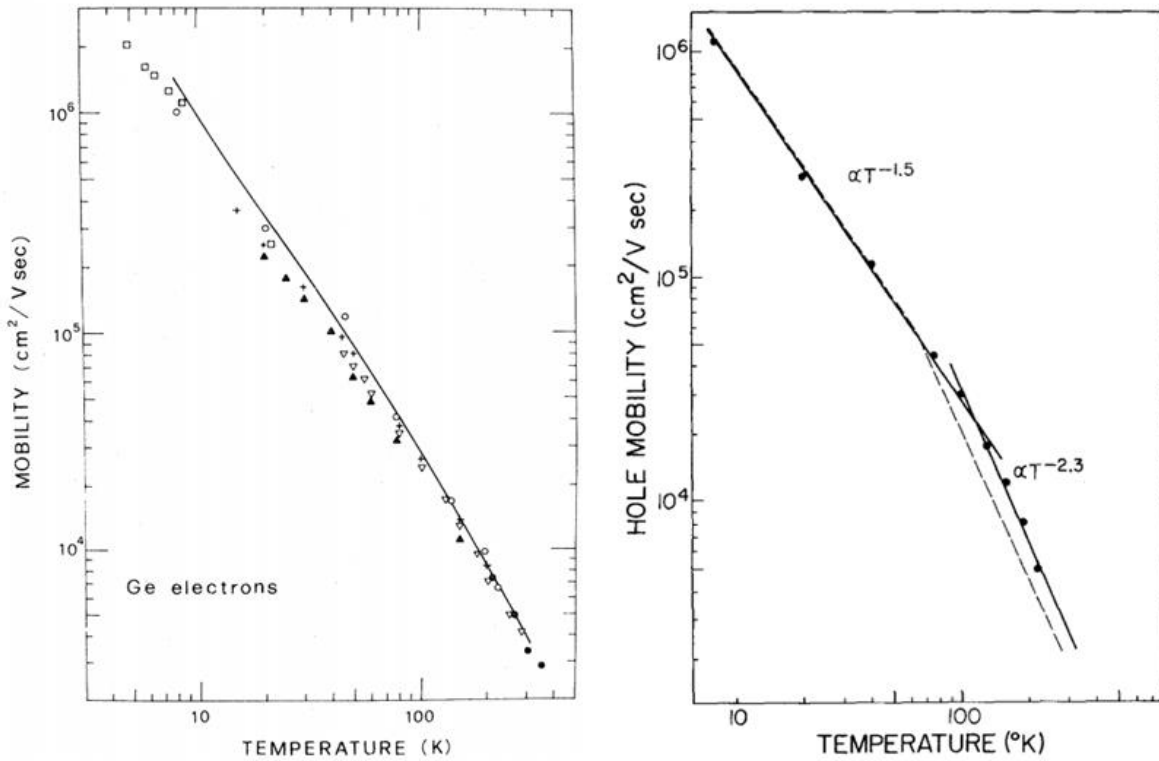


Figure 3.7. Charge carrier mobility in germanium as a function of temperature. The left panel shows electron mobility [44] and the right panel shows hole mobility [43]. The data points indicate experimental measurements and the solid lines show theoretical dependence.

The mobility and lifetime together give an important measure of material suitability for radiation detector applications [2] [50]. Greater mobility results in higher drift velocity for moving charge carriers, meaning they can quickly move to electrodes and contribute to a usable signal before encountering trapping centers. A higher lifetime represents a longer average time that the charge carriers move freely. A good combination high mobility and lifetime translates into full charge collection, meaning better detector performance. Table 3.2 shows this quantity for common detector materials. The characteristic drift length for a charge carrier is given by  $\mu\tau E$ . For high charge collection efficiency, it is best to have  $\mu\tau E \gg d$ , where  $d$  is the detector thickness. Germanium has been useful for detectors because of its favorable material properties. The density and atomic number are higher than Si, giving better detection efficiency for high-energy gamma-rays. The  $\mu\tau$  product is greater than  $1 \text{ cm}^2/\text{V}$ , high enough that efficient charge collection avoids signal degradation. Although other room-temperature semiconductor materials with high density and atomic number have been developed, relatively low  $\mu\tau$  product has slowed their implementation as highly performing gamma-ray spectrometers [2]. For example, a typical  $\mu\tau$  product in CdZnTe is about  $10^{-3}$ .

## 3.2 High-Purity Germanium Detectors

The previous section examined germanium in the context of other semiconductor detector materials and discussed general properties of semiconductors. In this section, the discussion is narrowed to high-purity germanium detectors. A brief historical overview is given, then common HPGe detector geometries are described and classes of electrical contacts are presented with theory relevant to each. Amorphous semiconductor contacts are presented as a viable alternative to conventional contacts, giving an advantage in the segmented detector fabrication process. These contacts will be the focus of the following chapters.

### 3.2.1 Historical Overview

Germanium detectors originated with the lithium-drifted, or Ge(Li) detector in the 1960s [3]. In this era, germanium could only be grown in sizable crystals with net ionized impurity concentration around  $10^{13} \text{ cm}^{-3}$ , not pure enough to deplete the large volumes needed for efficient gamma-ray detection. To overcome this limitation, lithium was added to one side of the p-type germanium crystal, diffused into the crystal as it was heated, and then “drifted” to fill appropriate sites in the crystal through the application of a specific voltage bias scheme [51]. Through this complex method, Li donors could precisely cancel acceptor impurities, thus giving nearly zero net impurity concentration. The detector could be depleted, but the impurities could still cause charge carrier scattering and therefore reduce mobility. The most serious issue with Ge(Li) detectors is the requirement that they be quickly cooled (within 1 hour for best results [52]) after the drifting process and remain continuously cooled. Any interruption in cooling that allows the crystal to warm significantly will allow Li atoms to diffuse and disrupt the compensated impurity distribution. The detector becomes inoperable until the Li drifting process is repeated. The detectors could only be formed from p-type material and the hole-blocking contact was necessarily the junction formed at the Li-diffusion surface. The opposite contact was either an electron-blocking metal surface barrier or undepleted p-type germanium.

High-purity germanium was developed in the 1970s [53] [54] [55] to replace the lithium-drifted germanium detector. Germanium is refined by zone-melting [56], where an RF coil is repeatedly passed along the ingot, creating a moving zone of melted material. Most impurities have a higher solubility in liquid germanium than solid, so these will tend to move with the molten zone and be concentrated at one side of the ingot after the process is completed, giving material with a net electrically active impurity concentration of  $\sim 10^{12} \text{ cm}^{-3}$ . The germanium is then grown into a single crystal via the Czochralski crystal growth method. Germanium is melted in an inert crucible and a seed crystal is dipped into the liquid surface, then pulled slowly upward in the presence of hydrogen gas to passivate some crystal defects and impurities [57]. An impurity sequestering happens during growth of the single crystal such that the seed end tends to be p-type and the tail end tends to be n-type [53]. This method allows boules of reasonable size (100 mm diameter) to be grown with net ionized impurity concentration around  $10^9 \text{ cm}^{-3}$ . HPGe detectors allow more flexibility than Ge(Li) detectors because they can be formed from either p-type or n-type Ge material and allow different types of contacts to be used.

The state-of-the-art germanium spectrometer today is a large-volume coaxial geometry detector made of HPGe material with an n<sup>+</sup> hole-blocking contact and a p<sup>+</sup> electron-blocking

contact [58]. A protective surface coating is applied to the side surface. These detectors have a robust fabrication process, largely due to the thick Li-diffused  $n^+$  contact, and are commercially available. Most modern HPGe detectors are simple spectrometers and do not provide position sensing.

Segmented planar detectors based on p-n junction contacts have been developed [59] [60] [61] [17] [21]. These detectors add position sensitivity to the excellent energy resolution already provided by conventional HPGe detectors, but some issues with long-term stability were encountered [17]. Also, the gap between strips required new fabrication process development due to inter-strip charge collection [62]. Segmented coaxial detectors have also been developed to combine the position sensitivity with large detector volumes [63] [64]. Modern nuclear physics instrumentation systems such as GRETA and AGATA are utilizing this technology. Segmented detectors with amorphous semiconductor contacts have been developed to provide a simpler fabrication process with all HPGe surfaces protected by a surface coating [65] [20] [66] [26] [11]. With this technology, detectors have been produced with fine electrode spacing on the order of  $50\ \mu\text{m}$  [15]. Today, the challenges for detector development center around reliably producing highly-performing, position-sensitive detectors with large volumes.

### 3.2.2 Common Detector Geometries

A description of common germanium detector geometries is helpful in later discussions. It should aid in understanding the performance issues that are encountered and the effects described in the next chapter.

#### 3.2.2.1 Planar Detector

A planar detector can be fabricated by cutting a disc from a crystal boule and creating electrical contacts on the flat faces as shown in Figure 3.8.

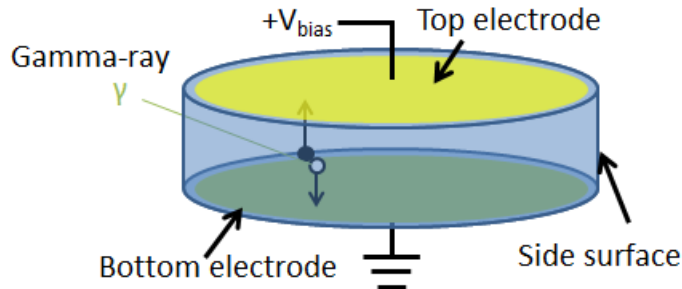


Figure 3.8. Illustration of a planar germanium detector.

The first generation of germanium detectors had this geometry. The construction of the detector is relatively simple because the contacts are created on flat surfaces. Calculation of the electric field is also simpler than other geometries. The diameter of a planar detector is essentially limited to available HPGe single-crystal boule diameters ( $\sim 100\ \text{mm}$ ), while the thickness is primarily limited by the ability to deplete the volume.

In order to operate the detector, a voltage  $V_b$  is applied to one contact so that this contact is like a reverse-biased diode. This reverse bias will enlarge the depletion region and cause some leakage current to flow. At the full depletion voltage  $V_d$ , the size of the depletion region reaches

the detector thickness  $d$ , and the detector is called “fully depleted.” Above this voltage, the electric field continues to increase linearly, as shown in Figure 3.9.

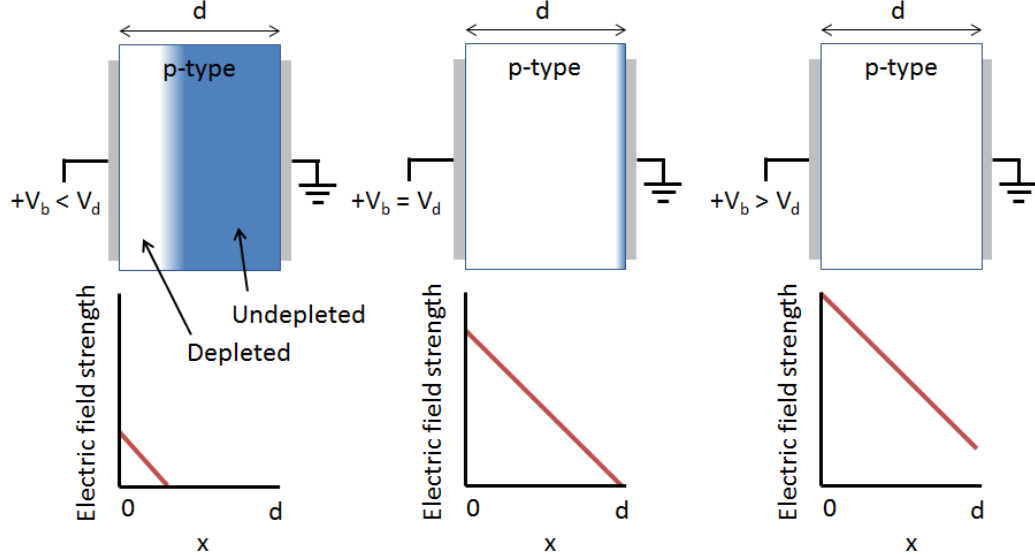


Figure 3.9. Illustration of depletion layer and electric field profile of a planar detector with varying bias.

The electric field magnitude at the top contact, assuming a constant impurity concentration throughout the detector, is [31] (p. 16)

$$E_{top} = \begin{cases} \sqrt{\frac{2qN_d}{\epsilon} V_b} & , V_b < V_d \\ \frac{V_b + V_d}{d} & , V_b > V_d \end{cases} . \quad (8)$$

Here  $q$  is the electronic charge,  $N_d$  is the net ionized impurity concentration, and  $\epsilon$  is the semiconductor dielectric constant. Ionized impurities in the semiconductor lattice represent a fixed space charge that tends to screen the electric field, reducing its magnitude linearly as a function of distance from the electrical contact. Above full depletion, the electric field magnitude as a function of depth in the detector is [31] (p. 17)

$$E(x) = \frac{V_b + V_d}{d} - 2V_d \frac{x}{d^2} , V_b > V_d . \quad (9)$$

The electric field magnitude at the bottom contact is [31] (p. 17)

$$E_{bottom} = \begin{cases} 0 & , V_b < V_d \\ \frac{V_b - V_d}{d} & , V_b > V_d \end{cases} . \quad (10)$$

In order to obtain a significant field throughout the volume, the detector must be “overbiased” with a voltage significantly greater than  $V_d$  to ensure a high field throughout the entire volume for efficient charge collection. Since the field profile has a slope given by the impurity concentration, it is critical to achieve a sufficiently low impurity concentration that the detector can be depleted at a reasonable voltage and has a relatively uniform field such that high

field at the bottom contact does not require an excessive field magnitude at the top contact. Figure 3.10 shows some calculated electric field profiles in a planar detector along with the field profile for a Ge(Li) detector. The latter case reveals the electric field from geometry alone, without the field screening effect from ionized impurity space charge, because it has been compensated by Li donors. The Ge(Li) detector has a constant electric field strength of  $V_b/d$ , while an HPGe detector will have a linearly varying field strength with an average value of  $V_b/d$ .

An integral part of testing a detector is determining the full depletion voltage so that the detector can be sufficiently overbiased during operation. The full depletion voltage is given by

$$V_d = \frac{qN_d d^2}{2\epsilon} . \quad (11)$$

One method of measuring full depletion voltage is a capacitance-voltage characteristic. A capacitor is formed by the electrode first near the depletion region and any undepleted material on the other side of the depletion region. Before any bias is applied to the detector, a thin capacitor is formed by the built-in depletion of the contact junction. As more bias is applied, the depletion region grows and the width of the capacitor increases. It reaches a maximum thickness when the depletion region reaches the opposite contact and the detector is fully depleted. A parallel plate capacitor has capacitance

$$C = \epsilon \frac{A}{d} , \quad (12)$$

where  $\epsilon$  is the dielectric constant of the intervening material (the semiconductor in this case),  $A$  is the cross-sectional area, and  $d$  is the distance between the plates. Since the detector capacitor is initially very thin, the capacitance is large. As a larger bias is applied, the thickness increases and the capacitance decreases. The capacitance reaches a minimum at full depletion and does not change with further applied bias.

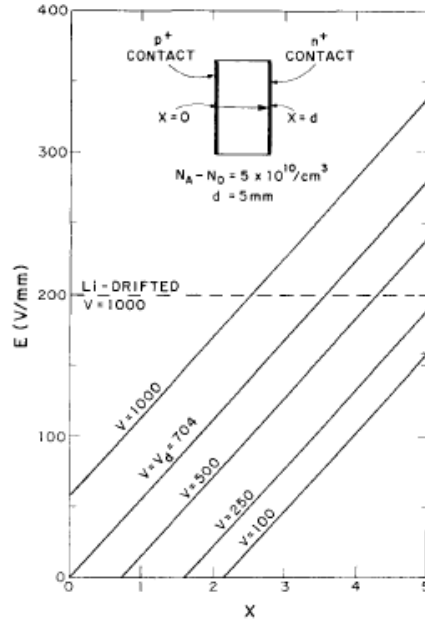
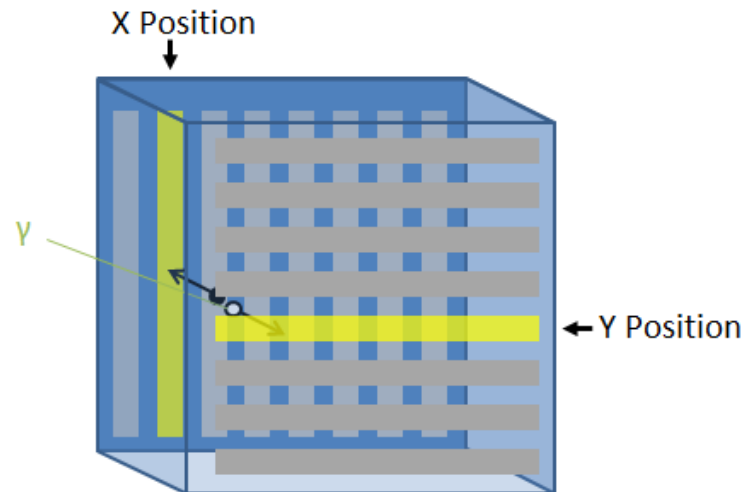


Figure 3.10. Illustration of electric field strength as a function of depth in a planar detector. [55]

### 3.2.2.2 Double-Sided Orthogonal-Strip Detector

A double-sided strip detector is a planar detector geometry with segmented electrodes on both faces to give two-dimensional position sensitivity. The electrodes form strips on the opposite faces of the crystal, with strips orthogonally oriented. Figure 3.11 shows a schematic of this electrode geometry, where the yellow strips indicate where most charge was collected for the interaction pictured.



**Figure 3.11.** Schematic illustration of the double-sided strip detector geometry. Separate electrodes give two-dimensional position sensitivity.

By distinguishing which strips have a signal, the horizontal interaction position is obtained from one side of the detector and the vertical position from the other. Since a signal is needed on both sides of the detector, it is required that both types of charge carrier be collected efficiently. This means a high  $\mu\tau$  product for both electrons and holes is needed.

This detector has the same electric field properties as a simple planar detector, but each electrode only senses charge in the nearby volume rather than the entire crystal. The interaction depth can be obtained by the arrival time difference of the charge carriers between the opposite sides [66]. For a detector with  $m$  strips on one side and  $n$  strips on the other, orthogonal strips effectively separate the detector into  $m * n$  pixels while needing only  $m + n$  readout channels, giving a reduced number of readout channels compared with a similar pixel detector.

### 3.2.2.3 Coaxial Detector

The coaxial detector geometry is another simple spectrometer type like the planar detector, but the geometry allows larger volume detectors to be fully depleted. Figure 3.12 shows a schematic of a closed-ended coaxial detector. A longer slice is cut from a crystal boule and formed into a cylinder. A well is bored out of the center from one side to form one contact. The opposite contact is the outer round surface and remaining flat face of the crystal. A non-contact side surface still exists on the back face between the center bore and outer surface. Most modern HPGe detectors are coaxial spectrometers because of the robust fabrication process and large detector volumes available.

The radial field profile for this geometry is shown in Figure 3.13. The geometry naturally gives a higher field near the inner contact, as seen for the Ge(Li) detector in Figure 3.13. In HPGe detectors, the impurity space charge screens the electric field as a function of distance. For this reason, coaxial HPGe detectors are constricted to deplete first from the outer contact to help even out the field profile. A few calculated field profiles are shown in Figure 3.13 for an HPGe detector depleted from the outside first.

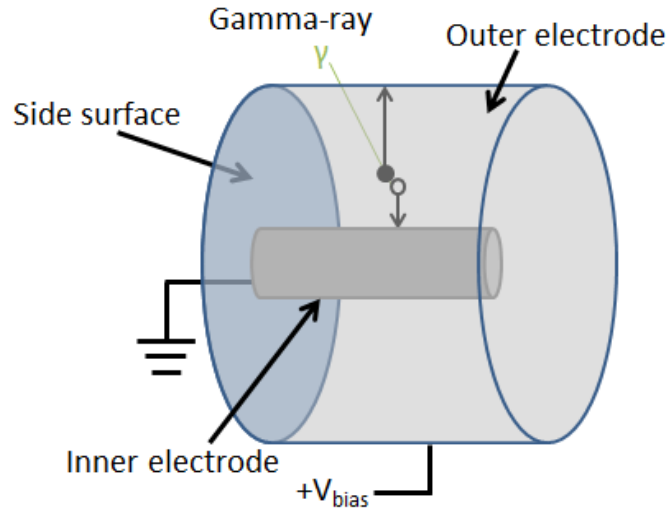


Figure 3.12. Schematic illustration of the coaxial detector geometry.

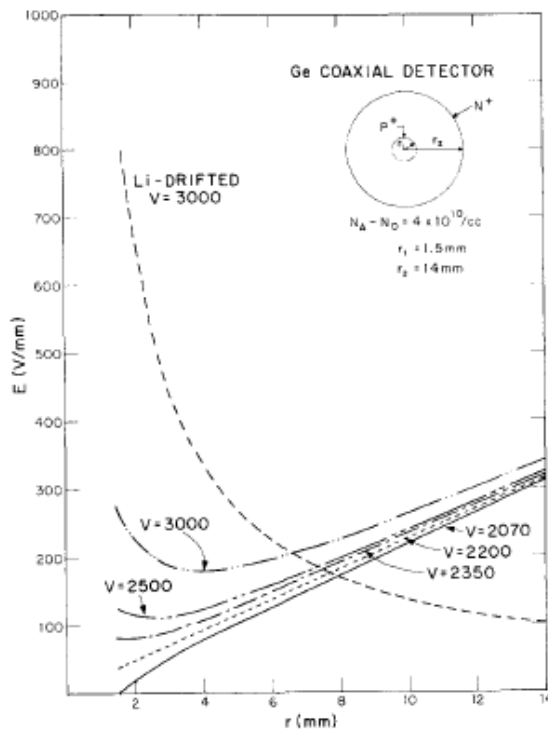


Figure 3.13. Calculated electric field strength as a function of radius in a coaxial germanium detector. [55]

A cylindrical geometry presents unique problems during processing. Most semiconductor processing and deposition equipment is designed for a flat wafer, so performing any operation on the non-flat surfaces can be challenging. Also, the inner bore is difficult to access and requires creative methods for forming the contact [55]. This detector geometry also has a side surface just like the planar geometry, which is not part of either contact. Care must be taken to protect this surface during some processing steps. One advantage the coaxial detector has over a planar detector is that the side surface affects a relatively smaller volume of the detector. The coaxial detector can be made longer, which keeps a constant side surface area but increases the detector volume.

### 3.2.2.4 Point Contact Detector

Another notable detector geometry is the point contact detector, a variation on the coaxial geometry. The n-type version was developed first [67] and the p-type, hole-collecting version more recently [68]. This design, shown in Figure 3.14, eliminates the center bore, instead opting for a small electrode on one circular face of the crystal with a small size to give small capacitance for reduced electronic noise. In Figure 3.14, a p-type point contact (PPC) detector is illustrated where holes are collected to the small contact and electrons are collected to the cylindrical face and flat, blank face.

The small electrode senses charge in only a small nearby volume. The rise time of the pulses is then short compared with overall drift time, meaning separate interactions in the crystal can be distinguished by arrival times. This allows discrimination between single-site and multi-site gamma-ray interactions in the detector.

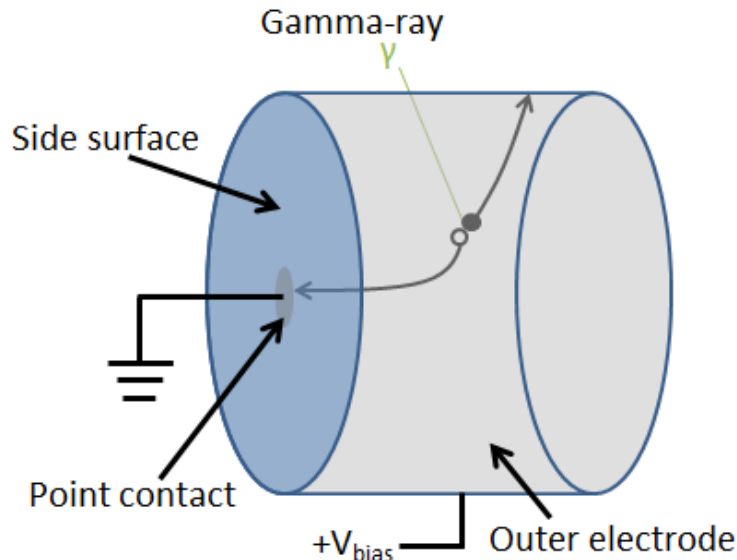


Figure 3.14. Schematic illustration of a p-type point contact detector.

The PPC geometry has many of the same features as the cylindrical geometry. The outer contact is the same, and a side surface still exists on one face between the point contact and the outer contact. The properties of this side surface can be a performance-limiting factor due to

surface leakage current and side surface charge collection [69]. In order to provide an electric field of the correct magnitude and direction in the center of the crystal, an impurity concentration gradient may be required.

### 3.2.3 Electrical Contact Properties

Electrical contacts play an important role on radiation detectors in minimizing leakage current. Contacts on opposite sides must block injection of the appropriate charge carrier to prevent current flow that would be many orders of magnitude higher than the expected signal from a radiation event. A reverse-biased diode is the typical charge injection blocking solution [31], blocking current flow in one direction and allowing it in the other. For a fully depleted detector, the positively biased contact must block hole injection and the negatively biased contact must block electron injection.

If the electrical contacts did not block charge injection, the semiconductor material would resistively drop the applied voltage, which in most cases would result in leakage current that is too high. Contacts that allow the free flow of charge in both directions are called ohmic contacts. To prove the case for blocking (non-ohmic) contacts, the semiconductor material can be examined in terms of its resistivity, which is given by

$$\rho = \frac{1}{nq\mu}, \quad (13)$$

where  $n$  is the carrier concentration of holes or electrons (one will dominate),  $q$  is the electronic charge, and  $\mu$  is the charge carrier mobility. Previously in this chapter, germanium was shown to have excessive leakage current at room temperature even with charge blocking. At 77 K, the leakage current is very low with blocking contacts, but with ohmic contacts the current is much too high. At this temperature, the carrier concentration is dominated by impurities, which can be as low as  $5 \times 10^9 \text{ cm}^{-3}$ . Using (13) and a mobility of  $4 \times 10^4 \text{ cm}^2/\text{V}\cdot\text{s}$ , this translates to a resistivity of  $31.2 \text{ k}\Omega\cdot\text{cm}$ . Assuming a cube 1 cm on a side, applying 1000 V across the detector would give 32 mA of leakage current. This is far beyond the limit for low-noise charge measurement. Similarly, high-purity Si can be grown with a resistivity of 50  $\text{k}\Omega\cdot\text{cm}$ , but using the same geometry and voltage, a leakage current of 20 mA would flow. However, this is not the case for all detector materials. CdZnTe can be grown with a resistivity of  $3 \times 10^{10} \Omega\cdot\text{cm}$ , which would give only 30 nA with the same assumptions as before. In conclusion, germanium detectors need charge injection blocking contacts, even at liquid nitrogen temperature, to achieve the low leakage current needed to operate as a high-resolution radiation detector.

The overall current flow in a detector under voltage bias comes from a few primary sources. The total current can be described by

$$I_{tot} = AJ_{hi} + AJ_{ei} + I_{surf} + I_{bulk}, \quad (14)$$

where  $A$  is the device cross-sectional area. Figure 3.15 illustrates these current sources, where holes (open circles) are repelled by the positively biased electrode at left and electrons (black circles) move away from the grounded, more negative electrode at right.

$I_{tot}$  is the current that is measured to pass through the detector. Forward-traveling holes and backward-traveling electrons generate a positive current and are indistinguishable in a current

measurement. The total current is the sum of four primary current contributions in ( 14 ). It is always desirable to reduce the total leakage current to minimize shot noise in the charge measurement.

Charge carrier injection at the contacts is described by the diode equation and scales with surface area. Separate contributions from hole injection ( $J_{hi}$ ) and electron injection ( $J_{ei}$ ) give charge carriers of opposite polarity moving in opposite directions, contributing to current flow in the same direction. In general, only contact area adjacent to depleted detector volume will contribute to these two terms. The leakage current injected at the contacts is a property of a particular contact and can be parameterized based on the different physics of the contact technologies, to be discussed later in this chapter.

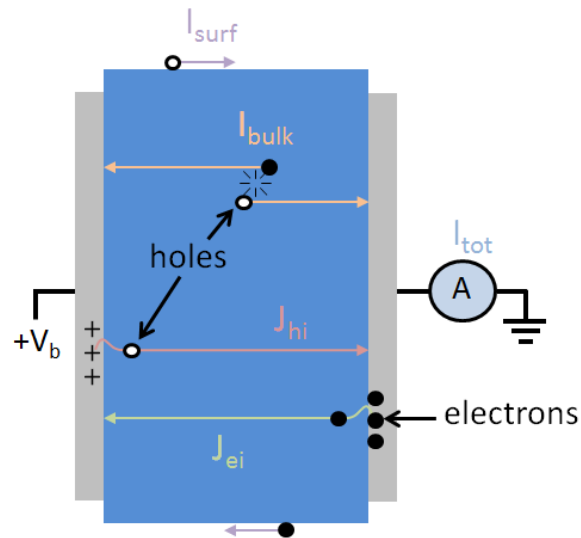


Figure 3.15. Sources of current in a radiation detector.

$I_{surf}$  is current flow along the outside surface due to a combination of surface states, which differ from bulk states due to the lack of 3D crystalline periodicity, and foreign materials adsorbed on the surface. This current flow is of a different nature than injection at the contacts and increases with temperature. The effects of this current may be mitigated by adding a guard ring electrode around the perimeter of the contact, taking up the surface current and leaving the center electrode(s) to see only non-surface current. A planar detector with a guard ring is pictured in Figure 3.16. A guard ring relaxes the requirement to minimize surface current, although fluctuations in the guard ring current can couple into readout electrodes, increasing electronic noise. Also, any resistance between the guard ring and ground can cause the guard ring to float to a higher potential than the center electrodes, which would put a stringent requirement on the resistance between the guard ring and other electrodes.

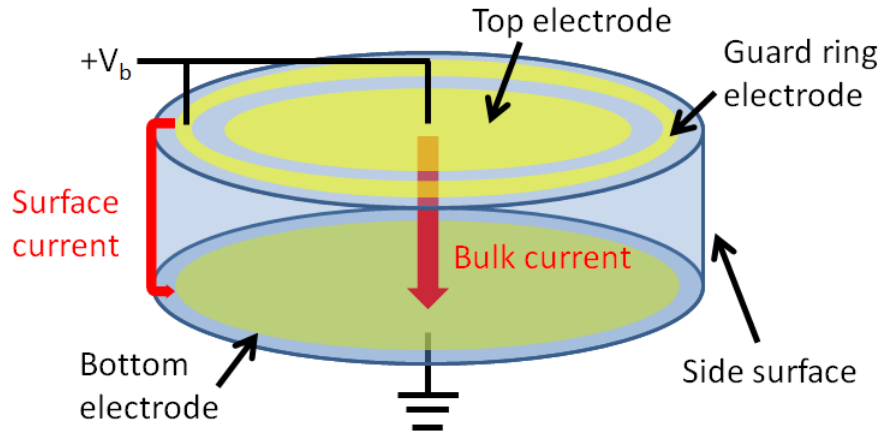


Figure 3.16. Illustration of a planar detector with a guard ring electrode configuration.

$I_{bulk}$  is current flow due to thermal generation of electron-hole pairs in the bulk material. This term increases with the depleted volume in the detector and dominates the leakage current in germanium at room temperature. At liquid nitrogen temperature, the thermally generated leakage current is much less than 1 pA and has no noticeable effect on electronic noise.

Since the surface current and bulk current can be reduced by other means, the charge injection at the contacts can be left as the primary contributor to detector leakage current. The necessity of a particular electric field magnitude was discussed in the previous section, which sets constraints for suitable electrical contact design. The contacts must allow application of significant electric field ( $\sim$ kV/cm) while injecting low leakage current. It is usually desirable to keep the total leakage current on sensing electrodes low enough that the electronic noise contribution to energy resolution is not significantly greater than the uncertainty from statistical variations.

### 3.2.4 Surface Passivation Properties

The exposed surface of single-crystal germanium can be quite sensitive to contaminants [5] [17] [70] [71]. The contact surfaces are somewhat resistant to surface contamination because electrical contacts have an inherent dead layer on the outermost surface. The non-contact side surfaces are a particular concern, however, because the germanium crystal is exposed. Additionally, for segmented detectors, the surface between electrodes must be considered.

Any contaminants deposited on an exposed germanium crystal surface can change the charge state on the surface, which changes the electric field in the nearby detector volume. Surface contaminants can also lower the surface resistivity, giving additional leakage current on surfaces that must hold a potential difference across the surface.

A protective layer, or “passivation,” is sometimes applied to protect the exposed crystal surface. The protective layer must be thin to prevent a large dead layer and have high resistivity to prevent excessive leakage current along the surface. The interface properties are also important, since any charge buildup at the surface will change the electric field in the nearby active detector volume. Amorphous silicon [72] and amorphous germanium [28] have been demonstrated as acceptable passivation layers on semiconductor detectors.

### 3.2.5 Types of Electrical Contacts

Contacts on high-purity germanium may be placed into a few categories based on the physics of how they operate. These different types reflect historical advances in the technology, yet there are advantages and disadvantages to each. All display blocking behavior, but they differ in achievable injection leakage current and specific behavior. Table 3.3 summarizes some key features of the classes of contacts discussed in this section.

This section describes the general properties of these classes of contacts used on HPGe detectors, concluding with the amorphous semiconductor contact technology that will be the focus of this dissertation. The relevant physics of each type of contact is described.

**Table 3.3. Summary of key features for the different classes of electrical contacts on HPGe detectors.**

Contact Type	Advantages	Disadvantages
Ion-implanted (B)	Thin, good electron blocking	No hole blocking, additional processing needed for segmentation
Li-diffused	Robust, good hole blocking	Thick, changes with time, transition region, difficult to segment, no electron blocking
Metal Schottky barrier	Thin, simple to construct, easily segmented, good electron blocking	Poor hole blocking, not robust, some lack of reproducibility
Amorphous semiconductor	Thin, blocks holes or electrons, doubles as passivation, easily segmented	Electron or hole blocking inferior to p-n junction, wide range of film properties

#### 3.2.5.1 Ion-Implanted Contacts

Ion implantation is a reliable process for forming a  $p^+$  or  $n^+$  region in semiconductors by bombarding them with energetic ions that form acceptor or donor states in the crystal after they come to rest. This technique can be used to create a thin layer a fraction of a micron in thickness that is highly n-type or p-type [73]. Boron, a group III element, is most commonly used in germanium as a p-type dopant to form an electron-blocking contact [74] [60]. Phosphorus is a common n-type dopant that has met with limited success in germanium to block hole injection [75]. Phosphorus does not seem to immediately occupy an adequate donor lattice site upon implantation, requiring annealing to achieve a sufficiently high carrier concentration. The damage after the contact formation process leaves a defect region susceptible to electrical breakdown at moderate electric field magnitude [76]. Boron-implanted contacts, on the other hand, do not require such annealing.

A schematic of a detector with a B-implanted contact is shown in Figure 3.17. The contact is sufficiently thin for most detector applications. The layer is low resistivity, so segmentation of electrodes on this contact surface requires etching through the implantation layer, leaving a bare surface that either requires an additional passivation step [59] or operating unpassivated [77]. The B-implanted region forms part of a p-n junction that acts as a diode. Figure 3.18 shows the band diagram and built-in depletion region for a p-n junction at thermal equilibrium. The bandgap  $E_g$ , conduction band (CB), valence band (VB), and Fermi level  $E_f$  are indicated on the

band diagram. The built-in voltage  $V_{bi}$  is the difference between the Fermi levels of the p-type and n-type material. For each type of charge carrier, a concentration gradient drives diffusion toward the other side of the junction, giving current directed toward the right of the diagrams below. Charge carriers in the depletion region experience electric field drift that moves current toward the left side of the diagrams. At equilibrium, the diffusion current and electric drift current are of opposite direction and equal magnitude, so no net current flows.

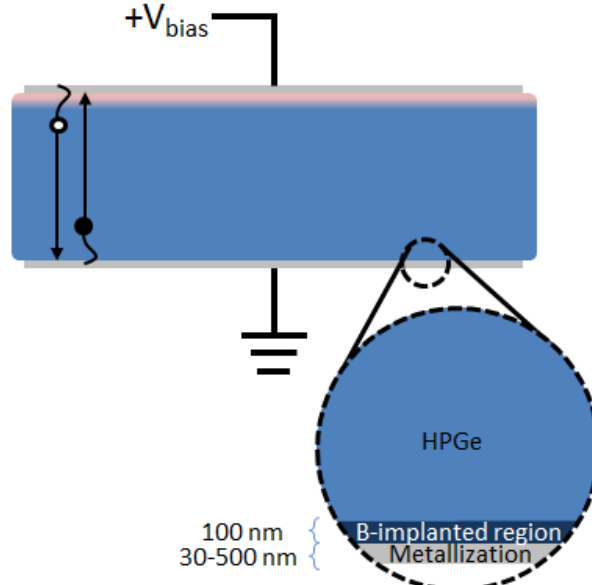


Figure 3.17. Illustration of a detector with a B-implanted contact.

The center diagram of Figure 3.18 shows a forward-biased junction, meaning the p-type side is positively biased with respect to the n-type side. The applied bias  $V_a$  counteracts the built-in voltage and the depletion region decreases. The diffusion current increases beyond the drift current and a positive current flows. Conversely, when the junction is reverse-biased by applying a negative voltage to the p-type side as shown in the right diagram, drift current dominates, giving a negative current value.

The current-voltage behavior for the p-n junction is given by [49]

$$J = J_s \left[ e^{\frac{V_a}{kT}} - 1 \right], \quad (15)$$

where  $J$  is the current per unit area,  $J_s$  is the saturation current,  $V_a$  is the voltage across the junction,  $k$  is the Boltzmann constant, and  $T$  is the temperature. For forward bias, defined as  $V_a > 0$ , the term in brackets increases rapidly as seen in Figure 3.19. For  $V_a < 0$ , or reverse bias, the current approaches a constant value, the saturation current.

An HPGe detector with ion-implanted contacts is operated as a reverse-biased diode to take advantage of the low and constant value of reverse bias current. The attainable leakage current is low enough that electronic noise is not significantly impacted for temperatures below 140 K [78].

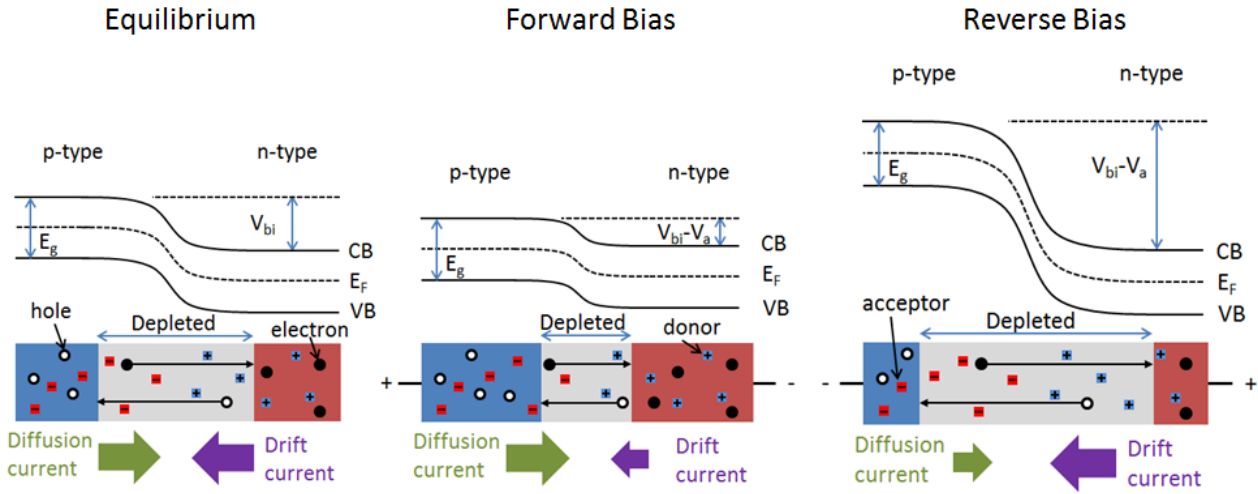


Figure 3.18. Band diagram and depletion region for a p-n junction at equilibrium, forward bias, and reverse bias.

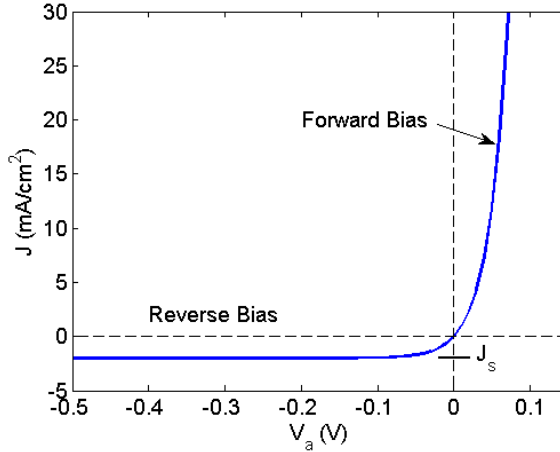


Figure 3.19. Example of an ideal diode current-voltage characteristic.

### 3.2.5.2 Li-Diffused Contacts

While many electrically active impurities occupy substitutional sites on the crystal lattice, lithium is unique in that its small atomic diameter allows it to occupy interstitial sites and readily diffuse throughout the crystal. Diffusion of Li occurs much more rapidly than other impurities in germanium; at  $700^\circ \text{ C}$  (a temperature where data for several elements are available), the diffusion coefficient for B, As, P, and other elements is below  $10^{-11} \text{ cm}^2/\text{s}$  [79], while it is nearly  $10^{-5} \text{ cm}^2/\text{s}$  for Li [80]. Li acts as a shallow donor energy state in germanium, making the crystal more n-type with increasing Li concentration. The rapid diffusion allows a p-n junction to be formed without using ion implantation, thus avoiding the associated radiation damage.

Li-diffused contacts are formed by depositing Li (usually by evaporation) on the surface of the germanium crystal and then heating the crystal to facilitate rapid diffusion of Li into the lattice. Li diffuses inward from the surface source and creates a p-n junction that blocks holes

using the same physics as described in the previous section. Excessive heating is undesirable for germanium because it decreases carrier lifetime as it facilitates diffusion of other impurities on the surface into the crystal, creating charge carrier traps. The diffusion is carried out over a few minutes at 300-400° C in order to provide adequate diffusion depth but avoid significant Li concentration throughout the entire crystal [81]. This process is identical to the first step in creating a Li-drifted Ge(Li) detector, but instead of drifting the Li donors throughout the crystal volume to compensate acceptor impurities, the HPGe material far from the Li-diffused contact is kept intact.

The Li forms a gradual diffusion profile in the germanium, giving a significant donor concentration up to 1 mm thick. This is advantageous because the contact is robust and resilient to surface defects because such damage rarely reaches deep enough to pass the undepleted contact region. However, such a thickness is a disadvantage for highly interacting x-rays or charged particles because of the larger dead layer. The contact thickness is by contrast to the p-n junction formed by ion implantation, which forms an abrupt and highly doped region that is contained in a ~100 nm layer. Li diffuses somewhat rapidly at room temperature, so repeated temperature cycling can have an effect on the performance of this contact, primarily in the form of a thickening dead layer. Even at operating temperature, the contact may thicken appreciably over the span of years [72] [82]. In addition, the gradual doping profile can create a transition region where the electric field is too low to reliably drift carriers, but significant numbers of them still make it to the active region. This creates pulses with a slow rise time, which can contribute to the low-energy background [83]. Figure 3.20 shows a detector with a Li-diffused contact to show its structure.

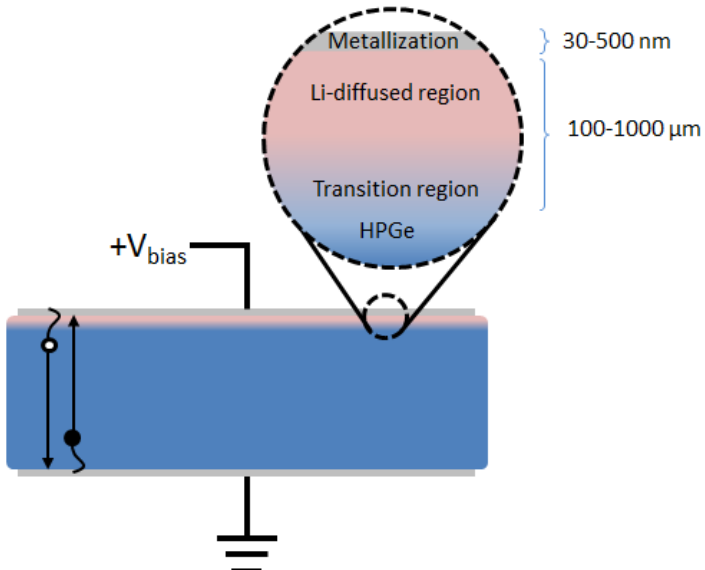


Figure 3.20. Illustration of a detector with a Li-diffused contact.

Li diffusion is a reliable contact technology, but applications are limited by the contact thickness. Measurement of low-energy photons and charged particles incident on the Li-diffused contact is hampered by the large dead layer. This can be mitigated by careful removal of

additional material to form a thinner dead layer [84]. Segmenting a Li-diffused contact can be difficult as the low resistivity requires physically separating electrodes, an arduous process that requires material removal up to a millimeter between the electrodes [62] [85]. Etch processes have some finite aspect ratio and mechanical cutting is limited by the tool size. A mask for the Li evaporation is possible, but this is limited by the diffusion profile of Li, keeping the strip spacing to a minimum of about 1 mm [61]. Additionally, diffusion of Li can change the performance over time or with temperature cycling.

### 3.2.5.3 Metal Schottky Barrier Contacts

A simple method of forming a contact on germanium is a metal in physical contact with the crystal. To ensure reliable electrical contact with no intervening oxide or other foreign layer, the metal is usually deposited directly on the germanium by evaporation or sputtering. Figure 3.21 shows an illustration of a metal Schottky contact on a germanium detector. These contacts are simple to fabricate and may be segmented using a shadow mask during deposition. The metal is only a few tens of nm thick and the contacts do not have a significant dead layer. However, adhesion and general mechanical robustness can be an issue with such a thin layer of metals that may not adhere well to germanium [86].

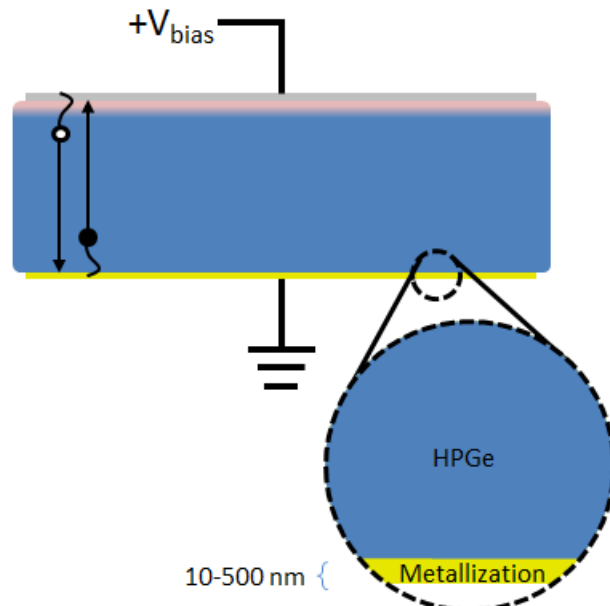
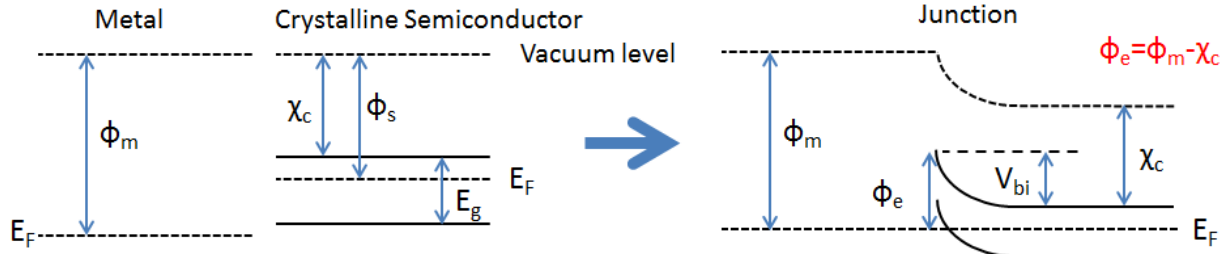


Figure 3.21. Illustration of a metal Schottky contact on germanium.

The Schottky model describes a junction between a metal and a crystalline semiconductor [87]. This model is based on alignment of energy levels of electrons in a solid and describes the energy required for an electron in the metal to move into the semiconductor. Figure 3.22 shows a schematic of a metal-semiconductor junction, where the vertical axis is increasing electron energy and the horizontal direction is one spatial dimension. Besides an intermediate region within  $\sim 3kT$  of the Fermi level, all electron states are occupied below  $E_F$  and unoccupied above  $E_F$ . The metal work function  $\phi_m$  is the potential difference between the vacuum level (free

electron) and the metal's Fermi level, where conduction occurs. The quantity  $\phi_m$  is the energy required to move an electron out of the metal into vacuum. The semiconductor also has a work function  $\phi_s$ . However, most electron conduction in the semiconductor side occurs at the bottom of the conduction band, with energy  $\chi_c$  below the vacuum level. The bandgap is also shown as  $E_g$ .



**Figure 3.22.** Band structure of a metal-semiconductor junction according to the Schottky model. The left picture shows the materials when separated and the right picture shows when the two are brought into contact and reach thermal equilibrium.

When the two solids are joined, electrons from one side of the junction may reach a lower energy by shifting to the other material until the Fermi levels are equalized and thermal equilibrium is achieved. The right side of Figure 3.22 illustrates this condition. If there is a shift of charge carriers, minimum energy is reached but electrical neutrality is no longer locally conserved. This manifests itself as bending of the semiconductor bands near the junction. In the illustration of Figure 3.22, electrons moved from the semiconductor to the metal after initial contact, leaving a region of positive space charge in the semiconductor region near the metal and forming a small depletion region and a built-in voltage  $V_{bi}$ . Overall charge is still conserved, so a thin layer of negatively charged electrons exist at the interface to cancel the positive space charge in the depletion region. An energy difference  $\phi_e$  is required for an electron to move from the metal to the semiconductor. This is known as the electron barrier height and is given by

$$\phi_e = \phi_m - \chi_c. \quad (16)$$

According to this model, the barrier height depends only on these two material properties. Notable quantities not included in this description are semiconductor typeness and impurity concentration or a description of the interface surface. In order to create a large electron barrier height on a particular semiconductor, one would simply use a metal with the highest possible work function. This explains why gold has often been used as a metal Schottky contact on germanium [5] [88]. Table 3.4 shows  $\phi_m$  for selected metals.

In this example, holes move freely between the two sides because the valence band, where holes easily move, intersects the Fermi level. In order to provide a hole barrier, a low work function metal such as magnesium would be used. Since hole energy increases in the direction of decreasing electron energy, the hole barrier is measured in the downward direction from the Fermi level to the valence band edge. The hole barrier height is given by

$$\phi_h = \chi_c + E_g - \phi_m. \quad (17)$$

If the Fermi level lies within the semiconductor bandgap, a barrier may exist for both holes and electrons.

**Table 3.4. Work function of selected metals. [89]**

Element	Work function (eV)
Ag	4.6
Al	4.2
Au	5.3
Co	5.0
Cr	4.5
Hf	3.9
Mg	3.66
Nd	3.2
Pd	5.22
Pt	5.64
Y	3.1

According to Schottky theory, metals with high work function such as Au or Pd should be used to give a high electron barrier and low work function metals like Al or Mg should give a high hole barrier. However, in practice, all metals tend to give a large electron barrier and a low hole barrier [86]. An effect called Fermi level pinning [90] causes the Fermi level of the metal to align with the germanium band levels in a way that is dependent on the surface states as well as the metal work function. Accounting for this effect, the electron barrier is given by [86]

$$\phi_e = a(\phi_m - \chi_c) + (1 - a)(E_g - \phi_0), \quad (18)$$

where  $a$  is the pinning coefficient and  $\phi_0$  is the intrinsic Fermi level of the germanium crystal. An  $a$  value of one would revert to the original Schottky model, while an  $a$  value of zero represents no dependence of barrier height on the metal work function (strong pinning). The pinning coefficient for germanium has been measured at 0.16 [86] and 0.02 [91], indicating strong Fermi level pinning in Schottky contacts on germanium. This means the metal work function has only a small effect on the electron barrier of a Schottky contact on crystalline germanium. The hole barrier is estimated in a similar fashion as before:

$$\phi_h = E_g - \phi_e. \quad (19)$$

The Schottky model describes a metal-crystalline semiconductor junction, giving electron and hole barrier heights expected for various metals on a particular semiconductor. It applies in a rudimentary way to amorphous-crystalline semiconductor junctions because conduction in the amorphous layer is largely facilitated by variable-range hopping of carriers around the Fermi level [92], making it similar to a metal in that conduction primarily occurs near the Fermi level. The metal work function is replaced with the amorphous material work function, which can be estimated by

$$\phi_{eff} = \chi_a + \frac{1}{2}E_{g,a}. \quad (20)$$

The amorphous semiconductor electron affinity is  $\chi_a$  and the bandgap that would exist if the amorphous material were crystalline is  $E_{g,a}$ . Half the bandgap is used because the intrinsic Fermi level for elemental semiconductors is at the middle of the bandgap [49]. Room for improvement exists to account for the spreading distribution of conducting states in the amorphous layer and the lower density of states when compared with a metal.

A Schottky barrier acts as a diode similar to the p-n junction, but the saturation current is given by a different expression to reflect the different underlying physics. The current in an ideal Schottky barrier is [87]

$$J = A^* T^2 e^{\frac{-\phi_B}{kT}} \left[ e^{\frac{V_a}{kT}} - 1 \right], \quad (21)$$

where  $J$  is the current density,  $T$  is the device temperature, and  $k$  is the Boltzmann constant. The parameter  $A^*$  is the Richardson constant, which has a derived value of  $120.173 \text{ Acm}^{-2}\text{K}^2$ , but experimental values vary and depend on the materials involved [49]. The generic barrier height  $\phi_B$  should be replaced by either  $\phi_e$  or  $\phi_h$ , whichever is appropriate. The barrier height appears in an exponential term, making current strongly dependent on temperature. The general current-voltage behavior is identical to the diode described previously for the p-n junction, where the reverse-bias current is small and constant with voltage. For radiation detector contacts, reverse biasing is used to minimize leakage current for the large applied bias needed to supply sufficient electric field strength, so the term in brackets can often be ignored because  $V_a \gg kT$ . Instead, the focus is on minimizing the saturation current term by maximizing barrier height.

### 3.2.5.4 Amorphous Semiconductor Contacts

An amorphous semiconductor is a solid that lacks the long-range crystalline order of a crystalline semiconductor. Amorphous layers are formed by sputtering [27], evaporation [93], or damage to a crystal lattice [94] while a single-crystal semiconductor is formed with much time and effort through the Czochralski method or other crystal growing techniques. Amorphous semiconductor atoms still arrange in a diamond-like structure, but due to inefficient stacking, there is a much higher defect density. Many of these defects are vacancies or voids. These unoccupied lattice sites leave "dangling bonds," a semiconductor valence state not occupied in a covalent bond [95]. The dangling bonds have less binding energy than covalent bonds and therefore more easily contribute to conduction. In amorphous semiconductors, the overall band structure of the crystalline semiconductor, a consequence of crystal periodicity, is partially disrupted.

The bandgap is occupied by a large number of defect states [96] and band edges are blurred, as illustrated in Figure 3.23. Although the band edges still exist, they are termed "mobility edges" [96] as the difference between the gap and bands is less substantial than in a crystal. Electrons moving within the mobility band have some degree of enhanced mobility compared with a random network of atoms, but frequent scattering and trapping reduces charge movement substantially compared to the crystalline mobility. Conversely, charge carriers that would normally be forbidden to move in the gap region have a significant number of defect states available to them. They can move from defect to defect in a process called phonon-assisted hopping (sometimes called variable-range hopping), allowing significant conduction near the

Fermi level in the gap region. This process is strongly dependent on the density of defect states near the Fermi level and the temperature of the material. Conduction near the Fermi level by this hopping process is the dominant source of charge movement in amorphous semiconductors [97].

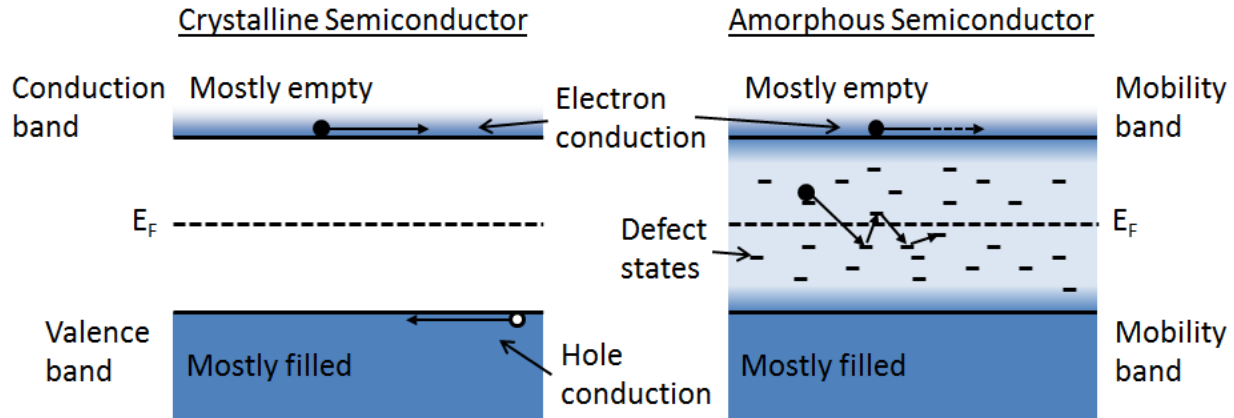


Figure 3.23. Schematic band structure and charge carrier motion in crystalline and amorphous semiconductors.

The large number of defect states near the Fermi level in the bandgap causes an amorphous-crystalline semiconductor junction to behave somewhat like a Schottky contact because of a similar physical mechanism. Since both sides of the junction are semiconductors, they may be of similar material or perhaps even the same material, differing only in their structure. This results in similar Fermi levels, meaning the amorphous semiconductor Fermi level usually lies within the bandgap of the crystalline semiconductor, providing a barrier for injection of both holes and electrons. This has been demonstrated on high-purity germanium detectors [93] [27] [26].

A model to describe amorphous-crystalline junctions was developed by Brodsky and Dohler [97] to include the effect of amorphous defect states on the junction. A metal provides charge carriers within a few  $kT$  of the Fermi level with a density of states around  $10^{23} \text{ cm}^{-3} \text{ eV}^{-1}$ . The crystalline semiconductor side of a junction has very few states in the bandgap. An amorphous semiconductor may typically have states with density  $10^{18}$  to  $10^{20} \text{ cm}^{-3} \text{ eV}^{-1}$  around the Fermi level, orders of magnitude lower than a metal, but many orders of magnitude higher than the semiconductor bandgap. For this reason, an amorphous-crystalline junction can easily be described in terms of the Schottky model, but the model can be improved by accounting for the lower density of states and penetration of the field into the amorphous layer.

Figure 3.24 shows a schematic of the electron density of states as a function of electron energy for an amorphous-crystalline semiconductor junction. The vertical axis is increasing electron energy, while the horizontal axis represents increasing density of states as distance increases from the origin. Although the amorphous semiconductor lacks long-range order, there are "mobility band edges" that provide increased carrier mobility, analogous to band edges in crystalline semiconductor. However, here we only consider states near the Fermi level as these are responsible for most conduction in the amorphous layer [92] [95] [97] [98] [99]. Near the amorphous layer Fermi level  $E_F^{am}$ , there are many defect states in what would be the bandgap of the semiconductor, providing a slowly varying density of states with energy. Here we assume a

constant density of states  $N_f$  within a few  $kT$  of the Fermi level.  $N_f$  has units  $\text{cm}^{-3}\text{eV}^{-1}$ . The crystalline side shows the typical  $\sqrt{E}$  dependence for density of states [49] at the band edges and zero states within the bandgap. The bandgap  $E_g$  and Fermi level for the crystalline side  $E_F^{cr}$  are also indicated. The unperturbed electron barrier height is  $\phi_e^0$ .

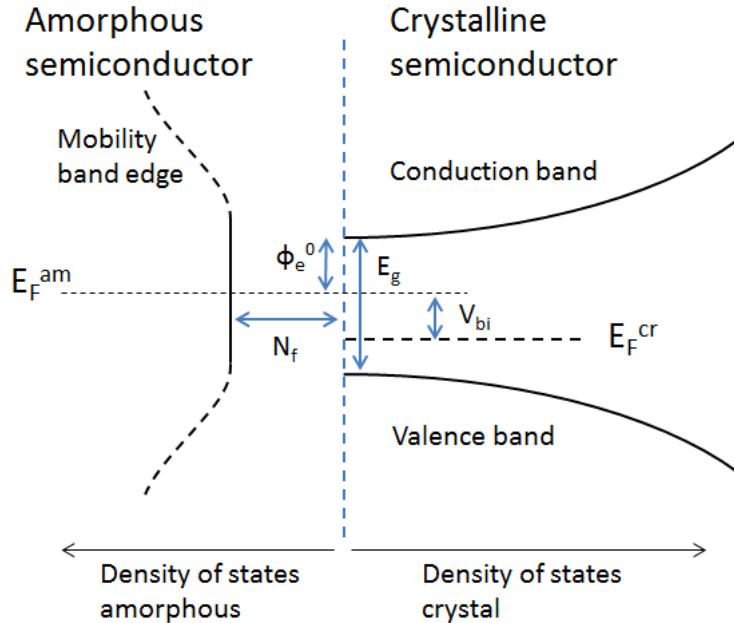


Figure 3.24. Schematic of energy vs. density of states for an amorphous-crystalline semiconductor junction. Adapted from [97].

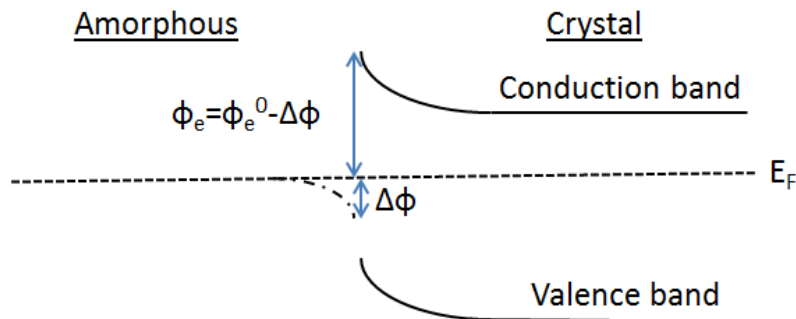


Figure 3.25. Band structure of an amorphous-crystalline junction with barrier lowering due to field penetration in the amorphous layer. Adapted from [97].

The built-in voltage  $V_{bi}$  is given by the difference between Fermi levels on the two sides:

$$V_{bi} = E_F^{am} - E_F^{cr}, \quad (22)$$

but unlike a metal, only a portion is seen on the amorphous side due to the lower density of states. This has the same effect as image charge barrier lowering in a metal Schottky barrier [100], yet the physical cause is slightly different. Figure 3.25 shows an energy diagram

illustration of the potential  $\Delta\phi$  appearing on the amorphous side. This does not occur in a metal-semiconductor junction because a conductor can always rearrange charge carriers so that the field inside is zero. The amorphous semiconductor does not have the available states to completely cancel the field.

The quantity  $\Delta\phi$  can be interpreted as a lowering of the zero-bias barrier height  $\phi_B^0$ , so the junction can be described as a Schottky barrier with an added barrier lowering term due to the potential in the amorphous layer. Adding this new piece to the Schottky diode equation in (21) gives the current-voltage behavior for an amorphous-crystalline junction as

$$J = A^0 T^2 e^{\frac{-(\phi_B^0 - \Delta\phi)}{kT}} \left[ e^{\frac{V_a}{kT}} - 1 \right], \quad (23)$$

where  $J$  is the current density,  $T$  is the device temperature,  $V_a$  is the applied bias, and  $k$  is the Boltzmann constant. The Richardson constant  $A^*$  has been replaced by a generic pre-factor  $A^0$  to allow for a different value, since one side of the junction is now an amorphous semiconductor rather than a metal. The hole barrier  $\phi_h^0$  or electron barrier  $\phi_e^0$  would replace the generic term  $\phi_B^0$ , depending on whether electron or hole blocking is being examined.

The barrier lowering expression proposed by Brodsky and Dohler depends on applied bias and on the ratio between the net ionized impurity concentration  $N_d$  and  $N_f$ . In high-purity germanium the impurity concentration is normally much smaller than the amorphous density of states so that  $N_d \ll N_f$  and we may accurately describe the barrier lowering as

$$\Delta\phi = \sqrt{\frac{2(V_a - V_{bi})N_d}{N_f}}. \quad (24)$$

The implication is that the apparent barrier height depends on the applied voltage  $V_a$ , meaning an increase in current with increased bias. The current-voltage behavior is illustrated in Figure 3.26.

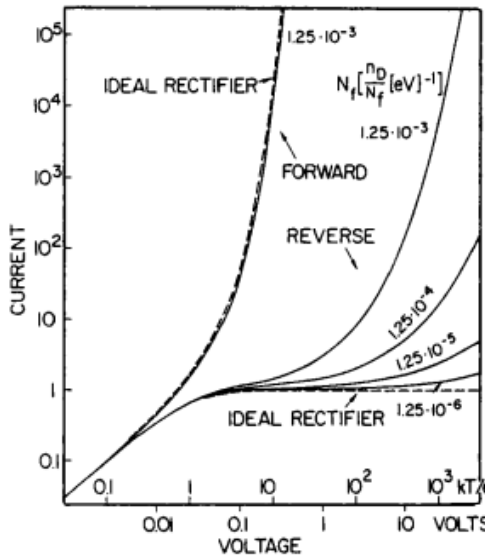
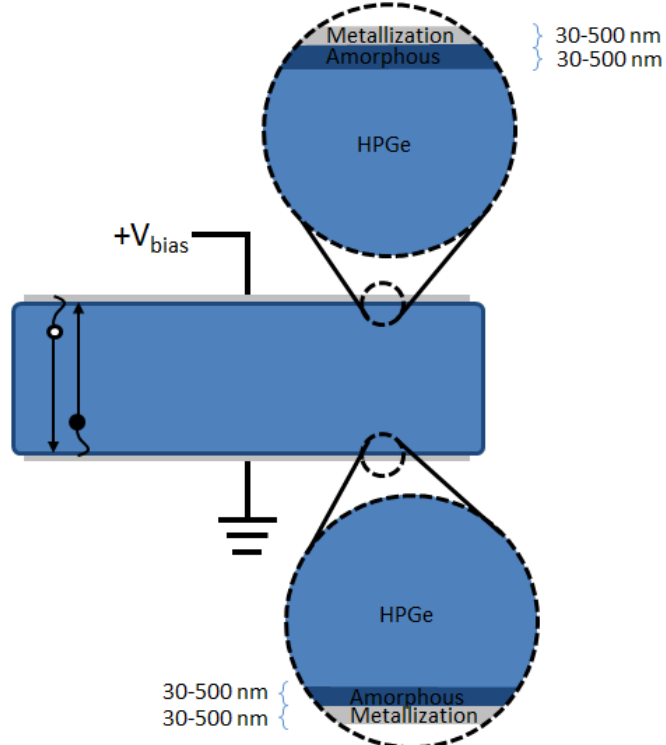


Figure 3.26. Predicted behavior of an amorphous-crystalline junction compared to the ideal rectifier of Schottky theory. [97]

The reverse-biased ideal rectifier, according to Schottky theory, reaches a saturation current that is independent of applied bias, provided breakdown has not occurred. The amorphous junction experiences additional barrier lowering with increasing reverse bias, meaning an increase in current even without electrical breakdown. The level of increase depends on the density of states in the amorphous layer and the dopant concentration in the crystal.

Figure 3.27 illustrates a detector with amorphous semiconductor contacts on both sides and amorphous semiconductor passivation. The same or similar amorphous layers can provide electron blocking on one contact and hole blocking on the other contact. The amorphous semiconductor is a high-resistivity film, so metal electrodes can be deposited directly on the amorphous layer and, when the metal is segmented, form separated electrodes with sufficient resistance between them. This eliminates an etching or passivation step for the inter-electrode region. Amorphous semiconductors have also been shown to be a suitable passivation layer on germanium detectors [28]. A simple fabrication process is possible where amorphous semiconductor is deposited on all surfaces of a germanium crystal and metal electrodes are deposited in the pattern desired, giving a completely passivated detector with a thin dead layer on all surfaces. This added flexibility makes amorphous semiconductor contacts and passivation ideal for segmented detectors, especially those with small spacing between electrodes.



**Figure 3.27. Illustration of a detector with amorphous semiconductor contacts and passivation.**

There are several parameters to investigate in the fabrication process for amorphous semiconductor contacts, adding complexity over a similar study for metal-semiconductor contacts. The deposition of amorphous semiconductor layers in most recent studies of amorphous semiconductor contacts [26] [27] [101] and in the present work is done by RF

sputtering. Sputtering is a relatively complex process compared to evaporation. In addition to film thickness, other parameters such as sputter gas composition and pressure as well as applied power can be changed. The pressure and power affect the deposition rate, which can affect the film structure. Changing the sputter gas pressure also changes the rate of bombardment from electrons and ions, which can change the film properties [102]. Also, the amorphous film can be sensitive to the sputter gas composition, with hydrogen being a particularly important consideration [26] [103]. Because conduction is largely determined by charge hopping between localized states near the Fermi level, the film resistivity of amorphous semiconductors is quite sensitive to the density of defect states near the Fermi level  $N_f$ . Hydrogen in the amorphous film interacts with the “dangling bonds” that form most of the defect states [104], effectively passivating them and increasing resistivity [105] [103].

The large number of parameters in the sputtering process alone is a motivator for the present work in understanding the amorphous semiconductor contacts. This dissertation presents a systematic study that should be helpful in understanding which process parameters are critical for consistently obtaining electrical contacts on HPGe detectors that give low leakage current and form a suitable passivation layer. This comes in addition to the challenges that already exist in the preparation of the HPGe crystal surface before the contacts are formed. The next chapter will examine the present challenges with amorphous semiconductor contacts and passivation in the context of various problems that can occur in HPGe detectors.

## Chapter 4 Fabrication Challenges with High-Purity Germanium Detectors using Amorphous Semiconductor Contacts

The advantages and features of high-purity germanium (HPGe) detectors were described previously. However, challenges still exist that require additional development today, especially for the amorphous semiconductor contact technology. While these contacts more easily lend themselves to segmented electrodes and full passivation, the fabrication process is not as highly developed as that for conventional doped layer contacts. Amorphous semiconductor contacts must be formed with certain fabrication process parameters in order to reduce leakage current, provide long-term stability, give sufficient inter-electrode impedance, and form a suitable passivation layer that does not collect moving charge carriers. In this chapter, these four requirements are described in detail and methods of characterization are presented.

### 4.1 Leakage Current

Leakage current generates shot noise, which adds uncertainty to the energy measurement in gamma-ray spectroscopy. For radiation detector development, an important goal is reducing leakage current in the detector to minimize electronic noise. The most important reduction in leakage current comes from cooling the germanium crystal below  $\sim 140$  K. The majority of applications have a fixed operating temperature determined by the cryostat heat load and available cooling power. Adding a guard ring mitigates the contribution to the measurement from surface leakage current, leaving charge injection at the contacts as the most significant source of leakage current. Reducing leakage current through development of the electrical contacts is an important area of research in advancing amorphous semiconductor contact technology. Reducing the surface leakage current could also enable detectors with no guard ring, which would increase the active volume of detectors and eliminate the dead material between detectors in a multi-detector system.

Amorphous semiconductor contacts do not block charge injection as well as conventional doped-layer contacts [93] because of the underlying physics, so fabrication process development is especially important to ensure the leakage current attained with these contacts is at an acceptably low level. Amorphous-crystalline semiconductor junctions behave somewhat like a Schottky barrier, only with a barrier lowering term added to account for electric field penetration in the amorphous layer [97], as discussed in the previous chapter. The current density expression is repeated here for convenience. The voltage dependence term from ( 23 ) in brackets is omitted because it is insignificant at high values of reverse bias. The current density is

$$J = A^0 T^2 e^{\frac{-(\phi_B - \Delta\phi)}{kT}}, \quad (25)$$

where  $A^0$  is the pre-factor,  $T$  is the device temperature,  $\phi_B$  is the barrier height,  $\Delta\phi$  is the barrier lowering term, and  $k$  is the Boltzmann constant.

The Fermi level of the amorphous layer generally falls within the bandgap of germanium, meaning the junction can block either holes or electrons, but the barrier height will not be particularly high for either. The barrier height in this case would be less than the bandgap for both holes and electrons, so injection leakage current from the contacts would be significantly higher than any thermally generated charge carriers surmounting the bandgap energy. An investigation into the effect of the fabrication process on barrier height is useful because even a small increase in barrier height translates to a large reduction in leakage current due to the exponential dependence on temperature. A precise knowledge of the pre-factor could also be helpful in predicting the magnitude of the leakage current. Separately measuring the exponential barrier height and pre-factor leakage current components could provide information about the origin of the leakage current, which could inform further fabrication strategies to reduce leakage current.

Multiple methods exist for measuring barrier height for a particular contact [106], each with its own set of advantages and operational requirements. Contacts can be studied by a single-junction device where one contact is under study and the opposite contact is ohmic [107]. This allows a simple device where a contact fabrication process can be studied individually. This is not a feature of modern radiation detectors, so the present work utilizes devices with two blocking contacts in order to ensure the results are applicable to operational radiation detectors and avoid any complications with forming ohmic contacts.

The work presented in Chapter 5 centers on reducing leakage current in amorphous semiconductor contacts. The barrier height and pre-factor can be measured by fabricating a detector with amorphous semiconductor contacts and acquiring a current-voltage characteristic at multiple different temperatures. Performing a fit to ( 25 ) allows calculation of the barrier height and pre-factor. However, since the detector has two different blocking contacts, some consideration must be given to the contribution from each.

## 4.2 Long-Term Stability

A change in amorphous semiconductor contact characteristics has been noted [26] [101] when the detector goes through a "temperature cycle," here defined as warming from operating temperature ( $\sim 80$  K) to room temperature ( $\sim 295$  K) and cooling again to operating temperature. Such temperature cycling is necessary throughout the operational lifetime of any germanium detector for initial testing, moving among cryostats, or evaporating off impurities accumulated on cold surfaces during operation. Temperature cycling also occurs inadvertently through depletion of liquid nitrogen or failure of mechanical coolers. Additionally, detectors may be stored for some time before use, so it is important to know whether the contacts will still perform as expected even if the detector has been stored at room temperature for several months.

When a detector is kept cold for an extended period of time, particles in the vacuum environment can stick to the surface and possibly contribute to increased leakage current. In the past, temperature cycling the detector was used as a method to "boil off" such contaminants and reduce leakage current [108] [109]. However, as will be shown in a later chapter, fully passivated detectors do not generally experience any change due to vacuum impurities.

For some detectors fabricated with amorphous semiconductor contacts, increased leakage current is observed after each temperature cycle [26]. The change with temperature cycling is

dependent on the fabrication process [26]. For example, some I-V curves are shown for two detectors with amorphous germanium (a-Ge) contacts in Figure 4.1 for multiple temperature cycles. The a-Ge contact sputtered at low pressure (7 mTorr) shows significantly increased leakage current each time the detector is temperature cycled and re-tested. The other detector, with an a-Ge contact sputtered at higher pressure (15 mTorr), shows very little change with each test. A study of the stability of various contacts, presented in Chapter 6, is a necessary step in identifying fabrication processes that consistently provide low leakage current over a long period of time that includes many temperature cycles. Past work in this area, such as that presented in Figure 4.1, have not differentiated between any changes in leakage current as a result of temperature cycling or those caused by detector storage at room temperature between cycles. Knowing which is the cause provides information about the mechanism of change in the contacts and possible strategies for overcoming the instability.

Experimental study of this property involves fabrication of detectors using various recipes and then measuring the leakage current. The detector is cooled to liquid nitrogen temperature for testing, then warmed to room temperature and held there for some time. In some cases, the detector is exposed to air when warm, so full passivation is beneficial in eliminating confounding factors from deposited surface contaminants. A measure of the change in leakage current observed at several temperature cycles can give an indication of the long-term stability of each contact and the impact of different fabrication processes.

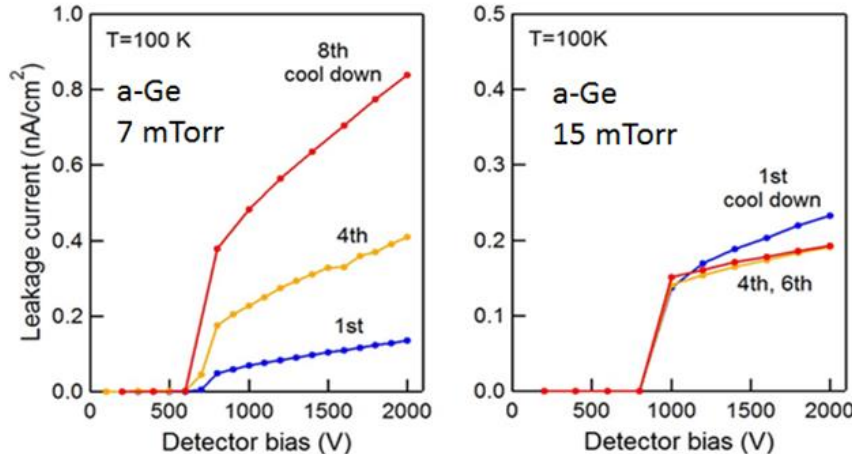


Figure 4.1. Change in leakage current as a function of temperature cycle for two different detectors with a-Ge contacts. [110]

### 4.3 Inter-electrode Impedance

Position-sensing germanium detectors with multiple electrodes may have additional sources of capacitance and resistance that can degrade noise performance. These are pictured schematically in Figure 4.2. The reader is referred to section 2.3 for a discussion on electronic noise. When multiple electrodes are present on a detector, the inter-electrode resistance appears in the parallel resistance term and contributes to thermal noise. The resistance between nearby electrodes must be kept high, above  $\sim 10^9 \Omega$ , to avoid excessive noise. Using an amorphous semiconductor layer between electrodes as passivation is helpful in this regard because it can

prevent surface contaminants from producing a low-resistivity surface. However, the properties of the amorphous layer are important, as the resistivity can vary by orders of magnitude [105] [103], so the amorphous layer must be prepared in an appropriate manner to avoid a low-resistance path between adjacent electrodes.

The capacitance between electrodes adds to the input capacitance for each input channel. Increasing capacitance increases the noise contribution from voltage noise and 1/f noise, so reducing the inter-electrode capacitance is a consideration in segmented detectors. The electrode geometry largely determines this parameter, but the contact material does play a role by changing the dielectric constant. For the geometry shown in Figure 4.2, about half the field lines between the two electrodes would pass through the amorphous semiconductor layer and the dielectric constant of the amorphous material would change the capacitance. The dielectric constant of germanium is 16, and the value for a-Ge is approximately the same [97], so the capacitance between electrodes due to the underlying contact layer is increased by a factor of ~16 over the case of vacuum.

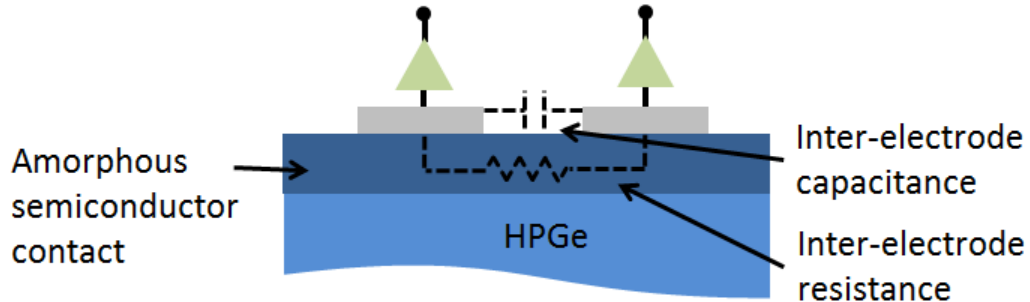


**Figure 4.2. Equivalent circuit elements between two electrodes.**

The challenge lies in developing a single layer that fulfills many different requirements. The layer must provide charge blocking (either electron or hole), form a suitable protective layer, have high resistance, and a low dielectric constant. Amorphous semiconductor layers fulfill these requirements reasonably well, but their deposition must be done with the correct parameters to give sufficiently high resistivity to provide high inter-electrode resistance. Since the inter-electrode capacitance is largely determined by geometry, it can be calculated to a reasonable degree of accuracy. The resistance, however, is determined by the amorphous semiconductor film resistivity, conduction on the outside surface, and conduction at the interface between the amorphous layer and HPGe, all of which are difficult to predict. For this reason, it is necessary to make some measurement of inter-electrode resistance, which can be accomplished by a current-voltage characteristic between two electrodes. When a guard ring device is fabricated on an amorphous semiconductor contact area, the region between electrodes gives an appropriate measurement of inter-electrode resistance given by the fabrication process used on that surface. Figure 4.3 illustrates the guard ring resistance measurement. A bias  $V_b$  is applied to the detector so that that volume directly under the top electrodes is depleted to give a high-resistivity layer. A bias  $V_{GR}$  is applied to the guard ring and kept much smaller than the detector bias  $V_b$  so the bulk electric field lines remain perpendicular to the top surface. When  $V_{GR}=0$ , the current through the center contact is the result of leakage current through the contacts.

When a guard ring bias is applied, the center contact current is contact injection leakage current plus some current flow directly between the guard ring and center contact. As seen in Figure 4.4, the current-voltage measurement data typically show a straight line, indicating resistor-like behavior. A linear fit to these data gives a line whose slope is the center contact-guard ring conductance, and its reciprocal is the resistance between the center contact and guard ring.

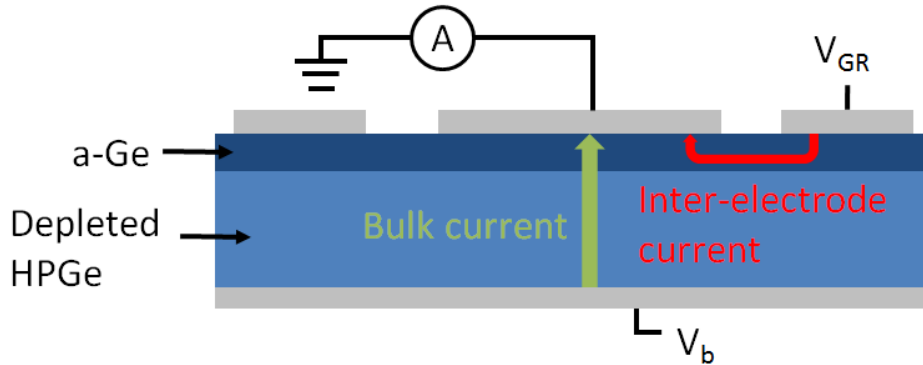


Figure 4.3. Illustration of inter-electrode resistance measurement.

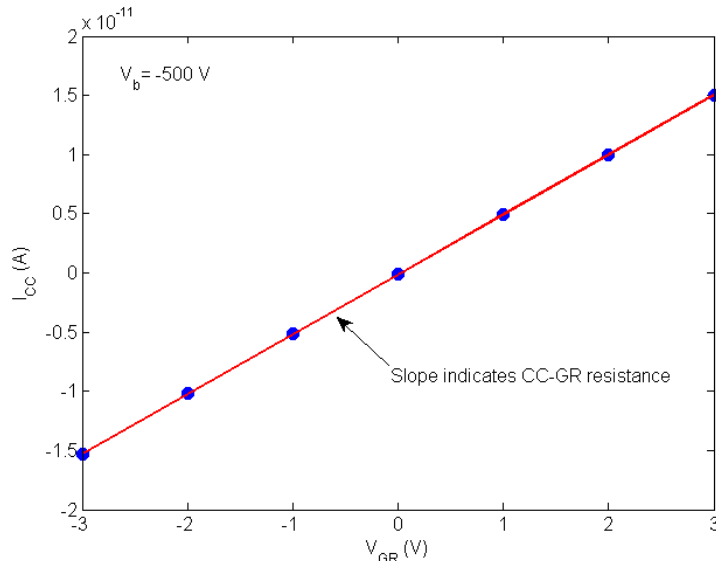


Figure 4.4. Example data showing inter-electrode resistance measurement.

## 4.4 Surface Passivation

It is also important to consider non-contact surfaces on the detector as these can affect the electric field in the active volume of the detector and hamper performance. It is never desirable for non-contact surfaces to collect moving charge carriers. The surface passivation adds a protective layer to mitigate the effects of surface contaminants, but this must be done with care to avoid the presence of surface charge that could significantly change the electric field inside

the active volume. In this section two effects related to the passivation of non-contact surfaces are discussed. The first is called surface channels, where charge is present on the side surface of a detector. The second is inter-electrode charge collection, where moving charge carriers are collected to the surface between adjacent electrodes.

#### 4.4.1 Surface Channels

When non-contact side surfaces have charge present at the surface, it is called a surface channel [111]. The charge will modify electric field lines due to applied bias and attract or repulse moving charges. Field lines will terminate on the non-contact side surface and cause charge carriers to be collected to this surface rather than directly to an electrode. Collection to the side essentially halts charge movement since surface conduction is much slower than movement in the bulk crystal material. The radiation-induced free charge is collected to the side prematurely, giving a signal deficit and hurting spectral performance. Additionally, modified field lines can change the expected position response of a segmented detector, possibly distorting gamma-ray images. For instance, in the case of a strip detector, two collimated data sets acquired under adjacent strips may give an apparent position difference larger or smaller than the actual strip pitch.

The surface channel effect has an impact near the edges of a planar detector, especially in thicker detectors. A guard ring can mitigate the effects of surface channels by removing the affected volume from the active volume. However, this reduces detection efficiency and is especially bad for Compton imaging systems with multiple detectors as the guard ring material represents an absorber between imaging elements. Although a guard ring is often helpful in taking up surface leakage current, this can be done with a very thin guard ring electrode, so the surface channel effect dominates the guard ring thickness. Surface channels can also be an issue with PPC detectors since they may prevent charge from being collected to the point contact. Because the point contact senses charge in only a small adjacent volume, altering the path of moving charge away from the point contact can vastly change the signal properties.

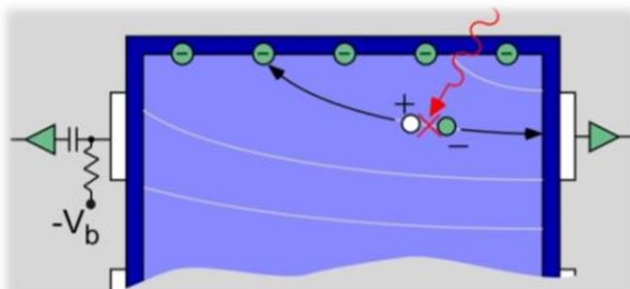


Figure 4.5. Illustration of electric field alteration due to a surface channel. [110]

Figure 4.5 illustrates the altered path of drifting charge carriers due to a surface channel. Here, a net negative charge exists on the side surface and acts as depleted p-type material, where ionized acceptors would give a net negative space charge. The surface charge bends electric field lines, attracting moving positive charge carriers and preventing some from reaching the appropriate electrodes on the left side of the figure. Since the charges spend less time in the immediate vicinity of the electrodes, the induced signal is smaller than expected. This degrades

energy resolution, increases low-energy background, and renders the event useless in position determination. It is important to select side surface passivation material that gives overall charge neutrality in order to avoid a surface channel effect.

#### 4.4.2 Inter-Electrode Charge Collection

The region between electrodes can also collect charge carriers [26] in an effect called inter-electrode charge collection or charge collection to the gap. The present work described in Chapter 7 centers on this subject. The inter-electrode surface must have sufficient resistivity to provide adequate electrical separation of electrodes. If electric field lines terminate on this surface, detrimental effects occur in the detector.

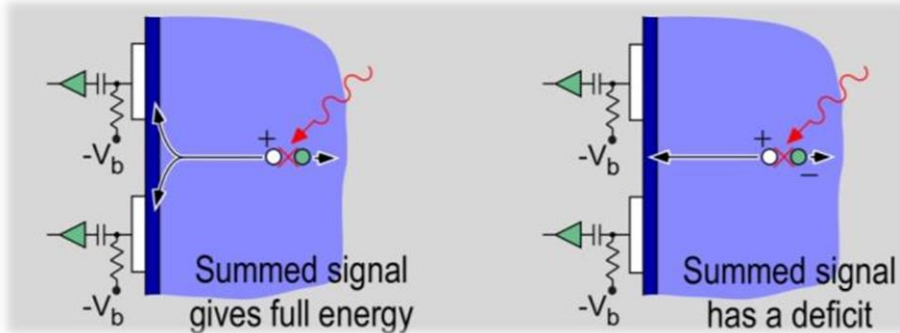


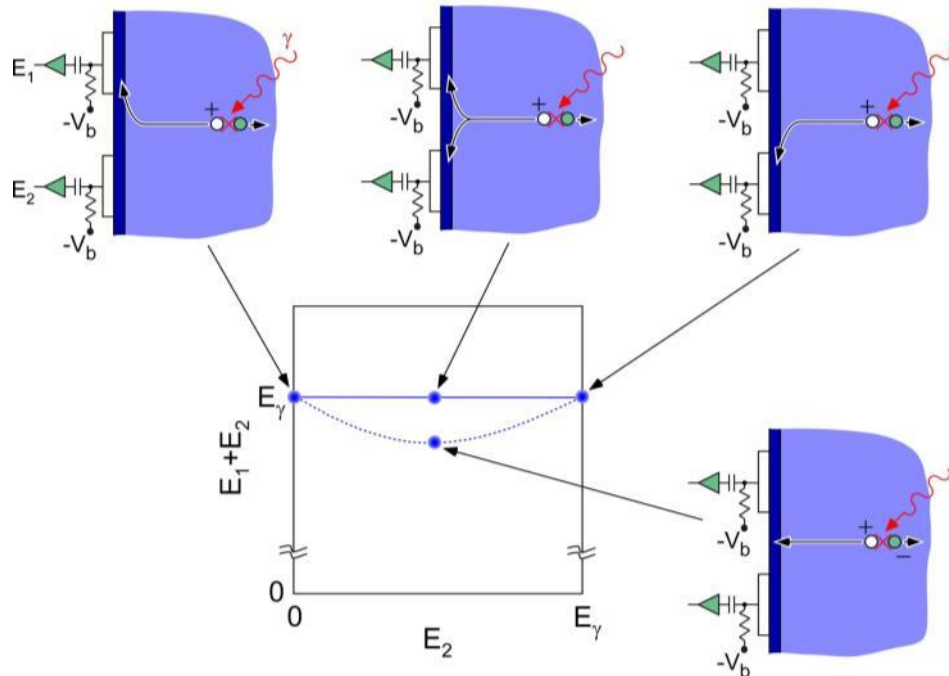
Figure 4.6. Illustration of inter-electrode charge collection. [110]

Figure 4.6 illustrates a process that can occur if field lines terminate on the inter-electrode surface. An interaction that occurs under the gap between the strips of a strip detector will cause charge carriers to drift toward the contact surface. Far from the surface, they drift in a perpendicular fashion toward the inter-electrode surface region. In the ideal case, they deviate toward the metal electrodes as they approach and the summed signal from both strips gives the expected energy. However, if electric field lines pass through the inter-electrode region then charge can be collected to this region, and the summed signal from the two strips is lower than expected because the charge carriers are not fully collected in the measurement time.

Figure 4.7 schematically illustrates the observed effect of inter-electrode charge collection by a plot of the sum of the energy from two adjacent electrodes as a function of the energy in one of those electrodes. The left side of the plot represents events where electrode 1 exhibits a signal equivalent to the full gamma-ray energy. Similarly, the right side of the plot shows events where strip 2 receives maximum signal. Events shown in the center of the plot were shared approximately equally by the two strips as the charge drifted directly toward the center of the gap between strips. In an ideal case the charge would deviate toward the strips as it drifts closer to them, giving a summed signal equivalent to the full signal observed when the interaction was under a single strip. In the case of inter-electrode charge collection, there is a deficit in the sum of the two strips because charge was collected to the gap between strips.

The magnitude of the deficit depends on the electrode geometry. For strip detectors with pitch-to-gap ratios around two, this effect usually causes a deficit around a few percent of the total signal amplitude for the photopeak, a significant contribution compared to intrinsic germanium energy resolution (~0.2% FWHM at 662 keV). Any inter-electrode passivation

process must seek to minimize inter-electrode charge collection. It should also be noted that this effect is not unique to amorphous semiconductor contacts [112]. Conventional doped contacts require removal of material in the inter-electrode region to provide electrical separation, and this region is sometimes left unpassivated. Such a process has in some cases been reported to show no observable surface charge collection [77].



**Figure 4.7.** A plot of the type used for investigating inter-electrode charge collection. The sum energy of two adjacent electrodes is plotted against the energy of one of those electrodes. [110]

An important method for evaluating inter-electrode charge collection is low-energy gamma-ray measurements [66] [14]. Using a strip detector and illuminating the opposite surface of the electrodes being examined, we can facilitate drift of a certain number of charge carriers across the detector thickness. In principle, any gamma-ray source of the relevant energy range could be used, but low-energy sources are beneficial for two reasons. A small charge cloud is advantageous for best precision as the charge cloud should be smaller than the gap between strips, or else some charge will always be collected directly to electrodes and the deficit will be more difficult to observe. It is also beneficial to have the interactions well away from the electrodes examined so that no events originate inside the gap between electrodes.

This chapter presented some of the present challenges with HPGe detectors using amorphous semiconductor contacts. All of the challenges discussed can be addressed through improvements in the detector fabrication process. The challenge of reducing leakage current is addressed in Chapter 5, long-term stability is studied in Chapter 6, and Chapter 7 discusses the study of inter-electrode charge collection.

# Chapter 5    Leakage Current

In Chapter 4, present challenges in high-purity germanium (HPGe) detectors with amorphous semiconductor contacts were presented. This chapter focuses specifically on leakage current, one of those challenges presented with amorphous semiconductor contacts. A self-contained study on electron injection leakage current is presented, with some background, a summary of the experiments conducted, results of the investigation, and conclusions.

The context is first given, describing why this is a challenge and the effect of leakage current on semiconductor radiation detectors. This is followed by a summary of previous work in this area. Next is some detail about the experimental methods and analysis methods. Results are then presented showing the effect of various fabrication process parameters on detector leakage current. Finally, some conclusions from this aspect of the work are given.

## 5.1    Background

High-Purity Germanium detectors operate by drifting charge carriers in an electric field, which inevitably drifts some leakage current across the detector. Bulk leakage from thermally generated charge carriers is minimized by cooling. Effects from surface current, though troublesome, can be mitigated by using a guard ring. Leakage current by injection at the contacts remains, however, and there is no distinction between charge carriers injected at a contact and those created by radiation ionization; they are sensed by electrodes in the same way. An important goal of contact development is reducing leakage current to keep associated electronic noise to a minimum.

### 5.1.1    Effect on Detectors

Leakage current comprises a background to the drifting charge carrier signal induced by radiation interactions. For typical charge-sensitive preamplifier measurements, it appears as shot noise [31], giving an increasing noise contribution as shaping time is increased. This is in contrast to other parameters such as detector capacitance, which contributes increasing electronic noise at lower shaping times [37]. For radiation interactions at 662 keV, the uncertainty contribution from leakage current exceeds uncertainty from statistical variation when leakage current is above a few nA. Therefore, the goal in contact development is to produce contacts whose electronic noise contribution is much less than the statistical variation inherent to the detector material.

It is also desirable to reduce surface leakage current, though a guard ring can take up surface leakage current in order to separate this effect from sensing electrodes. In this case, the guard ring current itself does not contribute to shot noise in the measurement (since it is on a different electrode), but some practical limitations still apply. The guard ring cannot float to a significantly different potential than nearby sensing electrodes or the expected drift path of mobile charge carriers will be disturbed. This places a limitation on guard ring leakage current for a given resistance between the guard ring and sensing electrodes. Also, fluctuations in the guard ring current can capacitively couple to sensing electrodes. Lowering surface leakage

current is not necessarily part of contact development, since it depends more on the surface passivation layer (or surface conditions if no passivation is used) of the side non-contact surface. However, amorphous semiconductor contacts have been shown to be suitable for both contacts and passivation layers [28] [93], so it would be advantageous to find a process that produces an amorphous layer that can function well as a coating for both functions to simplify the fabrication process.

### 5.1.2 Previous Work

Plentiful work has been devoted to contacts of all types on silicon [49] [107] [106], but much less has been published to quantify differences in blocking contacts on germanium detectors. Some work has been published regarding metal Schottky contacts on germanium crystals [86] [91] [113] [114] [115] [116] [117]. These studies are fairly extensive and have some important conclusions. Metal-Ge Schottky contacts are subject to similar Fermi level pinning as seen in metal-Si Schottky contacts, meaning the metal-Ge contacts are generally only suitable for blocking electrons. A notable exception is sputtered yttrium, reported to form a suitable hole-blocking contact [118]. Other issues have been noted, like poor adhesion for Au layers on germanium [86].

Doped layer contacts such as Li-diffused contacts and ion-implanted contacts have been studied extensively [74] [75] [119] and the achievable leakage current for this type of contact is very low. However, the focus of these studies is practical matters of detector operation, like proper parameters to form the contacts and their ability to withstand high electric fields [76].

Less work has been done for amorphous semiconductor contacts [27] [93]. Amman et al. have shown some barrier height values for various amorphous germanium (a-Ge) and amorphous silicon (a-Si) films on germanium, but the number of samples was small and no measure of reproducibility was made [26]. Hull et al. made a large number of measurements and varied appropriate fabrication process parameters, but showed no measure of reproducibility and made no attempt to show any connection between process parameters and leakage current parameters [101].

There is much to be gained from a systematic study of amorphous semiconductor contacts on germanium detectors. Unlike metal Schottky contacts or impurity-based contacts, the barrier heights for amorphous semiconductor junctions tend to center around half the bandgap of germanium [26] [101]. This grants flexibility in that a single fabrication process yields a contact that can block either holes or electrons [27], but will not be excellent at blocking either. There is reason to believe that the barrier height will be affected by the fabrication process since the Fermi level of amorphous semiconductors can shift with varying hydrogen content [120] and the film morphology changes significantly with sputter pressure [102]. The pre-factor is typically dependent on the materials on both sides of the interface as well as the interface properties [49], so the fabrication process should also affect this value. Studying the dependence of barrier height and pre-factor of amorphous semiconductor contacts on germanium detectors could yield an improved fabrication process with lower detector leakage current.

## 5.2 Detector Fabrication

About 45 HPGe detectors were fabricated with amorphous semiconductor contacts in order to characterize the leakage current of those contacts as a function of fabrication process parameters. All had the planar detector geometry because it is simpler to fabricate using the current methods than a coaxial detector, and large detector volumes are not needed. A guard ring electrode structure was used on the top surface of the detectors to allow separate measurement of the bulk injected leakage current and the surface leakage current.

An effort was made to keep the overall fabrication process constant except for the deposition of one contact, which was the contact under study. The top contact and side surface passivation were formed by sputtering a-Ge with some hydrogen content in the sputter gas. The hydrogen was necessary to achieve sufficient resistivity on the side surface to avoid significant leakage current. Generally, the top contact and side passivation were not studied, but were used to provide adequate charge injection blocking at the top contact and give low side surface leakage current.

The bottom, full-area contact was formed by sputtering a-Ge or a-Si with varying deposition parameters. One key parameter is the sputter gas hydrogen content, which was varied by using different cylinders of source gas, each consisting of 0-35% H<sub>2</sub> and the remainder being argon. Some of the hydrogen gas becomes incorporated into the amorphous film, with the hydrogen content of the film being related to the amount of hydrogen in the sputter gas [121]. The amount of hydrogen in the amorphous layer can vastly change the resistivity as well [103]. In this study, source bottles of sputter gas containing 0%, 7%, 17.5%, and 35% H<sub>2</sub> were used. The uncertainty on these numbers is unknown. The sputter chamber also retained some residual water vapor from before it was pumped to high vacuum. Based on residual gas analyzer measurements of the sputter chamber before sputter gas was injected, the residual hydrogen content was <0.5%. This should not be a significant change for film sputtered in 7% H<sub>2</sub> or above, but the films sputtered in pure Ar may experience significant shifts in resistivity based on varying levels of residual water vapor in the sputter chamber.

Another varied sputter parameter was the sputter gas pressure. A minimum gas pressure is necessary to maintain the plasma, but the specific pressure value varies among different sputter systems, depending on the sputter system technology and the geometry. The MRC sputter system used for this study was an RF diode sputtering system with a minimum pressure around 3 mTorr for maintaining a plasma. A maximum pressure also exists where electrons scatter too often and cannot gain enough energy to ionize sufficient neutral atoms before being captured. However, an even lower practical limit on maximum sputter gas pressure exists because of the reduced deposition rate with higher gas pressure. In this study, the sputter gas pressure was varied from 7 mTorr to 23 mTorr. Before the plasma was ignited, the gas pressure was measured by a Pirani gauge, giving a precision of  $\pm 0.1$  mTorr. However, some long-term systematic error is possible due to a drift in the gauge calibration over the period of months.

The other varied contact deposition parameter was the amorphous film thickness. It is unknown what film thickness is required for a robust amorphous-crystalline junction, so the thickness was varied for some detector contacts to assess whether a systematic difference was present based on the film thickness. In-situ measurement of deposition rate is difficult for

sputtering, so the thickness of the amorphous contacts was estimated by a calibration on a glass slide. The glass slide was painted with lines of picein wax and a-Ge or a-Si was sputtered on the slide for a fixed time with some commonly used sputter gas pressures. The wax was then removed and the thickness of the amorphous film was measured with a profilometer. Based on this sample, the thickness of amorphous contacts on detectors was estimated by multiplying the deposition time by the measured rate of deposition on the glass slide. The deposition rate for a-Si is different from a-Ge due to different sputter yields for different materials. Varying sputter gas pressure will also change the deposition rate because the sputtered atoms scatter more often in higher gas pressure. The estimated uncertainty on amorphous contact film thickness is about 5% of the film thickness.

The detectors were fabricated from HPGe material purchased from Ortec [58]. An example boule slice of HPGe material is shown in Figure 5.1 as it appeared when received from the manufacturer. An HPGe slice was cut into multiple smaller samples, each having a geometry like that shown in Figure 5.2. The top surface was a square 18 mm on a side and the thickness was about 10 mm. In order to facilitate handling during the fabrication process, handles were left on the sides, but they remained undepleted during testing. The contact under test was formed on the bottom surface.

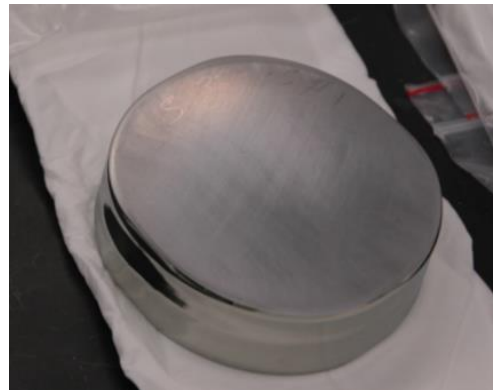


Figure 5.1. Photograph of an HPGe slice as received from Ortec.

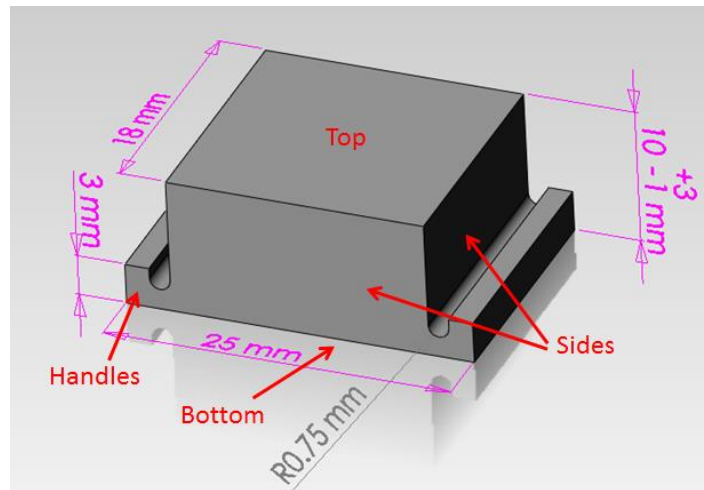


Figure 5.2. The crystal sample geometry used for the leakage current study.

After the sample was cut into the desired geometry, the surfaces were lapped and chemically polished. The sequence of deposition steps is shown in Figure 5.3. The sample was briefly etched in 4:1 HNO<sub>3</sub>:HF and loaded in an RF-diode sputtering system. A-Ge was sputtered on the top and sides in a similar fashion for each detector to give a consistent hole-blocking contact and surface passivation layer. The detector was then flipped over and a-Ge or a-Si was sputtered on the bottom surface to form the contact under study.

Metal electrodes were formed by thermal evaporation of aluminum from a tungsten filament on the entire bottom surface. Aluminum was then deposited on the top surface to form two electrodes defined by shadow masks. One was a guard ring to take up surface leakage current, while the other was a center contact. When the detector was completed, it was stored in a nitrogen-purged box until a testing cryostat was available. A more detailed description of the fabrication process is given in Appendix A.

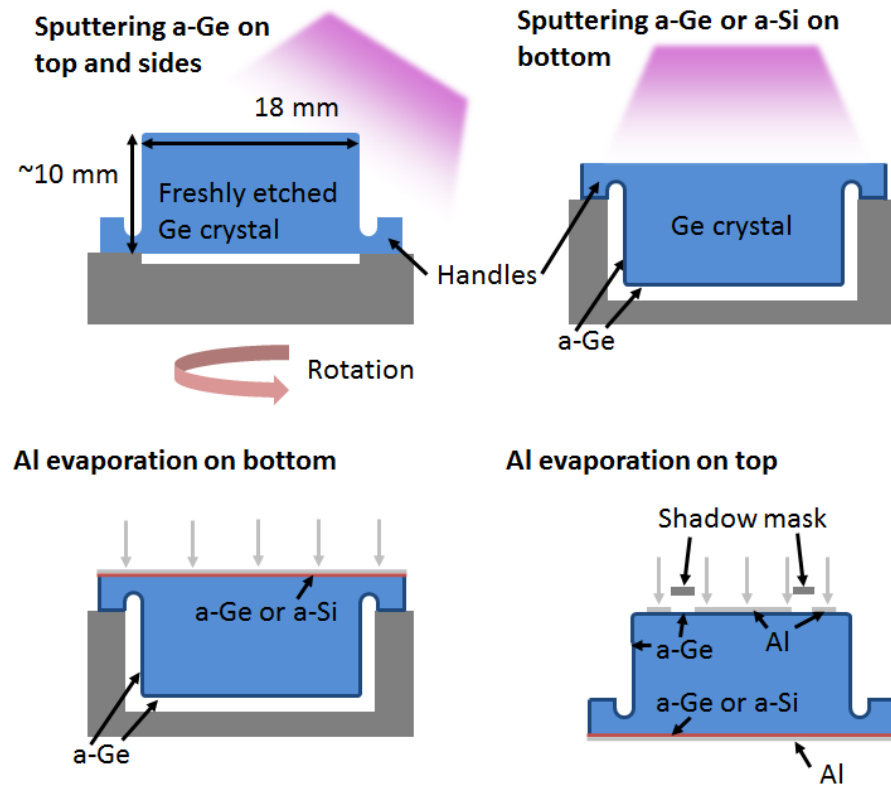


Figure 5.3. Schematic illustration of the sequence of depositions used to fabricate a guard ring planar detector used in the leakage current study.

### 5.3 Current-Voltage Testing

The detectors fabricated for this study were characterized in terms of leakage current using the current-voltage characteristic acquired at various temperatures. Each detector was loaded in a variable-temperature cryostat as shown in Figure 5.4. A voltage bias was applied to the bottom electrode and the top electrodes were monitored by picoammeters. The readout scheme is shown in Figure 5.5. Additionally, the first time a crystal sample was used, the full depletion voltage

was measured by observing the voltage at which the detector capacitance reached a minimum. This was done by adding a square pulse to the high-voltage input and observing the pulse height on the center contact with a preamplifier. A more detailed description of the current-voltage testing and circuit diagram is given in Appendix B.

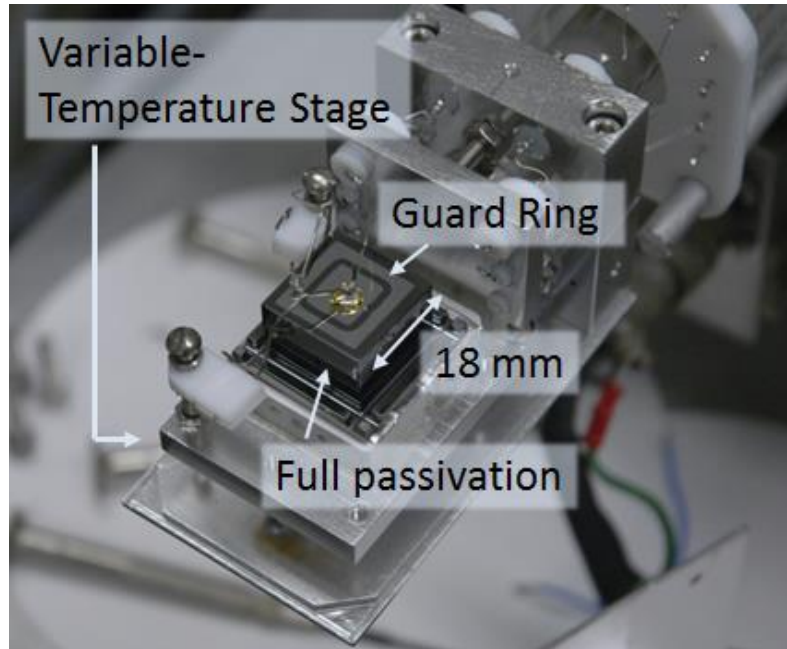


Figure 5.4. Photograph of a guard ring detector in the single-detector, variable-temperature cryostat.

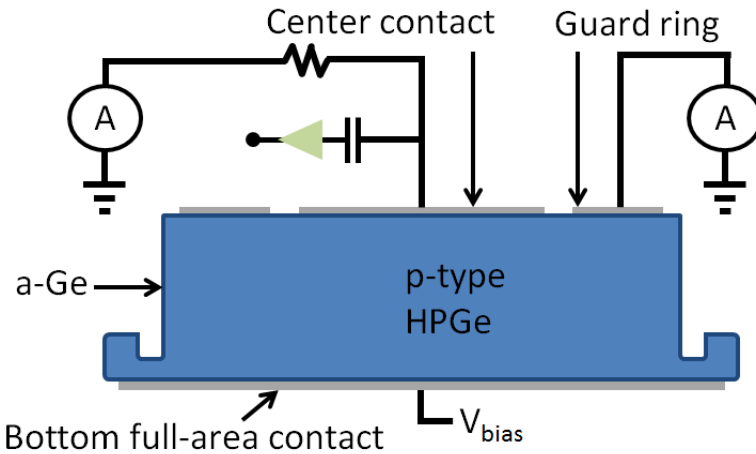


Figure 5.5. Readout schematic for current-voltage testing.

After the detector was cooled to  $\sim 80$  K, a current-voltage characteristic was acquired. If no electrical breakdown occurred, the detector was heated and the process repeated for several different temperatures. A more detailed description of the cryostat, testing apparatus, and testing procedure is given in Appendix B.

The study was confined to measuring electron injection leakage current on p-type HPGe crystals for some practical reasons. First, the fabrication process described uses a common

amorphous semiconductor layer for the top contact and the side surface passivation. Detectors using a-Ge with some hydrogen as the side passivation layer were found to have sufficiently low surface leakage current for precision measurements, but the detectors with a-Ge containing no hydrogen or any a-Si side surface passivation did not give low surface leakage current. This constricted the top contact to be a-Ge. Additionally, for good electrical separation between the center contact and guard ring, the detector had to be depleted initially from the top contact. This allows measurement of either electron injection at the bottom contact with p-type material or hole injection at the bottom contact with n-type material. The measurements conducted with n-type material had additional complications from higher leakage current from the top contact due to the lower electron barrier of a-Ge compared to its hole barrier.

## 5.4 Analysis

The current-voltage data for each detector were analyzed at multiple temperatures and characterized with the barrier height and pre-factor. These parameters were obtained using a current-temperature fit with Brodsky barrier lowering. The basis for the method of analysis is the assumption that each contact behaves as a Schottky diode with reverse-bias leakage current given by

$$J = A^0 T^2 e^{-\frac{\phi_B - \Delta\phi}{kT}}, \quad (26)$$

where  $J$  is the current density,  $A^0$  is the pre-factor,  $T$  is the detector temperature,  $\phi_B$  is the barrier height,  $\Delta\phi$  is the Brodsky barrier lowering term, and  $k$  is the Boltzmann constant. The term in brackets that appeared in (23) is neglected because  $V_a \gg kT$ , where  $V_a$  is the voltage seen across a contact.

An example I-V data set is shown in Figure 5.6 for a detector with an a-Ge bottom contact sputtered in 7 mTorr Ar with 7% H<sub>2</sub>.

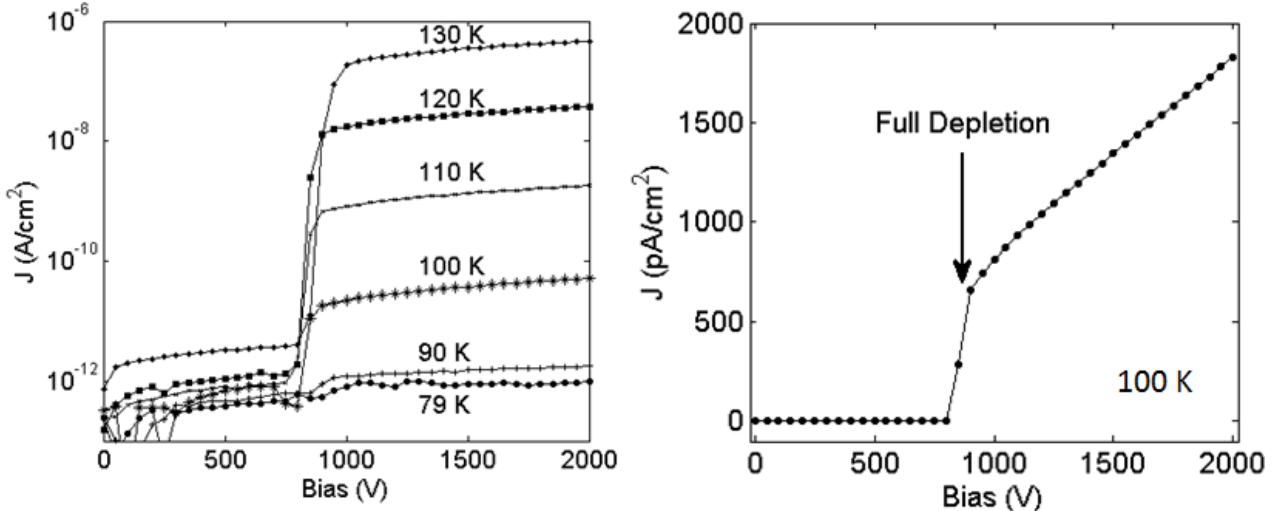


Figure 5.6. Example current-voltage data. The left panel shows a set of I-V data acquired at various temperatures. The right panel illustrates one I-V curve acquired at 100 K.

The current was normalized by the center contact area to give a current density per unit area  $J$ . The absolute value of current and voltage were taken to display results in a manner that is easy to understand and to facilitate later data processing, which includes logarithms. These data show the familiar I-V curve shape: a small, slowly rising current below full depletion voltage  $V_d$ , a rapid step at full depletion, and a steeper current rise above full depletion. In order to describe the overall I-V behavior, we need to separate the contribution from different current sources. At low bias, only the top contact contributes leakage current, while above full depletion both contacts contribute to current flow. There is some difficulty in extracting useful information from the I-V data below full depletion, so only the bottom contact is analyzed. Therefore, an effort is made to subtract the contribution from the top contact to isolate the bottom contact leakage current.

Amorphous semiconductor contacts have a barrier lowering term that varies according to the electric field magnitude at the contact [97]. For the detector configuration used here, we combine the electric field magnitude at the top contact in (8) and the barrier lowering term seen in (24) to get the barrier lowering behavior. Below full depletion voltage, the size of the depletion region is increasing with the square root of bias, and so too will the leakage current due to barrier lowering. Barrier lowering for the top contact below full depletion is

$$\Delta\phi_1 = \sqrt{2V \frac{N_d}{N_{f1}}} , \quad V < V_d , \quad (27)$$

where  $V$  is the applied bias,  $N_d$  is the net ionized impurity concentration, and  $N_f$  is the density of states in the amorphous layer. Above full depletion voltage  $V_d$ , the depletion width no longer changes, but the field is still increasing linearly with bias. The barrier lowering for this contact becomes

$$\Delta\phi_1 = \frac{V+V_d}{d} \sqrt{\frac{\epsilon}{qN_{f1}}} , \quad V > V_d , \quad (28)$$

where  $\epsilon$  is the permittivity of the crystal. The opposite contact contributes no charge injection below full depletion. Its barrier lowering term above full depletion is

$$\Delta\phi_2 = \frac{V-V_d}{d} \sqrt{\frac{\epsilon}{qN_{f2}}} , \quad V > V_d . \quad (29)$$

Then (27), (28), and (29) are used to replace the barrier lowering term in (26) for the two contacts. The total leakage current in the detector due to injection at the contacts is

$$J_{tot} = \begin{cases} A_1^0 T^2 e^{\frac{-\phi_1}{kT}} e^{\frac{1}{kT} \sqrt{2V \frac{N_d}{N_{f1}}}} & , \quad V < V_d \\ A_1^0 T^2 e^{\frac{-\phi_1}{kT}} e^{\frac{1}{kT} \frac{V+V_d}{d} \sqrt{\frac{\epsilon}{qN_{f1}}}} + A_2^0 T^2 e^{\frac{-\phi_2}{kT}} e^{\frac{1}{kT} \frac{V-V_d}{d} \sqrt{\frac{\epsilon}{qN_{f2}}}} & , \quad V > V_d \end{cases} . \quad (30)$$

The parameters  $A_1^0$ ,  $\phi_1$ , and  $N_{f1}$  apply to the first contact to be depleted, while the parameters  $A_2^0$ ,  $\phi_2$ , and  $N_{f2}$  apply to the opposite contact. One can now separate the contribution from the two contacts.

Below full depletion, only one contact injects charge. By estimating relevant parameters from I-V data below  $V_d$ , its contribution can be subtracted at all bias values, leaving only current due to bottom contact charge injection. Rearranging (30) for  $V < V_d$  gives

$$kT \ln J_{tot} = kT \ln A_1^0 + 2kT \ln T - \phi_1 + \sqrt{2 \frac{N_d}{N_{f1}}} V^{\frac{1}{2}}, \quad V > V_d. \quad (31)$$

Using a plot with the substitution

$$y_1 = kT \ln J_{tot} \quad (32)$$

$$x_1 = V^{1/2} \quad (33)$$

should give linear behavior for the current below full depletion. The slope of this line  $m_1$  allows calculation of the top contact density of states:

$$N_{f1} = \frac{2N_d}{m_1^2}. \quad (34)$$

$N_d$  is calculated from measured depletion voltage of the detector and the detector thickness. The offset of the line is a combination of the barrier and pre-factor,

$$A_1^0 T^2 e^{\frac{-\phi_1}{kT}} = e^{\frac{b_1}{kT}}, \quad (35)$$

where  $b_1$  is the line offset. Although this measurement does not give the individual parameters  $A_1^0$  and  $\phi_1$ , it does give everything necessary to describe the top contact current.

Figure 5.7 shows the top contact current estimation on the example data from the right panel from Figure 5.6. Black circles indicate current measurements, while the fit is shown as a red line. The horizontal range of the fit is chosen to avoid the uncertain low-voltage region and the discontinuity at full depletion.

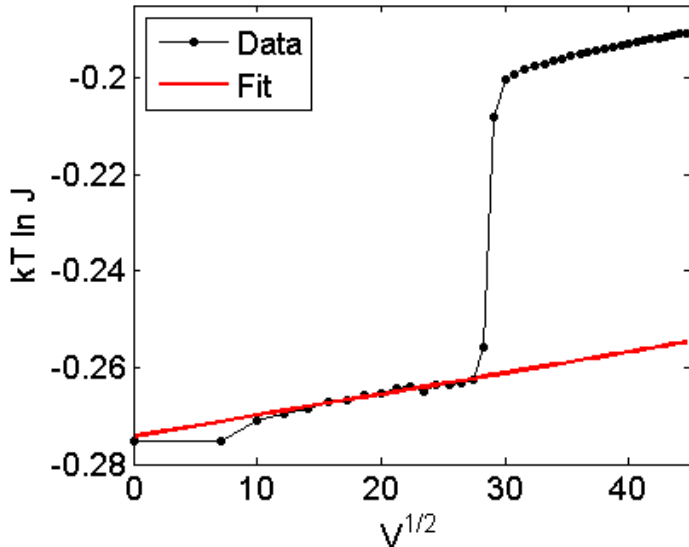


Figure 5.7. Top contact current estimation by fitting the I-V curve below full depletion.

The top contact current is then subtracted at all voltages. For voltages below full depletion, this subtraction should bring the current to approximately zero. Although in this case it has no impact on the parameter extraction from the bottom contact, it is confirmation that the subtraction is the correct magnitude. Figure 5.8 shows an example of the subtraction. The measurement is normally designed such that top contact injection current is less than bottom contact injection current, so the top contact current subtraction is normally not a large portion of the overall current above full depletion. However, in some cases, such as when the bottom contact has a large barrier height, it is more important.

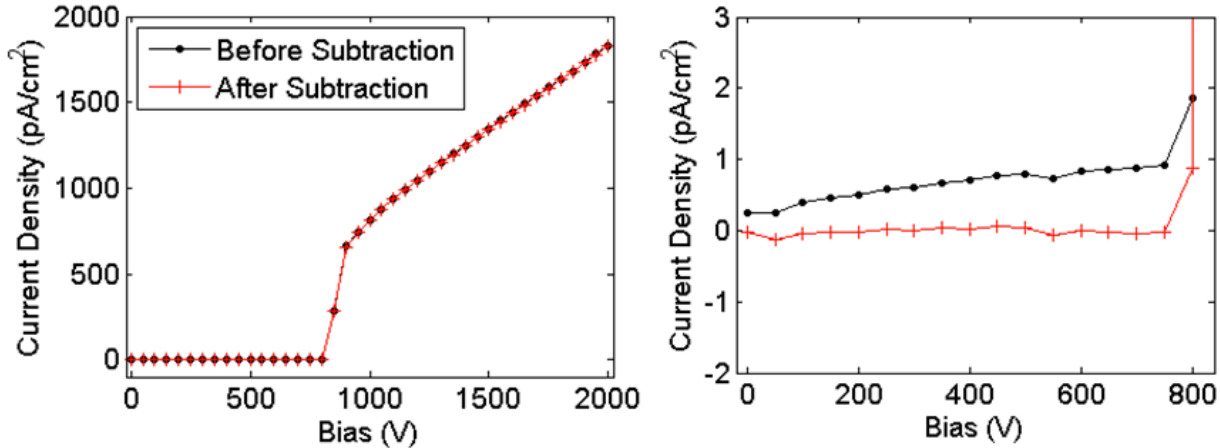


Figure 5.8. Top contact current subtraction. The left panel shows the full I-V curve before and after subtraction. The right panel is a zoom on the current below full depletion.

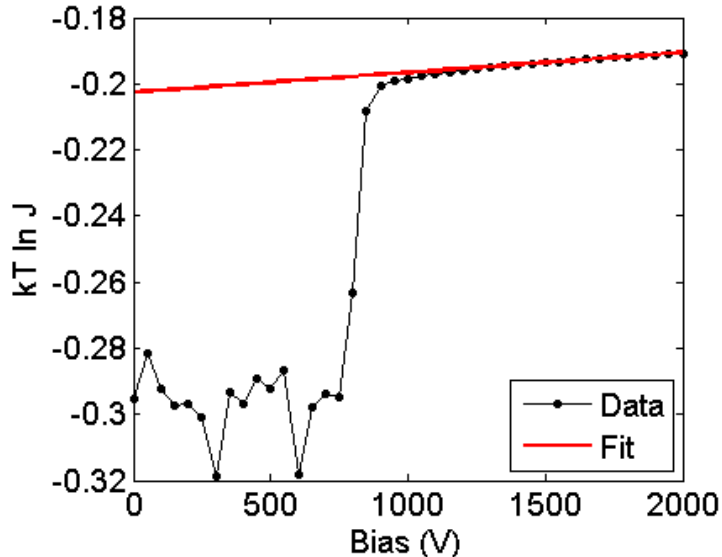


Figure 5.9. Example of a fit to the portion of the I-V curve above full depletion. The data have been corrected for the top contact contribution and only data above full depletion voltage are used for the fit.

Only the bottom contact current should remain after the subtraction, characterized as

$$J_2 = A_2^0 T^2 e^{-\frac{\phi_2}{kT}} e^{\frac{1}{kT} \frac{V-V_d}{d} \sqrt{\frac{\epsilon}{qN_{f2}}}} . \quad (36)$$

We can estimate the density of states for the bottom contact in order to find the barrier lowering term for this contact. Using the substitution

$$y_2 = kT \ln J_2 \quad (37)$$

$$x_2 = V \quad (38)$$

gives a plot like that in Figure 5.9. A fit region well above full depletion is chosen and we use

$$N_{f2} = \frac{\epsilon}{qm_2^2 d^2} \quad (39)$$

to calculate the bottom contact density of states.

Now that we have all parameters to define the barrier lowering terms, we finally do a fit on current vs. temperature to separate the contribution from the barrier height and pre-factor. This can be done for all voltage values measured, but practically, the highest voltage value available is chosen to best avoid any non-uniformity in the depletion layer. We first make the substitution

$$y = \ln \frac{J_{tot}}{T^2} \quad (40)$$

$$x = \frac{1}{T} . \quad (41)$$

Only data at temperatures high enough to contribute significant current are included, which normally omits data below 100 K. Due to the measurement limitation of the equipment, only current values of at least a few pA can be accurately measured.

The current-temperature data, plotted as described above, are fit with a line. The plot is shown in Figure 5.10 for the example data of the previous plots in this section.

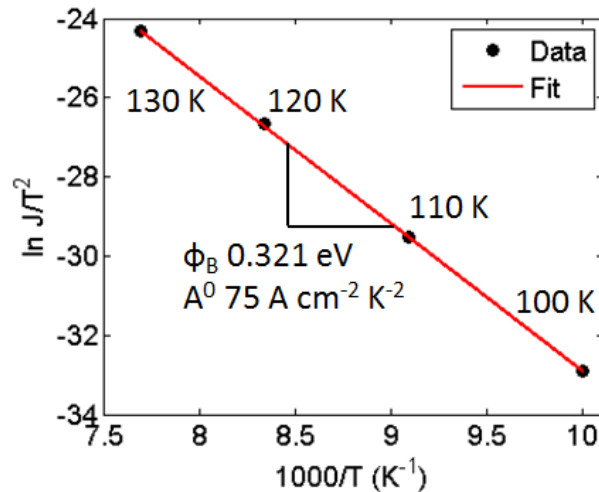


Figure 5.10. Current-temperature fit to example data. The slope gives a barrier height of 0.321 eV and the offset of the line gives a pre-factor of  $75 \text{ A cm}^{-2} \text{K}^{-2}$ .

The slope of the line allows calculation of the bottom contact barrier height

$$\phi_2 = -km + \Delta\phi_2 \quad (42)$$

and the offset of the line gives the pre-factor:

$$A_2^0 = e^b . \quad (43)$$

This analysis method is the basis for the barrier height and pre-factor values given in the results section.

## 5.5 Results

The results of the electron injection leakage current study are presented in this section. Eleven crystal samples were used in fabricating about 45 detectors to generate the data presented. All detectors were guard ring devices and the parameters presented are for the bottom full-area contact. Analysis was performed in the same way for all samples as described in the previous section. Some attempt is made to connect fabrication process parameters with variations in leakage current for the contacts under study. The studied contacts were a-Ge and a-Si deposited with varying sputter pressure, hydrogen content, and film thickness.

### 5.5.1 Reproducibility

After initial analysis of some results, it was clear that there was significant variation in leakage current for similar detectors. In order to more properly investigate, five detectors were fabricated in rapid succession using the same crystal sample and the same fabrication process with a-Ge contacts sputtered in 15 mTorr Ar with 7% H<sub>2</sub> for both the top and bottom contacts. Except for the amount of material removed in the initial cleanup etch, the process was kept as constant as possible given the current equipment and methods, and the detectors were tested soon after the detector was completed. The current-voltage characteristic at 100 K for the five detectors is shown in Figure 5.11. The variation among the five detectors is significant. The first three detectors had less material etched away during the cleanup step. These used 1 minute in 20:1 HNO<sub>3</sub>:HF, removing about 4  $\mu$ m of material, while the last two detectors were prepared using 1 minute in 4:1 HNO<sub>3</sub>:HF, which removes about 17  $\mu$ m of material. There is no clear connection between the amount of material removed in the cleanup etch and the detector leakage current. The level of variation for the five detectors is more than expected.

Another measure of reproducibility is the current at a given temperature for all detectors fabricated using the same process. Figure 5.12 shows the current-voltage characteristic at 100 K for all detectors with a-Ge contacts sputtered in 15 mTorr Ar with 7% H<sub>2</sub>. The step at full depletion is expected to occur at different voltage values because of different crystal thicknesses and impurity concentrations. However, one might expect the leakage current to be the same order of magnitude for all detectors, but this was not the case.

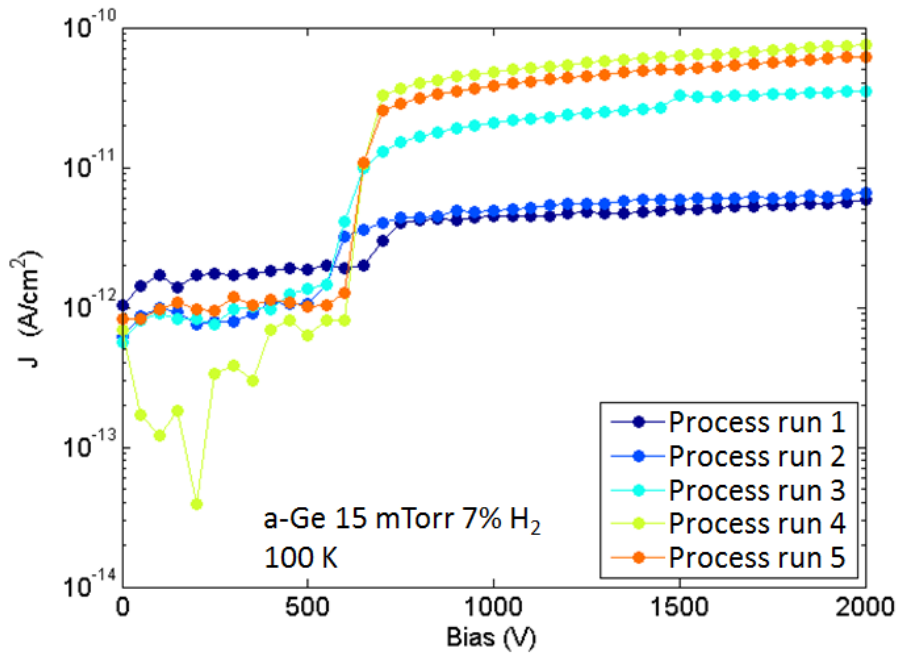


Figure 5.11. Current-voltage curves for five detectors fabricated in rapid succession using the same fabrication process on the same crystal. The data acquired at 100 K are shown for all five detectors.

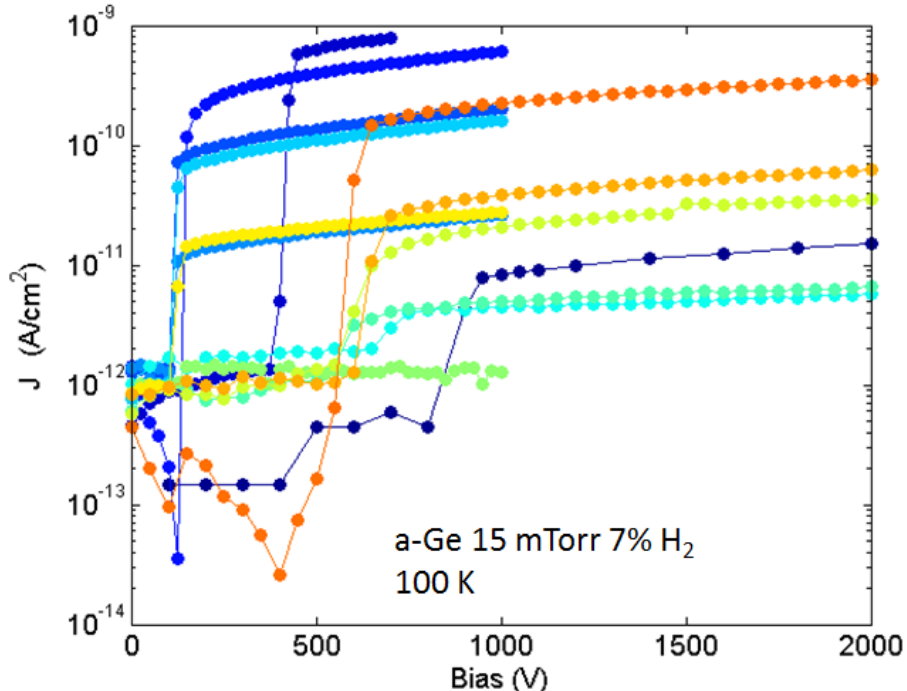


Figure 5.12. Current-voltage characteristic for all detectors fabricated with a-Ge in 15 mTorr Ar (7% H<sub>2</sub>). Data were acquired at 100 K.

A similar comparison is shown in Figure 5.13 for a slightly different process. All detectors fabricated with a-Ge sputtered in 7 mTorr Ar (7% H<sub>2</sub>) atmosphere showed significant variation in the magnitude of leakage current.

The large variation in leakage current is reflected in the calculated barrier height and pre-factor values. There is a large spread in these parameters for detectors made using the same fabrication process, making an analysis of the impact of process parameters more difficult. However, we can search for trends in the data to reach some conclusions, even if definite statements about single detectors are meaningless.

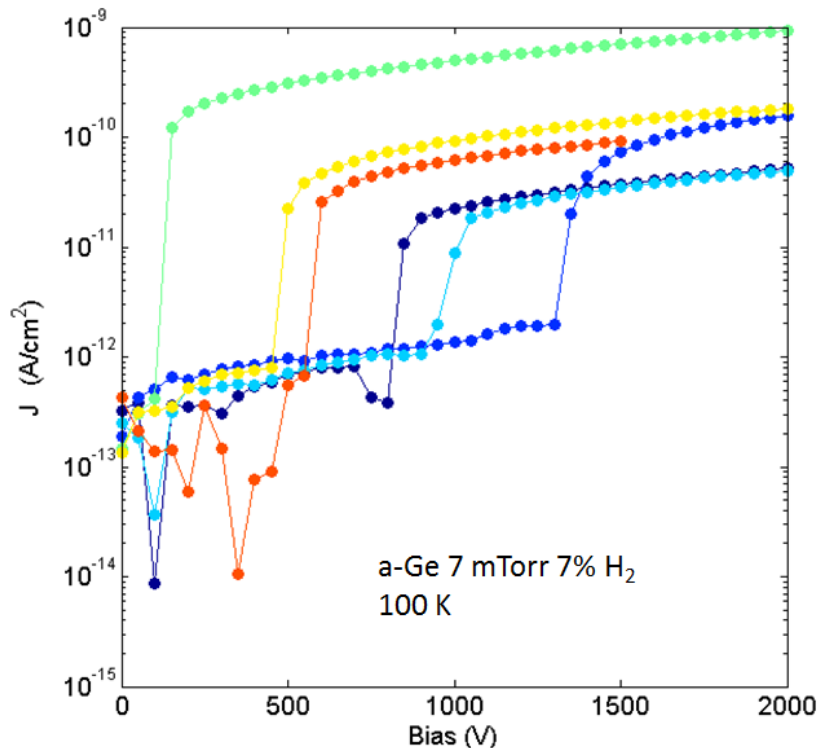


Figure 5.13. Current-voltage characteristic at 100 K for all detectors fabricated with a-Ge sputtered in 7 mTorr Ar (7% H<sub>2</sub>) atmosphere.

## 5.5.2 Effect of Hydrogen Content

Samples were fabricated using different sputter gases, all chiefly argon with some hydrogen. The hydrogen content in this section refers to the percentage of hydrogen in the source gas, but this does not necessarily correspond to the amount of hydrogen in the amorphous film [121]. Figure 5.14 shows the electron barrier as a function of sputter gas hydrogen content. The different materials a-Ge and a-Si are split into different series because they may respond differently to varying hydrogen content. The a-Ge data are split into two series with different sputter pressure to minimize other possible important factors, but each series still contains a significant number of detectors. The corresponding pre-factor is shown in Figure 5.15. On each

plot, different color markers represent the data from each series and a line is drawn through the average values to guide the eye.

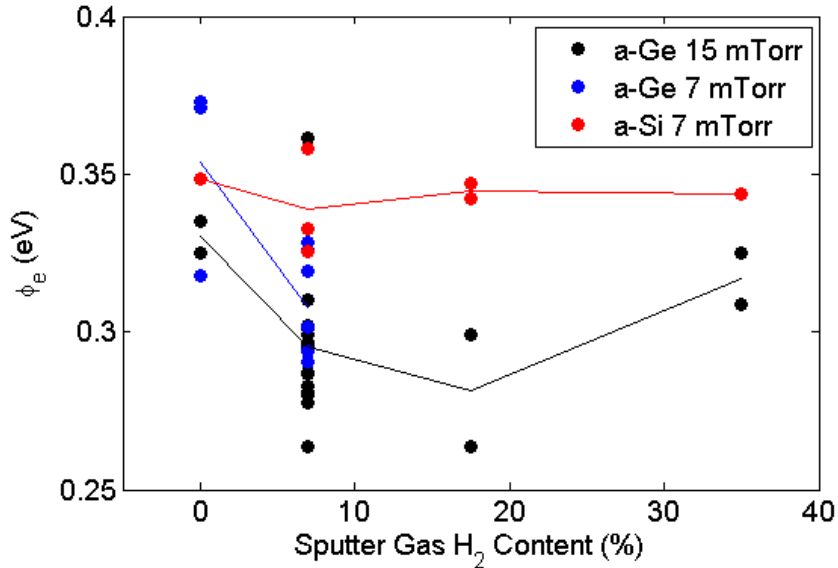


Figure 5.14. Electron barrier as a function of hydrogen content of the sputter gas.

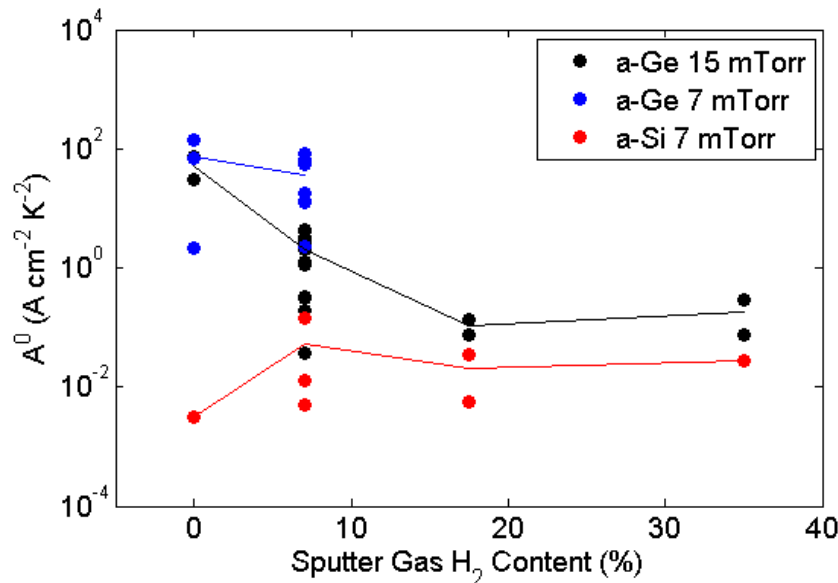


Figure 5.15. Pre-factor as a function of sputter gas hydrogen content.

With the level of reproducibility and number of samples in this study, it is difficult to make clear conclusions from these data. From the data available, it seems that the electron barrier does not show a significant trend with hydrogen content for any of the data series. The pre-factor for electron injection does not show a significant trend for either a-Si or a-Ge sputtered at 7 mTorr, but the a-Ge sputtered at 15 mTorr tends to show a smaller pre-factor at higher H<sub>2</sub> content.

Even with the level of variation, one apparent conclusion is the difference between a-Si and a-Ge. The a-Si contacts generally showed a higher electron barrier height and a lower pre-factor, both of which combine to give lower electron injection leakage current. All detectors with a-Ge contacts, regardless of other fabrication parameters, had an average electron barrier of  $0.304 \pm 0.026$  eV, where the uncertainty is given as the standard deviation of the sample of 34 detectors. All detectors with an a-Si contact had an average electron barrier of  $0.339 \pm 0.012$  eV for a total of 9 detectors. The pre-factor for a-Ge detectors was  $19 \pm 33$   $\text{A cm}^{-2} \text{ K}^{-2}$ , compared to a pre-factor for a-Si of  $0.026 \pm 0.045$   $\text{A cm}^{-2} \text{ K}^{-2}$ . The pre-factor values varied over several orders of magnitude, so the standard deviation is highly influenced by the higher values for a few detectors. These numbers must be used with caution because they are based on a range of fabrication parameters, some of which are shown in this section to influence electron barrier and pre-factor. The numbers mentioned above are for all available detectors, but the range of fabrication parameters is not evenly represented.

### 5.5.3 Effect of Sputter Pressure

Detectors were fabricated with varying sputter gas pressure during deposition of the bottom contact. The pressure is monitored with a Pirani gauge during the deposition sequence with a precision of about 0.1 mTorr.

Figure 5.16 shows the extracted electron barrier for all a-Ge contacts deposited in 7%  $\text{H}_2$  gas as a function of sputter gas pressure. The presented data set is confined to 7%  $\text{H}_2$  sputter gas in order to eliminate that variable while still leaving a significant data set. Figure 5.17 shows the associated pre-factor for the same contacts.

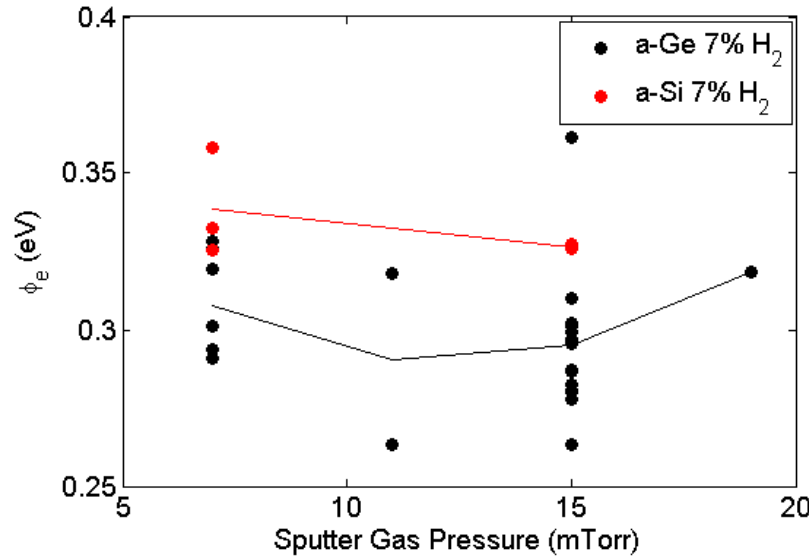


Figure 5.16. Electron barrier as a function of sputter gas pressure for all a-Ge contacts with 7%  $\text{H}_2$  sputter gas.

The electron barrier data do not show a significant trend. The pre-factors for a-Ge in Figure 5.17, however, show a generally declining value with increasing sputter pressure. There were

not sufficient a-Si data to draw meaningful plots of varying sputter pressure. Only 7 mTorr and 15 mTorr were tried, and the latter data set contains only a couple of detectors.

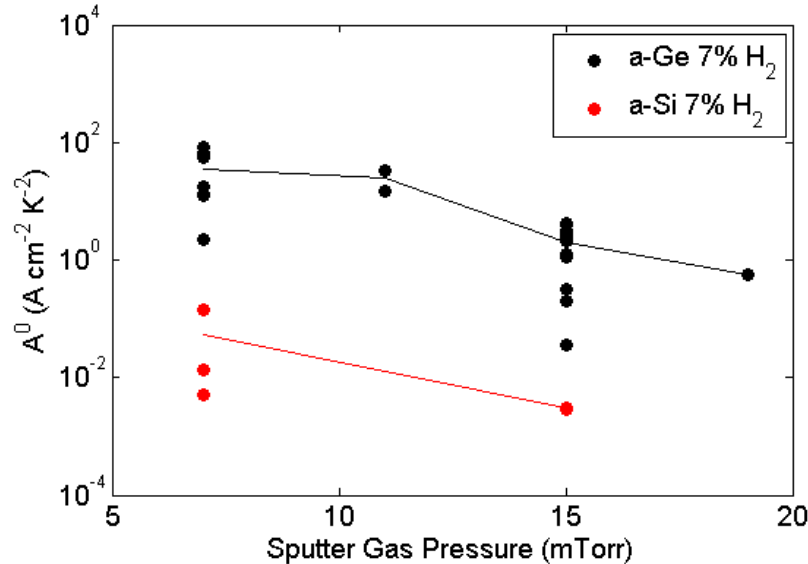


Figure 5.17. Pre-factor as a function of sputter gas pressure for all a-Ge contacts with 7% H<sub>2</sub> sputter gas.

#### 5.5.4 Effect of Film Thickness

Detectors were fabricated with various amorphous semiconductor film thicknesses. The thickness values here are presented in terms of number of deposition sequences, giving an arbitrary unit of measurement proportional to actual film thickness within one data series. These numbers are not directly comparable with different sputter pressure because of different amount of gas scattering, or among different materials because of differing sputter yield for the materials. As with varying hydrogen content, the data are divided into three major data sets to reduce the number of variables. The a-Ge deposition process carried out at 7 mTorr saw about 70 nm per deposition sequence, while the 15 mTorr a-Ge process had about 100 nm per sequence. The a-Si deposition, which was run at a higher power, had about 120 nm per deposition sequence.

The electron barrier height as a function of contact thickness is shown in Figure 5.18, where black markers represent a-Ge contacts sputtered in 15 mTorr gas, blue markers represent a-Ge contacts sputtered in 7 mTorr gas, and red markers represent a-Si contacts sputtered in 7 mTorr gas. Lines are drawn through the average values to guide the eye. Figure 5.19 shows the associated pre-factor values with a similar graphical representation.

There does not seem to be a significant trend in any of the data for varying film thickness. A variation in leakage current was not expected for different film thicknesses since the properties of the interface serve as the theoretical basis for the blocking behavior of the contacts. This data set provides experimental confirmation of this prediction.

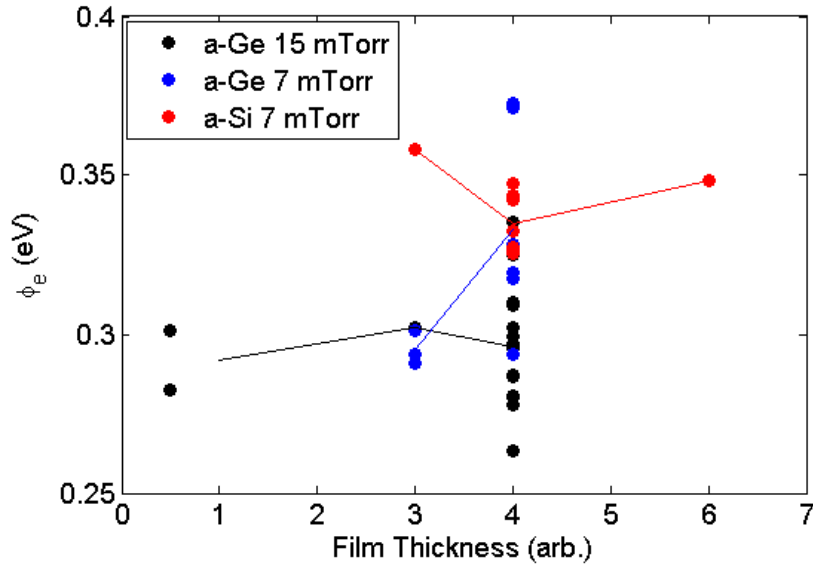


Figure 5.18. Electron barrier as a function of amorphous semiconductor film thickness.

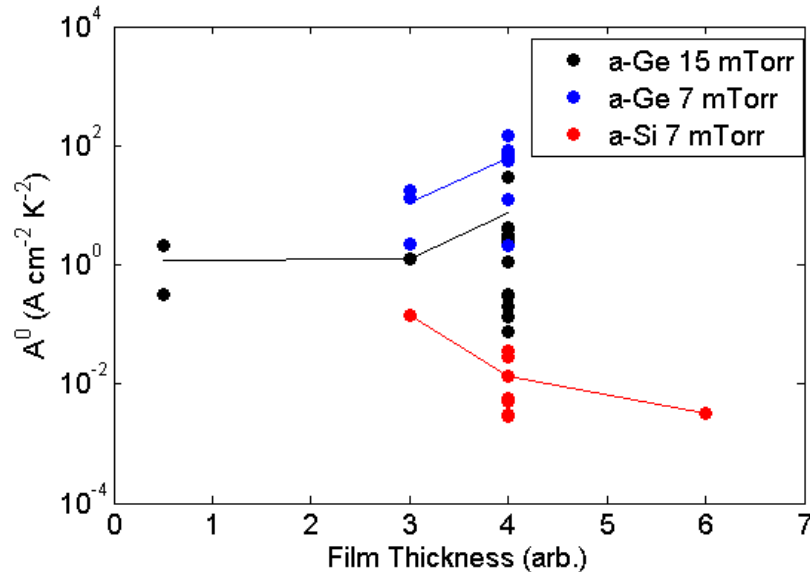


Figure 5.19. Pre-factor as a function of amorphous semiconductor film thickness.

## 5.6 Conclusions

A systematic study of the electron injection leakage current was presented for a set of about 45 detectors fabricated with a-Ge and a-Si contacts. The amorphous semiconductor contacts were sputtered with varying sputter gas pressure, sputter gas hydrogen content, and film thickness, and an attempt was made to assess the impact of those fabrication process parameters on the detector leakage current. The detector leakage current for each detector was measured at several temperatures and the electron barrier height and pre-factor were extracted from the data.

The reproducibility of electron injection leakage current is a major issue with the measurements in this study. Even using the same crystal and the same process multiple times was not predictable, nor was the same process on different crystals. There are many possible reasons for the lack of reproducibility in this study, but it is not necessarily an inherent limitation of amorphous semiconductor contacts.

There is a clear motivation for future work focusing on the causes of variation in leakage current for one fabrication process. One avenue for improvement is the etching process to clean the surfaces before contact deposition. The wet chemical etch is quite chaotic and the resulting surface depends on how well the acid is mixed, agitation of the crystal, materials on the surface before etching, and how the crystal is dried afterward. Differences in texture are often clearly visible, even when the same procedure is attempted multiple times. A likely reason is that the 4:1  $\text{HNO}_3:\text{HF}$  mixture is quite aggressive and removes about 17  $\mu\text{m}/\text{min}$  of germanium. Any minor defect will quickly be amplified as material continues to be removed at a rapid rate. One possible alternative is chemical-mechanical polishing of flat surfaces to remove foreign layers and obtain a very flat surface, then cleaning the surface with a light etch to remove only a small amount of material. This could result in a more controlled etching process and more consistent surface preparation. Another avenue for improvement is with the sputtering system. The source gas cylinders have a gas composition that is not precisely known. Using new, high-purity source gas could provide some better control during the sputter deposition. The RF diode sputtering system used in this work also causes significant heating of samples during sputtering, which adds another uncertain parameter. Using an RF magnetron sputtering system could reduce the level of heating (also reducing the variation in heating) and reduce the level of bombardment by electrons, which can alter the film structure. If such bombardment were found to be essential to good contact performance, it could be done in a more controlled manner using substrate biasing.

One conclusion is clear from the leakage current data even with a relatively large spread in values. The electron barrier for a-Si contacts is almost always higher than a-Ge contacts, regardless of hydrogen content, sputter pressure, or film thickness. Similarly, the pre-factor for a-Si is significantly lower than for a-Ge. These two factors combine to give lower electron injection leakage current for a-Si, making these contacts better suited for negatively biased (electron-blocking) contacts.

Some trends can be observed with fabrication process parameters. The a-Ge electron barrier seems largely unaffected by hydrogen content or sputter pressure, but the pre-factor tends to be lower for higher hydrogen content and for higher sputter pressure. Film thickness did not seem to play a significant role in either barrier height or pre-factor for a-Ge and a-Si. Although it is difficult to say with much certainty, it seems that higher hydrogen content and higher sputter pressure may be desirable for obtaining low leakage current. The a-Si barrier height and pre-factor seemed largely independent of hydrogen content and film thickness.

Future work in studying variations in leakage current would be beneficial in understanding what factors are important. The reproducibility issues should be addressed first in order to improve reliability of measurements for a specific fabrication process. It would also be beneficial to perform a study on a larger number of samples. For expediency, a good approach would likely involve simultaneous fabrication and testing of multiple detectors.

# Chapter 6 Long-Term Stability

This chapter describes the methods, measurements, and results for investigating long-term contact stability, another key challenge with amorphous semiconductor contacts on germanium detectors. After the contacts are formed, the detector can spend substantial time at room temperature, especially when a multi-detector system is being built. Also, it is inevitable that a germanium detector, after being operated cold for some time, will need to be warmed. The fabrication process has a profound effect on contact stability [26]. Identifying and understanding important factors in providing stability will yield an improved fabrication process and perhaps give clues as to what changes may take place in the contacts over time. This chapter describes a study of the electron injection leakage current in several detectors with amorphous semiconductor contacts formed under various conditions. The detectors were tested over a period of weeks to months with several temperature cycles to assess their long-term stability.

## 6.1 Background

The first germanium radiation detectors were Germanium Li-drifted, or Ge(Li) detectors [3]. Although quite revolutionary in achievable energy resolution, these detectors could not be allowed to warm to room temperature or the Li would diffuse around the crystal and disrupt the precise compensation profile, making the detector inoperable [81]. High-purity germanium detectors represented a major advance in technology by eliminating the problem of decompensation in the bulk, but changes in the contacts can still be an issue.

Detector warming is essentially inevitable over the life of a radiation detector. After fabrication, the detector must be tested for quality assurance, but in most cases it must then be transferred to a different cryostat or at least transported to a different location, which is most prudently done warm. Even during operation by the end user, some occasions arise where something in the cryostat needs to be adjusted or a person may simply forget to fill liquid nitrogen, or a mechanical cooler may fail. Therefore, it is preferable to build a stable detector rather than insist it always stay cold. Additionally, detectors operated in a high-radiation environment may suffer damage from ions or neutrons, which can be repaired by annealing at high temperature [76]. Numerous temperature cycles (up to  $\sim$ 40) may result from annealing radiation damage in an HPGe detector.

Long-term stability is well-established for detectors with conventional contacts based on electrically active impurities. Amorphous semiconductor layers are fundamentally different from doped crystalline semiconductor layers, so it is important to evaluate the long-term stability of contacts and passivation formed by amorphous semiconductor layers. Although it is generally good practice to avoid unnecessarily warming any germanium detector, it should be emphasized that commercial detectors with conventional contacts are routinely warmed with no ill effect. Attaining a similar level of confidence in segmented detectors using amorphous semiconductor contacts is the ultimate goal of this work.

### 6.1.1 Effect on Detectors

Because electrical contacts are an integral part of a detector, changes in the contacts due to temperature cycling or elapsed time can have significant effects on detector performance. The most obvious change is a change in leakage current after the detector is warmed and re-tested. Small increases will appear as an increase in electronic noise, but too severe an increase can cause preamplifier saturation or detector breakdown, either of which would mean the end of the detector's usefulness. With amorphous semiconductor contacts, the leakage current typically increases or decreases with each successive temperature cycle [110]. The effect is usually not so severe that a single temperature cycle would destroy a detector, as was the case with Ge(Li) detectors, but several cycles tend to have a cumulative effect that limits the number of cycles if there is a significant increase in current. The change in leakage current with each temperature cycle is not always the same, and the physical change taking place is unknown. Other changes with temperature cycling of detectors include worsening of surface channels or electrical breakdown. Studying these other effects could be valuable in identifying stable fabrication processes and understanding the change with temperature cycling, but they are beyond the scope of this study. This chapter presents a systematic study on the electron injection leakage current for detectors with amorphous semiconductor contacts.

### 6.1.2 Previous Work

Very little work has been published on temperature cycling or long-term stability of amorphous semiconductor contacts. In the past, temperature cycling a detector with conventional impurity-based contacts was sometimes used as a method to drive off surface contaminants and reduce leakage current [108] [109]. Changes in amorphous semiconductor contact performance are mentioned only briefly in studies of contact leakage current [26] [101]. No systematic study of long-term stability has been published.

The purpose of this study is to investigate the reason for differences in the change seen with temperature cycles, such as the different magnitude of the change between temperature cycles, and the reasons why some contacts show increasing leakage current while others give decreasing current. The ultimate goal is to identify important fabrication process parameters and optimize a fabrication process that can reliably produce amorphous semiconductor contacts that are stable over time, so that they could be used on a detector with no ill effect for many temperature cycles. Currently, the mechanism of change in the amorphous semiconductor layer is unknown, so a study of this type could also shed light on what physical changes are taking place in the film and possibly guide future studies. An investigation of the material properties would also be beneficial, but is beyond the scope of this work.

## 6.2 Current-Voltage Testing

The same detectors fabricated for the leakage current study presented in Chapter 5 were also used for this study. The detectors were p-type planar detectors with a-Ge top contacts and side passivation and either a-Ge or a-Si contacts on the bottom surface. A guard ring electrode structure was used on the top surface to separate the bulk injection current and surface leakage current. The same variations in fabrication process parameters described in Chapter 5 were used

here, including different sputter gas hydrogen content, sputter gas pressure, and amorphous film thickness.

After initial testing and acquisition of I-V curves at various temperatures, the detector was warmed to room temperature and held there for some time. In some cases, the detector was kept under continuous vacuum while warm, but in some cases the detector was exposed to air. After about 24 hours or more, the detector was again cooled to cryogenic temperature and I-V characteristics were acquired at various temperatures. Figure 6.1 shows the temperature profile of a detector in a typical cycle.

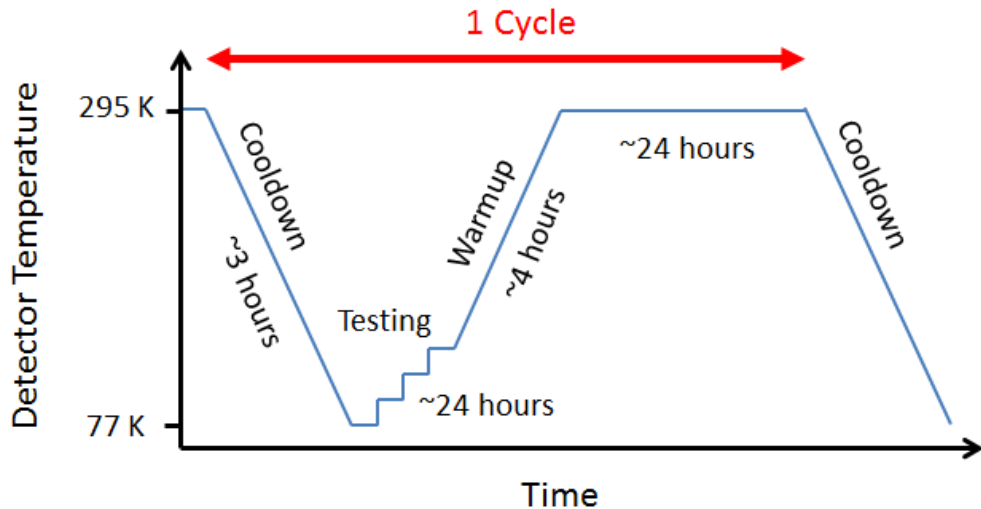


Figure 6.1. Schematic illustration of detector temperature during a temperature cycle.

The cycle began when the detector was cooled, a process that took about 3 hours. After settling at the base temperature (around 80 K), a current-voltage characteristic was acquired and the detector was then warmed to a higher temperature. The process was repeated for 10 K increments until the current became too high, about  $10^{-7}$  A, where the circuit series resistance dropped significant voltage. When testing was complete, the detector was warmed to room temperature (295 K) over 4 hours and kept there about 24 hours, although the time warm sometimes varied substantially. This process was repeated several times for each detector until electrical breakdown occurred or the crystal was needed for other tests.

This was a time-consuming process, sometimes taking months to acquire data over several temperature cycles. To facilitate expedient testing, a variable-temperature cryostat capable of handling multiple detectors was designed and constructed. The design was based on the same principles as the single-detector cryostat used in the leakage current study of Chapter 5, only in a larger size to accommodate multiple detectors and the associated readout channels. Although this has been done for similar studies before [101], building such a cryostat had unique challenges due to the large high-vacuum chamber, stringent requirements for base leakage current, low base temperature, and the addition of a large variable-temperature stage. The reader is referred to Appendix B for details concerning the design and construction of this cryostat.

### 6.3 Analysis

The temperature cycling analysis was designed to focus on changes in the leakage current, since this is a measure of interest in detector operation. Analysis of all cycles is conducted at one temperature, reminiscent of what is observed by end users who operate a detector at the base temperature determined by the cryostat and may see changes in the leakage current over time. An example set of I-V characteristics at one temperature over several temperature cycles is shown in Figure 6.2. This example was chosen because it shows a significant increase in leakage current over several temperature cycles. As initially tested, the detector had 50 pA/cm<sup>2</sup> leakage current density at 2000 V, which could give reasonable electronic noise performance. However, after 11 temperature cycles, the leakage current had increased to more than 700 pA/cm<sup>2</sup>, a value much more likely to hurt energy resolution.

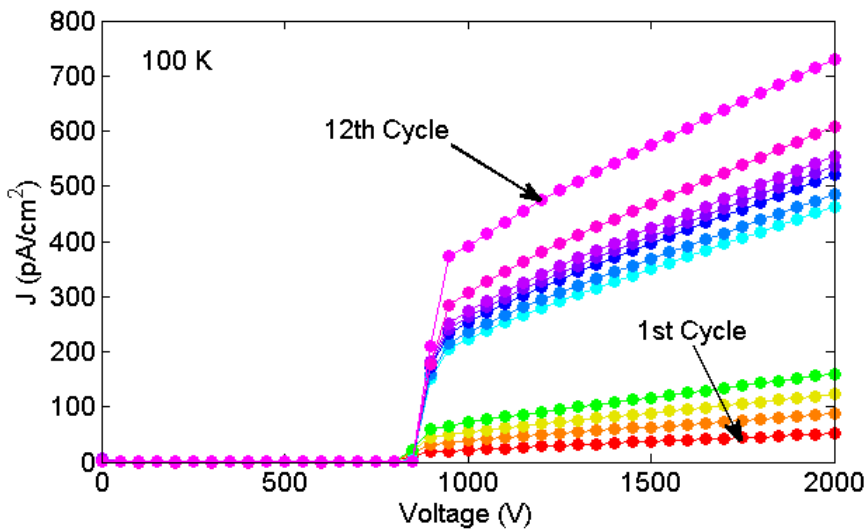


Figure 6.2. Example of I-V data at 100 K over several temperature cycles.

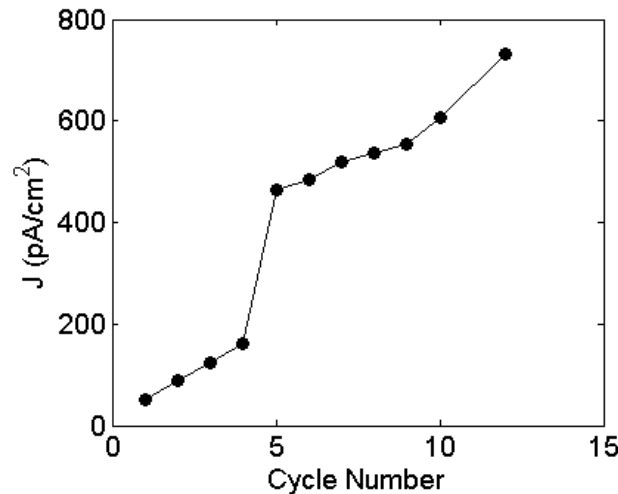


Figure 6.3. Plot of leakage current density vs. temperature cycle at a specific temperature and bias.

Although Figure 6.2 makes it clear that leakage current is changing with temperature cycles, all of the information is not needed, and it is difficult to compare different fabrication processes on the same plot. We can condense the information by focusing on the current at a specific voltage as a function of temperature cycle number. The result is a simple plot as shown in Figure 6.3, where the data from Figure 6.2 have been selected at 2000 V bias.

It was suspected that the time the detector spent warm between cycles was related to the change in current and perhaps responsible for the discontinuities like the large change from cycle 4 to cycle 5 in Figure 6.3. However, as Figure 6.4 shows, the time spent warm before a cycle is not a good predictor of the change in current for that cycle. The normalized change in current for cycle  $i$  is defined as  $\frac{J_i}{J_{i-1}}$ . The time warm is measured from the time the detector reached 295 K

to the time liquid nitrogen was added for the next cycle. This is approximately the time the detector spends at room temperature. There is no clear correlation between the change in current for a particular cycle and the time warm for that cycle. There also seemed to be no correlation between exposure to air and the magnitude of the change in current.

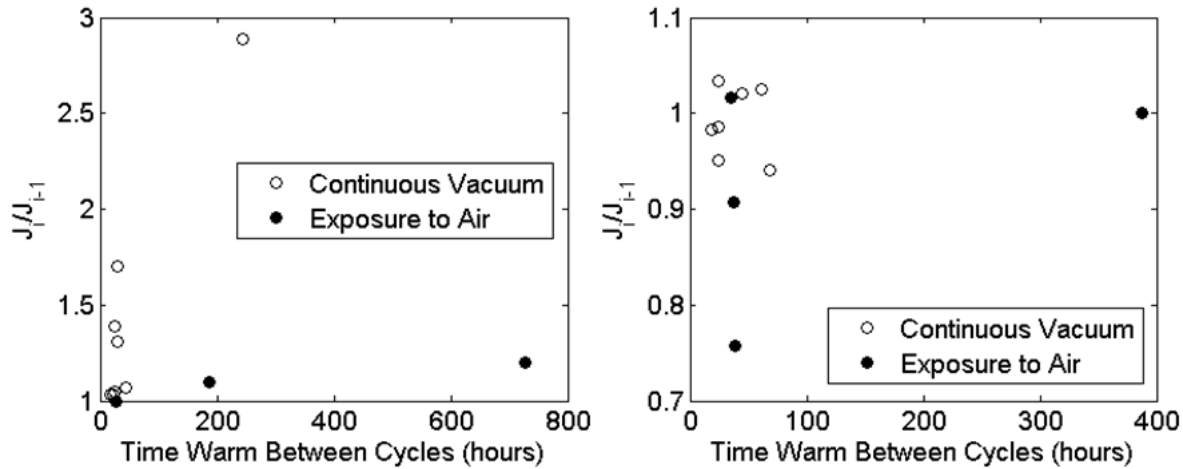


Figure 6.4. Normalized change in current as a function of time warm between cycles. The left panel shows the example data from previous plots, while the right panel shows data from another detector to clearly illustrate the role of air exposure.

The change in current between cycles was found to correlate with cumulative time the detector spent at room temperature rather than time warm between cycles. Therefore the plot used in the temperature cycle analysis is of the style shown in Figure 6.5. This is normalized to the initially measured current at cycle 1. Using this type of plot, changes in the current among different fabrication processes can be directly compared.

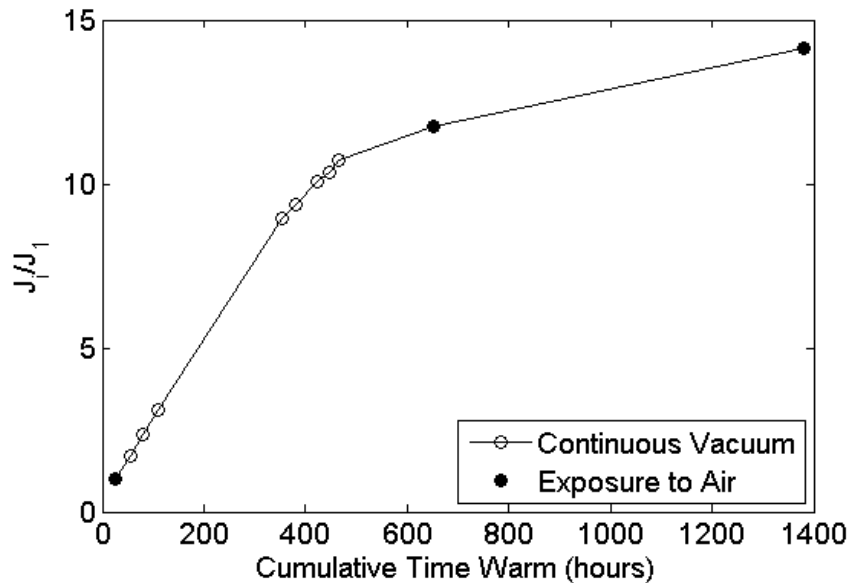


Figure 6.5. Example data shown as current normalized to the initially measured current vs. cumulative time spent at room temperature.

## 6.4 Results

The results of several detectors tested with multiple temperature cycles are presented here. An attempt is made to correlate fabrication process parameters with varying degrees of stability over time. The ultimate goal of this study is to determine a fabrication process associated with the most stable and reliable amorphous semiconductor contact. This section presents the results from about 25 detectors with a-Ge and a-Si contacts that were tested over several temperature cycles, in some cases reaching more than 10 cycles.

### 6.4.1 Effect of Time Warm

The physical change that takes place in amorphous semiconductor contacts over time is not currently known. The change in leakage current each time the detector is tested after being at room temperature can seem unpredictable. In most cases, a detector will exhibit either monotonically increasing or monotonically decreasing leakage current each time the detector is temperature cycled, but the magnitude of the change is not always the same.

As the previous section indicated, the change in leakage current is not directly related to time warm between cycles or the number of temperature cycles. The relevant parameter seems to be the time the detector has spent at room temperature. The leakage current shows a relatively rapid change initially with time warm and eventually levels off to a much lower rate of increase after hundreds of hours at room temperature. This discovery brought new insight into the data analysis when comparing different fabrication processes because it explains some of the differences seen among different temperature cycles that vary in the time the detector spent warm. Subsequent sections reporting the effect of various fabrication process parameters on

long-term stability will show the total change in leakage current as a function of cumulative time the detector has spent at room temperature.

Exposure to ambient air seemed to make no difference compared with cycles where the detector was kept continuously under high vacuum. Although the possibility exists that surface contaminants from the air could deposit on the surface and change the contact properties, it seems that the surface passivation is properly protecting the detector from unwanted changes due to its surroundings.

#### 6.4.2 Effect of Sputter Pressure

Detectors that had been fabricated with different sputter gas pressure were tested over several temperature cycles. The sputter gas pressure was found to be an important parameter for long-term contact stability. The a-Ge contacts were studied because more of these detectors were fabricated than those with a-Si contacts, and 7% H<sub>2</sub> gas was chosen because it was shown to have generally good contact properties and had the greatest success rate in making useful detectors. All crystals were from the same crystal boule.

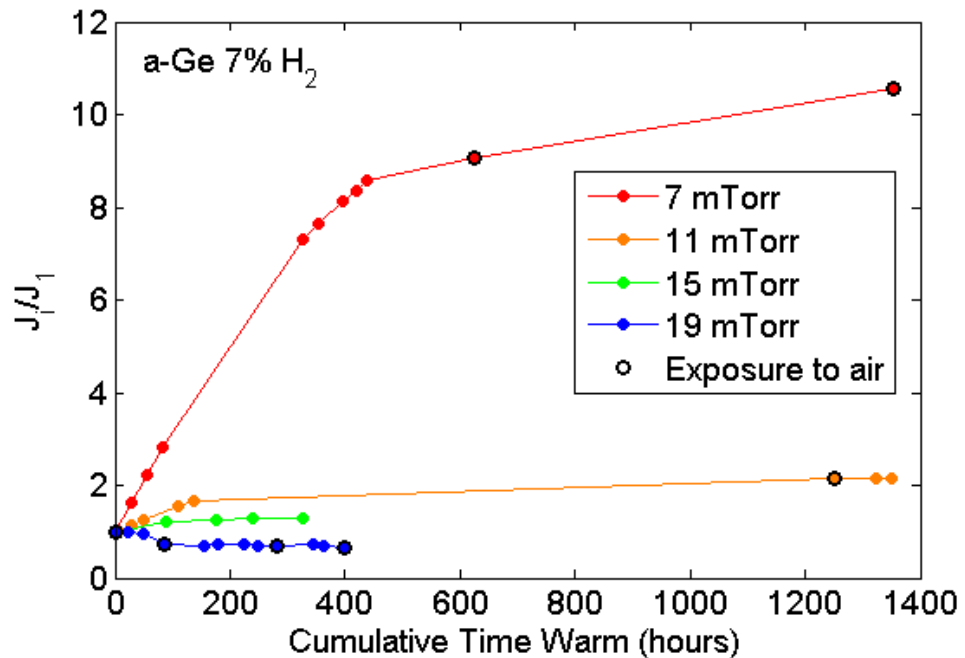
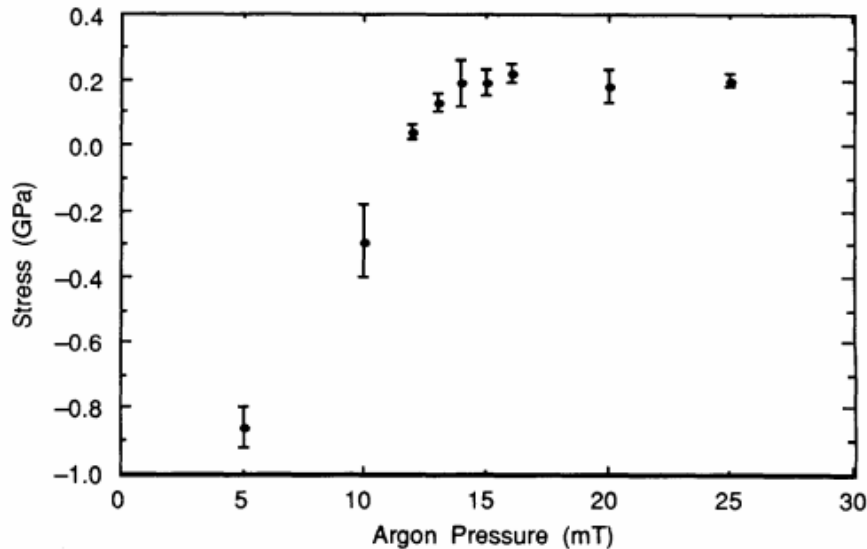


Figure 6.6. Leakage current density ratio as a function of total time warm for a-Ge contacts sputtered in various gas pressures. All used 7% H<sub>2</sub> sputter gas and crystals were taken from the same boule.

The detectors with contacts sputtered in lower pressure showed the most change with time. The electron injection current for these detectors increased dramatically over time, while those sputtered in higher pressure showed a slight decrease with time. The detector with an a-Ge contact sputtered in 7 mTorr gas showed more than a ten-fold increase in electron injection leakage current after ~1400 hours at room temperature. The detector with an a-Ge contact sputtered in 11 mTorr gas showed only twice the leakage current after the same amount of time, while even higher sputter pressure yielded a-Ge contacts with very slow changes in leakage

current. At 15 mTorr, the leakage current changed only by ~10% after 300 hours warm, while the contact sputtered in 19 mTorr had slightly decreasing leakage current with time. The changes are leakage current for these detectors are shown in Figure 6.6.

This pattern matches well with measured stress in RF-sputtered a-Ge films in a study by Fahnlund using a different sputtering system [102]. Figure 6.7, from that work, shows a high magnitude of compressive stress in a-Ge sputtered at low pressure due to Ar atom inclusion and fewer voids. By contrast, films sputtered in higher pressure have tensile stress with a lower magnitude. A crossover point of zero stress occurs near 13 mTorr.



**Figure 6.7. Measured film stress in RF-magnetron sputtered a-Ge as a function of sputter pressure. [102]**

The a-Si contacts were not studied sufficiently to provide a satisfactory comparison of different sputter pressures. Only contacts sputtered in 7 mTorr and 15 mTorr were fabricated and only a couple of 15 mTorr detectors were successfully tested.

#### 6.4.3 Effect of Hydrogen Content

Some detectors with contacts of varying hydrogen content were compared for long-term stability. A single crystal sample from LBL-grown material was fabricated multiple times with the bottom contact being a-Ge sputtered in 15 mTorr gas of varying hydrogen content. The HPGe material used in this section was drawn from a different crystal boule than the HPGe used in the previous section. A different crystal boule was used because multiple studies were done in parallel and all available crystals were used that were known to be good detector material. Differences among the different crystal samples are discussed later. The total change in leakage current as a function of total time warm for these four detectors is shown in Figure 6.8. Note the compressed vertical axis with respect to Figure 6.6.

The first three detectors with hydrogen content up to 17.5% showed nearly identical behavior, all having less than a 10% increase in electron injection leakage current after about 200 hours at room temperature. The final detector, with 35% hydrogen content, had slightly decreasing leakage current with time, but the magnitude of the change was still relatively small.

This detector suffered from a moderate surface channel effect, making the I-V data more difficult to interpret.

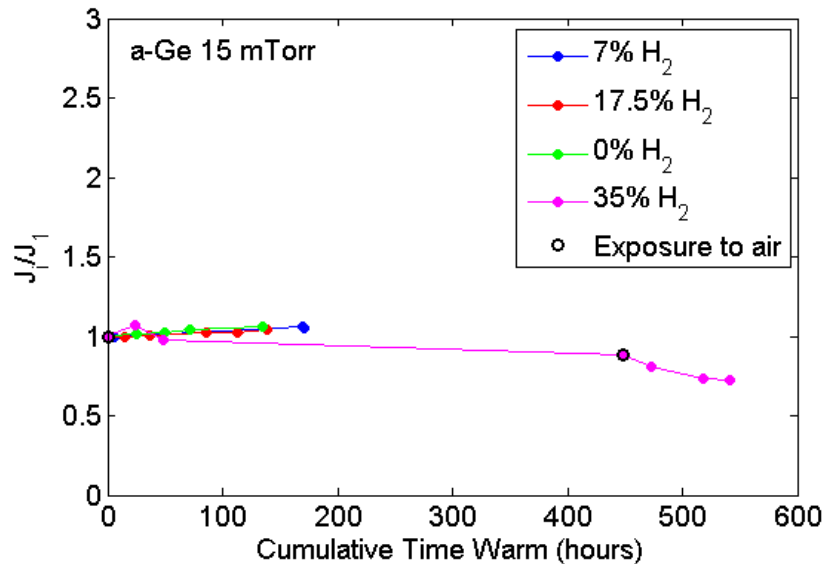


Figure 6.8. Leakage current density ratio as a function of total time warm for detectors with a-Ge contacts sputtered at 15 mTorr with gases of varying hydrogen content. All detectors were made using the same crystal sample.

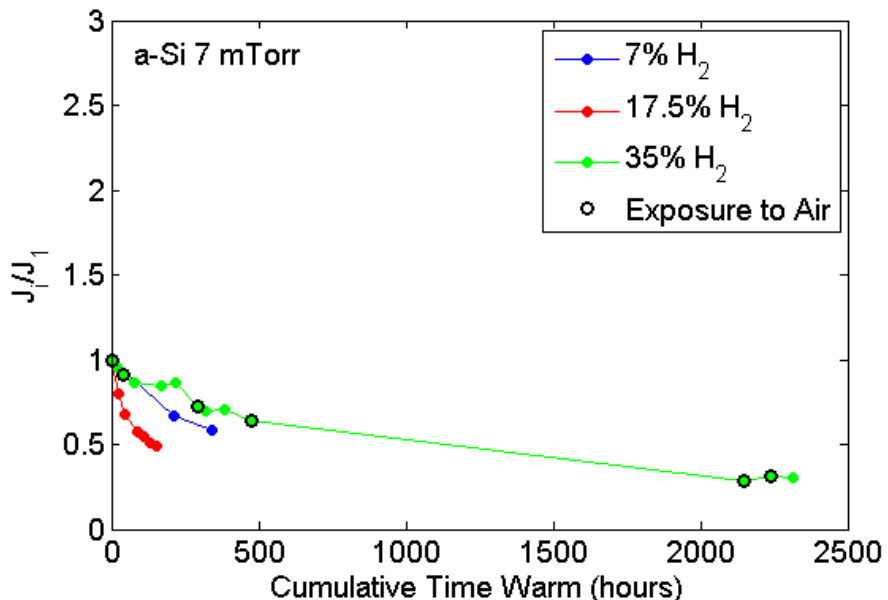


Figure 6.9. Leakage current density ratio as a function of total time warm for detectors with a-Si contacts sputtered at 7 mTorr with gases of varying hydrogen content. All crystal samples were from the same boule.

Some detectors with a-Si contacts with varying hydrogen content were also compared. These were sputtered at 7 mTorr and used crystals from the same boule of Ortec-grown material. All showed typical behavior of a-Si contacts, with decreasing electron injection leakage current as a

function of time warm. Some differences in the amount of change were observed with no observed trend related to hydrogen content. Again, the detector sputtered with 35% H<sub>2</sub> gas suffered from a moderate surface channel effect, causing slightly erratic behavior because the I-V curve was more difficult to interpret.

#### 6.4.4 Effect of Film Thickness

The effect of film thickness was also studied for a-Ge contacts on crystal samples from the same boule. Figure 6.10 shows total change in current as a function of total time warm for a-Ge contacts sputtered in 15 mTorr Ar with 7% H<sub>2</sub> gas for two different amounts of time. Two samples had the standard thickness used for most detectors in this study, while the green trace shows a detector with a thinner contact layer. The overall change in current was larger and more erratic for the thinner contact.

The thickness of the amorphous semiconductor film was estimated from profilometry measurements on glass sample slides with painted stripes. A-Ge was sputtered on the glass sample slide at the same sputter pressure. The stripes were then removed and a profilometer was used to measure the a-Ge thickness on the slide. For the a-Ge contact deposition on a detector, the contact thickness was estimated by multiplying the deposition time by the measured deposition rate from the glass slide. The uncertainty on film thickness is estimated at about 5% of the measured thickness.

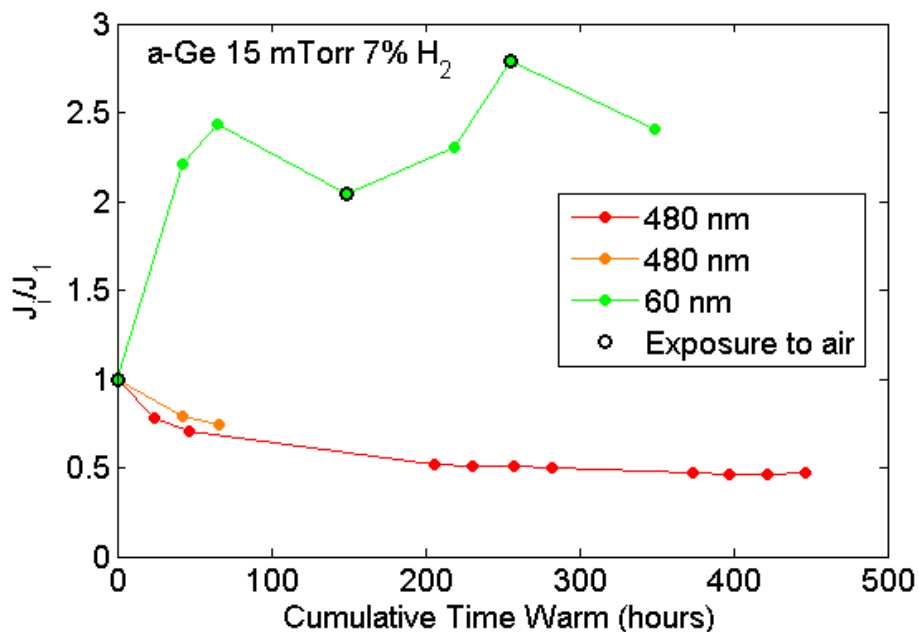


Figure 6.10. Leakage current density ratio as a function of total time warm for detectors with a-Ge contacts sputtered at 15 mTorr gas with 7% H<sub>2</sub> content. The number of depositions was different, giving different values for estimated contact thickness.

### 6.4.5 Reproducibility

Detectors made with the same contact fabrication process were compared to assess the reproducibility of contacts with long-term stability. Figure 6.11 shows the total change in current as a function of time warm for multiple detectors with a-Ge contacts sputtered at two different pressures. Although there are some variations among detectors fabricated using the same process, the difference due to varying sputter pressure was significantly greater than the differences among the detectors tested. The detectors with a-Ge contacts sputtered in 7 mTorr gas all showed a substantial increase in leakage current over many hours at room temperature, while all detectors with a-Ge contacts sputtered in 15 mTorr gas showed relatively small changes. The 7 mTorr process is associated with an increase in current that is about an order of magnitude after several hundred hours warm. The 15 mTorr process, by contrast, is associated with changes in leakage current on the order of 10% after hundreds of hours warm. The detectors were made using crystals from three different boules, two having been purchased from Ortec (“Ortec 1” and “Ortec 2”) and another having been grown at LBL (called “LBL1”). All HPGe material was p-type with a net ionized impurity concentration ranging from  $5 \times 10^9 \text{ cm}^{-3}$  to  $2 \times 10^{10} \text{ cm}^{-3}$ .

The variations among different detectors using the same fabrication process showed a pattern relating to the crystal boule used as source material. Figure 6.12 shows the total change in current as a function of time warm for three different detectors, all fabricated with a-Ge contacts sputtered in 15 mTorr gas with 7% H<sub>2</sub> content. Those detectors using material from the boule Ortec2 showed a slight decrease in leakage current over time, while detectors made from the other boules showed slightly increasing leakage current around 5% and 25%.

Multiple detectors made with the same a-Si process showed similar behavior, seen in Figure 6.13. All detectors, made with material from three different boules, had decreasing electron injection leakage current as a function of time at room temperature. There did not seem to be any significant differences among the three detectors.

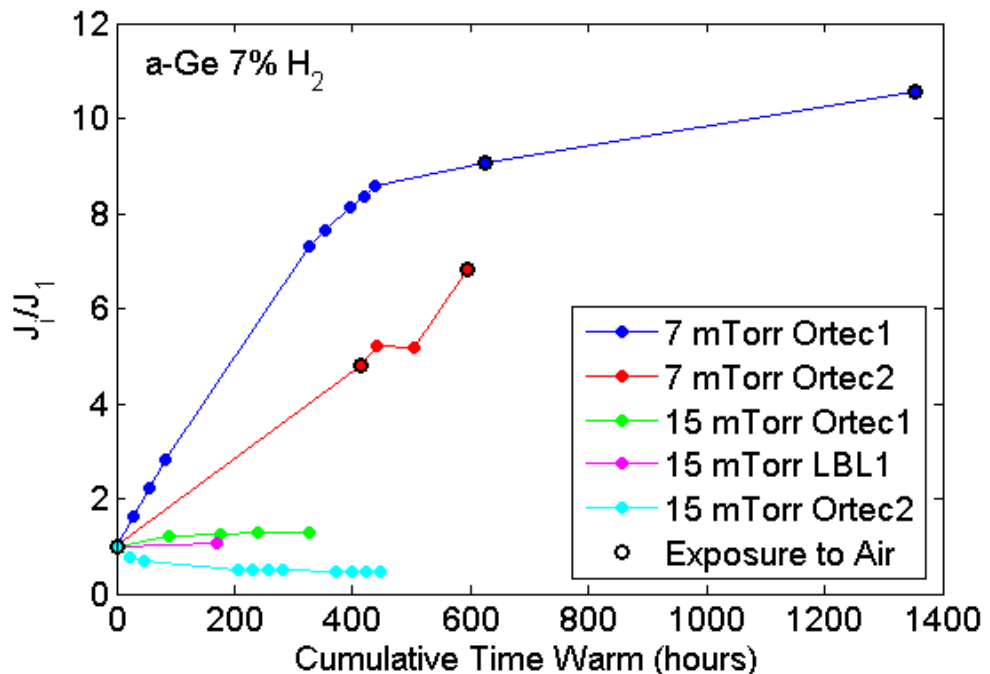


Figure 6.11. Leakage current density ratio as a function of total time warm for detectors with a-Ge contacts sputtered in 7% H<sub>2</sub> gas. Detectors made with crystals from three different boules are pictured.

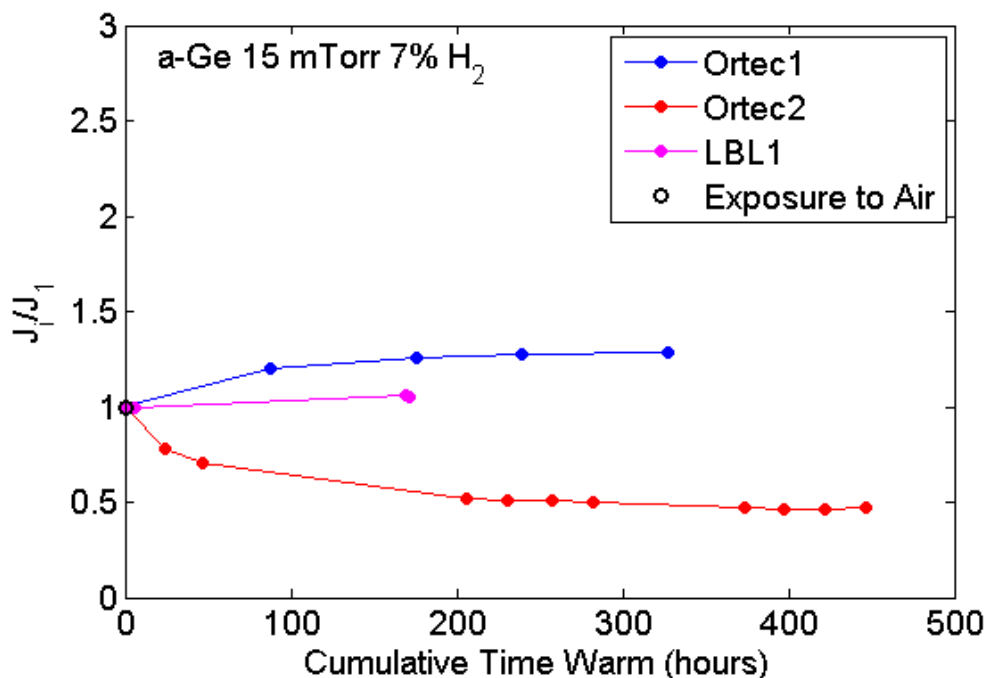


Figure 6.12. Leakage current density ratio as a function of total time warm for detectors with a-Ge contacts sputtered in 15 mTorr 7% H<sub>2</sub> gas. Detectors made with crystals from three different boules are pictured.

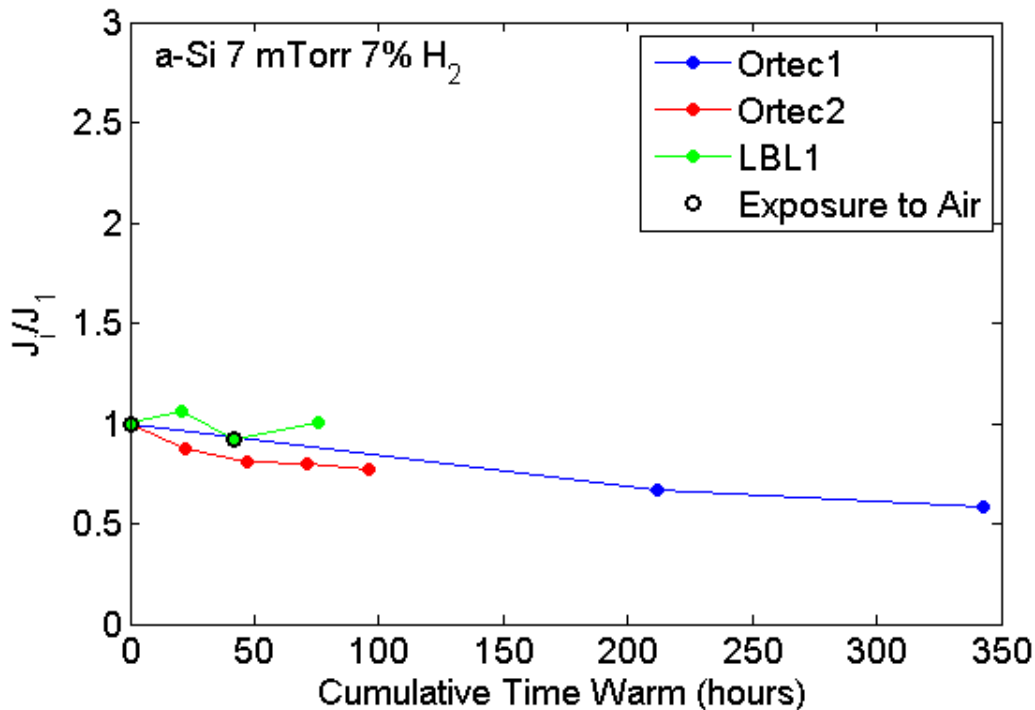


Figure 6.13. Leakage current density ratio as a function of total time warm for detectors with a-Si contacts sputtered in 7 mTorr 7% H<sub>2</sub> gas. Detectors made with crystals from three different boules are pictured.

## 6.5 Conclusions

This chapter presented a study of long-term stability of amorphous semiconductor contacts on HPGe detectors. About 25 detectors were evaluated for their long-term electron injection leakage current over a period of months, with several temperature cycles during that time. The detectors had a-Ge and a-Si contacts sputtered in varying sputter gas pressure with varying sputter gas hydrogen content. This study confirmed the results of previous work, indicating that the fabrication process has a strong impact on the long-term stability of amorphous semiconductor contacts. Obtaining stable contacts is critical for sustained operation of HPGe detectors. It is desirable to have a process that produces detectors with performance independent of temperature cycling or storage at room temperature.

A new metric was developed for evaluating the long-term stability of detector leakage current. The time at room temperature, rather than the number of temperature cycles, is the relevant parameter in assessing the change in the contacts. Additionally, exposure to air made little difference compared to when the detector was kept in high vacuum, suggesting that the fully passivated detectors are resistant to external contaminants. This would confirm the usefulness of the amorphous semiconductor layers as surface passivation.

For a-Ge contacts sputtered at 15 mTorr, hydrogen content makes little difference in long-term stability. However, the gas pressure in which a-Ge contacts are sputtered is critical in determining both the magnitude and direction of their change in leakage current with time. It is

desirable to sputter the contacts at a minimum of 15 mTorr gas pressure to give good stability. It seems beneficial to use the highest gas pressure possible, provided the reduced deposition rate is not detrimental to the process. One detector seemed to suggest that using a thin a-Ge layer (<300 nm) may decrease the long-term stability of an otherwise stable process.

For a-Si contacts, the electron injection leakage current shows a slight decrease over time and depends very little on hydrogen content. This makes a-Si contacts an even more attractive option as electron-blocking contacts, considering that they have initially low leakage current, which will only decrease if the detector is warmed. The change diminishes with time.

The measurements at varying sputter pressure suggest that intrinsic film stress is the relevant property affecting changes in the contact over time. Since the change depends on time warm rather than other factors, the film could have a slow creep over time to alleviate intrinsic stress. The re-settling of the interface layer could cause a change in leakage current. If the activation energy for movement of atoms is in the appropriate range, the film creep could be observable at room temperature but not at cryogenic temperature.

# Chapter 7 Inter-Electrode Charge Collection

This chapter describes a study on inter-electrode charge collection, another challenge of amorphous semiconductor contacts identified in Chapter 4. This effect can hurt the performance of segmented detectors, showing an energy deficit in events where charge is shared among multiple electrodes. This chapter discusses the effect of inter-electrode charge collection on segmented detectors and previous work studying this effect. This is followed by a description of strip detector fabrication performed for this study and measurements conducted using those strip detectors. Results and conclusions regarding the influence of the fabrication process on inter-electrode charge collection are presented.

## 7.1 Background

For segmented electrode detectors, the inter-electrode region has a similar requirement to side surfaces in that it should not collect moving charge carriers. Treating this surface sometimes requires additional fabrication steps and its properties can impact detector performance [26] [66] [112].

### 7.1.1 Effect on Detectors

Segmentation can be performed on virtually all types of contacts [59] [60] [85] [15] [77] [62], but similar requirements apply to all. Appropriate processing of the inter-electrode region is essential to segmented detector performance. There must be sufficiently high impedance between electrodes to keep electronic noise to a minimum and the surface must inhibit collection of charge carriers to the inter-electrode region.

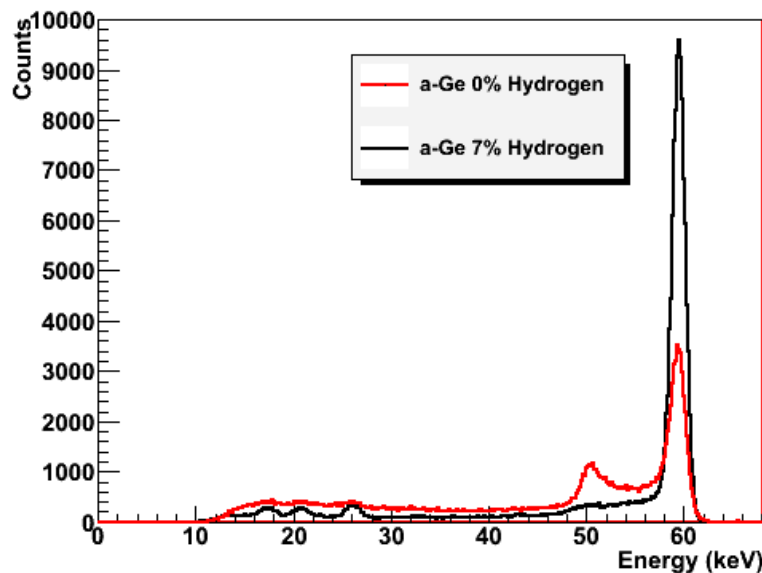
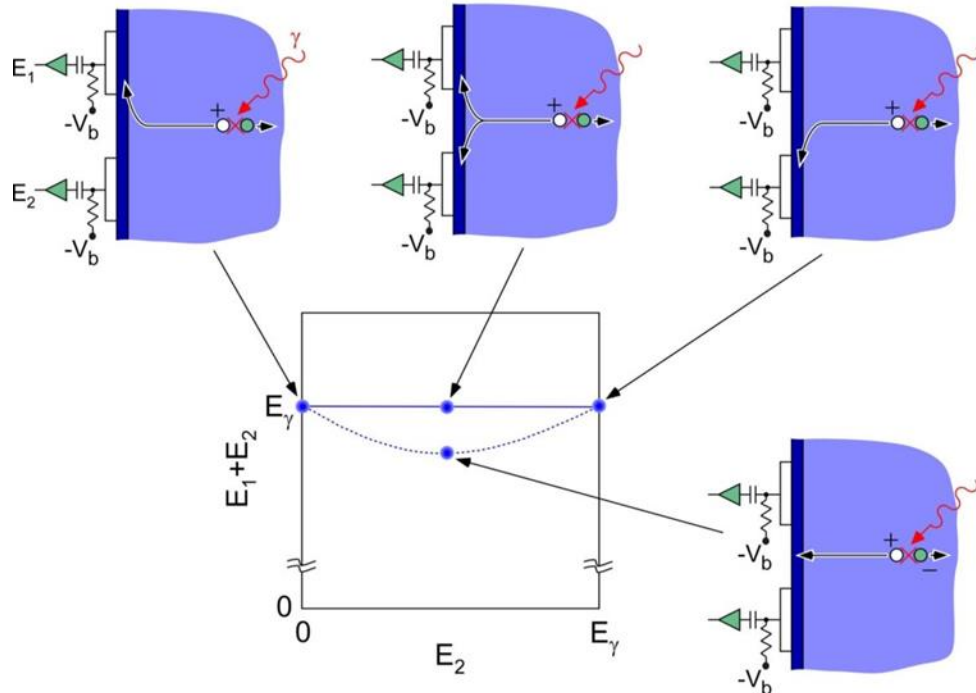


Figure 7.1. Summed energy spectra of two adjacent strips from two detectors with a-Ge contacts. One had no added hydrogen in the amorphous layer, while the other had 7%  $\text{H}_2$  content.

Any passivation material (or lack thereof) on the inter-electrode surface can be detrimental to detector performance if moving charge is collected directly to that surface. These charge carriers will not drift through the maximum weighting potential of any electrodes, so even a sum of the signals from adjacent electrodes will not yield the full signal that is sensed when charge carriers drift directly to an electrode. This is observed by a class of events in the summed energy spectrum with lower energy than expected. These may appear in a “ghost peak” near the full-energy peak [112] or spread throughout the lower energy continuum of the energy spectrum. Figure 7.1 shows the energy spectra of two adjacent strips for two detectors with a-Ge contacts. Each spectrum contains 250,000 radiation events. The red trace shows the spectrum from a detector with a large degree of inter-electrode charge collection and the black trace shows the spectrum from a detector with almost no inter-electrode charge collection. The detector that collects charge carriers to the gap between strips (red) has deteriorated energy resolution and a sizable “ghost peak” below the 60-keV full-energy peak. The detector with no inter-electrode charge collection (black) shows an energy spectrum with no serious defects and typical energy resolution of 1.2 keV FWHM.

If poor spectral performance exists in a segmented electrode detector, it can be directly attributed to inter-electrode charge collection by examining the summed energy as a function of one electrode energy [66] [65]. Other analysis methods have also been used to examine inter-electrode charge collection [62] [77] [112].



**Figure 7.2. Illustration of a method for examining inter-electrode charge collection.** The plot shows the sum energy of two adjacent electrodes as a function of the energy for one of those electrodes. Additional illustrations show the type of events that contribute to different regions on the graph. [110]

An illustration of summed energy from two adjacent electrodes as a function of energy from one of those electrodes is shown in Figure 7.2 with accompanying illustrations of the types of events giving rise to the features on the plot. Charge carriers drifting toward two adjacent electrodes may drift directly toward one of those electrodes, giving sets of events that appear at the full gamma-ray energy at the left and right sides of the plot in Figure 7.2. The charge carriers drifting toward the gap between the electrodes will either be split between the two electrodes and drift directly toward them, or continue straight toward the gap between electrodes. These two possibilities will give events in the center of the plot, where those collected directly to the gap show a summed energy lower than the full gamma-ray energy. A method of evaluating inter-electrode passivation technologies involves examining whether a plot like Figure 7.2 shows a summed energy deficit for a detector fabricated with that inter-electrode surface process.

### 7.1.2 Previous Work

A handful of methods have been identified for dealing with this issue [26]. One pursued by Protic and Krings involves etching away any inter-electrode layer, leaving an unpassivated surface with no observable charge loss [77]. This structure, illustrated in Figure 7.3, gives good results and has the added benefit of a lower dielectric constant in the inter-electrode region, but this method may not be compatible with applications that require a fully passivated detector. A very small gap, about 50  $\mu\text{m}$  in width, was used for this method.

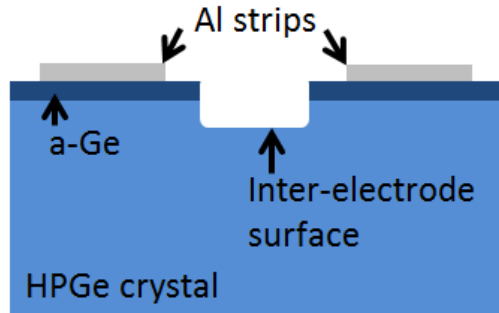


Figure 7.3. Schematic illustration of the etched inter-electrode region strategy for eliminating charge deficit.

Another approach involves nearby non-sensing electrodes to shape the electric field, forcing charge to sensing electrodes [14] [66]. An additional electrode is placed between sensing electrodes and biased such that it repels the charge carriers that might be collected to that surface, thereby forcing them to the sensing electrodes. This approach is illustrated in Figure 7.4 and has shown success in eliminating the charge sharing deficit. This method limits the position sensitivity achievable in the detector because sensing electrodes cannot be placed as close together as they could be with no steering electrode. A minimum spacing is still required between each pair of electrodes. Also, the additional electrodes are a potential source of electronic noise via surface leakage current or lower inter-electrode resistance, and the additional complication of adding more wires and a voltage source is a potential source of problems. Analysis methods can also correct for spectral abnormalities [112] [62] by measuring and correcting for the known response of a particular detector.

There is some evidence the fabrication process can affect the degree of inter-electrode charge collection [14]. This is a prospect worth pursuing because it is preferable to eliminate

detrimental effects in the detector rather than correcting in analysis, and field-shaping electrodes will limit the achievable electrode spacing and geometry. Though a previous study hinted at the importance of added hydrogen in the amorphous layer, it is unknown how much hydrogen is needed, or what effect the sputter pressure may have. Other external factors have not been studied, such as the impact of electric field magnitude, charge carrier polarity, or gamma-ray energy.

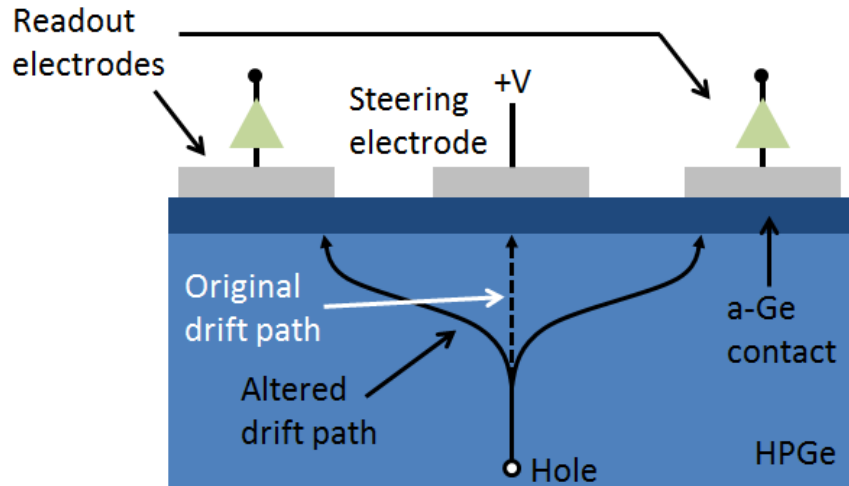


Figure 7.4. Schematic illustration of the steering electrode approach to eliminating charge sharing deficit.

Photolithography can be used to define electrode structures as a more flexible alternative to shadow masks, but the effects of this process on inter-electrode charge collection have not been assessed. This method involves the application of a thin coating of photoresist, an acid-resistant liquid. Baking the device drives out solvents in the photoresist and the layer becomes hard and acid-resistant. The layer is then exposed to ultraviolet (UV) light through a mask pattern and a developer selectively removes only the area that was exposed to UV light in the case of positive resist, or only the area that was covered in the case of negative resist. The patterned mask allows the material underneath to be etched according to the mask pattern. Photolithography provides additional flexibility in forming electrode structures because it can produce smaller features (down to a few  $\mu\text{m}$ ) than shadow masks and the mask design does not need to use self-supporting structures. However, the bake step and additional exposure to chemicals have an unknown effect on the detector surface, especially for inter-electrode charge collection. The previous fabrication process work on inter-electrode charge collection used shadow masks only [14], and other detectors made using photolithography have not been studied for their charge sharing properties [15] [25]. One study has been done on an HPGe detector made with photolithography [77], but the removal of the a-Ge layer between adjacent strips is a major difference.

## 7.2 Strip Detector Testing

In order to assess the impact of the fabrication process on inter-electrode charge collection, six double-sided strip detectors (DSSDs) were fabricated with amorphous semiconductor

contacts sputtered in varying conditions. Multiple non-guard ring electrodes are needed so there can exist an inter-electrode region that is protected from side surface effects. Although a simple two-electrode device with a guard ring would suffice for this study, full 5 x 5 double-sided orthogonal strip detectors were fabricated to best represent the detectors for which this effect is seen. This should leave little doubt as to the relevance of the measurements and suitability of the detectors to function as three-dimensional position-sensitive gamma-ray spectrometers.

### 7.2.1 Fabrication

The detectors were prepared using crystal samples from the same HPGe material used for the guard ring detectors described in Chapter 5. Two crystal samples were used, both p-type with a net ionized impurity concentration around  $7 \times 10^9 \text{ cm}^{-3}$ . Both had a square cross-section 18 mm on a side, and one crystal was 13 mm thick, while the other was 7 mm thick. Each crystal was first fabricated into a guard ring detector and demonstrated to have low leakage current before testing as a DSSD. The 13 mm thick crystal fully depleted around 500 V and the 7 mm thick crystal depleted around 150 V. The initial fabrication was similar to the guard ring detector fabrication process described in Chapter 5, where a-Ge was sputtered on the top and sides of a freshly etched germanium crystal and a-Ge or a-Si was sputtered on the bottom surface. Aluminum was then thermally evaporated on the top and bottom contacts, with the first five detectors having electrodes defined by a series of shadow masks. Figure 7.5 shows the sequence of shadow masks used for aluminum evaporation on each side of the DSSDs used in this study.

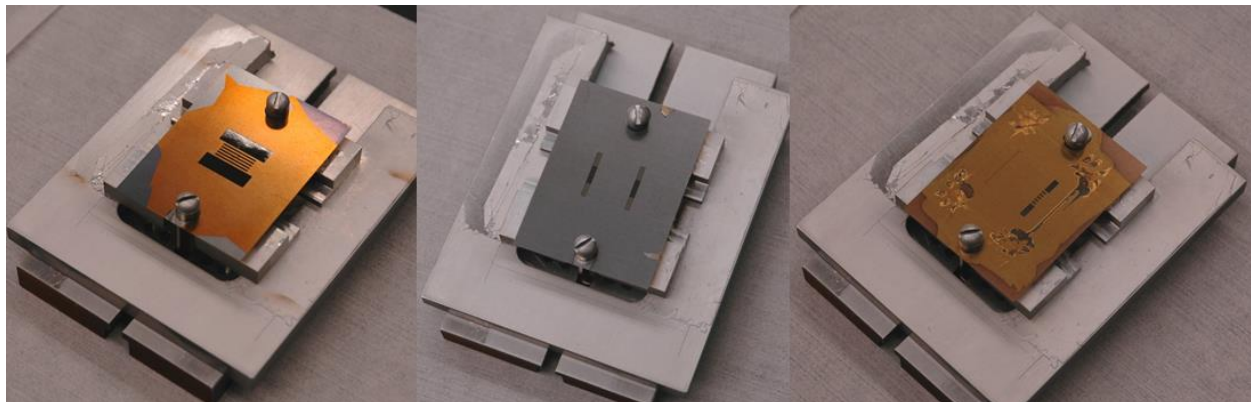


**Figure 7.5. Photograph of shadow masks for strip detector fabrication.** The left photo shows the mask to define the strips and parallel part of the guard ring. The center photo shows the mask to define the connecting component of the guard ring, while the photo on the right shows the mask for depositing wire bonding pads.

An outside, self-supporting mask cannot be made with an open ring for the guard ring, so two masks and separate deposition sequences were needed to form the electrode structure on each side. The first mask (left panel of Figure 7.5) had open areas for the five strips and parallel component of the guard ring. The second mask (middle panel of Figure 7.5) was for the perpendicular connecting area of the guard ring. The electrodes only needed about 50 nm of Al to form a reliable electrical connection to the entire area, but the wire bonding process used for electrical connections to the strips required a thicker layer. It is not desirable to expose a large area to more metal evaporation than is necessary, because molten Al pieces emitted from the hot

filament can sometimes land on the detector, which will damage the surface. Therefore, a final mask with small open windows (seen in the right panel of Figure 7.5) was used to form bonding pads on the strips and guard ring during the last deposition of 500 nm Al.

After the Al electrodes were defined, the detector was placed in a mount with nearby readout boards. Ultrasonic wire bonding was used to connect the board traces and the detector electrodes. A soft, uniform surface is required for this process, necessitating the thicker Al layer. Figure 7.6 shows a completed detector with annotated dimensions. The guard ring was relatively wide to ensure the strips were isolated from surface channel effects. The five strips were 10 mm in length and placed on a 1 mm pitch with a 0.5 mm gap between. The 1:1 strip-to-gap ratio is larger than what is normally used in order to emphasize the inter-electrode charge collection effect. The strips were orthogonally oriented on opposite surfaces of the detector.

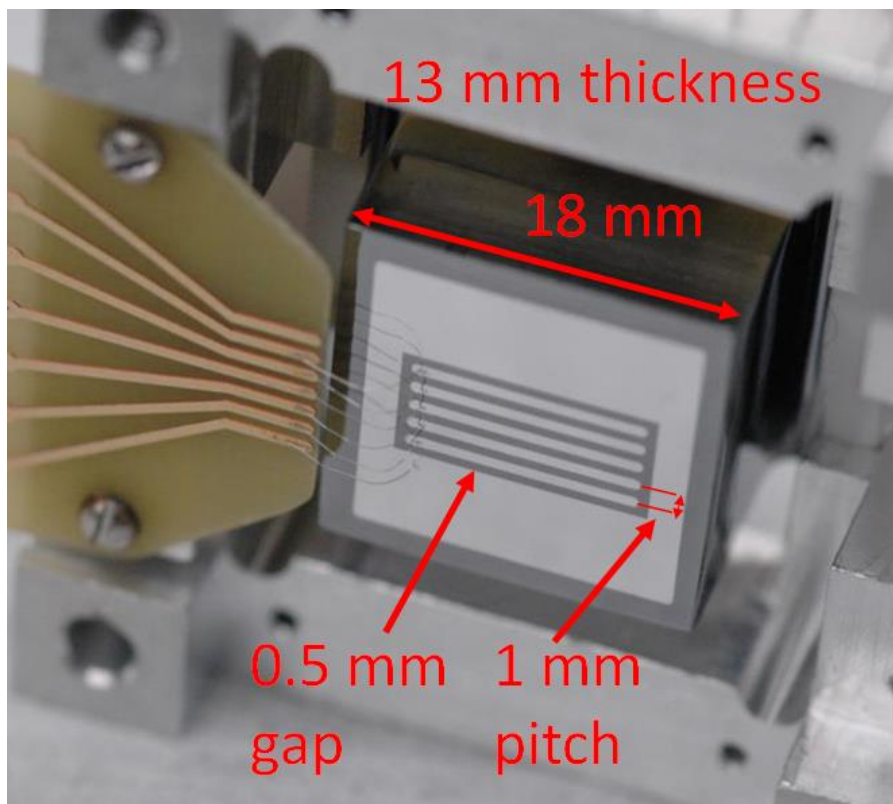


Figure 7.6. Photograph of a double-sided strip detector fabricated for this study.

One detector was also fabricated using a photolithography process to define the Al electrodes in order to determine if the different processing would affect the inter-electrode charge collection. For the detector made using photolithography, an Al layer thick enough for wire bonding (>500 nm) was deposited on the entire top and bottom surfaces of the detector, a layer of positive photoresist was applied to those surfaces by spin-coating, and the detector was baked at 90° C for 30 minutes. The photoresist was exposed to UV light with a thin transparency mask using the same electrode pattern used for the shadow masks on other detectors. After the photoresist was developed, the detector was etched in 0.5% HF to remove Al from the top and bottom surfaces to define the electrode pattern. The remaining photoresist was then removed

with an acetone rinse. Finally, the detector was wire-bonded in the same fashion as the previous detectors.

For strip detectors, the electrodes are sometimes too small to easily make electrical contact using spring clips or pogo-pins. Wire bonding is a suitable method for connecting small electrodes to a nearby circuit board by ultrasonic excitation. A tungsten tip is used to press pure aluminum wire of 2 mil thickness onto a detector electrode. When the tungsten tool is excited with ultrasonic power while pressing down on the wire, the Al wire and Al electrode stick together. The wire is carried to the nearby circuit board and the process is repeated on the gold trace to complete the connection. Electrical connections can be soldered at the other end of the breakout board. The wire-bond connection between the tan breakout board and the detector can be seen on the left side of Figure 7.6.

## 7.2.2 Experiments

A total of 6 DSSDs were tested for inter-electrode charge collection. The cryostat was evacuated using a turbomolecular pump, and after cooling to  $\sim 78$  K, each detector was manually tested with ammeters to check for acceptably low leakage current. For all detectors tested, the summed strip leakage current was less than 1 pA and the guard ring current was never above a few pA. After the detector was found to have low leakage current and to produce pulses of the expected shape in response to gamma-ray irradiation, the turbopump was disconnected to minimize vibration and an ion pump was used to keep high vacuum in the cryostat. See Appendix C for more details about the cryostat and testing apparatus.

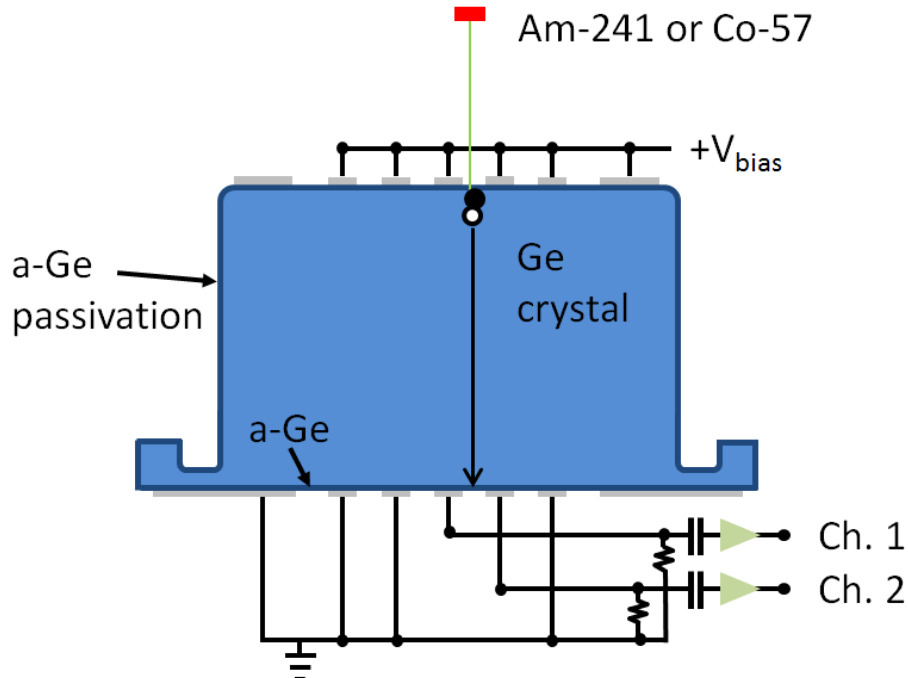


Figure 7.7. Illustration of inter-electrode charge collection measurement. A low-energy source creates a charge cloud that drifts across the crystal toward a series of strips. Two adjacent strips are read out and their sum is examined for a summed energy deficit.

For most measurements, the detector was biased and read out as shown in Figure 7.7, where high-voltage bias was applied to all top electrodes. A low-energy source, either Am-241 or Co-57, was used to illuminate this side of the detector and pulses from the strips on the opposite side were read out with preamplifiers. Two adjacent strips were AC-coupled to preamplifiers and read out to determine the extent of energy deficit for events collected to the gap between them. These two strips were held at DC ground potential through  $1\text{ G}\Omega$  resistors and all other electrodes on this side were connected directly to ground.

A low-energy source produces nearly all charge carriers close to the illuminated surface, allowing a set of events consistently arising from a region of the detector far from the strips being examined. Around 70% of 59.54 keV gamma-rays are stopped in the top 1 mm of germanium. The charge carriers of one type (either hole or electron) drift across nearly the entire detector thickness, so it can safely be assumed that no events originate in the inter-electrode region being examined.

All detectors were also illuminated with a Co-57 source and the gamma-rays with 122.1 keV energy were compared with 60-keV gamma-rays to determine whether gamma-ray energy had an impact on inter-electrode charge collection. The size of the initial charge cloud from gamma-rays in this energy range is likely dominated by the range of photoelectrons in the germanium [122]. Based on NIST Estar electron range data [123], the photoelectron range is  $1.4 \times 10^{-3}\text{ cm}$  and  $4.4 \times 10^{-3}\text{ cm}$  for 60 keV and 122 keV photons, respectively. The mobile charge carriers liberated by ionizing radiation undergo diffusion during the time it takes to drift across the detector thickness, which tends to expand the size of the charge cloud. Using a saturation drift velocity of  $10^7\text{ cm/s}$  [43], the holes took about 130 ns to drift across a detector of 1.3 cm thickness. The lateral diffusion coefficient is [31]

$$D_{\perp} = \frac{\mu k T}{q}, \quad (44)$$

where  $\mu$  is the charge carrier mobility,  $k$  is the Boltzmann constant,  $T$  is the detector temperature, and  $q$  is the electronic charge. A lateral diffusion coefficient of  $270\text{ cm}^2/\text{s}$  is obtained from (44) using a temperature of 78 K and a mobility of  $4 \times 10^4\text{ cm}^2/\text{V}\cdot\text{s}$ . The standard deviation of charge cloud size due to diffusion is  $\sqrt{D_{\perp} t}$  [31], where  $t$  is the collection time, giving a value of  $5.9 \times 10^{-3}\text{ cm}$ . The size of the charge cloud after drift across the detector can be taken to be a combination of expansion from diffusion and the initial size. Using the expression [124]

$$r_f = \sqrt{r_i^2 + r_d^2}, \quad (45)$$

where  $r_f$  is the final charge cloud size,  $r_i$  is the initial charge cloud size, and  $r_d$  is the contribution due to diffusion, gives  $r_f$  values of  $6.1 \times 10^{-3}\text{ cm}$  for 60 keV and  $7.4 \times 10^{-3}\text{ cm}$  for 122 keV. Both of these estimates are significantly smaller than the 0.5 mm gap between strips.

A small number of Ba-133 and Cd-109 measurements were also conducted, but low event rates made these impractical to use for a detailed study. Other studies of this type included Cs-137 measurements, but detection efficiency for the small active area on these detectors makes this impractical due to the very low rate of full-energy events. The important factor here is the measurement of charge that drifts to adjacent electrodes rather than originating in the gap.

Each detector was analyzed for inter-electrode charge collections on the two opposite sides. The top contact was always formed using the same process, providing a control measurement, while the bottom strips provided a study of the effect of varying contact preparation on the inter-strip charge collection. Each detector was first examined for inter-electrode charge collection at the bottom contact, then it was flipped over and the top contact was examined using the same procedure. In order for it to be flipped over, it had to be warmed to room temperature and exposed to atmosphere for a few minutes.

Some detectors were tested for reproducibility. Most detectors were tested at least twice using the same test procedure, and one detector was tested multiple times in the same fashion over the period of about a week. Another detector was stored in a dry box for about 2 months after the first round of testing and then subjected to a second round of testing. To test reproducibility of the fabrication process, one crystal was fabricated two different times using the same a-Ge 15 mTorr 7% H<sub>2</sub> process. A different crystal was also fabricated using this same process to test reproducibility on different crystals.

Some detectors were tested with varying bias conditions as well. Detectors that could withstand either bias polarity without breakdown were tested for both electron and hole collection on the same contact by changing the bias polarity. Detectors were also tested at varying bias to determine the effect of electric field strength on inter-electrode charge collection.

### 7.2.3 Weighting Potential Calculation

To examine inter-electrode charge collection, it is helpful to understand the mechanics of how the electrodes sense charge from radiation ionization. The weighting potential described by the Shockley-Ramo theorem is a tool to predict the amount of induced charge on an electrode as a result of the presence of external charge. The weighting potential is a mathematical quantity determined by the electrode geometry and the material properties [34] [35] [36]. The amount of induced charge on an electrode is measured by an attached preamplifier and, after some pulse processing as described in Chapter 2, the quantity is converted to energy. See Appendix D for an overview of the Shockley-Ramo theorem with more detail.

Charge collection to the inter-electrode gap is undesirable since the maximum signal amplitude is achieved only when charge is completely collected to electrodes. Since the weighting potential for any particular electrode decreases with distance from that electrode, the weighting potential for all electrodes will be lower in the inter-electrode regions. Charge moving in these regions will induce less charge on all electrodes, meaning the sum of all electrode signals has a deficit. Once charge carriers are collected to the surface, they are unlikely to reach an electrode within the measurement time because conduction is much slower in the amorphous layer compared with the crystalline bulk.

Electrostatic calculations were conducted to determine the effect of charge collection to the gap between strips using the software package Maxwell. A two-dimensional model of the detector geometry was created with the metal electrode geometry and a-Ge layer. The weighting potential for one electrode is calculated by setting the potential of that electrode to 1 V and all others to 0 V. The weighting potential for one strip is shown in Figure 7.8. Thickness of the metal electrodes is exaggerated and the a-Ge is too thin to be visible in this figure.

Examining the magnitude of the weighting potential at the top surface allows one to see the effect of charge being collected to this surface. The weighting potential for one strip gives an indication of the signal magnitude for that strip when charge is collected to the surface. The electrode configuration used for experiments was simulated to determine the weighting potential at the surface for two adjacent strips as well as their sum. Figure 7.9 shows how the weighting potential  $V_w$  approaches a value of one near the electrode, drops rapidly in the gap, and reaches zero near other electrodes. For this geometry, the sum of the two adjacent strip weighting potentials dips to 0.84 in the center of the gap.

The sum of the two adjacent strip weighting potentials gives an indication of the expected signal if charge is collected directly to the surface (E field does not turn aside to strips) and the signal of the strips is summed. Charge collected directly under a strip will give maximum signal, while charge collected in the gap will have a lower signal. Events in the center of the gap will be 16% lower in magnitude than those collected directly under strips. If a significant number of events were collected to the gap, it would be a serious detriment to HPGe detector energy resolution, which is normally around 0.2% at 662 keV.

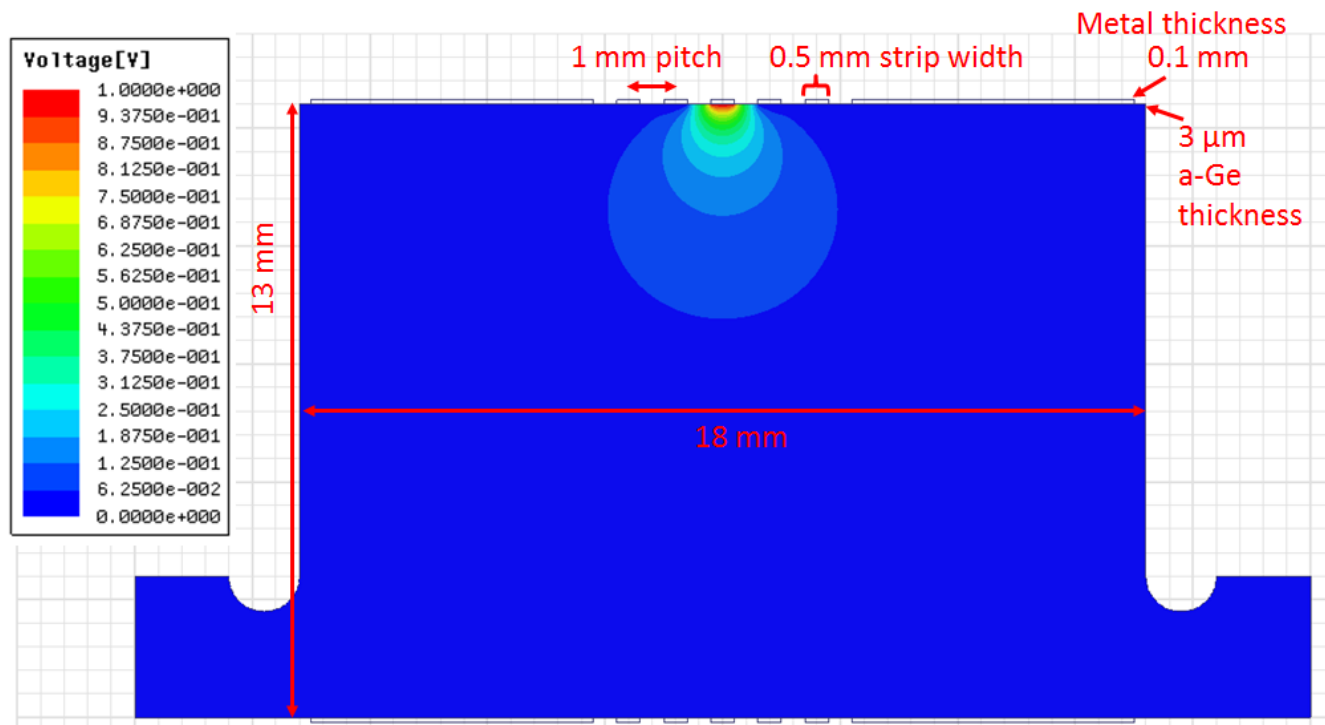


Figure 7.8. Weighting potential of one strip in the geometry used for inter-electrode charge collection measurements.

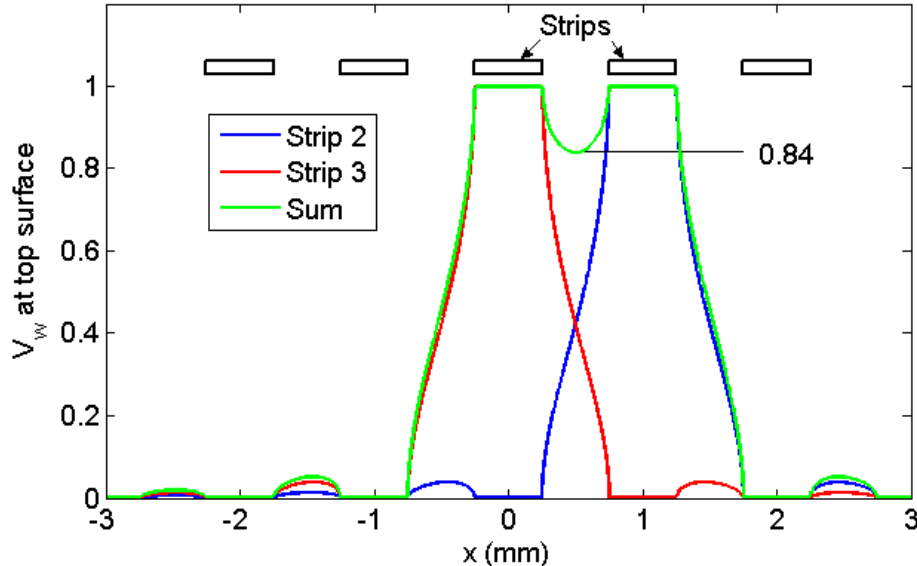


Figure 7.9. Simulated estimate of signal magnitude for strips in the experimental electrode configuration. The red and blue curves show the weighting potential for two individual strips evaluated at the top surface. The green curve is the sum of the red and blue curves. The black rectangles indicate the positions of the strip electrodes along the x axis.

#### 7.2.4 Data Processing

The goal of the data processing was to obtain the energy sensed in two adjacent strips for each radiation event. For each data run, preamplifier waveforms were collected for two adjacent strips when at least one of those strips had a signal above a threshold equivalent to about 10 keV. This section details the process by which energy values were calculated using the acquired waveforms.

A trapezoidal filter was applied to each waveform according to the filter design described by Jordanov [125]. Many parameters were optimized initially, such as peaking time, gap time, and decay constant. For later data runs, the same parameters were always used because the detector geometry and electronic components did not change. Based on the optimization, a peaking time of 9  $\mu$ s and a gap time of 150 ns were used. A preamplifier decay constant of 340  $\mu$ s was determined by an exponential fit to the decay portion of a set of pulser events.

For the acquired detector data, each waveform was baseline-corrected by subtracting the average of the first 7  $\mu$ s of samples from the entire waveform. A digital trapezoidal filter was applied to each baseline-corrected waveform using the optimized peaking time, appropriate gap time, and estimated decay constant from pulser data. Figure 7.10 shows two example waveforms from adjacent strips for the same event. The trapezoidal filter output is overlaid in red. The upper panel shows a waveform for a strip that collected the full charge from a 60-keV gamma-ray interaction. The trapezoidal filter output was significantly over the 10 keV threshold and the shape resembles a trapezoid. The lower panel shows a waveform with essentially no signal and the trapezoidal filter output is largely determined by electronic noise.

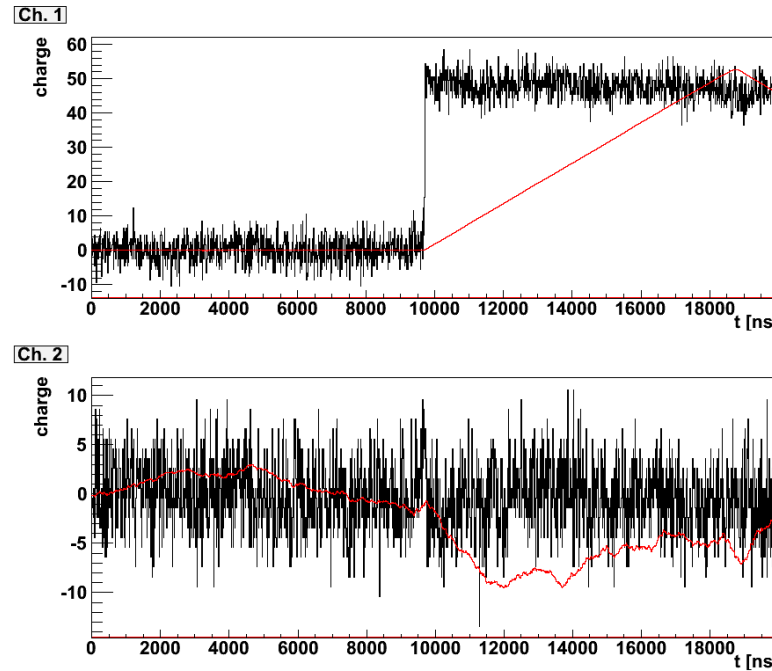


Figure 7.10. Example raw waveforms acquired with the SIS3302 digitizer (black) with digital trapezoidal filter output (red). Note the different vertical scales for the two panels.

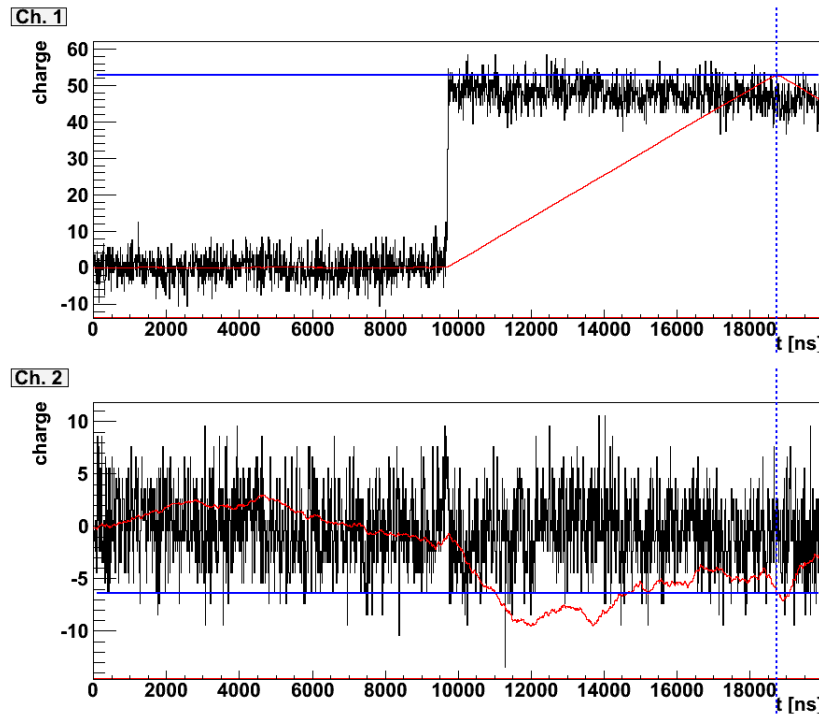
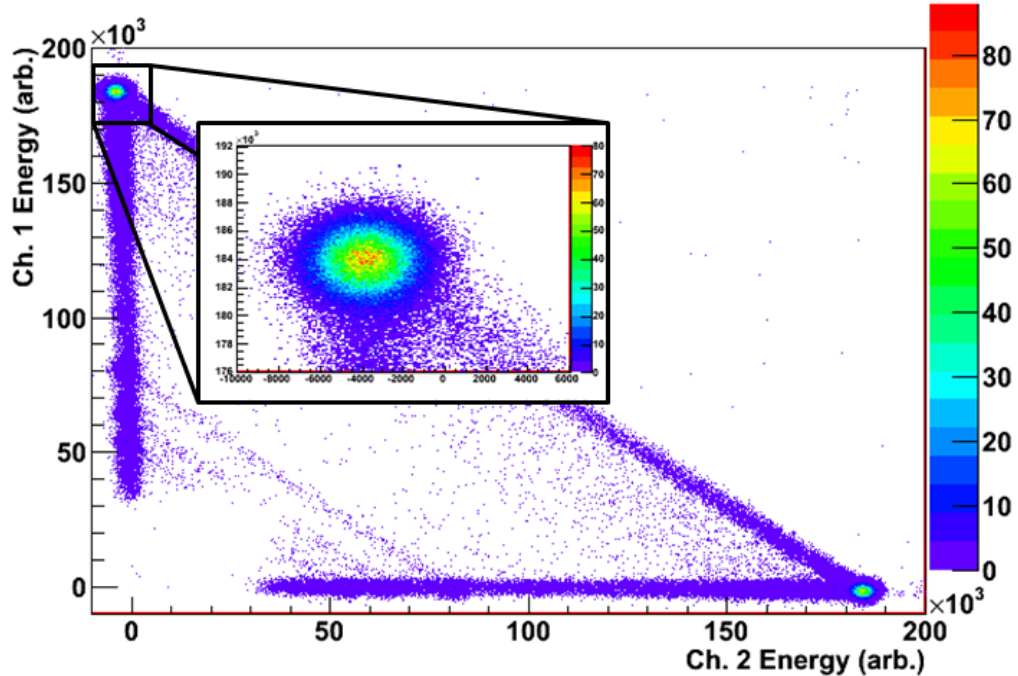


Figure 7.11. Example waveforms (black) overlaid with trapezoidal filter output (red). Blue lines indicate horizontal and vertical positions of the value chosen for energy determination.

The next step in data processing was determining event energy from the trapezoidal filter output. While the simplest approach would be to take the maximum value of the trapezoidal filter output, this tends to over-estimate the values because it picks up the maximum noise excursion. This effect is especially pronounced for waveforms near zero energy, because the noise may be much larger than the signal. Instead, the energy was determined by taking the maximum of the trapezoidal filter output if it is above a certain threshold, otherwise taking the trapezoidal filter output at the same time index as the maximum for the triggered channel. This concept is illustrated in Figure 7.11 for the same waveforms that were shown previously (black) and their trapezoidal filter output (red). The upper panel shows a 60-keV event in channel 1, which is above the threshold of 10 keV. The horizontal blue line shows the maximum value for this filter output and the vertical, dashed blue line shows the time index where this maximum occurred. Since channel 2 has no observable signal and its filter output did not cross the threshold, its energy is determined by taking its trapezoidal filter output at the time index determined by channel 1 (the vertical blue, dashed line). The channel 2 energy determination value is denoted by another horizontal blue line.



**Figure 7.12.** Plot of channel 1 energy vs. channel 2 energy for a typical Am-241 measurement. The inset shows a zoomed view of one full-energy lobe, which has a mean negative value for the non-triggered channel.

A significant signal cross-talk effect was discovered in the data where an induced signal occurs on one channel due to a signal on the other channel. This effect is most likely due to unintended capacitive coupling between the two signal paths in the cryostat. Since only two strips were examined in these experiments, every event will have the cross-talk effect because both strips will either have a significant signal or be directly adjacent to a strip with significant signal.

The cross-talk effect became noticeable during energy calibration. It was observed that the full-energy peak for one channel, after being correctly calibrated for energy, would not have the correct energy when the channels were summed. This was true even when showing only events with zero energy in the other channel. Figure 7.12 shows a plot of uncalibrated energy values for channel 1 vs. channel 2. Two lobes in the figure contain most of the events, where all charge was sensed in one channel. Ideally these lobes would be at zero energy for the channel not sensing full energy, but instead are located at negative energy values for the non-triggered channel. This indicates a negative coefficient for cross-talk between the two channels. Such electronic cross-talk in germanium strip detectors has been discussed by others [62] [112], albeit with a positive coefficient. A common theme for this work and others is that the induced cross-talk is a small percentage (~1%) of the signal from a neighboring channel.

A correction was applied to eliminate this effect and recover more accurate values of energy in the two channels. By examining events in the baseline peak of one channel, one can see that they are proportional to the signal in the other channel, as shown in Figure 7.13. The constant of proportionality was estimated by finding the slope of this set of events, and each event was corrected by adding a percentage of the energy from the other channel. The raw set of events (black) is slanted toward negative values, while the corrected events (red) are forced to form a vertical line. After this correction, values for both channels are scaled so that full-energy peaks are at the correct energy value.

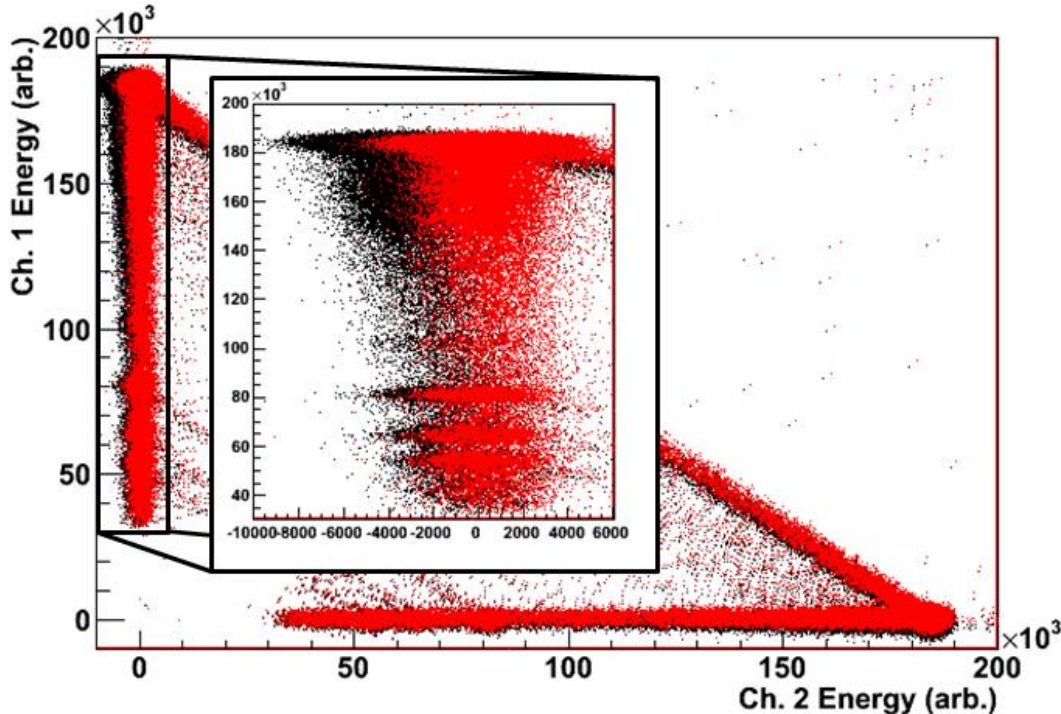


**Figure 7.13.** Energy of channel 1 vs. energy of channel 2 shown as in Figure 7.12. The black marks indicate raw energy values, while red markers indicate cross-talk-corrected energy values. The inset shows a zoomed image of the class of events where channel 2 has zero energy.

The final product of an inter-electrode charge collection measurement is a charge sharing plot of the energy sum for the two adjacent strips vs. the energy for one strip. This is the type of plot discussed in section 7.1 and is shown in Figure 7.14. No charge collected to the gap would result in a horizontal distribution of events centered about the black line, which indicates the incident photon energy (59.54 keV in this case). A dip in the summed value of events near the center of the graph indicates charge was collected to the inter-electrode region. A series of vertical slices is taken across the data set, corresponding to varying values of channel 2 energy. The mean value of a Gaussian fit to each vertical slice is shown in Figure 7.14 by black circles. A scatter plot of these mean values should suffice to show the extent of charge loss to the gap, so plots comparing different detectors will use these fit mean values. The summed energy deficit was quantified in some cases by performing a Gaussian fit to a histogram of these mean values. Another important parameter is the number of events that experience significant charge sharing between the adjacent strips. This shared event ratio was quantified as a ratio of the number of events in a window covering the center of a plot like Figure 7.14 to all events in a certain summed energy range. The summed energy range was 48 to 62.5 keV, and the window including charge sharing events included the entire energy range from 48-62.5 keV, but excluded the single-channel events for the two strips. These classes of events can be seen by the vertical ridge and the diagonal ridge at the left and right edges of Figure 7.14.

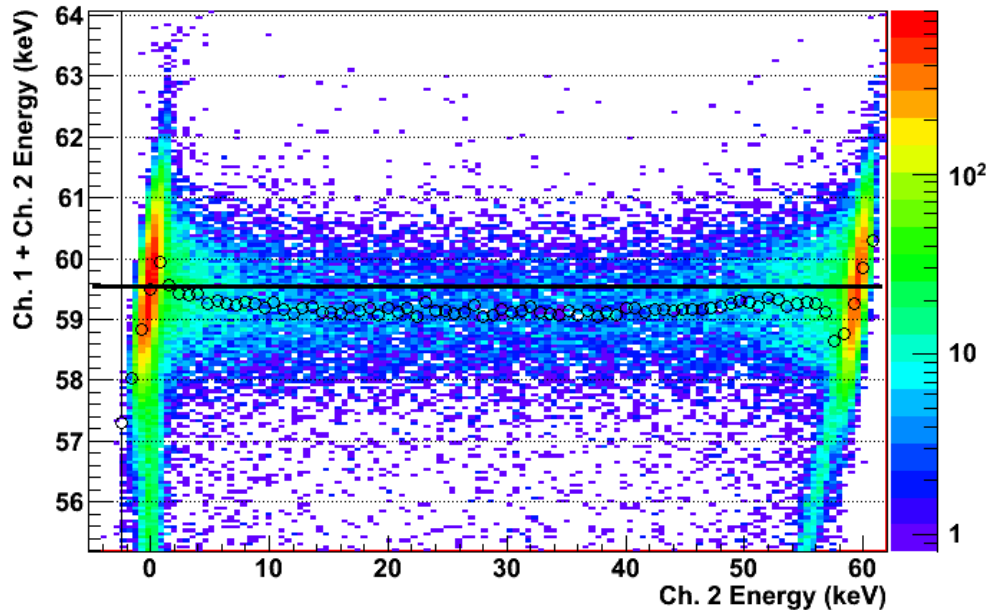


Figure 7.14. Charge sharing plot example for Am-241 measurement. The sum of the two adjacent strip energies is on the vertical axis and one of the strip energies is on the horizontal axis. The black horizontal line indicates the incident photon energy and the black circles show the mean of a Gaussian fit to several vertical slices along the horizontal direction.

## 7.3 Results

This section details the results obtained for inter-electrode charge collection measurements on the strip detectors described previously. A total of six detectors were tested for their inter-electrode charge collection properties. The results show the difference between a-Ge with and without hydrogen, the reproducibility of the a-Ge contact fabrication process with hydrogen, and a comparison with an a-Si contact.

### 7.3.1 a-Ge with no Hydrogen

One detector was fabricated with an a-Ge bottom contact sputtered in 15 mTorr Ar and no added hydrogen. Some residual water is present in the sputter chamber after pumping, giving hydrogen by dissociation in the plasma. The hydrogen content of the sputter gas due to the residual water is estimated at about 0.5% maximum, based on residual gas analyzer measurements. The Am-241 charge sharing plot is shown in Figure 7.15 with the source energy indicated by the bold, horizontal black line. The data were acquired at 1500 V, about 1000 V above full depletion. A high level of energy deficit is observed for events split between the two strips, amounting to 16% of the full gamma-ray energy. The number of events with energy split between the two strips is also significant. About 30% of the events between 48 and 62 keV have significant sharing between the two strips. The result of these two effects is a poorly reconstructed summed energy spectrum as shown by the red trace in Figure 7.1.

The thin, black curve of Figure 7.15 shows the prediction from an electrostatic calculation for the case where charge carriers are collected directly to the bottom surface. The high level of agreement between this prediction and the measured data indicates the charge carriers are indeed collected directly to the gap between strips and no lateral electric field exists between the strips.

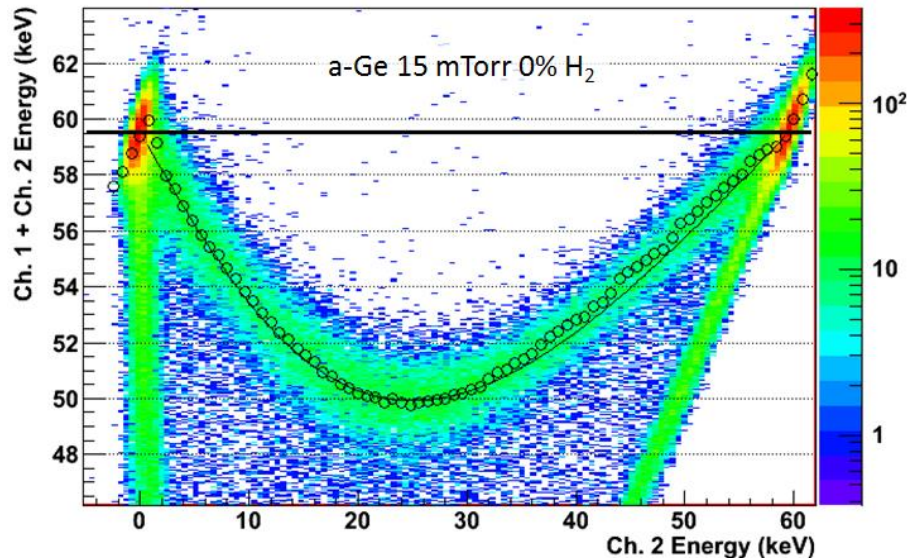


Figure 7.15. Charge sharing plot for one detector with a bottom contact created by sputtering a-Ge in 15 mTorr Ar. No hydrogen was added. The data, acquired at 1500 V, are for holes collected to the bottom contact. The thin black curve shows the estimated response as determined by the weighting potential for events collected directly to the gap.

Figure 7.16 shows different data sets acquired with this detector with different colors indicating different data sets at varying bias. Open markers show data sets acquired when the detector was recently biased and filled markers indicate data sets where the detector was already biased at least one hour prior to data acquisition. The two data sets at 1500 V, biased for more than one hour prior to data acquisition, show a high level of reproducibility with no discernible difference within measurement precision. For the data where the detector was already biased more than one hour, lowering the bias tends to lower the deficit to 12.5% of the full gamma-ray energy at 675 V bias. However, in all cases the deficit is  $>10\%$ . For two data sets, the detector was biased less than one hour prior to data acquisition. In both of these cases, the deficit is less than what was observed for similar data sets where the detector was biased for more than one hour. This is possibly due to some accumulation or depletion of charge at the interface layer that changes the charge collection properties of the inter-electrode layer.

After initial testing, the detector was stored in a dry box at room temperature for about 2 months. It was then re-tested in the same manner to assess long-term stability. The second test gave nearly identical results, again having a 16% deficit for shared events and 30% of full-energy events having significant charge sharing between the strips. Figure 7.17 shows a comparison of charge sharing before and after dry box storage, showing no observable difference within measurement precision. Both data sets were acquired at 1500 V bias and the detector was biased for more than one hour prior to data acquisition.

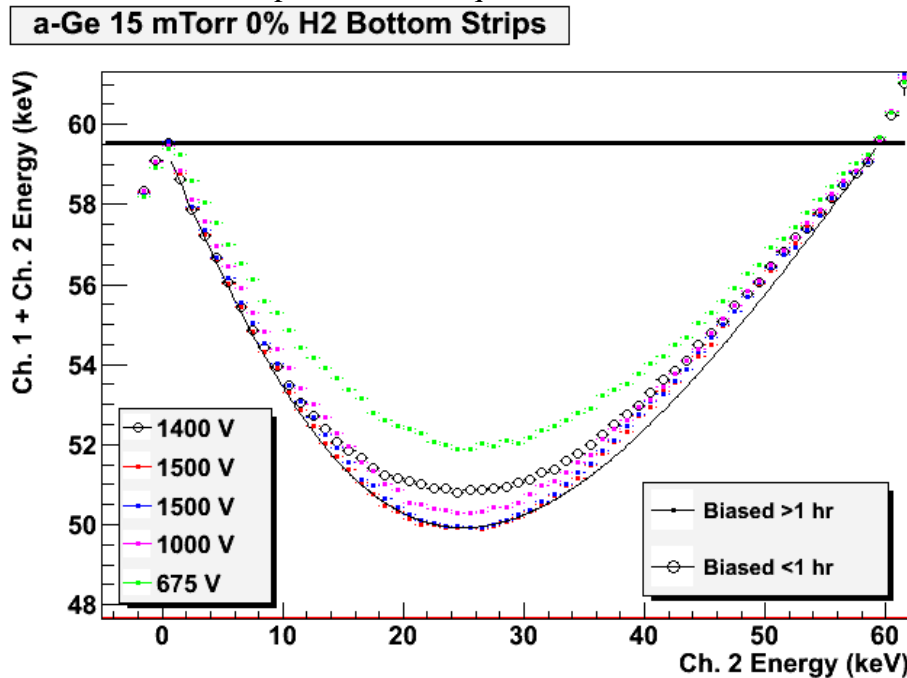
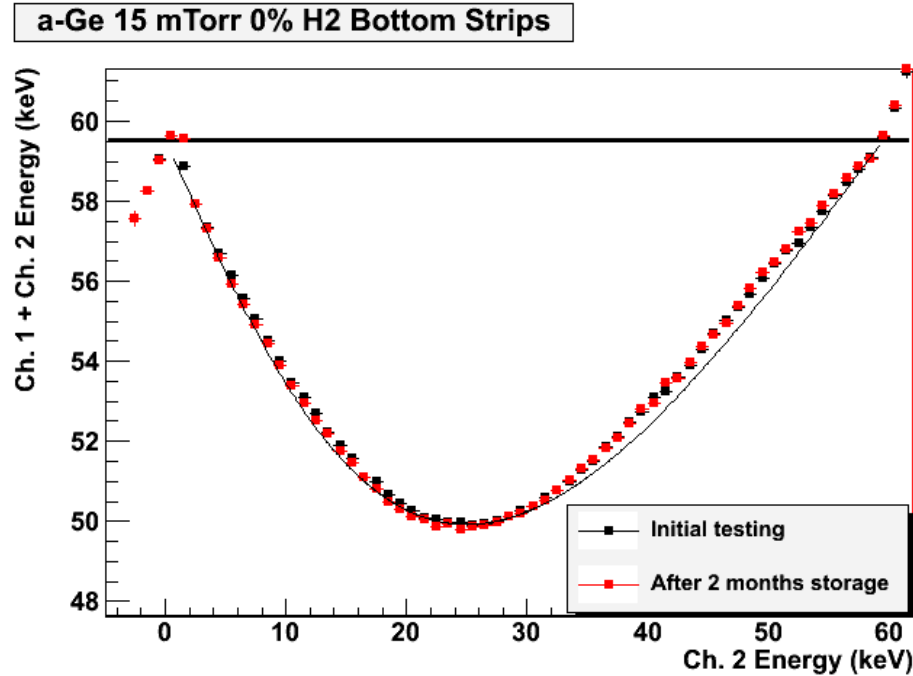


Figure 7.16. Charge sharing plots for the detector with an a-Ge bottom contact sputtered in 15 mTorr Ar with no added hydrogen. Different data sets have varying bias. Open markers indicate data sets acquired when the detector was recently biased, while filled markers show data sets acquired when the detector was biased for more than 1 hour prior to acquisition. The data are for holes collected to the bottom contact.



**Figure 7.17.** Charge sharing plot for one detector with the bottom contact created by sputtering a-Ge in 15 mTorr Ar with no added hydrogen. Different data sets were acquired at 1500 V bias before and after storage in a dry box. The data are for holes collected to the bottom contact.

Table 7.1 summarizes the data acquired for the a-Ge bottom contact sputtered in 15 mTorr with 0% H<sub>2</sub> at varying bias. All were acquired on the same detector with the a-Ge bottom contact collecting holes. The deficit generally decreases with decreasing bias, although for the case when the detector was recently biased when data acquisition began, the deficit was relatively less when compared with other data at similar voltages. The shared event ratio increased as the voltage bias decreased.

**Table 7.1.** Summary of inter-electrode charge collection data for a-Ge with 0% H<sub>2</sub>.

Bias	Time Biased	Max. Deficit	Shared Ratio
1400 V	0.5 hours	14.3%	30%
1500 V	5 hours	16.0%	29.9%
1500 V	23 hours	16.0%	29.8%
1000 V	28 hours	15.5%	32.0%
675 V	30 hours	12.5%	37.4%

### 7.3.2 a-Ge with Hydrogen

The a-Ge contact sputtered in 15 mTorr Ar with 7% H<sub>2</sub> gas was shown to have relatively low leakage current and good stability over time, so this process was tested extensively to determine its usefulness on segmented detectors. This process is currently being used for the NCT and GRIPS detectors [25] [126]. Figure 7.18 shows the charge sharing plot for one detector made with this process.

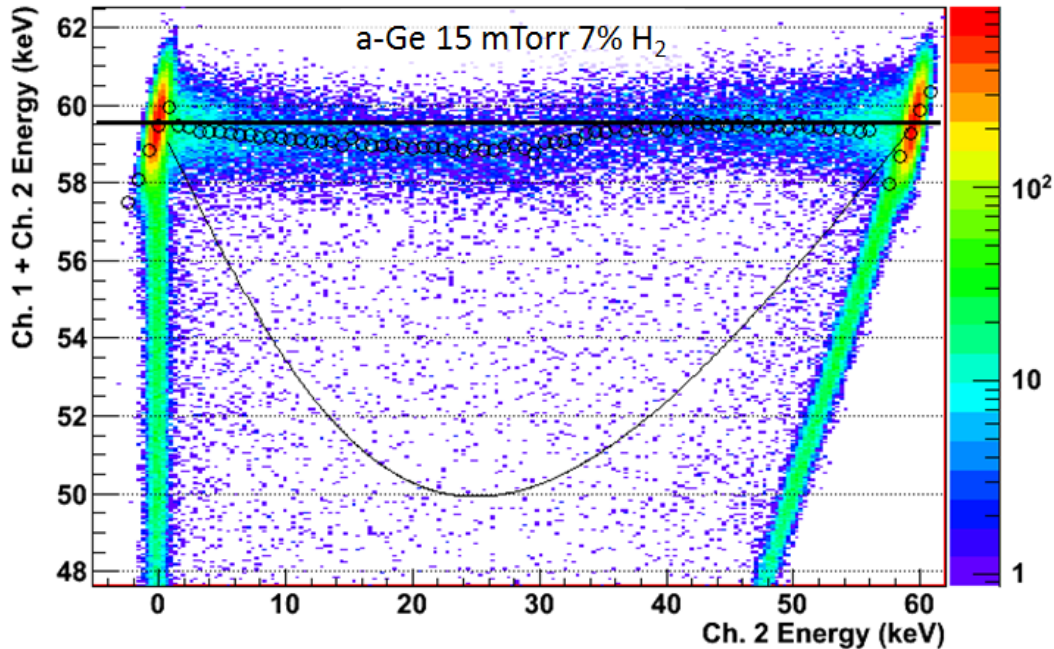


Figure 7.18. Charge sharing plot for one detector with a bottom contact created by sputtering a-Ge in 15 mTorr 7%  $\text{H}_2$ . The thin black curve shows the estimated response as determined by the weighting potential for events collected directly to the gap. The data, acquired at 1500 V, are for holes collected to the bottom contact.

There is almost no observable charge loss, in stark contrast to the a-Ge contact with no hydrogen content discussed in the previous section. The deficit is less than 1%, compared with about 16% for the a-Ge with no hydrogen. Only about 11% of events had significant charge sharing between the strips.

### 7.3.2.1 Reproducibility

One detector was tested multiple times in the same manner. The bottom contact was a-Ge sputtered in 15 mTorr Ar with 7%  $\text{H}_2$  and all experiments were performed at 1500 V bias. The bottom strips were examined while illuminating with an Am-241 source at the top side and the detector was biased such that the bottom strips were collecting holes. The bias was turned off at some points during the week or so of data collection. Figure 7.19 shows a comparison of the data sets collected on different days. The six data sets show an average deficit of 0.7% of the full gamma-ray energy, which is significantly smaller than the 16% deficit observed in a-Ge with no hydrogen. The markers in the plot have vertical error bars indicating the one-sigma uncertainty on the slice Gaussian fit. There are statistically significant differences among the data sets primarily due to variations in the asymmetric shape, shown particularly well with the red, green, and light blue data points that have an average of zero charge loss. The reason for the asymmetry is unknown.

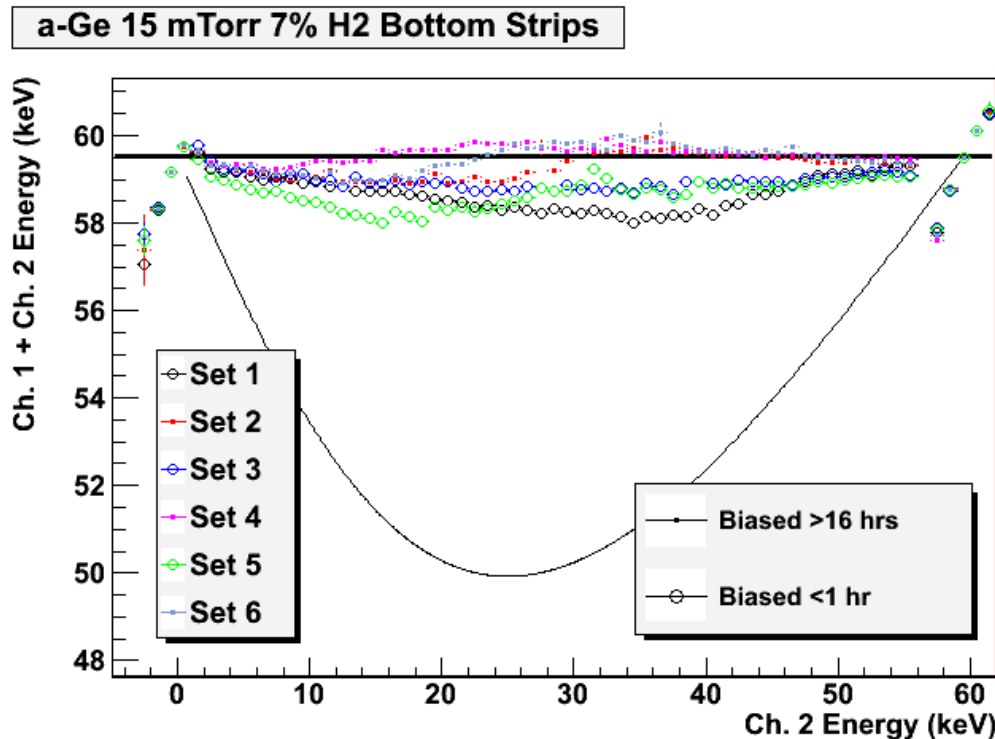


Figure 7.19. Charge sharing plot for bottom strips on one detector with an a-Ge bottom contact sputtered in 15 mTorr Ar (7% H<sub>2</sub>). Each series is indicated by a different color and represents a separate data set, all taken at 1500 V bias. Open markers represent those data sets where the detector was recently biased, while filled markers represent data where the detector had been biased for a long time prior to data acquisition. The data are for holes collected to the bottom contact.

A small but significant difference was observed between data sets where the detector was recently biased and those where it had already been biased for a long time (>16 hours). The open markers in Figure 7.19 indicate data sets acquired when the detector had been biased for less than an hour. These have an average energy deficit of 1.4%, while the data sets acquired when the detector had been biased for at least 16 hours had an average energy deficit of 0.2%. For these data sets, where the detector was biased for a long time, the charge loss is on par with the energy resolution of the detector. All consistently had 6.8% of all full-energy events with significant charge shared between the two strips. The results are summarized in Table 7.2. The ratio is less than the 11% value obtained with another detector using the same a-Ge fabrication process, but the difference is attributed to a thicker crystal in that case, which would allow more time for diffusion and a larger charge cloud once it reached the readout electrodes.

The measurement itself was shown to be reproducible, but the fabrication process should also be examined for reproducibility. Three detectors were fabricated with the same process, where the bottom contact was formed by sputtering a-Ge in 15 mTorr Ar (7% H<sub>2</sub>) atmosphere with a thickness of ~480 nm. One crystal was used for two different fabrication runs using the same process. A different crystal was also fabricated into a strip detector using the same process. The results, shown in Figure 7.20, indicate that the process is reproducible on the same crystal and across different crystals. The two crystals were different sizes, but all three detectors were tested

at about 1000 V over full depletion. The level of variation was  $<1$  keV, on par with the level of variation seen in the same detector tested over multiple days.

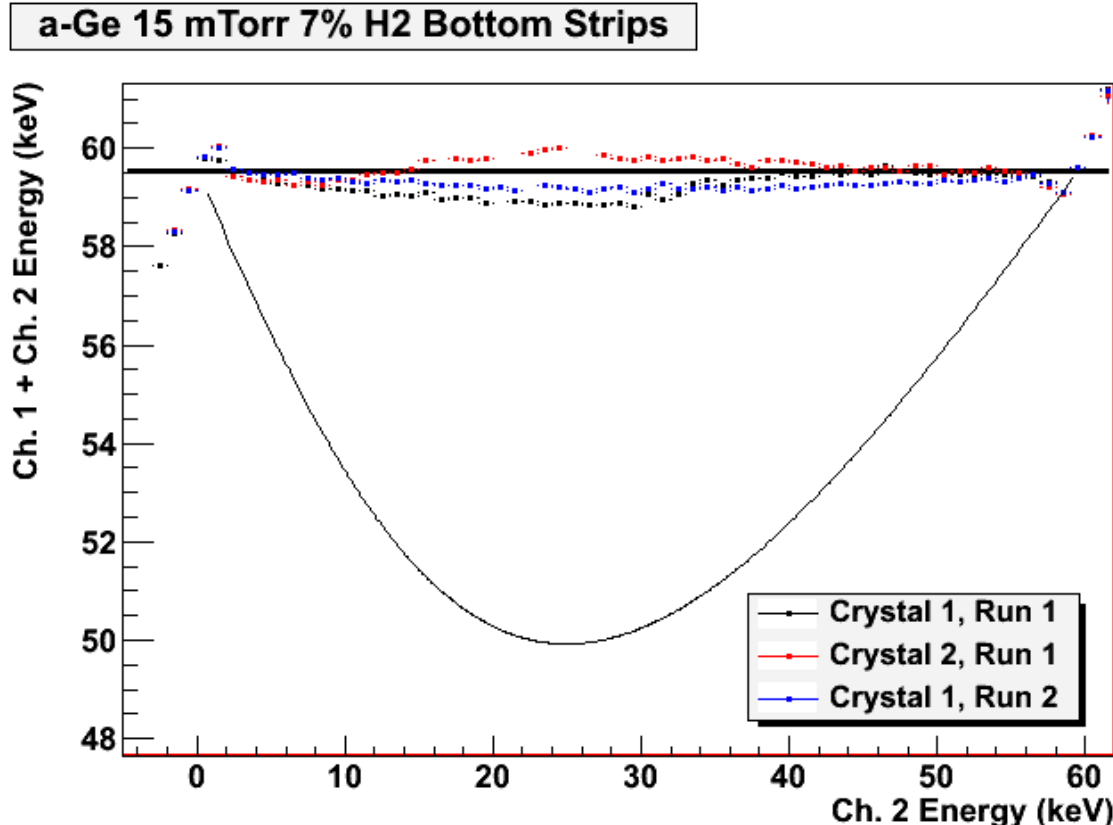


Figure 7.20. Charge sharing plot for three detectors having the bottom contact formed by the same fabrication process. All had the bottom contact formed by sputtering a-Ge in 15 mTorr Ar (7% H<sub>2</sub>) atmosphere with a thickness of  $\sim 480$  nm. One crystal was fabricated twice in the same fashion and a different crystal was fabricated in the same way. All data were acquired at about 1000 V more than depletion voltage. All data are for holes collected to the bottom contact.

Table 7.2. Reproducibility of inter-electrode charge collection data on the same detector.

Date Acquired	Time Biased	Max. Deficit	Shared Ratio
6/4/13	<1 hour	1.7%	6.8%
6/5/13	>16 hours	0.6%	6.7%
6/6/13	<1 hour	0.9%	6.8%
6/7/13	>16 hours	<0.2%	6.8%
6/11/13	<1 hour	1.4%	6.7%
6/12/13	>16 hours	<0.2%	6.8%

### 7.3.2.2 Effect of Electric Field Strength

A detector with an a-Ge contact sputtered in 15 mTorr Ar with 7% H<sub>2</sub> was examined at different bias voltages to determine whether varying the electric field strength at the contact

would affect the inter-electrode charge collection. The p-type crystal was fully depleted at 500 V and the electric field strength at the hole-collecting bottom contact varied from about 350 V/cm to about 1000 V/cm. Figure 7.21 shows three different measurements with no significant variation. The average deficit for the vertical slice fits varied less than 0.1 keV for the three data sets. Increasing electric field caused the fraction of shared events to decrease, presumably due to shorter collection time and a smaller charge cloud size when it reached the readout electrodes. At a bias of 1000 V, the shared event ratio was 21.9%, compared to 18.1% at 1500 V and 16.1% at 1900 V.

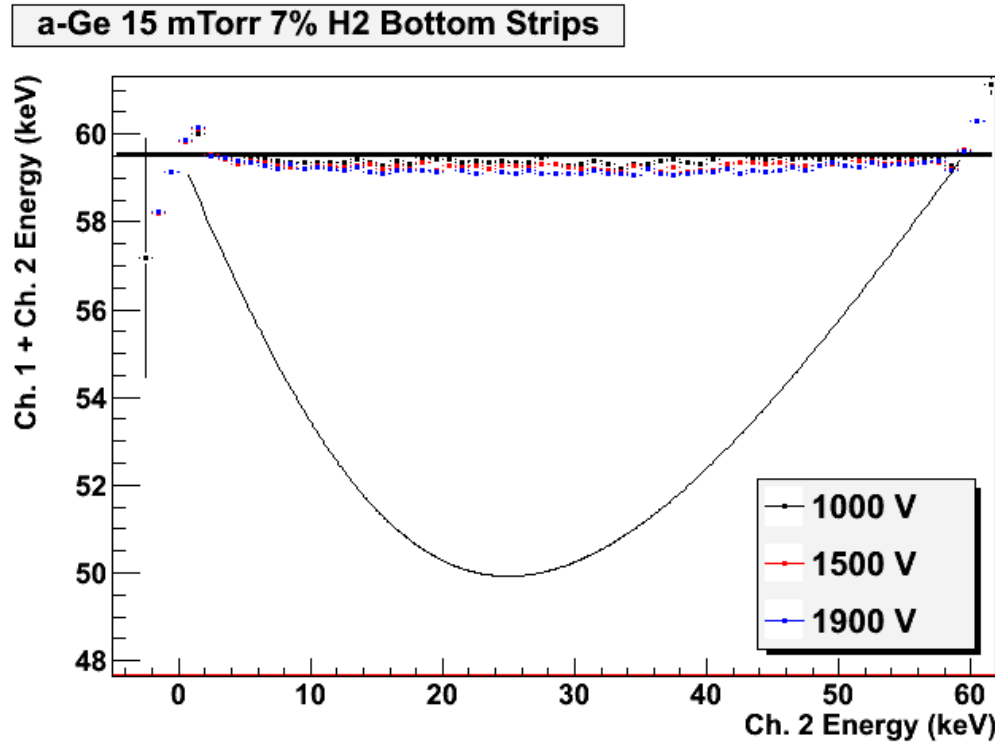


Figure 7.21. Charge sharing plot for one detector with an a-Ge contact sputtered in 15 mTorr Ar with 7% H<sub>2</sub> at varying positive bias. The examined strips were collecting holes. The detector fully depleted at 500 V.

Most data sets were acquired according to the biasing scheme shown in Figure 7.7, where a positive bias was applied to the top, the low-energy source was near the same side, and the bottom electrodes collected holes. Taking advantage of the bipolar blocking nature of amorphous semiconductor contacts, one detector was then biased with the opposite polarity so that the bottom electrodes were collecting electrons. Figure 7.22 shows the charge sharing plot for the bottom contact at various bias values, indicating no significant difference due to charge carrier type collected or electric field strength. The one-sigma error bars are generally too small to be visible. In all cases the deficit was less than 0.5% of the full gamma-ray energy. As was the case with holes, increasing bias tended to decrease the fraction of shared events between the strips. However, the fraction was always higher for electron collection than for hole collection. At 1000 V bias (collecting holes), the shared fraction was 21.9%, while at -1000 V (collecting electrons), the shared fraction was 31.7%.

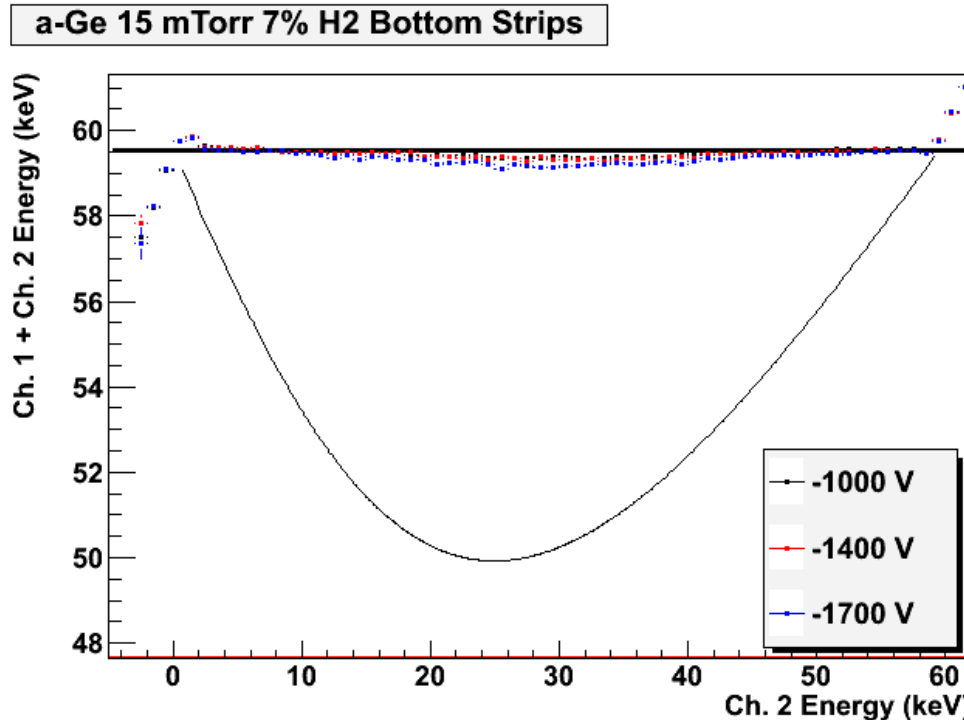


Figure 7.22. Charge sharing plot for one detector with an a-Ge contact sputtered in 15 mTorr Ar with 7% H<sub>2</sub> at varying negative bias. The examined strips were collecting electrons. The detector fully depleted at -500 V.

Table 7.3 summarizes the effect of varying electric field for inter-electrode charge collection. All experiments were carried out on the bottom contact of one detector, which was a-Ge sputtered in 15 mTorr Ar with 7% H<sub>2</sub>. The electrode readout for this detector was slightly different than for all other experiments. The three odd-numbered strips were connected to one channel and the two intervening strips were connected to the other channel. In this way, four gaps were examined instead of just one, but this probably caused a different shared event ratio compared with other experiments. The summed energy deficit, however, showed no difference compared to experiments with the normal two-strip electrode configuration. It should be emphasized that the low values of energy deficit seen in Table 7.3 are near the limit of detectability for a deficit since they are on par with the energy resolution of the detector system.

Table 7.3. Effect of electric field strength on a-Ge contacts sputtered in 15 mTorr Ar with 7% H<sub>2</sub>.

Carrier Collected	Detector Bias	Max. Deficit	Shared Ratio
Holes	1000	0.4%	21.9%
Holes	1500	0.4%	18.1%
Holes	1900	0.6%	16.1%
Electrons	-1000	0.2%	31.7%
Electrons	-1400	0.2%	28.7%
Electrons	-1700	0.4%	27.4%

### 7.3.2.3 Effect of Charge Carrier Polarity

Under the normal bias scheme, the top contact collects electrons while the bottom contact collects holes. The top contact was also a-Ge sputtered in 15 mTorr Ar with 7% H<sub>2</sub>, but it is subject to slightly different conditions during fabrication compared with the bottom contact, so it is worth examining the top contact inter-electrode charge collection properties as well. Figure 7.23 shows a charge sharing plot for electron collection at the top strips for one detector. It appears qualitatively the same as the previous plots for the bottom contact, with only a small deficit for events shared between adjacent strips. The deficit is about 1.7%, slightly more than what was seen for the same process for the bottom contact. The shared fraction of events was 18.8%.

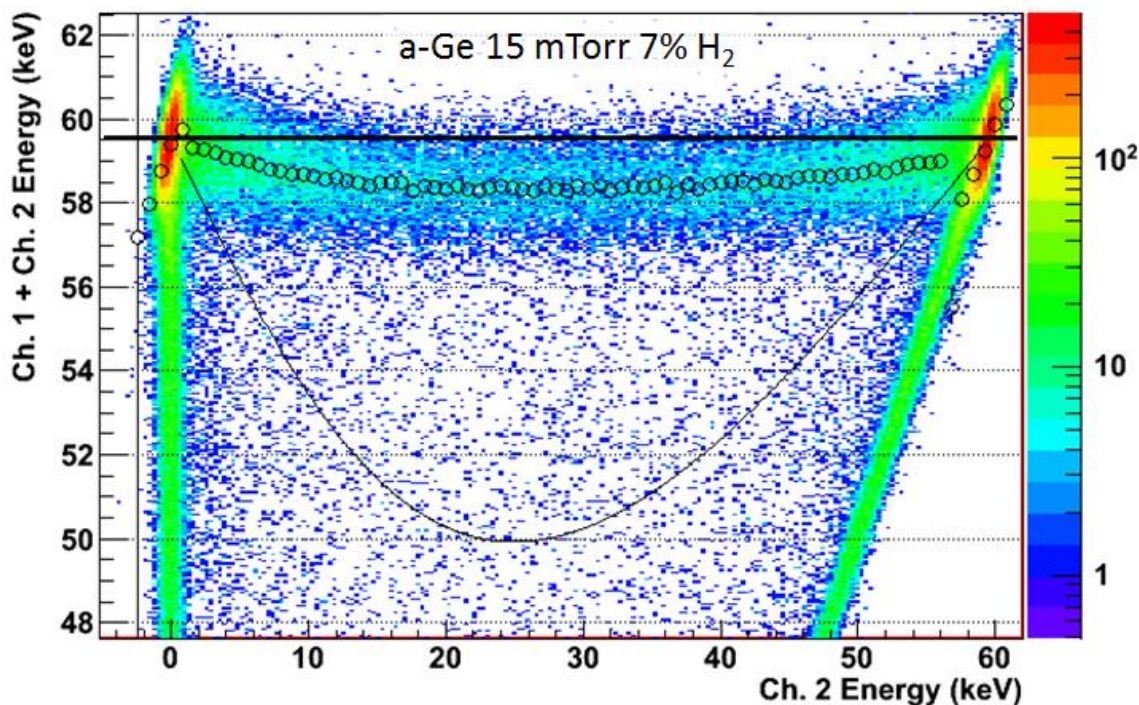
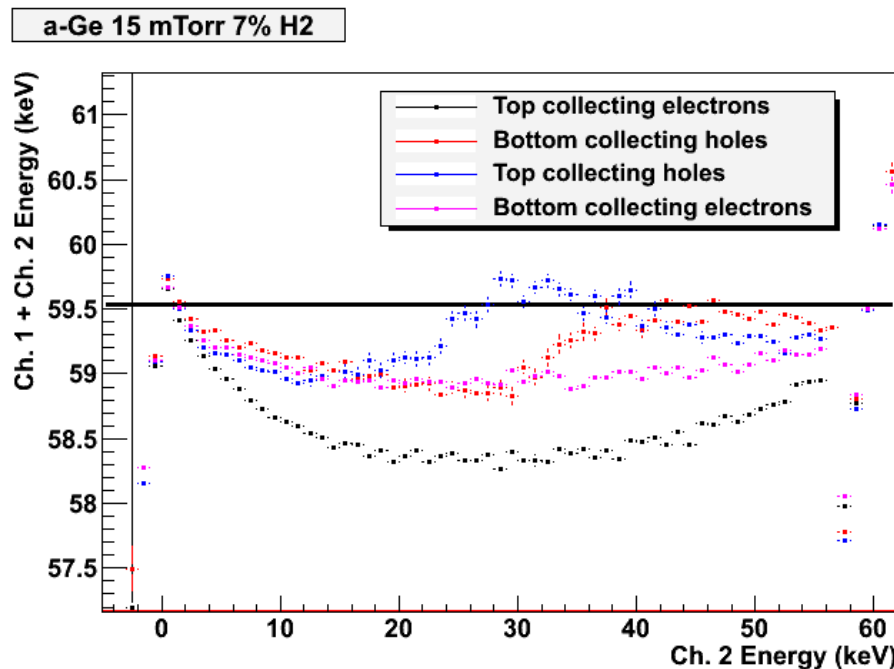


Figure 7.23. Charge sharing plot for the top electrodes of one detector. The top contact was created by sputtering a-Ge in 15 mTorr Ar (7% H<sub>2</sub>) gas. The data are for electrons collected to the top contact.

The top contact collecting electrons shows slightly more deficit compared with the bottom contact collecting either charge carrier or the top collecting holes. Figure 7.24 shows a direct comparison of both charge carriers for the top and bottom contacts using the same basic fabrication process parameters. The top contact collecting holes had the same shared event ratio to the bottom contact collecting holes, around 11%. The results for contacts on different surfaces for different charge carrier polarities are summarized in Table 7.4. All data in this table are from one detector with a-Ge contacts on the top and bottom sputtered in 15 mTorr Ar with 7% H<sub>2</sub>. All data were acquired at +1500 V or -1500 V bias.

**Table 7.4. Inter-electrode charge collection characteristics of different contacts and charge carrier polarity.**

Detector Surface	Carrier Collected	Max. Deficit	Shared Ratio
Bottom	Holes	0.4%	11.3%
Bottom	Electrons	0.9%	18.6%
Top	Holes	0.6%	11.3%
Top	Electrons	1.7%	18.8%



**Figure 7.24.** Comparison of the top and bottom contact processes collecting both charge carrier polarities. All contacts studied were a-Ge contacts sputtered in 15 mTorr Ar with 7% H<sub>2</sub>.

### 7.3.2.4 Effect of Photolithography

The initially fabricated detectors used shadow masks to define the electrode pattern during thermal evaporation of the aluminum. A more versatile fabrication process is possible using photolithography, but one key difference is the bake to harden the photoresist. To mimic the photolithography process to determine whether it has any deleterious effect on inter-electrode charge collection, one detector was tested as initially fabricated with no bake, then baked at 90° C for 30 minutes and re-tested. The detector had a-Ge contacts on the top and bottom sputtered in 15 mTorr Ar with 7% H<sub>2</sub>.

The data shown in Figure 7.25 were collected under the typical biasing scheme where the detector is depleted from the top contact first. The black markers show the result for the bottom contact collecting holes with 1500 V bias (1000 V above depletion). The red markers show results for the same measurement after the bake. Aside from some slight variations in the asymmetric behavior, there was no significant change. The blue markers show the result for data acquired for the top contact collecting electrons at -1500 V bias. The magenta markers represent

the same data after the bake, indicating almost no observable change. It seems that inter-electrode charge collection for both the top and bottom contacts was not significantly affected by the bake.

One detector was fabricated with an a-Ge bottom contact sputtered in 15 mTorr Ar (7% H<sub>2</sub>) gas, just like three previously tested detectors, but this time the electrodes were defined using photolithography rather than a shadow mask. Figure 7.26 shows the charge sharing plot for the bottom electrodes collecting holes. There is no observable energy deficit in the energy sum. Figure 7.27 shows the charge sharing plot for the top electrodes collecting electrons. There is some minor energy deficit, comparable to what was observed in previous detectors not processed with photolithography. The shared event ratio was the same for this detector made using photolithography as it was for the same crystal sample when fabricated using shadow masks. These data were acquired at  $\pm 1000$  V bias, about 850 V above full depletion.

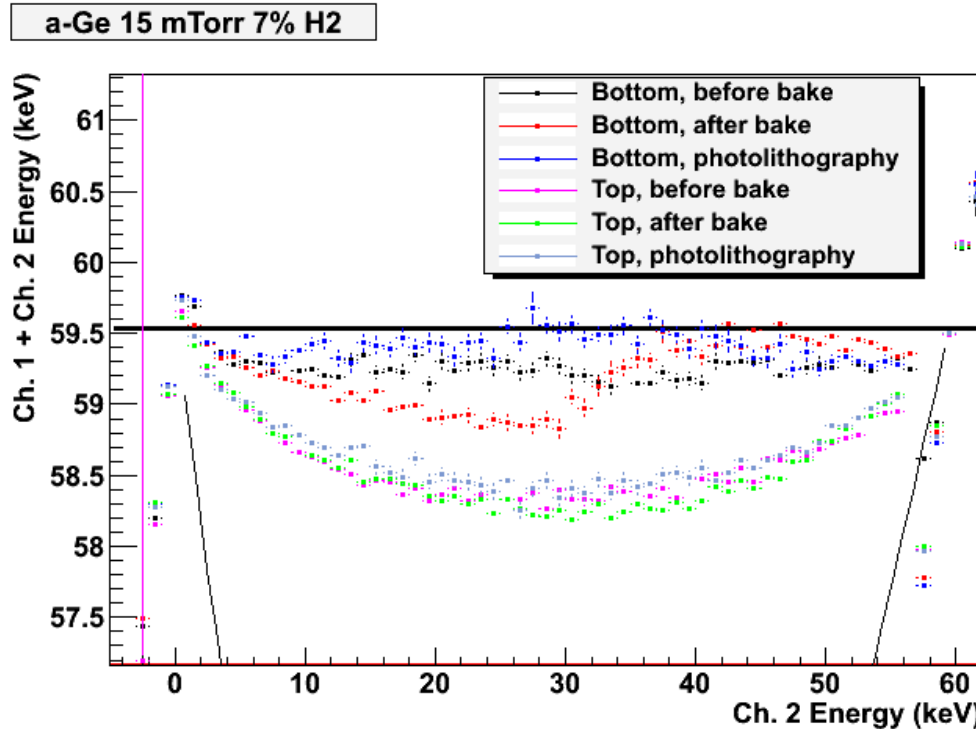


**Figure 7.25.** Data for the evaluation of the effect of photolithography on a-Ge contacts sputtered in 15 mTorr Ar with 7% H<sub>2</sub>. One detector was tested with no bake (black and magenta) and again after a 30 minute bake at 90° C (red and green). Another detector was fabricated with photolithography and tested in the same way (blue and purple).

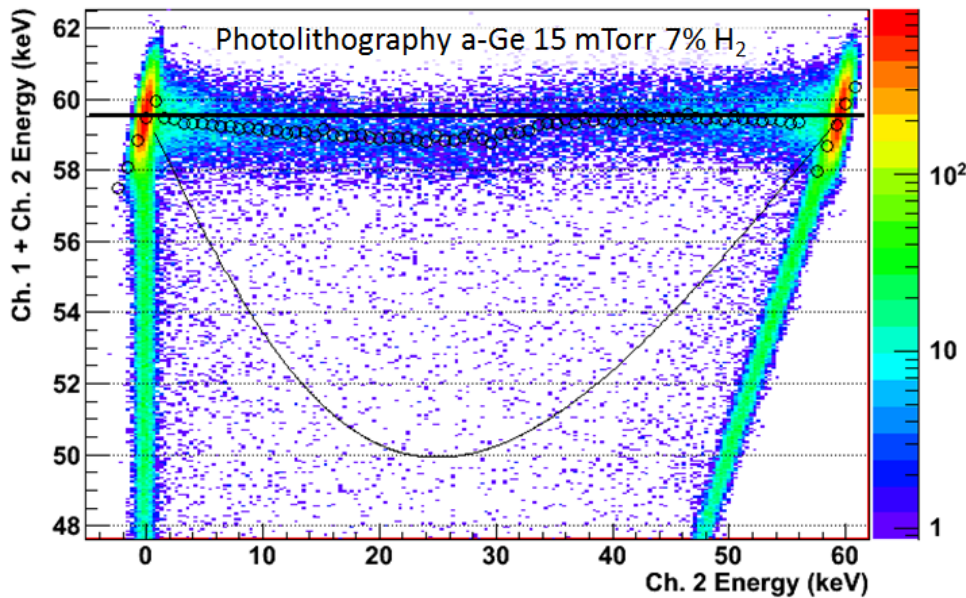


Figure 7.26. Charge sharing plot for a detector fabricated with an a-Ge bottom contact sputtered in a-Ge 15 mTorr Ar (7% H<sub>2</sub>) with electrodes patterned using photolithography. The data, acquired at 1000 V, are for bottom electrodes collecting holes.

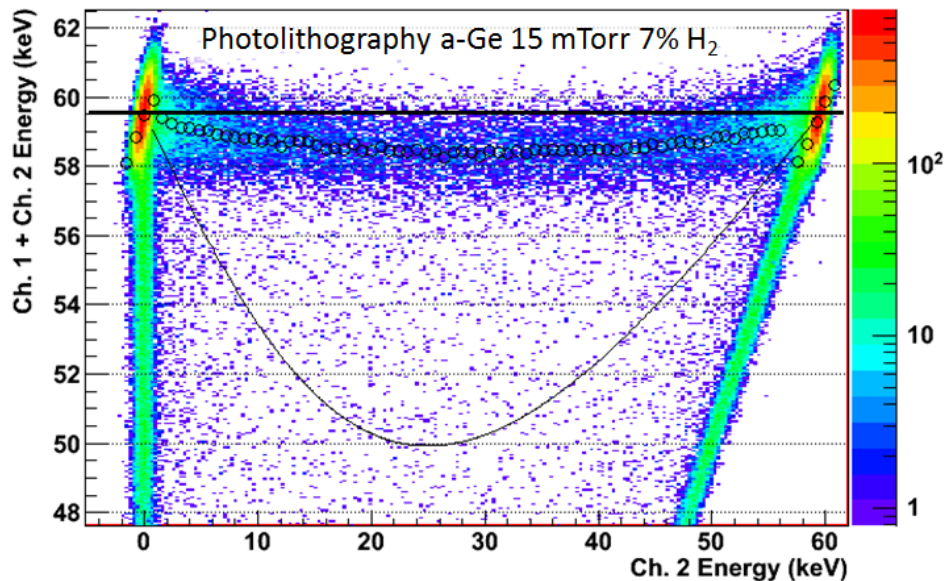


Figure 7.27. Charge sharing plot for a detector fabricated with an a-Ge top contact sputtered in a-Ge 15 mTorr Ar (7% H<sub>2</sub>) with electrodes patterned using photolithography. The data, acquired at -1000 V, are for top electrodes collecting electrons.

### 7.3.3 a-Si with Hydrogen

One detector was fabricated with an a-Si bottom contact sputtered in 7 mTorr Ar (7% H<sub>2</sub>) gas. The detector was tested in the same fashion as previous detectors with a-Ge contacts. The behavior was nearly identical to the a-Ge with hydrogen. There was almost no observable

charge loss, with the maximum deficit being less than 0.7% of the gamma-ray energy. The shared event ratio was 6.8%, about the same as what was seen for a detector made from this crystal sample using a-Ge with 7% H<sub>2</sub>.

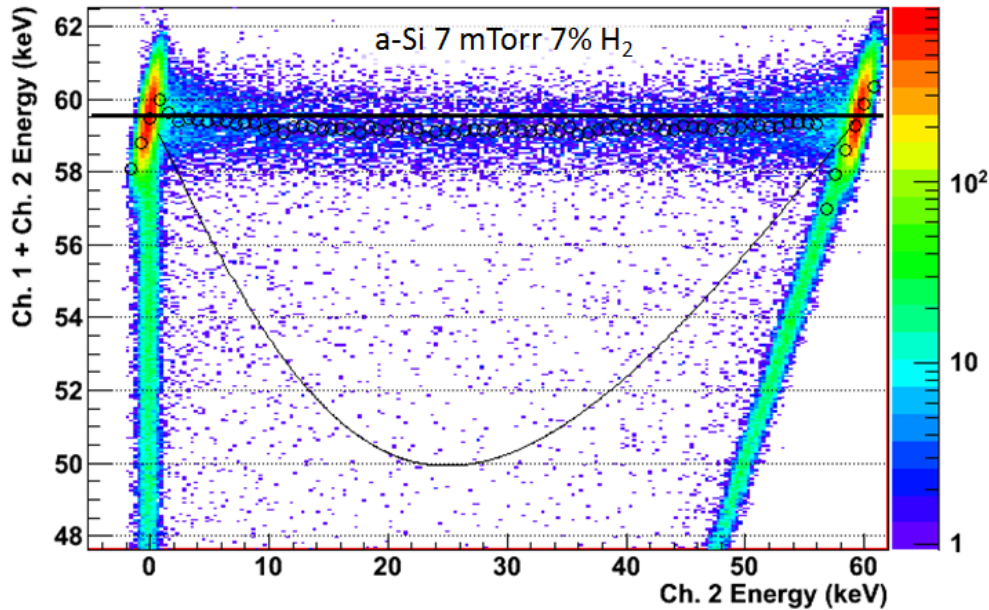


Figure 7.28. Charge sharing plot for one detector with a bottom contact created by sputtering a-Si in 7 mTorr Ar (7% H<sub>2</sub>). The data, acquired at 1000 V, are for bottom electrodes collecting holes.

## 7.4 Conclusions

A total of 6 DSSDs with a-Ge and a-Si contacts were examined for their inter-electrode charge collection properties. Table 7.5 summarizes the differences among the contact types studied, indicating that a-Ge sputtered in 15 mTorr gas with no added hydrogen is not useful as an inter-electrode passivation layer. The large energy deficit for shared events and high ratio of shared events gives very poor spectral performance. The observed charge deficit for shared events matched very well with the expected deficit if charge carriers were collected directly to the contact surface and no lateral electric field existed. However, the addition of 7% H<sub>2</sub> in the sputter gas drastically reduces the charge deficit and number of shared events. A-Si with 7% H<sub>2</sub> performs similarly to the a-Ge with 7% H<sub>2</sub>. The a-Ge with added hydrogen has much higher resistivity than a-Ge with no added H<sub>2</sub>, which may have something to do with the improved charge sharing performance.

In most cases, there is almost no observable energy sum deficit for a wide variety of conditions, including a wide range of electric field magnitudes, collecting either type of charge carrier, and after undergoing a photolithography bake. The effect is reproducible on the same crystal and on different crystals. An exception is the slightly larger 1-2% deficit observed for electron collection when the same process is used on the top contact. The a-Ge process makes a suitable hole-blocking contact for segmented detectors, giving low leakage current that is stable over time and providing inter-electrode passivation that does not collect charge to the gap between electrodes. Photolithography may be freely used without deleterious effects on inter-

electrode charge collection properties. The electron-blocking contact can be formed using a-Si sputtered in 7 mTorr Ar (7% H<sub>2</sub>) atmosphere. This process gives reliably low electron injection leakage current, is stable with time, and does not collect charge to the gap between electrodes. On all a-Ge contacts tested there was a slow change with time the detector was biased. The effect could be due to some change in the charge at the interface as it approaches a steady state due to a combination of buildup from leakage current and depletion from charge moving out of the amorphous layer.

**Table 7.5. Summary of charge sharing results for different contacts.**

Material	Surface	Collecting	Det. Thickness	Max. Deficit	Shared Ratio
a-Ge 0% H <sub>2</sub>	Bottom	Holes	13 mm	16%	30%
a-Ge 7% H <sub>2</sub>	Bottom	Holes	13 mm	0.6%	11%
a-Ge 7% H <sub>2</sub>	Bottom	Holes	7 mm	0.2%	6.8%
a-Si 7% H <sub>2</sub>	Bottom	Holes	7 mm	0.6%	6.8%
a-Ge 7% H <sub>2</sub>	Top	Holes	13 mm	0.6%	11.3%
a-Ge 7% H <sub>2</sub>	Top	Electrons	13 mm	1.7%	18.8%
a-Ge 7% H <sub>2</sub>	Top	Electrons	7 mm	0.9%	11%
a-Ge 7% H <sub>2</sub>	Bottom	Electrons	13 mm	0.4%	-

# Chapter 8     Conclusions

High-purity germanium (HPGe) detectors occupy a unique position among detector technologies, standing to fill important roles where excellent energy and position resolution are required along with high detection efficiency. These detectors revolutionized gamma-ray spectroscopy in decades past and have enjoyed many technological improvements since then [1]. Although some HPGe detector designs are a mature and commercialized technology, improvement is needed, particularly in the fabrication and characterization of new designs.

Amorphous semiconductor contacts can provide a simpler fabrication process for highly segmented, position-sensitive HPGe detectors, taking advantage of their bipolar blocking nature and suitability as a surface passivation layer. However, this contact technology still needs additional development, especially in the key areas of reducing leakage current, achieving long-term stability, eliminating surface channels and inter-electrode charge collection, and obtaining sufficiently high inter-electrode impedance. Solving these issues could lead to a greatly improved fabrication process suitable for providing reliable and highly performing detectors.

Three systematic studies on the leakage current, long-term stability, and inter-electrode charge collection properties of amorphous semiconductor contacts on HPGe detectors were presented. The impact of varying the sputter gas hydrogen content, sputter gas pressure, and amorphous film thickness was assessed.

## 8.1 Significant Findings

This dissertation has summarized a body of work intended to improve high-resolution, position-sensitive germanium detectors by systematically evaluating fabrication processes and their impact on important detector characteristics. The first major component was a systematic study of the amorphous semiconductor contact fabrication process with the aim of assessing which factors are important in obtaining reliable blocking contacts. About 45 detectors were fabricated with a-Ge and a-Si contacts formed by sputtering in an atmosphere of varying pressure and hydrogen content. The thickness of the amorphous layer was also varied.

Some key findings yielded an improved process for these contacts and should inform future studies. The a-Si contacts have significantly lower electron injection leakage current than a-Ge contacts due to a combination of a higher temperature-dependent electron barrier and lower temperature-independent pre-factor. Although the number of a-Si samples was small, the findings indicate that their electron blocking behavior is relatively insensitive to fabrication conditions such as hydrogen content, sputter pressure, and thickness. The a-Ge contacts showed a lower pre-factor for higher hydrogen content and higher sputter pressure, giving slightly lower electron injection leakage current for those processes compared with low hydrogen content and low sputter pressure. The reproducibility of leakage current for multiple detectors using the same fabrication process was found to be the biggest issue using the current equipment and methods.

The long-term stability of the contacts is an important factor that is heavily influenced by the fabrication process. It was shown that sputter gas pressure makes an immense difference in the

long-term stability of a-Ge contacts. Contacts formed by sputtering in gas with less than about 13 mTorr pressure show significantly increasing electron injection leakage current the longer they are kept at room temperature. A rapid change occurs initially, followed by a slower change in leakage current after the detector has been warm for hundreds of hours. Contacts formed by sputtering in gas above 13 mTorr are significantly more stable. The hydrogen content does not seem to play a substantial role in long-term stability. It was also found that a-Si contacts consistently show a decrease in electron injection leakage current with little dependence on hydrogen content.

Another key finding regarding long-term stability was the evidence that it is the time a detector spends at room temperature, rather than the number of temperature cycles, that is related to leakage current changes in the detector. This provides a useful metric for comparing different fabrication processes both in the present work and in the future.

The a-Ge and a-Si contacts were also assessed for their suitability on segmented detectors. It was shown that a-Ge contacts with no hydrogen collected charge carriers directly to the gap between strips, resulting in a substantial deficit in the energy sum of two adjacent strips. This process is not suitable for segmented detectors. However, a-Ge contacts with some hydrogen content show almost no energy sum deficit, making them suitable for segmented detectors as a combination contact and inter-electrode passivation layer. Electron-blocking contacts formed by an a-Si layer also showed good performance with almost no energy sum deficit for adjacent strips.

In summary, the combined result of these findings is a robust fabrication process where the hole-blocking is formed by a-Ge with some hydrogen content and sputtered in high pressure gas. This forms a suitable hole-blocking contact that is stable at room temperature and functions well as a passivation layer. Although hole-blocking data were not obtained in the present work, it is a simple extension of Schottky theory to deduce that the a-Ge recipes with low electron barriers will have large hole barriers, since the sum of the two barriers is the bandgap of the semiconductor material. This is confirmed by previous work with a-Ge on HPGe detectors [26]. Also, the present work routinely utilized a-Ge hole-blocking contacts and they were found to have relatively low injection leakage current. The electron-blocking contact is formed by a-Si, giving low electron injection leakage current that slightly decreases if the detector is warmed. This layer can also function as an inter-electrode passivation layer.

## 8.2 Future Work

Although the study of long-term stability yielded important results, that knowledge could be channeled to more useful work in this area. Now that a useful metric of leakage current as a function of total time warm has been identified, this measurement could be applied to a wider range of process parameters, including a wider range of sputter pressures (shown to be an important parameter in this work). An expanded study with a larger sample size of detectors could help solidify some of the conclusions. The current work on long-term contact stability was relatively limited due to the time-consuming nature of the measurements. Future work could expand on this study to give a better indication of whether the detectors could be operated for years with significant time warm during that period. More materials-oriented studies of the

amorphous layer could also be valuable in discovering more about the physical mechanism of change in the contacts.

The systematic study of the amorphous semiconductor contact fabrication process in this work uncovered a level of reproducibility that is not understood. Future work could be helpful in identifying what part of the process is primarily responsible for the levels of variation. Initial areas for investigation would be the surface preparation etch process, where a relatively aggressive wet etch gives some degree of unpredictability that is visible as different surface textures after the etch. One alternative is chemical-mechanical polishing followed by a light chemical etch to remove only a small amount of material. Another avenue for improvement in reproducibility is the sputtering process. The sputtering process could be improved by careful monitoring of the pressure gauge reading, base pressure before sputtering, and the amount of heating during sputtering. Other unknown factors exist such as the gas purity and precise deposition rate. Any future study using the current methods would ideally incorporate a large number of samples and statistical analysis to draw clear conclusions.

An expanded investigation of fabrication process parameters would also be beneficial to find the limits of parameters like sputter gas pressure and hydrogen content. A more thorough study of a-Si contacts would also provide valuable information.

The inter-electrode charge collection work could also be expanded with a study of the role of contact thickness, sputter pressure, and wider variation in hydrogen content. There are also open questions as to the long-term stability as well as the inter-electrode impedance properties of the different contact fabrication processes. A study of non-contact passivation layers would also be beneficial because it could be extended to other HPGe detector types, such as the p-type point contact detector.

## References

- [1] K. Vetter, "Recent Developments in the Fabrication and Operation of Germanium Detectors," *Annual Review of Nuclear and Particle Science*, vol. 57, pp. 363-404, 2007.
- [2] P. N. Luke and M. Amman, "Room-Temperature Replacement for Ge Detectors - Are We There Yet?," *IEEE Transactions on Nuclear Science*, vol. 54, no. 4, pp. 834-842, 2007.
- [3] D. V. Freck and J. Wakefield, "Gamma-Ray Spectrum obtained with a Lithium-drifted p-i-n Junction in Germanium," *Nature*, vol. 193, p. 669, 1962.
- [4] H. M. Mann, "Progress in the application of semiconductor detectors to nuclear physics experiments," *IEEE Transactions on Nuclear Science*, vol. 12, no. 2, pp. 88-98, 1965.
- [5] A. J. Tavendale, "Semiconductor nuclear radiation detectors," *Annual Review of Nuclear and Particle Science*, vol. 17, pp. 73-96, 1967.
- [6] "The Official GRETA homepage," [Online]. Available: <http://greta.lbl.gov>.
- [7] "The Official AGATA homepage," [Online]. Available: <http://www-w2k.gsi.de/agata>.
- [8] J. Simpson, "The AGATA Project," *Journal of Physics G*, vol. 31, pp. S1801-S1806, 2005.
- [9] M. A. Deleplanque, I. Y. Lee, K. Vetter, G. J. Schmid, F. S. Stephens, R. M. Clark, R. M. Diamond, P. Fallon and A. O. Macchiavelli, "GRETA: utilizing new concepts in gamma-ray detection," *Nuclear Instruments and Methods in Physics Research A*, vol. 430, pp. 292-310, 1999.
- [10] J. C. Philippot, "Automatic Processing of Diode Spectrometry Results," *IEEE Transactions on Nuclear Science*, vol. 17, no. 3, pp. 446-488, 1970.
- [11] K. Vetter, M. Burks and L. Mihailescu, "Gamma-ray imaging with position-sensitive HPGe detectors," *Nuclear Instruments and Methods in Physics Research A*, vol. 525, pp. 322-327, 2004.
- [12] L. Mihailescu, K. M. Vetter, M. T. Burks, E. L. Hull and W. W. Craig, "SPEIR: A Ge Compton camera," *Nuclear Instruments and Methods in Physics Research A*, vol. 570, pp. 89-100, 2007.
- [13] K. P. Ziock, W. W. Craig, L. Fabris, R. C. Lanza, S. Gallagher, B. K. P. Horn and N. W. Madden, "Large Area Imaging Detector for Long-Range, Passive Detection of Fissile Material," *IEEE Transactions on Nuclear Science*, vol. 51, no. 5, pp. 2238-2244, 2004.
- [14] M. Amman and P. N. Luke, "Position-sensitive germanium detectors for gamma-ray imaging and spectroscopy," *Proceedings of the SPIE*, 2000.
- [15] J. Headspith et al., "First Experimental Data from XH, a Fine Pitch Germanium Microstrip Detector for Energy Dispersive EXAFS (EDE)," *IEEE Nuclear Science Symposium Conference Record*, pp. 2421-2428, 2007.
- [16] V. R. McCready, R. P. Parker, E. M. Gunnersen, R. Ellis, E. Moss, W. G. Gore and J. Bell, "Clinical tests on a prototype semiconductor gamma-camera," *British Journal of Radiology*, vol. 44, no. 517, pp. 58-62, 1971.
- [17] J. F. Detko, "Progress toward a stable orthogonal strip germanium gamma camera," *IEEE Transactions on Nuclear Science*, Vols. NS-23, no. 1, pp. 538-542, 1976.

- [18] M. Singh, "An electronically collimated gamma camera for single photon emission computed tomography," *Medical Physics*, vol. 10, no. 4, pp. 421-427, 1983.
- [19] B. H. Hasegawa, B. Stebler, B. K. Rutt, A. Martinez, E. L. Gingold, C. S. Barker, K. G. Faulkner, C. E. Cann and D. P. Boyd, "A prototype high-purity germanium detector system with fast photon-counting circuitry for medical imaging," *Medical Physics*, vol. 18, pp. 900-909, 1991.
- [20] P. N. Luke, R. H. Pehl and F. A. Dilmanian, "A 140-element Ge Detector Fabricated with Amorphous Ge Blocking Contacts," *IEEE Transactions on Nuclear Science*, vol. 41, no. 4, pp. 976-978, 1994.
- [21] R. J. Cooper, G. Turk, A. J. Boston, H. C. Boston, J. R. Cresswell, A. R. Mather, P. J. Nolan, C. J. Hall, I. Lazarus, J. Simpson, A. Berry, T. Beveridge, J. Gillam and R. A. Lewis, "Position sensitivity of the first SmartPET HPGe detector," *Nuclear Instruments and Methods in Physics Research A*, vol. 573, pp. 72-75, 2007.
- [22] L. C. Johnson, D. L. Campbell, E. L. Hull and T. E. Peterson, "Characterization of a high-purity germanium detector for small-animal SPECT," *Physics in Medicine and Biology*, vol. 56, pp. 5877-5888, 2011.
- [23] R. P. Lin et al., "The Reuven Ramaty High-Energy Solar Spectroscopic Imager (RHESSI)," *Solar Physics*, vol. 210, no. 1, pp. 3-32, 2002.
- [24] S. Boggs, M. Bandstra, J. Bowen, W. Coburn, R. Lin, C. Wunderer, A. Zoglauer, M. Amman, P. Luke, P. Jean and P. von Ballmoos, "Performance of the Nuclear Compton Telescope," *Exp Astron*, vol. 20, pp. 387-394, 2005.
- [25] A. Y. Shih et al., "The Gamma-Ray Imager/Polarimeter for Solar flares (GRIPS)," in *Proc. of SPIE Vol. 8443*, 2012.
- [26] M. Amman, P. N. Luke and S. E. Boggs, "Amorphous-semiconductor-contact germanium-based detectors for gamma-ray imaging and spectroscopy," *Nuclear Instruments and Methods in Physics Research A*, vol. 579, pp. 886-890, 2007.
- [27] P. N. Luke, C. P. Cork, N. W. Madden, C. S. Rossington and M. F. Wesela, "Amorphous Ge Bipolar Blocking Contacts on Ge Detectors," *IEEE Transactions on Nuclear Science*, vol. 39, no. 4, pp. 590-594, 1992.
- [28] W. L. Hansen, E. E. Haller and G. S. Hubbard, "Protective surface coatings on semiconductor nuclear radiation detectors," *IEEE Transactions on Nuclear Science*, Vols. NS-27, no. 1, pp. 247-251, 1980.
- [29] M. J. Berger, J. H. Hubbell, S. M. Seltzer, J. Chang, J. S. Coursey, R. Sukumar, D. S. Zucker and K. Olsen, "XCOM: Photon Cross Sections Database," NIST, 1998. [Online]. Available: [www.nist.gov/pml/data/xcom](http://www.nist.gov/pml/data/xcom).
- [30] G. Knoll, *Radiation Detection and Measurement*, New York: Wiley, 2000.
- [31] H. Spieler, *Semiconductor Detector Systems*, New York: Oxford University Press, 2005.
- [32] F. E. Energy and T. A. Rabson, "Average Energy Expendited Per Ionized Electron-Hole Pair in Silicon and Germanium as a Function of Temperature," *Physical Review A*, vol. 140, no. 6, pp. 2089-2093, 1965.
- [33] S. Croft and D. S. Bond, "A Determination of the Fano Factor for Germanium at 77.4 K from Measurements of the Energy Resolution of a 113 cm<sup>3</sup> HPGe Gamma-ray

- Spectrometer Taken Over the Energy Range from 14 to 6129 keV," *Applied Radiation and Isotopes*, vol. 42, no. 11, pp. 1009-1014, 1991.
- [34] W. Shockley, "Currents to conductors induced by a moving point charge," *Journal of Applied Physics*, vol. 9, p. 635, 1938.
- [35] S. Ramo, "Currents induced by electron motion," in *Proceedings of the I.R.E.*, 1939.
- [36] Z. He, "Review of the Shockley-Ramo theorem and its application in semiconductor gamma-ray detectors," *Nuclear Instruments and Methods in Physics Research A*, vol. 463, pp. 250-267, 2001.
- [37] V. Radeka, "Low-noise techniques in detectors," *Annual Reviews in Nuclear Particle Science*, vol. 38, pp. 217-77, 1988.
- [38] C. Kittel, *Introduction to Solid State Physics*, John Wiley & Sons, Inc., 2005.
- [39] C. A. Klein, "Bandgap Dependence and Related Features of Radiation Ionization Energies in Semiconductors," *Journal of Applied Physics*, vol. 39, no. 4, pp. 2029-2038, 1968.
- [40] E. M. Conwell, "Properties of Silicon and Germanium," *Proceedings of the I.R.E.*, vol. 40, no. 11, pp. 1327-1337, 1952.
- [41] C. Szeles and M. C. Driver, "Growth and properties of semi-insulating CdZnTe for radiation detector applications," *Proc. of SPIE*, vol. 3446, 1998.
- [42] E. M. Conwell, "Properties of Silicon and Germanium: II," *Proceedings of the IRE*, vol. 46, no. 6, pp. 1281-1300, 1958.
- [43] G. Ottaviani, C. Canali, F. Nava and J. W. Mayer, "Hole drift velocity in high-purity Ge between 8 and 220 K," *Journal of Applied Physics*, vol. 44, no. 6, pp. 2917-2918, 1973.
- [44] C. Jacoboni, F. Nava, C. Canali and G. Ottaviani, "Electron drift velocity and diffusivity in germanium," *Physical Review B*, vol. 24, no. 2, pp. 1014-1026, 1981.
- [45] J. R. Haynes and W. Shockley, "The Mobility and Life of Injected Holes and Electrons in Germanium," *Physical Review*, vol. 81, no. 5, pp. 835-843, 1951.
- [46] eV Products, [Online]. Available: [www.evproducts.com](http://www.evproducts.com).
- [47] W. F. Beadle, J. C. C. Tsai and R. D. Plummer, *Quick Reference Manual for Semiconductor Engineers*, New York: Wiley, 1985.
- [48] J. C. Erickson, H. W. Yao, R. B. James, H. Hermon and M. Greaves, "Time of Flight Experimental Studies of CdZnTe Radiation Detectors," *Journal of Electronic Materials*, vol. 29, no. 6, pp. 699-703, 2000.
- [49] S. M. Sze, *Semiconductor Devices: Physics and Technology*, Wiley, 2002.
- [50] A. Owens and A. Peacock, "Compound semiconductor radiation detectors," *Nuclear Instruments and Methods in Physics Research A*, vol. 531, pp. 18-37, 2004.
- [51] E. M. Pell, "Ion Drift in an n-p Junction," *Journal of Applied Physics*, vol. 31, no. 2, pp. 291-302, 1960.
- [52] A. J. Tavendale, "Semiconductor lithium-ion drift diodes as high-resolution gamma-ray pair spectrometers," *IEEE Transactions on Nuclear Science*, vol. 13, no. 1, pp. 191-200, 1964.
- [53] W. L. Hansen, "High-purity germanium crystal growing," *Nuclear Instruments and Methods*, vol. 94, pp. 377-380, 1971.

- [54] R. D. Baertsch and N. R. Hall, "Gamma Ray Detectors made from High Purity Germanium," *IEEE Transactions on Nuclear Science*, vol. 17, no. 3, pp. 235-240, 1970.
- [55] J. Llacer, "Planar and Coaxial High Purity Germanium Radiation Detectors," *Nuclear Instruments and Methods*, vol. 98, pp. 259-268, 1972.
- [56] W. G. Pfann, "Zone Melting," *Science*, vol. 135, no. 3509, pp. 1101-1109, 1962.
- [57] E. E. Haller, "Germanium: From its discovery to SiGe devices," *Materials Science in Semiconductor Processing*, vol. 9, pp. 408-422, 2006.
- [58] "Ortec," [Online]. Available: <http://www.ortec-online.com>.
- [59] S. R. Amendolia et al., "Germanium microstrip detectors with 50 and 100 micrometer pitch," *Nuclear Instruments and Methods in Physics Research*, vol. 226, pp. 117-121, 1984.
- [60] D. Protic and G. Riepe, "High-resolution charged-particle spectroscopy with high-purity germanium detectors in the intermediate energy range," *IEEE Transactions on Nuclear Science*, Vols. NS-24, no. 1, pp. 64-67, 1977.
- [61] D. Gutknecht, "Photomask technique for fabricating high purity germanium strip detectors," *Nuclear Instruments and Methods in Physics Research A*, vol. 288, pp. 13-18, 1990.
- [62] S. Gros, N. J. Hammond, C. J. Lister, P. Chowdhury, S. M. Fischer and S. J. Freeman, "Performance tests of large area position-sensitive planar germanium detectors with conventional and amorphous contacts," *Nuclear Instruments and Methods in Physics Research A*, vol. 602, pp. 467-476, 2009.
- [63] M. Descovich et al., "The position response of a large-volume segmented germanium detector," *Nuclear Instruments and Methods in Physics Research A*, vol. 553, pp. 512-521, 2005.
- [64] G. S. King, F. T. Avignone, C. E. Cox, T. W. Hosbach, W. Jennings and J. H. Reeves, "Fabrication and performance tests of a segmented p-type HPGe detector," *Nuclear Instruments and Methods in Physics Research A*, vol. 595, pp. 599-604, 2008.
- [65] P. N. Luke, M. Amman, B. F. Phlips, W. N. Johnson and R. A. Kroeger, "Germanium orthogonal strip detectors with Amorphous-Semiconductor Contacts," *IEEE Transactions on Nuclear Science*, vol. 47, no. 4, pp. 1360-1363, 2000.
- [66] M. Amman and P. N. Luke, "Three-dimensional position sensing and field shaping in orthogonal-strip germanium gamma-ray detectors," *Nuclear Instruments and Methods in Physics Research A*, vol. 452, pp. 155-166, 2000.
- [67] P. N. Luke, F. S. Goulding, N. W. Madden and R. H. Pehl, "Low capacitance large volume shaped-field germanium detector," *IEEE Transactions on Nuclear Science*, vol. 36, no. 1, pp. 926-930, 1989.
- [68] P. S. Barbeau, J. I. Collar and O. Tench, "Large-mass ultralow noise germanium detectors: performance and applications in neutrino and astroparticle physics," *Journal of Cosmology and Astroparticle Physics*, vol. 9, pp. 9-28, 2007.
- [69] R. J. Cooper, D. C. Radford, E. Hull, K. Lagergren, P. Mullowney, M.-C. Lin, K. Paul, C. Athens and M. Loh, "Effect of a surface channel on the performance of a P-type Point Contact HPGe detector," *Nuclear Instruments and Methods in Physics Research A*, vol.

680, pp. 48-55, 2012.

- [70] R. D. Baertsch, "Surface Effects on P Type High Purity Germanium Detectors at 77 K," *IEEE Transactions on Nuclear Science*, vol. 21, no. 1, pp. 347-359, 1974.
- [71] P. E. Gibbons, J. H. Howes and S. Pyrah, "An encapsulated lithium drifted germanium diode for gamma ray spectrometry," *Nuclear Instruments and Methods*, vol. 45, pp. 322-324, 1966.
- [72] J. T. Walton, R. H. Pehl, Y. K. Wong and C. P. Cork, "Si(Li) X-Ray Detectors with Amorphous Silicon Passivation," *IEEE Transactions on Nuclear Science*, Vols. NS-31, no. 1, pp. 331-335, 1984.
- [73] Y. S. Suh, M. S. Carroll, R. A. Levy, M. A. Sahiner, G. Bisognin and C. A. King, "Modeling of Boron and Phosphorus Implantation Into (100) Germanium," *IEEE Transactions on Electron Devices*, vol. 52, no. 1, pp. 91-98, 2005.
- [74] H. Herzer and S. Kalbitzer, "Ion Implanted High-Purity Germanium Detectors," *Nuclear Instruments and Methods*, vol. 101, pp. 31-37, 1972.
- [75] G. S. Hubbard, E. E. Haller and W. L. Hansen, "Ion Implanted N-Type Contact for High-Purity Germanium Radiation Detectors," *IEEE Transactions on Nuclear Science*, vol. 24, no. 1, pp. 161-164, 1977.
- [76] R. H. Pehl and P. N. Luke, "High-purity germanium charged-particle detectors: A LBL-IUCF update," *Nuclear Instruments and Methods in Physics Research A*, vol. 242, pp. 103-110, 1985.
- [77] D. Protic and T. Krings, "Detection Characteristics of Ge Detectors with Microstructured Amorphous Ge Contacts," *IEEE Transactions on Nuclear Science*, vol. 51, no. 3, pp. 1129-1133, 2004.
- [78] R. H. Pehl, E. E. Haller and R. C. Cordi, "Operational characteristics of germanium detectors at higher temperatures," *IEEE Transactions on Nuclear Science*, vol. 20, no. 1, pp. 494-499, 1973.
- [79] W. C. Dunlap, "Diffusion of Impurities in Germanium," *Physical Review*, vol. 94, no. 6, pp. 1531-1540, 1954.
- [80] C. S. Fuller and J. A. Ditzenberger, "Diffusion of Lithium into Germanium and Silicon," *Physical Review*, vol. 91, no. 1, p. 193, 1953.
- [81] R. H. Pehl, R. C. Cordi and F. S. Goulding, "High-purity germanium: Detector fabrication and performance," *IEEE Transactions on Nuclear Science*, vol. 19, no. 1, pp. 265-269, 1972.
- [82] N. Q. Huy, D. Q. Binh and V. X. An, "Study on the increase of inactive germanium layer in a high-purity germanium detector after a long time operation applying MCNP code," *Nuclear Instruments and Methods in Physics Research A*, vol. 573, pp. 384-388, 2007.
- [83] R. D. Martin et al., "Characteristics of signals originating near the lithium-diffused N+ contact of high purity germanium p-type point contact detectors," *Nuclear Instruments and Methods in Physics Research A*, vol. 701, pp. 176-185, 2013.
- [84] D. Protic, T. Krings and R. Schleichert, "Development of Double-Sided Microstructured Si(Li) Detectors," *IEEE Transactions on Nuclear Science*, vol. 49, no. 4, pp. 1993-1998, 2002.

- [85] P. N. Luke, "Gold-mask technique for fabricating segmented-electrode germanium detectors," *IEEE Transactions on Nuclear Science*, Vols. NS-31, no. 1, pp. 312-315, 1984.
- [86] H. L. Malm, "Properties of Metal Surface Barriers on High Purity Germanium," *IEEE Transactions on Nuclear Science*, vol. 22, pp. 140-144, 1975.
- [87] W. Schottky, "Semiconductor theory of blocking-layer and point rectifier," *Zeitschrift fur Physik*, vol. 113, no. 5-6, pp. 367-414, 1939.
- [88] H. M. Mann, F. J. Janarek and H. W. Helenberg, "Preparation of large volume planar germanium detectors and results of their use in nuclear physics experiments," *IEEE Transactions on Nuclear Science*, vol. 13, no. 3, pp. 336-350, 1967.
- [89] W. M. Haynes, CRC Handbook of Chemistry and Physics, 92nd Edition, 2012.
- [90] A. M. Cowley and S. M. Sze, "Surface States and Barrier Height of Metal-Semiconductor Systems," *Journal of Applied Physics*, vol. 36, no. 10, pp. 3212-3220, 1965.
- [91] T. Nishimura, K. Kita and A. Toriumi, "Evidence for strong Fermi-level pinning due to metal-induced gap states at metal/germanium interface," *Applied Physics Letters*, vol. 91, p. 123123, 2007.
- [92] M. H. Brodsky, G. H. Dohler and P. J. Steinhardt, "On the Measurement of the Conductivity Density of States of Evaporated Amorphous Silicon Films," *Phys. Stat. Sol.*, vol. 72, pp. 761-769, 1975.
- [93] W. L. Hansen and E. E. Haller, "Amorphous germanium as an electron or hole blocking contact on high-purity germanium detectors," *IEEE Transactions on Nuclear Science*, Vols. NS-24, no. 1, pp. 61-63, 1977.
- [94] S. Prussin, D. I. Margolese and R. N. Tauber, "Formation of amorphous layers by ion implantation," *Journal of Applied Physics*, vol. 57, no. 2, pp. 180-185, 1985.
- [95] N. F. Mott, "Conduction in Non-crystalline Materials," *Philosophical Magazine*, vol. 19, pp. 835-852, 1969.
- [96] N. F. Mott and E. A. Davis, *Electronic Processes in Non-Crystalline Materials*, Oxford: Clarendon Press, 1971.
- [97] M. H. Brodsky and G. H. Dohler, "A new type of junction: Amorphous/crystalline," *Critical Reviews in Solid State and Materials Sciences*, vol. 5, no. 4, pp. 591-595, 1975.
- [98] W. Brenig, G. H. Dohler and P. Wolfe, "Theory of thermally assisted electron hopping in amorphous solids," *Z. Phys.*, vol. 1, p. 246, 1971.
- [99] V. Ambegaokar, B. L. Halperin and J. S. Langer, "Hopping conductivity in disordered systems," *Phys. Rev. B*, vol. 1, p. 246, 1971.
- [100] W. Schottky, "Vereinfachte und erweiterte Theorie der Randschicht-gleichrichter," *Zeitschrift fur Physik*, vol. 118, pp. 539-592, 1942.
- [101] E. L. Hull and R. H. Pehl, "Amorphous germanium contacts on germanium detectors," *Nuclear Instruments and Methods in Physics Research A*, vol. 538, pp. 651-656, 2005.
- [102] D. Fahnlund, B. Yang, K. Vedam, R. Messier and L. Pilione, "Intrinsic Stress in a-Germanium Films Deposited by RF-Magnetron Sputtering," *MRS Symposium Proceedings*, vol. 130, pp. 355-360, 1989.
- [103] W. Paul, A. J. Lewis, G. A. N. Connell and T. D. Moustakas, "Doping, Schottky barrier

- and p-n junction formation in amorphous germanium and silicon by RF sputtering," *Solid State Communications*, vol. 20, pp. 969-972, 1976.
- [104] G. A. N. Connell and J. R. Pawlik, "Use of hydrogenation in structural and electronic studies of gap states in amorphous germanium," *Physical Review B*, vol. 13, no. 2, pp. 787-804, 1976.
- [105] A. J. Lewis, "Use of hydrogenation in the study of the transport properties of amorphous germanium," *Physical Review B*, vol. 14, no. 2, pp. 658-668, 1976.
- [106] D. K. Schroder, *Semiconductor Material and Device Characterization*, Hoboken: Wiley, 2006.
- [107] A. Y. C. Yu and C. A. Mead, "Characteristics of Aluminum-Silicon Schottky Barrier Diode," *Solid-State Electronics*, vol. 13, pp. 97-104, 1970.
- [108] R. H. Pehl, N. W. Madden, D. F. Malone, C. P. Cork and D. A. Landis, "A variable temperature cryostat that produces in situ clean-up of germanium detector surfaces," *IEEE Transactions on Nuclear Science*, vol. 36, no. 1, pp. 190-193, 1989.
- [109] E. Haller, *Private communication*.
- [110] M. Amman, *LBNL internal presentation 12/13/2010*.
- [111] R. J. Dinger, "Dead layers at the surface of p-i-n detectors - A review," *IEEE Transactions on Nuclear Science*, Vols. NS-22, pp. 135-139, 1975.
- [112] R. J. Cooper, A. J. Boston, H. C. Boston, J. R. Cresswell, A. N. Grint, L. J. Harkness, P. J. Nolan, D. C. Oxley, D. P. Scraggs, I. Lazarus, J. Simpson and J. Dobson, "Charge collection performance of a segmented planar high-purity germanium detector," *Nuclear Instruments and Methods in Physics Research A*, vol. 595, pp. 401-409, 2008.
- [113] P. A. Tove, "The role of contacts to nuclear radiation detectors," *Nuclear Instruments and Methods*, vol. 133, pp. 445-452, 1976.
- [114] C. V. Bocciarelli, "Properties of metal to germanium contacts," *Physica*, vol. XX, no. 11, pp. 1020-1025, 1954.
- [115] A. Dimoulas, P. Tsipas and A. Sotiropoulos, "Fermi-level pinning and charge neutrality level in germanium," *Applied Physics Letters*, vol. 89, pp. 252110-, 2006.
- [116] J.-R. Wu et al., "Impact of fluorine treatment on Fermi level depinning for metal/germanium Schottky junctions," *Applied Physics Letters*, vol. 99, p. 253504, 2011.
- [117] Y. Zhou, M. Ogawa, X. Han and K. L. Wang, "Alleviation of Fermi-level pinning effect on metal/germanium interface by insertion of an ultrathin aluminum oxide," *Applied Physics Letters*, vol. 93, p. 202105, 2008.
- [118] E. L. Hull, R. H. Pehl, J. R. Lathrop and B. E. Suttle, "Yttrium hole-barrier contacts for germanium semiconductor detectors," *Nuclear Instruments and Methods in Physics Research A*, vol. 626, pp. 39-42, 2011.
- [119] G. Riepe and D. Protic, "High-purity germanium detectors with both contacts made by ion-implantation," *Nuclear Instruments and Methods*, vol. 165, pp. 31-34, 1979.
- [120] J. D. Joannopoulos and G. Lucovsky, eds., *The Physics of Hydrogenated Amorphous Silicon II*, Berlin: Springer-Verlag, 1984.
- [121] C. J. Fang, K. J. Gruntz, L. Ley and M. Cardona, "The hydrogen content of a-Ge:H and a-

- Si:H as determined by IR spectroscopy, gas evolution and nuclear reaction techniques," *Journal of Non-Crystalline Solids*, vol. 35, pp. 255-260, 1980.
- [122] F. Scholze and G. Ulm, "Characterization of a windowless Si(Li) detector in the photon energy range 0.1-5 keV," *Nuclear Instruments and Methods in Physics Research A*, vol. 339, pp. 49-54, 1994.
- [123] M. J. Berger, J. S. Coursey, M. A. Zucker and J. Chang, "Stopping-Power and Range Tables for Electrons, Protons, and Helium Ions," [Online]. Available: [www.nist.gov/pml/data/star/](http://www.nist.gov/pml/data/star/).
- [124] M. W. Bautz and J. A. Nousek, "Science Instrument (SI) Calibration Report for the AXAF CCD Imaging Spectrometer (ACIS)," 1999. [Online]. Available: [www2.astro.psu.edu/xray/docs/cal\\_report/cal\\_report.html](http://www2.astro.psu.edu/xray/docs/cal_report/cal_report.html).
- [125] V. T. Jordanov, G. F. Knoll, A. C. Huber and J. A. Pantazis, "Digital techniques for real-time pulse shaping in radiation measurements," *Nuclear Instruments and Methods in Physics Research A*, vol. 353, pp. 261-264, 1994.
- [126] A. Lowell et al., "Prospects for the 2014/2015 Nuclear Compton Telescope Balloon Campaign," *SPIE Proceedings*, vol. 8443, 2012.
- [127] M. H. Brodsky, M. Cardona and J. J. Cuomo, "Infrared and Raman spectra of the silicon-hydrogen bonds in amorphous silicon prepared by glow discharge and sputtering," *Physical Review B*, vol. 16, no. 8, pp. 3556-3571, 1977.
- [128] I. Chambouleyron and D. Comedi, "Amorphous silicon and germanium," in *Encyclopedia of Materials: Science and Technology*, Oxford, Elsevier Science, 2001, pp. 289-299.
- [129] L. Fabris, N. W. Madden and H. Yaver, "A fast, compact solution for low noise charge preamplifiers," *Nuclear Instruments and Methods in Physics Research A*, vol. 424, pp. 545-551, 1999.
- [130] Z. He, W. Li, G. F. Knoll, D. K. Wehe, J. Berry and C. M. Stahle, "3-D position sensitive CdZnTe gamma-ray spectrometers," *Nuclear Instruments and Methods in Physics Research A*, vol. 422, pp. 173-178, 1999.
- [131] H. L. Malm and R. J. Dinger, "Charge collection in surface channels on high-purity Ge detectors," *IEEE Transactions on Nuclear Science*, Vols. NS-23, no. 1, pp. 75-80, 1976.

## **Appendices**

## Appendix A Detector Fabrication

This appendix describes in greater detail the detector fabrication process used for the work in this dissertation.

### A.1 Crystal Preparation

Since HPGe crystals are no longer grown at LBNL, the crystal material is normally purchased from Ortec [58] as a slice taken from a boule with no additional carving. Figure A.1 shows an example of the slice as received. The sides have some smooth ripples due to variation in the crystal growth process and the top and bottom have a rough texture from the wire saw cutting performed by Ortec.

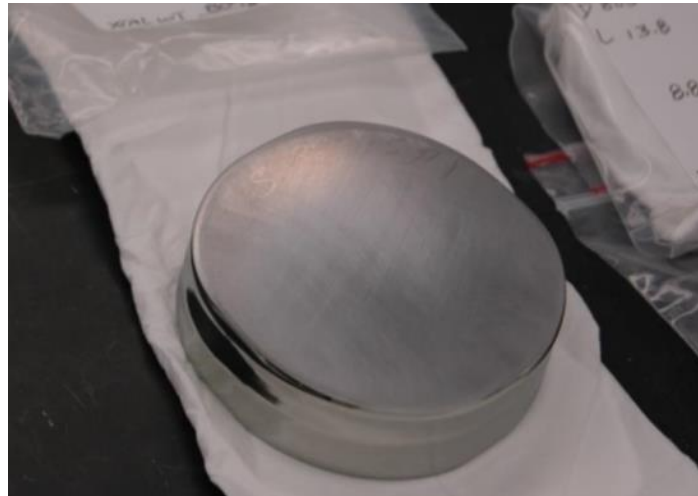


**Figure A.1. Photograph of a slice of high-purity germanium crystal purchased from Ortec.**

Table A.1 shows the specifications provided when requesting crystal slices. The geometry demands of a particular application change the diameter and thickness, so typical values are provided. The diameter is limited by the crystal growth process and the thickness is limited by net ionized impurity concentration, which acts with the thickness to determine full depletion voltage. The impurity concentration is given as a target range due to the difficulty of verifying this value on the manufacturing side.

**Table A.1. Crystal slice specifications.**

Parameter	Value Specified
Diameter	100 mm or as needed
Thickness	10-15 mm as needed
Finish	As cut; no additional grinding or polishing
Impurity concentration	$1-7 \times 10^9 \text{ cm}^{-3}$
Type	p-type
Crystallographic orientation	(100)
Etch pit density	$\sim 8000 \text{ cm}^{-2}$

P-type crystals are normally requested because the current fabrication process is more highly developed for p-type crystals than n-type crystals. The (100) crystal orientation has the highest electron drift velocity in germanium [44], so slices are specified so that a planar detector fabricated from the slice will have the best electron charge collection. The etch pit density is a measure of the dislocation density in the crystal. Too many dislocations result in excessive charge trapping in the detector, while too few dislocations gives difficulty in obtaining low intrinsic charge carrier concentration since dislocations serve as a getter for holes in germanium.

The crystal slice is next cut to the desired geometry. The slice is affixed to a graphite plate using wax and the graphite is stuck to a magnetic stainless steel plate. Care must be taken during this step to avoid excessive heating of the crystal when applying the molten wax. The assembly is held in place using a magnetic chuck. A thin-profile diamond grit wheel is used to very slowly slice the desired outside dimensions to form a rectangular prism. Figure A.2 shows a crystal slice being cut into multiple smaller samples. Then a rounded wheel 1.5 mm in width is used to grind channels through the crystal to separate the handles from the active crystal volume. A flat-edge grinding wheel is then used to grind the handles down to the desired thickness.

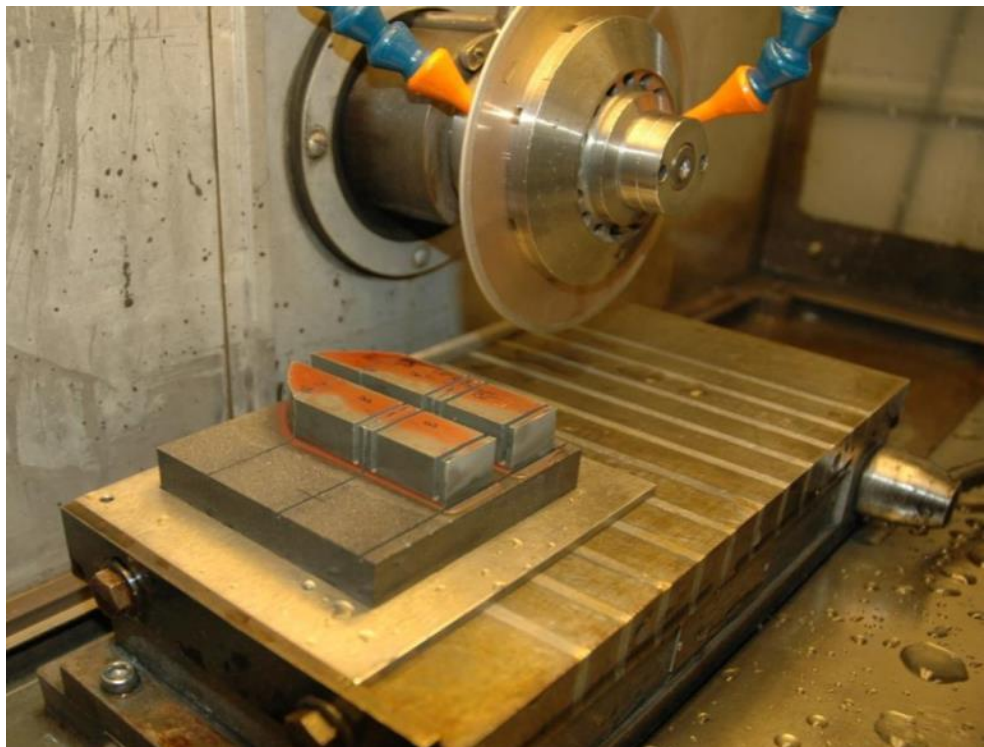


**Figure A.2. Photograph of grinding the crystal slice to the desired dimensions. A crystal slice is normally cut into multiple smaller samples.**

The grinding process can leave relatively large defects on the crystal surface, such as cracks, chips, or tool marks. Figure A.3. shows an example of the side surface left after cutting and grinding. The tool marks typically take an inordinate amount of chemical etching to remove, so lapping is preferable. Near the center of the photograph is a chip defect caused by the diamond saw. These are usually quite obvious as a shiny area is visible where a piece of the crystal

cleaved from the sample. This defect is not harmful by itself, but it often indicates the presence of cracks that go deeper into the crystal that will only become visible after a polish etch. These cracks can contribute to excessive leakage current.

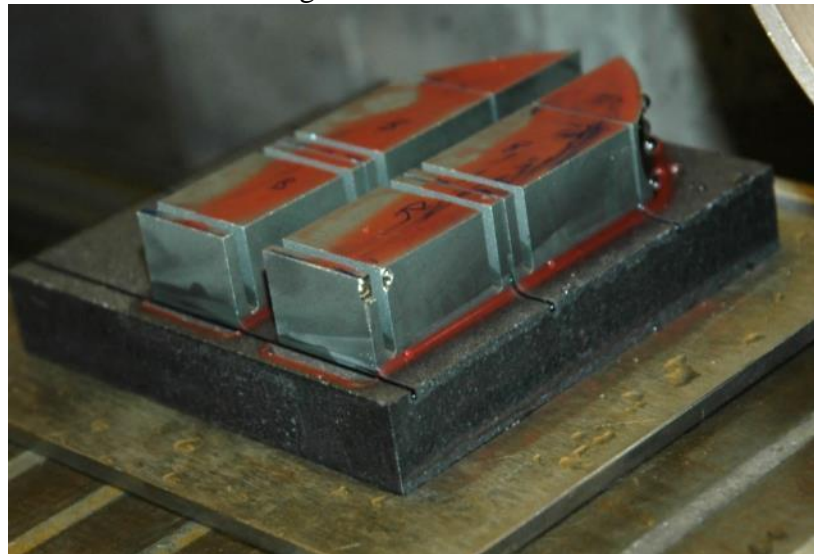


**Figure A.3.** Photograph of crystals partially through the cutting procedure. A large chip defect can be seen on one of the samples near the center of the photograph. Other side surfaces show the typical texture with saw marks.

These large defects are removed by lapping with 600 grit SiC followed by 1900 grit  $\text{Al}_2\text{O}_3$ . This leaves a matte texture that is uniform on a large scale and a roughness at the  $\sim 10 \mu\text{m}$  scale, seen in Figure A.4.

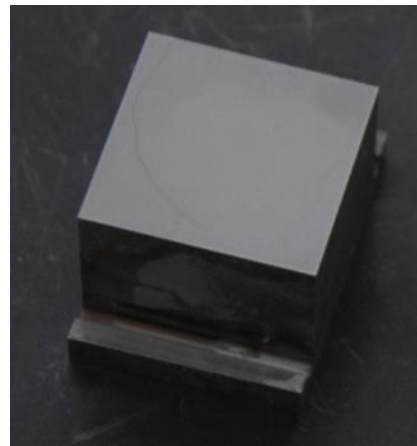


**Figure A.4.** Photograph of a crystal lapped with 1900 grit  $\text{Al}_2\text{O}_3$ . The top surface shows the matte texture left by lapping, while the sides, inaccessible to lapping, have the surface left by crystal cutting and some residual wax.

The sides with handles, not being totally flat, are not accessible to lapping. These retain the tool marks and wax from mounting to the graphite plate. The wax is removed with trichloroethylene (TCE) as the wax is resistant to the acid etch used in the next step. The lapped surface has a surface roughness small enough to be efficiently etched using acids. A 4:1  $\text{HNO}_3:\text{HF}$  mixture

has a high etch rate for germanium. The crystal is submerged in ~200 mL 4:1 HNO<sub>3</sub>:HF and continuously moved around by rotating the container for 2-3 minutes.

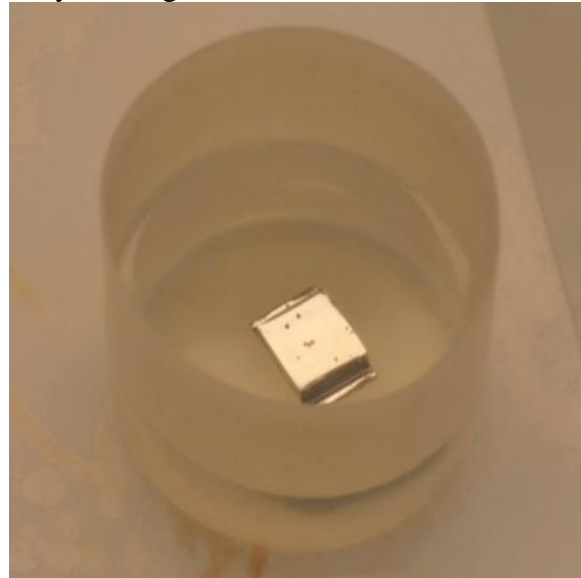


**Figure A.5. Photograph of germanium crystal in 4:1 HNO<sub>3</sub>:HF mixture.**

Figure A.5. shows a crystal in the 4:1 mixture just after being lowered into the liquid. A few bubbles appear, but the mixture becomes cloudy with a golden color after about a minute. After another minute, the liquid becomes quite warm and exudes brown vapor. During this step, it is important to keep the crystal from resting on one surface for too long to avoid uneven etching. Care must also be taken to avoid exposing the crystal to air during mid-etch as this leaves a rough surface. The etch is rapidly quenched by moving immediately to de-ionized water. The resulting surface is typically very smooth and shiny, with only mild and rounded wavy texture. Figure A.6. shows an example of a freshly polish-etched crystal. An absence of sharp features is a good indicator the crystal is ready for detector fabrication.

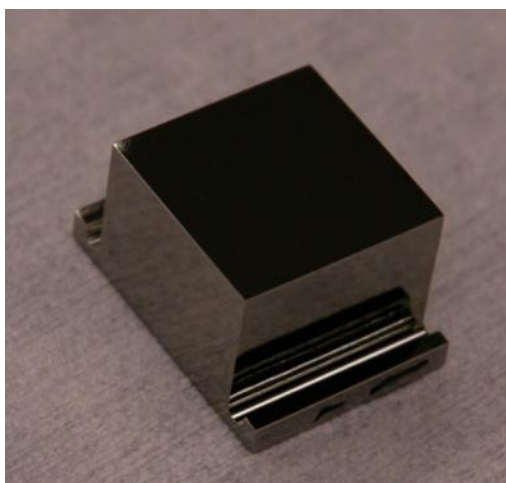


**Figure A.6. Photograph of a chemically polished germanium crystal.**

Crystal samples are re-processed several times and must undergo a cleanup step before the next fabrication. The first cleanup step is removal of aluminum by soaking in 1% HF for a few minutes. The crystal is turned over at least once so the surface on which the crystal rests is exposed to ample acid for Al removal. HF removes germanium oxides but does not etch crystalline germanium, so exposure to air during this step is acceptable. Dunking is common to remove bubbles that cling to the surface and may prevent etching under them. This is followed by a short (30-60 seconds) etch in 4:1  $\text{HNO}_3$ :HF with constant agitation. The crystal is held with Teflon tweezers and moved in a circular motion in the acid solution, then quenched in de-ionized water. This removes a-Ge from the surface and provides a smooth, clean surface on which to begin a new fabrication cycle.

Finally, before depositing layers on a crystal, a cleaning etch is done immediately prior to loading in the sputterer. This is a 30-60 second etch essential for obtaining a proper surface. The crystal is gripped using Teflon tweezers contacting the handles. The surface must be dry before etching and lowered rapidly into the acid solution. During etching, the crystal must be constantly in motion, quickly enough so surfaces are constantly exposed to fresh acid, but not so quickly that excessive turbulence results. It is important not to allow the crystal to emerge from the acid or contact the container as these can leave a rough surface. The crystal is then immediately dunked into de-ionized water, rinsed thoroughly, and rinsed in methanol. The methanol is blown away using dry nitrogen. Timing is critical in these steps. Too long a wait before the methanol rinse can leave water marks/contaminants on the surface, and taking too long to blow the methanol away leaves streaks on the side where contaminants remain after the alcohol evaporated away. The crystal is then inspected and loaded into the sputterer as quickly as possible. After this cleaning etch, care must be taken to avoid any contact with the sensitive detector surface. For the remainder of the fabrication process, only the handles should come into contact with any other object.

## A.2 Sputtering

The most sensitive stage in detector fabrication is formation of the contacts. The focus of this study is amorphous semiconductor contacts formed by RF diode sputtering. A nice feature of this fabrication process is the simplicity of coating the entire crystal with amorphous semiconductor material and then simply defining electrodes with any metal as desired. However, amorphous semiconductors differ widely in their properties based on sputter pressure [102], hydrogen content [127], and method of deposition [128].

After the surface cleaning etch described in the previous section, the crystal is placed on a small stand, shown in Figure A.7. . The crystal rests on two indium strips that contact the bottom of the wings. The stand provides a method of transferring the crystal to and from the sputterer without touching the crystal. The bottom surface is kept from touching the stand by the indium strips, but the distance is minimized to prevent material deposition on this bottom surface. The first sputter sequence is intended to deposit the top contact and add passivation to the side surfaces. Especially critical are the handle-free sides where there is no undepleted material to block surface current. Side surfaces with incomplete coating show a propensity for electrical breakdown, so it is important to ensure complete coverage of the entire surface. Scattering in the sputter gas causes atoms to be deposited from all directions, so the bottom edge

of the side will see a lower deposition rate as half its field of view is filled with the metal surface on which it rests. For this reason, it is important the stand has a vertical wall as close to the side surface as possible to allow best coating near the bottom edge. The effect is especially important for higher sputter pressure due to additional scattering. The crystal geometry with a handle around the entire perimeter does not have completely flat sides, so the crystal rests on a square of indium on a larger plate, seen in Figure A.8.

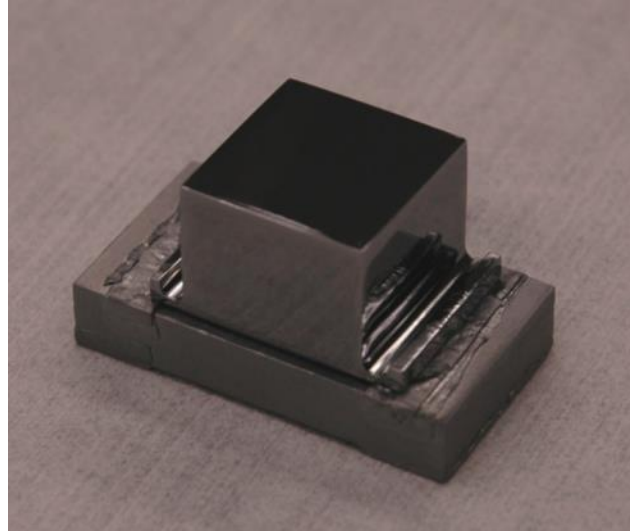


**Figure A.7.** Photograph of germanium crystal on a stand for the first sputtering sequence. The geometry allows maximum side coating by keeping the non-winged sides well away from obstructions.

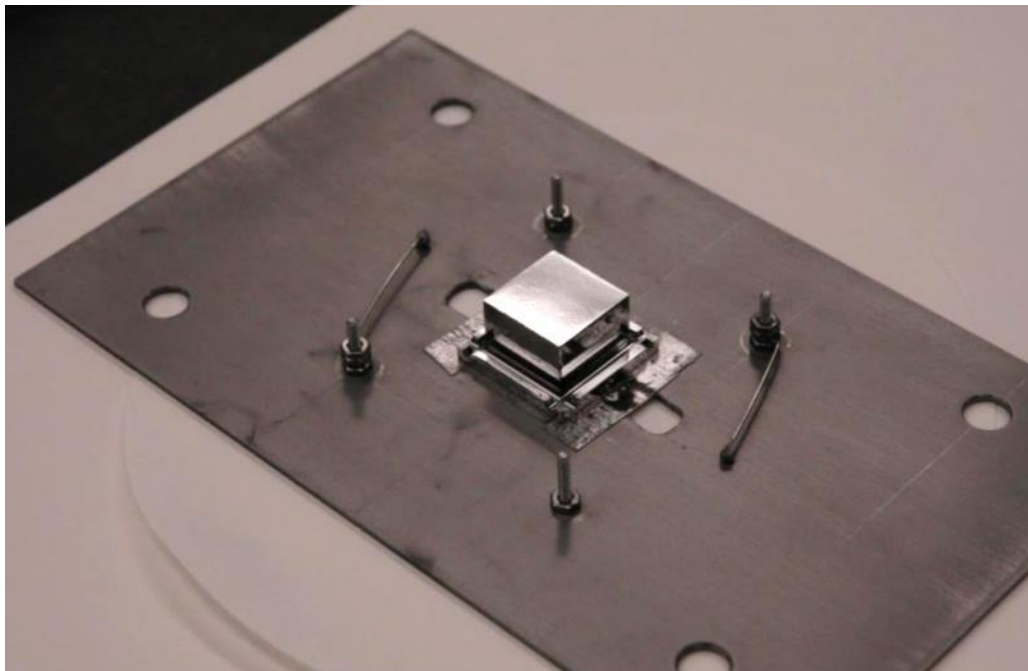


**Figure A.8.** Photograph of full-wing crystal geometry sputter stand. The crystal can rest on a flat surface as there are no critical non-winged edges where incomplete coating is an issue. The bottom surface rests on a square of indium strips with the center cut out so the active surface area makes no contact.

The stand is moved to a rotation stage in the MRC sputtering system, shown in Figure A.9. The stage is fixed under the Ge target and is rotated during deposition to allow a-Ge deposition on the top and sides of the crystal. For most fabrication runs, every effort is made to keep this sputtering step the same as a process control measure. The sample gets quite warm during deposition due to bombardment by electrons, so the deposition is done in pulsed sequences. Each sequence consists of 2 minutes deposition with plasma ignited followed by 5 minutes with no plasma to allow cooling. After the deposition is completed, the crystal is allowed to cool in vacuum for a time before the chamber is vented.



**Figure A.9.** Photograph of the inside of the main chamber of the MRC sputtering system. A crystal can be seen upper center on the rotation stage under the Ge target.

After deposition, the crystal surface typically has the same texture but a slightly darker color from the a-Ge. Figure A.10. shows a HPGe crystal before and after sputtering a-Ge on the top and sides. Next, the bottom surface is coated with an amorphous semiconductor layer. The HPGe crystal is flipped over and suspended by its handles on a mount. Great care must be taken to allow no contact to the bottom surface. An aluminum foil shield is placed around the crystal to prevent partial side coating, which has been associated with surface electrical breakdown. The assembly is placed on the cooled stage of the sputtering system and again pumped to  $10^{-6}$  Torr. A layer of a-Ge or a-Si is deposited with the desired gas pressure, gas composition, and thickness. Figure A.11. shows a crystal in the mount immediately after a-Si has been deposited

on the bottom surface. While a-Ge on the bottom surface has the similar dark color of a-Ge on the top and sides, a-Si has a wide variety of vivid colors, depending on the film thickness.

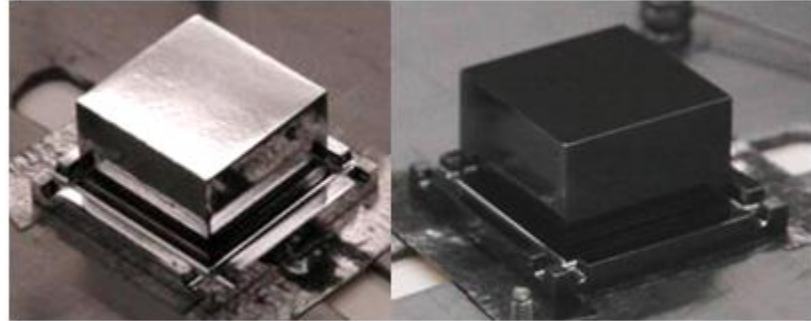


**Figure A.10.** Photograph of HPGe crystal before and after sputtering a-Ge on the top and sides. It gains a darker color but retains the original surface texture.

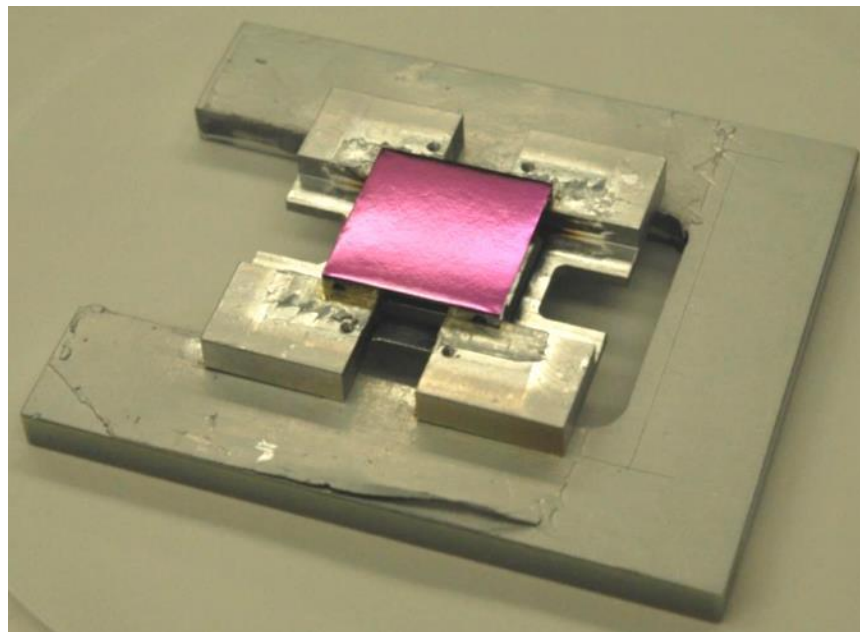


**Figure A.11.** Photograph of the bottom surface of HPGe crystal coated with a-Si.

With the sputtering sequence completed, the crystal is essentially a working detector. Only the electrodes need to be defined, usually by depositing metal in the desired pattern.

### A.3 Metal Evaporation

In order to apply bias to the detector and sense drifting charge carriers, a low-resistivity metal layer is needed. The detector is normally connected to the outside world using wires, but strapping a wire to the amorphous layer would not hold the entire surface at the appropriate bias because the amorphous layer has high resistance. Metal electrodes also provide a large area for electric field line termination, meaning more collection area for sensing moving charge in the crystal. Any metal can be used to define the electrodes. For this work, aluminum was used due to the low cost of the metal and excellent adhesion to germanium and amorphous semiconductor

surfaces. It is convenient to evaporate because Al has a relatively low melting point and the evaporation process does not significantly heat the detector, by contrast to sputtering. Aluminum is evaporated from tungsten filaments with Al pre-melted onto loops, seen in Figure A.12. . The crystal is next placed on a stand with two posts that allow alignment of the crystal to a shadow mask. For a planar guard ring detector, the entire bottom surface is covered with about 50 nm of aluminum. If the crystal has handles around the perimeter, no mask is used as the handles prevent Al deposition on the crystal sides. If the crystal has the two-handle geometry, a perimeter shadow mask is used to confine the Al deposition to a rectangle on the bottom surface of the crystal. For the top surface of the guard ring device, a shadow mask defines the outside of the guard ring and a metal ring defines the gap between the center contact and guard ring. Figure A.13. shows a detector ready for the top Al deposition.



**Figure A.12.** Photograph of tungsten filaments pre-loaded with aluminum.

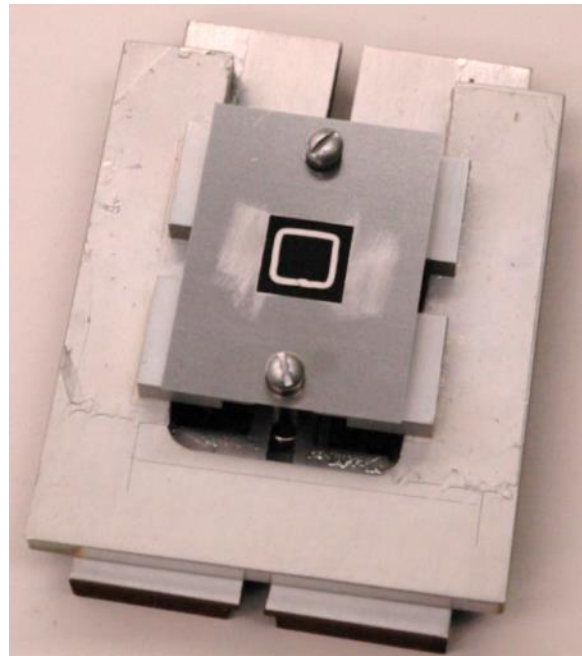


**Figure A.13.** Photograph of a detector ready for aluminum deposition of the top center contact and guard ring structure. A shadow mask defines the outside of the guard ring and a metal ring defines the gap between the electrodes.

Aluminum evaporation is conducted in a CHA AutoTech II evaporation system. The detector is loaded with appropriate masking under the filaments, seen in Figure A.14. The chamber is evacuated to  $10^{-7}$  Torr before deposition and usually remains at or below  $10^{-6}$  Torr during the entire evaporation process. For these detectors, a thickness of 50-100 nm is sufficient to give an even coating with high certainty of a low-resistance path to all parts of the electrode.

The major drawback to this method of Al deposition stems from the fact that Al has a relatively low melting point and becomes mostly liquid at the temperatures used for evaporation. The liquid adheres to the filament well enough, but occasionally hotspots develop and a bubble forms in the liquid. If this bubble pops, it can send small droplets of molten aluminum onto the detector surface. Since there is little heat loss in a vacuum, these droplets are still quite hot when they reach the crystal surface and cause localized damage due to thermal shock. Typically, even a small Al drop on an electrode means the electrode cannot sustain significant electric field. Figure A.15. shows an example of a sizable Al drop on an aluminized detector surface. A mark of this size leaves significant damage and necessitates a restart of the fabrication process, including lapping of the crystal. To reduce the occurrence of Al droplets landing on the detector, a mesh screen is placed between the filaments and detector to block objects of significant size. The deposition rate is reduced by about 50% when the screen is used.

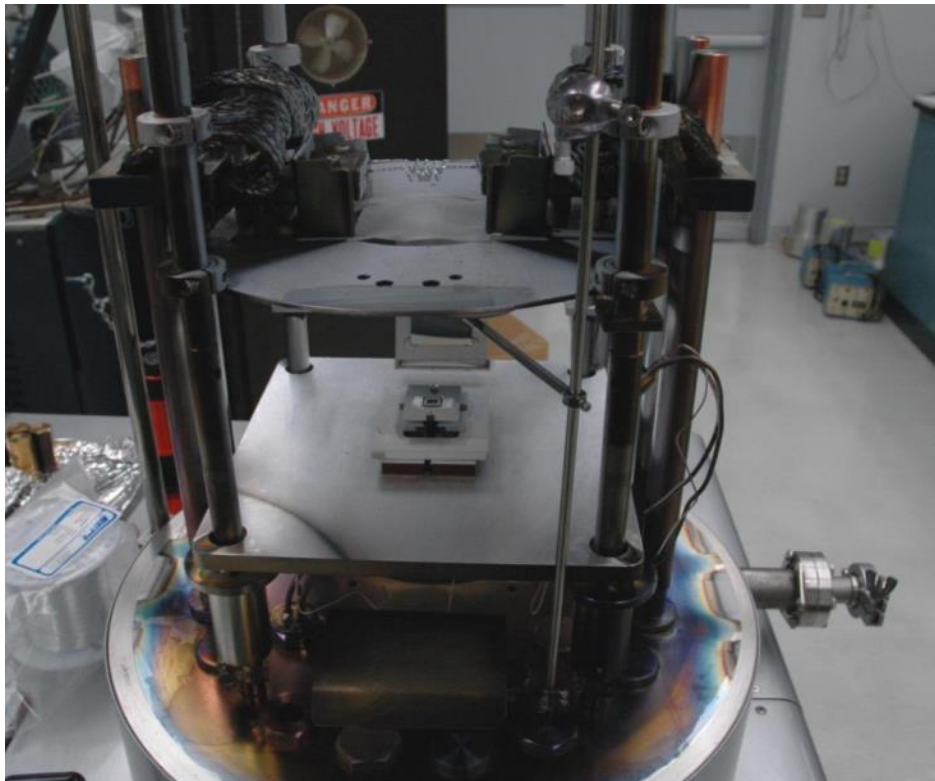


**Figure A.14. Photograph of a detector loaded in the evaporator, ready for aluminum evaporation.**

For the strip detectors used in the work described in Chapter 7, a series of shadow masks is used to define the guard ring and strip electrodes. The electrode structure is defined by two masks and an Al deposition exactly as described above. The wire bond sites require at least 500

nm Al to form a reliable bond, so a third deposition is conducted where only a small area of the mask is open and the screen is removed to increase the Al deposition rate.

Alternatively, detectors can have electrodes defined by photolithography. In this case, masks are placed around the perimeter of the detector to keep Al from depositing on the sides, but the contact area is open. An Al deposition of 500-700 nm is done with the screen in place.

Guard ring planar detectors are complete after the Al evaporation step and are loaded in a cryostat for testing. The strip detectors require wire bonding to form the electrical connections before they are loaded in a cryostat for testing.

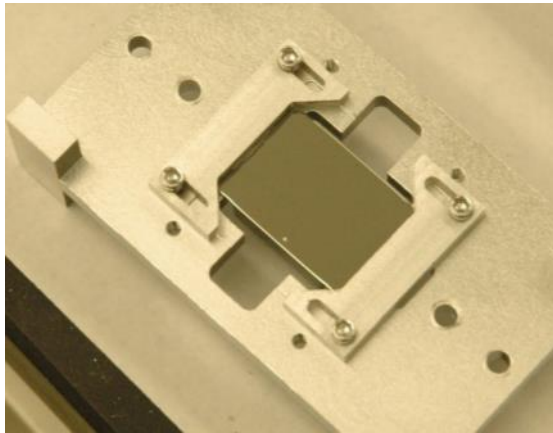


**Figure A.15. Photograph of aluminized detector surface showing a large Al drop. A drop of this size causes significant damage and the electrode will not sustain an electric field.**

## A.4 Photolithography

The electrode pattern can be formed by photolithography rather than shadow masks. In this process, the electrode structures do not need self-supporting mask structures and very fine features can be formed. This section describes the details of the process used for the DSSD fabricated using photolithography.

A positive photoresist compound S1818 is applied to the top and bottom by spin-coating, where the liquid compound is added and the detector spins at high speed to spread the liquid evenly. A detector immediately before and after the spin-coating process is shown in Figure A.16. The top and bottom faces are then exposed to ultra-violet (UV) light for 30 seconds through a mask pattern. The masks in this case are printed transparency films with an opaque pattern that exactly matches the metal mask pattern used for other detectors. The crystal is then rinsed in MF-24A developer, which selectively removes the S1818 area that was exposed to UV light, while leaving the un-exposed regions intact. Figure A.17 shows a crystal with the developed photoresist pattern. The red regions still have photoresist, while the silver region near the center has exposed Al that can be etched away. An etch in HF removes the exposed Al, and the remaining photoresist is removed by an acetone rinse.

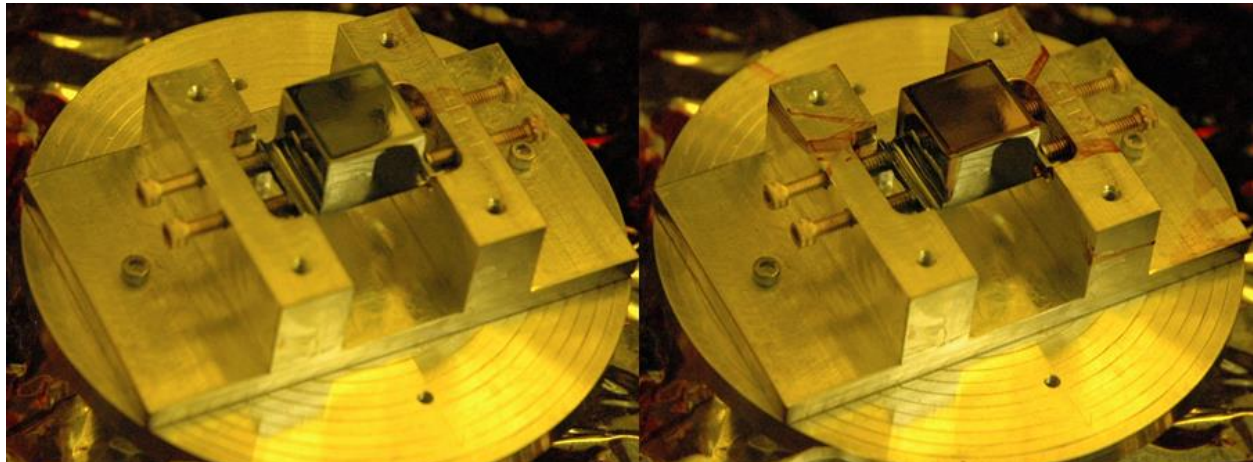


Figure A.16. Photographs of a detector before (left panel) and after (right panel) applying S1818 photoresist by spin-coating.

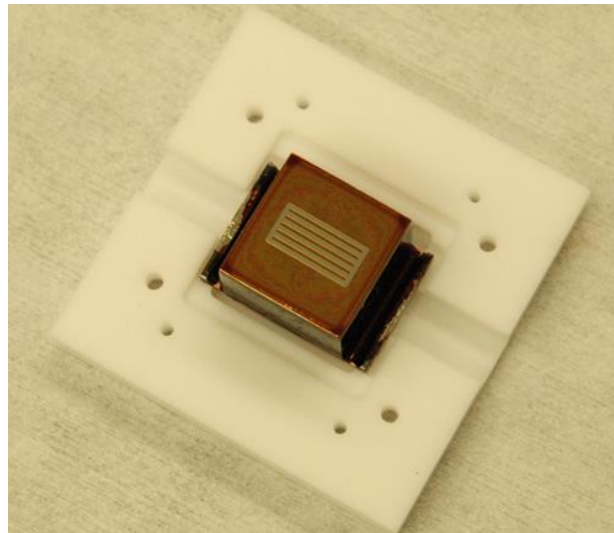
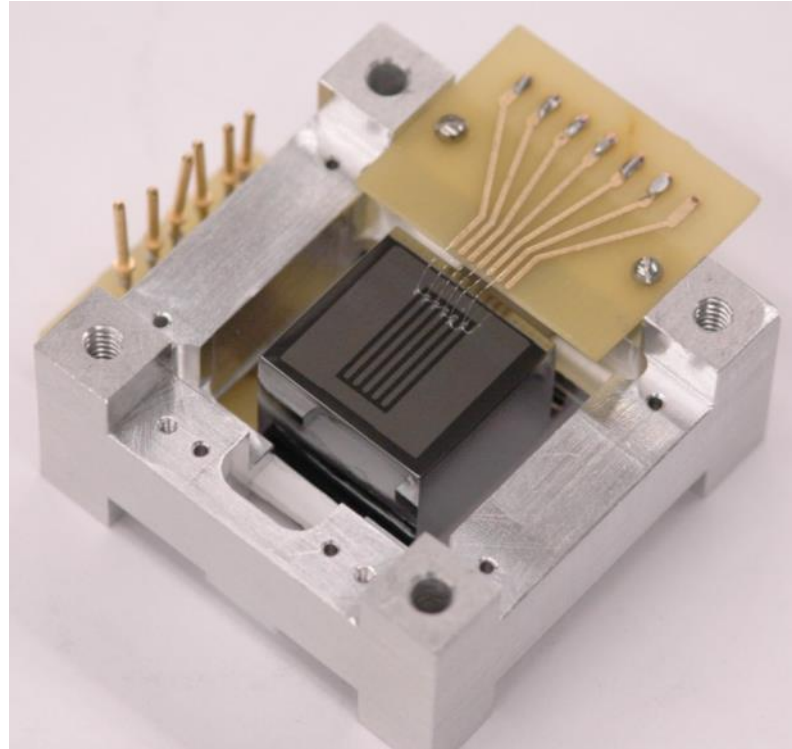


Figure A.17. Crystal with developed photoresist mask to form the strip electrode pattern.

## A.5 Wire Bonding

The strip detectors had electrode connections formed by wire bonding. For strip detectors, the electrodes are sometimes too small to easily make electrical contact using spring clips or pogo-pins. Wire bonding is a suitable method for connecting small electrodes to a nearby circuit board by ultrasonic excitation. A tungsten tip is used to press pure aluminum wire of 2 mil thickness onto a detector electrode. When the tungsten tool is excited with ultrasonic power while pressing down on the wire, the Al wire and Al electrode stick together with at least a few grams of force. The wire is carried to the nearby circuit board and the process is repeated on the gold trace to complete the connection. Electrical connections can be soldered at the other end of the breakout board. Figure A.18 shows the mounted detector in the center with wire bonds attached to each of five strips and one to the guard ring. The can be seen arcing toward the tan-colored breakout board at upper right.



**Figure A.18. Photograph of a strip detector test device in its mount with wire-bonded electrodes.**

The detector electrodes in the area for wire bonding require at least 500 nm for reliable bonds to form. Bond force is minimized to avoid damage to the germanium surface and pure Al provides a softer bonding surface. On the board, wire bondable soft gold provides the necessary soft bonding surface.

## Appendix B Current-Voltage Testing

The method used for extracting barrier height and pre-factor of the diode equation is a current-voltage characteristic. This method also gives hints of other effects such as surface channels or electrical breakdown characteristics. Even tests like strip detector charge collection experiments require verification that the detector has low leakage at high voltage bias. This section describes the method by which leakage current data are obtained.

### B.1 Single-Detector Cryostat

HPGe detectors must be operated at cryogenic temperature. Thermal insulation between the cold detector housing and the outside world is provided by a vacuum inside a cryostat. Cooling is accomplished in this work by liquid nitrogen and electrical connections are provided by a wiring system to the detector mount location.

At the beginning of this work, a single-detector cryostat shown in Figure B.1 was available for current-voltage testing. Use of this cryostat was preferred because it is a simple testing system known to function properly. The small size makes for faster vacuum pumping and cooling to base temperature. The interior mounting structure is shown in Figure B.2.

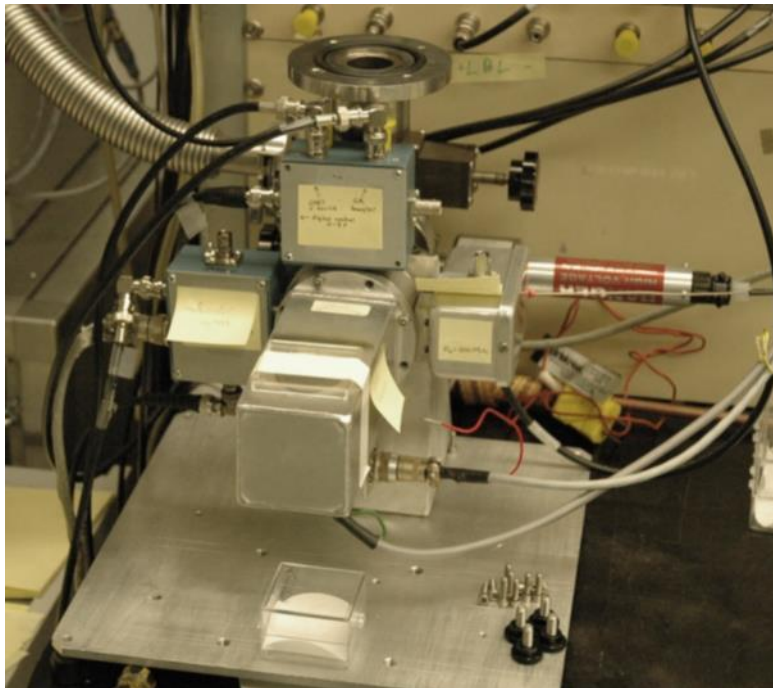
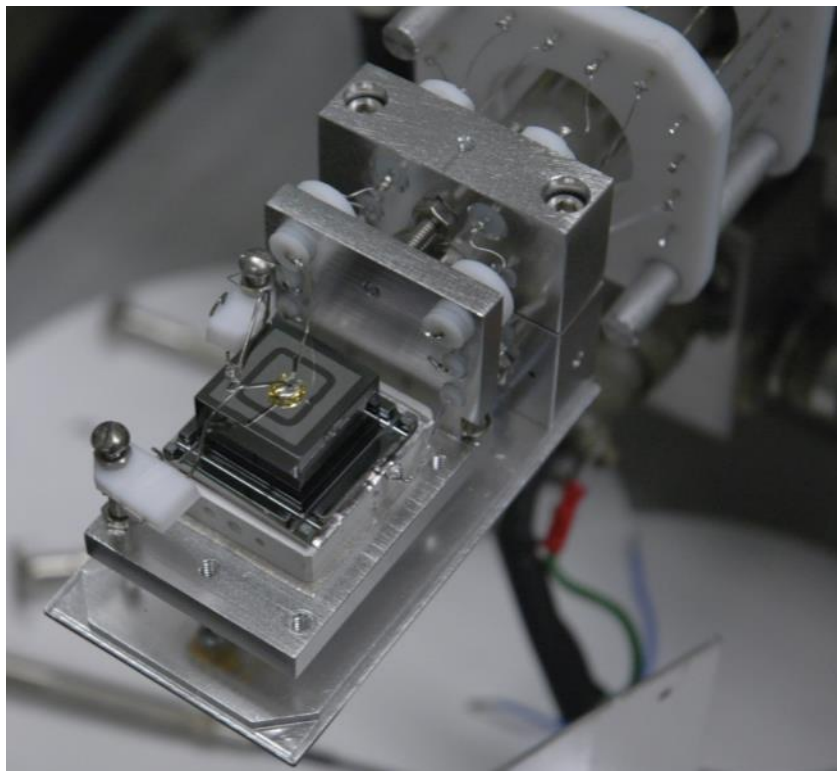


Figure B.1. Photograph of the single-detector variable-temperature cryostat for current-voltage testing.

The core of the cryostat is a horizontal tube (seen in upper right of Figure B.2) with a right-angle bend to provide a vertical opening (top of Figure B.1). A liquid nitrogen container is placed at the top of this opening so that the liquid nitrogen can fill the tube. Clamped to the horizontal portion of the tube is an aluminum structure (outer “L” shape in Figure B.2) that quickly cools to cryogenic temperature when the tube is filled. A cover can be attached to form

a complete enclosed box, called an infrared (IR) shield. Germanium is quite sensitive to IR radiation due to its low bandgap, which can generate significant current relative to the magnitude of leakage current that must be measured. Surrounding the detector with a light-tight, cold surface eliminates this problem. Another aluminum mount (smaller “L” in Figure B.2 lower left) is attached to the first aluminum structure by small stainless steel stand-offs so that a weak thermal connection exists. The thermal conductance can be adjusted by adding copper wires between the two stages of varying thickness and number. This is the variable-temperature stage on which the detector rests. This stage has a temperature sensor and a small heater so that the temperature of this stage can be uniformly elevated above 77 K. The base temperature is about 78.5 K, while the maximum is in excess of 170 K.



**Figure B.2. Photograph of the inside the small variable-temperature cryostat. This equipment is used for current-voltage testing.**

The detector needs a strong thermal connection to the mounting structure so that the temperatures of the sensor and detector are as close as possible. However, the detector is part of a circuit that must be held at a potential away from ground, so it must be electrically separated from the metal mounting structure. The detector rests on a stack of materials to fulfill these requirements. A plate of boron nitride is fastened to the variable-temperature stage with a sheet of indium between. The boron nitride is an excellent electrical insulator yet has high thermal conductivity. The indium sheet wedged between layers is a common practice when thermal conductance is needed because indium is a soft material and easily conforms to fill the small gaps between two nearly flat pieces. Atop the boron nitride is the high-voltage sheet, made of

copper so that it can be easily soldered to and still has good thermal conductivity. Another layer of indium is placed on top of the copper to provide a soft surface on which the germanium can rest. The detector is held down by two clips made of spring steel and having indium blob tips. These provide some downward pressure to hold the crystal in place and also provide an electrical connection to the two top electrodes.

Under normal operation, the cryostat is evacuated to the  $10^{-7}$  Torr range using a turbomolecular pump attached to the rear flange. If desired, the ion pump controller is activated, creating a brief surge in pressure as the ion pump starts. Both pumps are operated for about 20 minutes, then liquid nitrogen is added to fill the center tube. The pressure quickly drops as the interior components closely attached to the LN tube cool rapidly due to their small mass. The variable-temperature stage with the attached sensor cools more slowly due to the weak thermal connection. Figure B.3 tracks the temperature as a function of time during a cool from room temperature to base temperature. The detector reaches 80 K in about 2.5 hours. If the turbopump is needed elsewhere, the rear valve can be closed and the cryostat operated with only the ion pump.

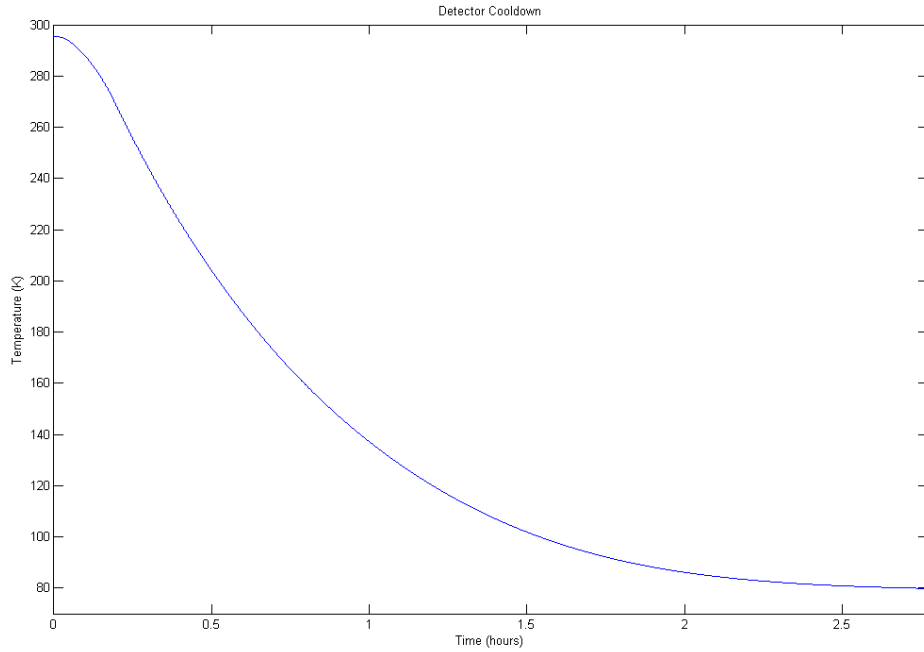


**Figure B.3. Cooldown curve for the variable-temperature stage of the single-detector cryostat.**

When testing is complete, the dewar is removed and the liquid nitrogen remaining in the cryostat tube is blown out using compressed air. The detector is brought to room temperature by slowly heating the variable-temperature stage and continuously flowing air into the tube. This usually takes about 3 hours, during which time gases evaporate from warming surfaces and the cryostat must be actively pumped using a turbopump.

Care must be taken to avoid direct contact between any cold components and the warm outside shell. Such a situation usually becomes obvious when the surrounding area develops ice

on the outside. Steps must also be taken to avoid a rise in pressure, which circumvents the vacuum insulation and may result in the cryostat icing over. Possible causes are turbopump failure (when no shutoff valve is present), vacuum leaks, or opening a valve at the wrong time.

The cryostat interior is electrically very simple. Several wires provide a current path from the outside world directly to the variable-temperature stage on which the detector rests, each passing through a vacuum feed-through and suspended by insulators at several points to prevent contact to grounded surfaces. At some point along its path, each wire must have a stainless steel section to prevent thermal conduction through the wire from the outside to the cold stage. Due to the low current being measured in a detector, it is important that all parts of the measurement circuit have high-quality insulators between the wire and ground. Selection of the feed-through is important as some vacuum feed-throughs use low-quality insulators that allow current flow to ground at about the same level that is being measured. The amount of current flow can change with ambient conditions, especially relative humidity. Inside the cryostat, PTFE insulators are normally used because this material is machineable, high-resistivity, and vacuum-safe. The wires must pass through the IR shield without allowing light through. PTFE screws with a hole drilled through the center are normally used due to convenience and the quality of the material.

## B.2 Multi-Detector Cryostat

A large number of detectors were fabricated, all of which needed at least a couple of days for testing for each temperature cycle. For several temperature cycling measurements, the whole testing process can take months. For this reason it was thought best to design a second cryostat to facilitate testing space for multiple additional detectors. This cryostat was primarily used for extended temperature cycling tests after a detector had proven to function normally in the smaller cryostat.

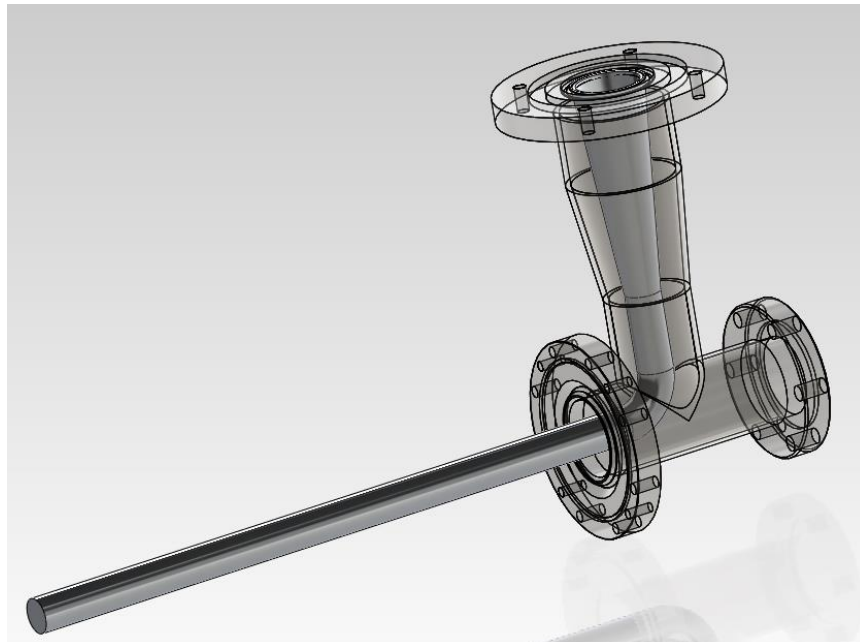


**Figure B.4.** CAD model of the multi-detector cryostat coldfinger. The flanged tee is made transparent to show the LN tube inside.

The cryostat was designed and built from scratch around one existing piece. The coldfinger is a relatively delicate and complicated piece with several vacuum seals and weld joints. It must withstand a very large number of temperature cycles between cryogenic and room temperature and tolerate some flex due to weight on the LN tube itself. Figure B.4 shows a schematic of the coldfinger assembly. A stainless steel flanged tee creates a junction for the vacuum pump (at right), the cryostat (at left), and the liquid nitrogen dewar (top). The interior of this tee will be part of the cryostat vacuum, so all joints must be leak-free. A stainless steel tube protrudes from the top flange down into the tee, makes a 90-degree bend, and extends into the cryostat volume. This tube is filled with liquid nitrogen during operation to provide cooling directly to the detector cold stage. This coldfinger assembly has a longer than normal tube, making it ideal for a large cryostat. The assembly was one of dozens manufactured in decades past for cryostats that have since been disassembled. It was convenient to begin with an already existing complicated part, and duplicating the coldfinger assembly would be quite costly today.

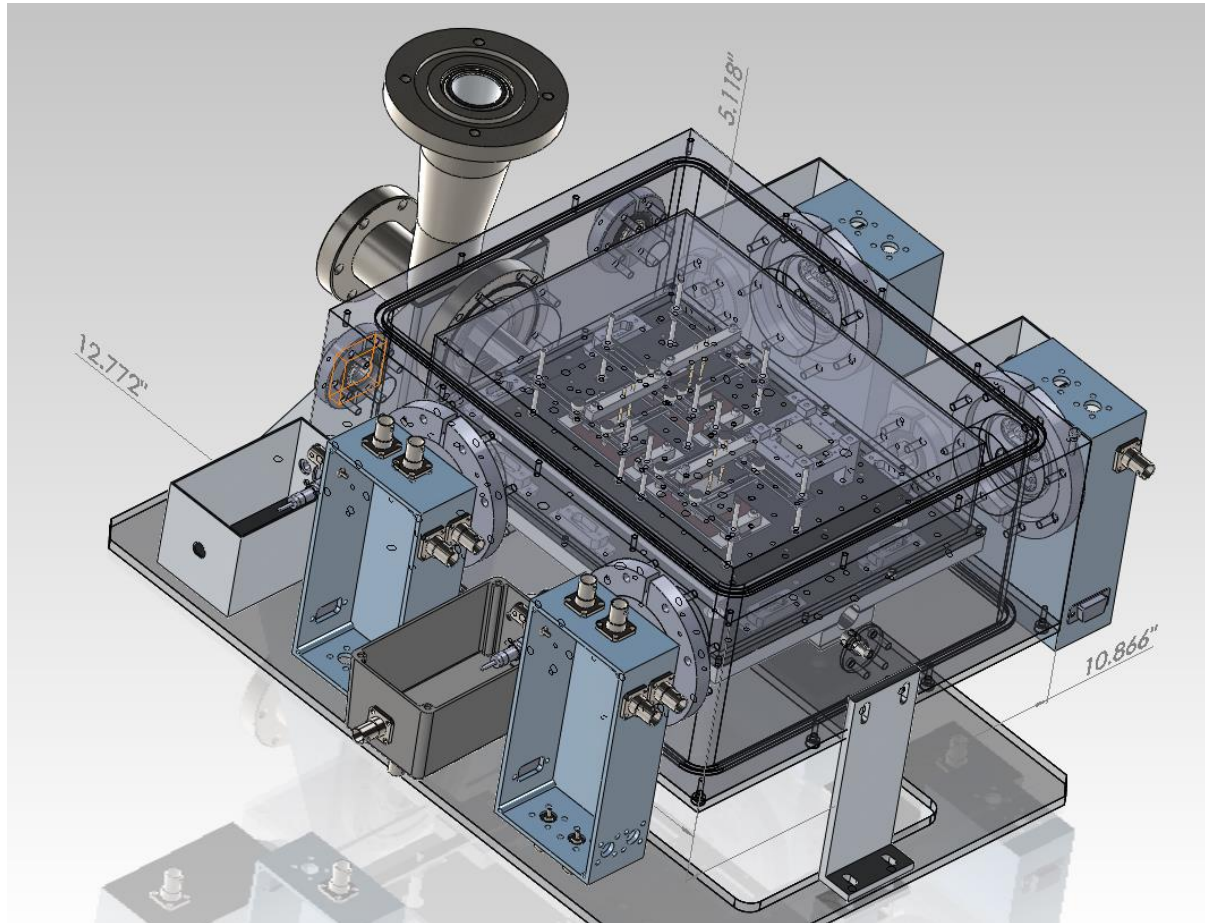


**Figure B.5. CAD model of the multi-detector cryostat in the final (as used) configuration. Outer dimensions are shown for scale. Example detectors with various mounting schemes are shown mounted inside.**

Figure B.5 shows a CAD model of the multi-detector cryostat as it was used for testing. The coldfinger assembly can be seen at the upper left. The cryostat was designed with a large

chamber surrounding the coldfinger with several Accu-Glass electrical feedthroughs to provide maximum versatility, using common D-type pin configurations. High voltage and thermometry feedthroughs were separate. A large cold plate was mounted directly to the coldfinger and supported at the far end to alleviate strain on the weld joints. Since it was supported by the cryostat wall, which sits at room temperature, it was necessary to create a large thermal break using polycarbonate and stainless steel connecting pieces, ultimately supported by nylon set screws. A thin aluminum infrared shield (shown partially transparent in Figure B.5) bolts to the cold plate and forms a box over the cold plate area.

The variable-temperature stage is another aluminum plate that is supported slightly above the large cold plate. It is supported by a thin stainless steel structure that attaches to the cryostat wall on either side and passes through holes in the cold plate. Plastic spacers in the support structure provide additional thermal resistance to prevent the plate from heating at the support points. Cooling power is provided to the variable-temperature stage by several copper wire connections to the cold stage. Like the single-detector cryostat, a thermometer provides temperature readout of the stage and a heater allows elevation to the desired temperature.

The variable-temperature stage was designed to be modular so it can support a variety of mounting schemes and detector geometries. For most I-V testing, detectors were mounted to the stage on electrically insulating and thermally conducting boron nitride pads. High voltage was provided to a copper sheet on the BN and the detector would sit on an indium sheet on top of the copper. Detectors were held down with pogo-pins affixed to a crossbar above. The pogopins press down to give thermal contact and provide electrical connections to the top contact and guard ring. Figure B.6 shows a photograph of the cryostat interior with detectors mounted as described.

The external circuit is nearly the same as the one described for the single-detector cryostat in the previous section. Computer-controlled ISEG high-voltage power supplies pass through an external RC low-pass filter (gray external boxes in Figure B.6) and into the cryostat via high-voltage feed-throughs. The guard ring is read out directly to a Keithley 6487 picoammeter. The center contact is also connected directly to a picoammeter for current-voltage testing, but can also be AC-coupled to a preamplifier inside the readout boxes (blue boxes in Figure B.6). Custom-built relay switching boxes allow multiplexing of all detector readout to two picoammeters.

The base pressure of the cryostat is typically low  $10^{-6}$  mbar at room temperature and low  $10^{-7}$  mbar at cryogenic temperature. Base temperature is about 82.5 K and the stage can be heated to at least 160 K. When the turbopump is needed elsewhere, it can be valved off and the cryostat pumped by an ion pump when the cryostat is cold.

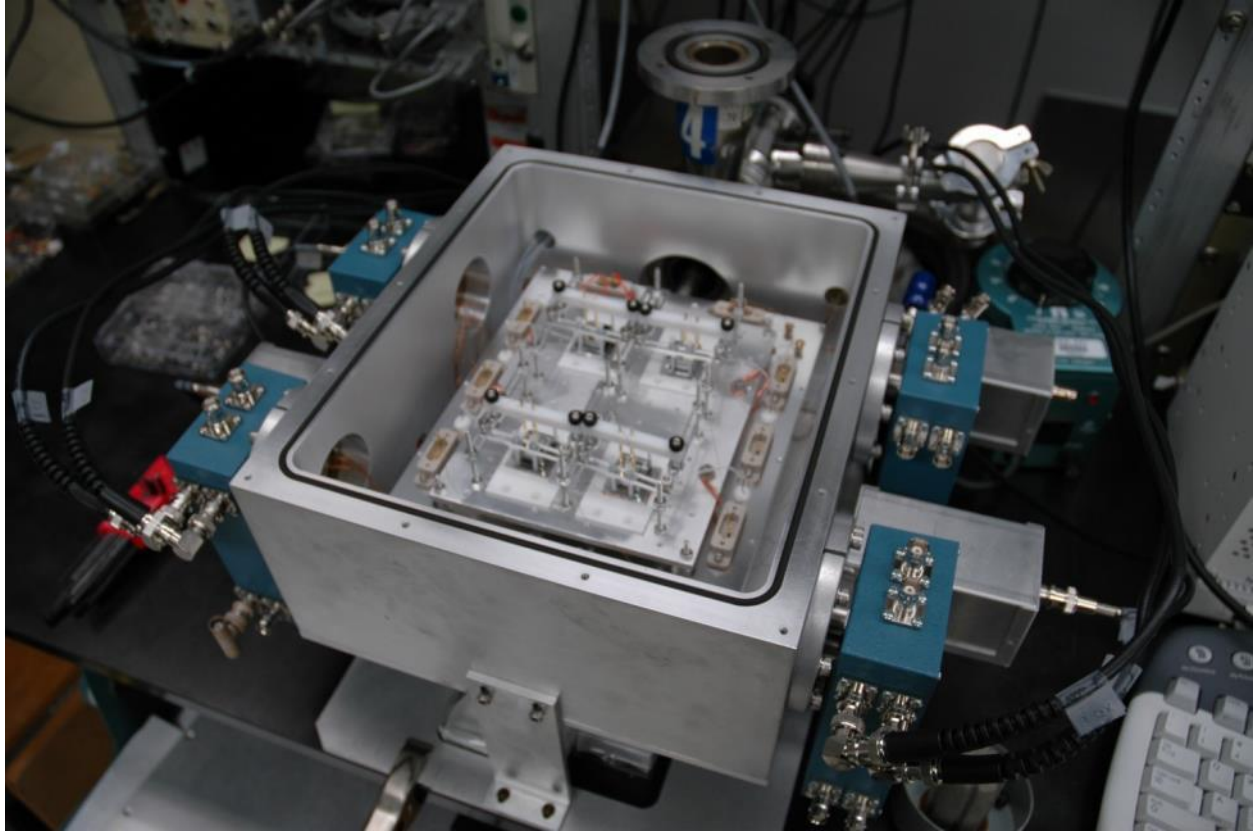


Figure B.6. Photograph of the multi-detector cryostat with four detectors loaded for testing. The top plate and infrared shield are removed to show the variable-temperature stage with mounted detectors.

### B.3 Measurement Equipment

The measurement system for current-voltage system involves a simple circuit and provision for fine current measurement and a pulse height measurement system. It is typical to filter the high-voltage input to ensure a steady DC bias level. Figure B.7 illustrates the circuit used for the current-voltage measurement system in the single-detector variable-temperature cryostat.

For this measurement system, two separate RC low-pass filters are placed between the Canberra 3125 high-voltage power supply and the bottom electrode of the detector. The RC circuits are designed to quench any high-frequency components picked up by various means before they reach the detector. The filter box attached to the cryostat has a pulser input to allow a test pulse to be inserted across the detector capacitance in order to measure the detector capacitance. The filters have some series resistance that will drop voltage as current passes through. This limits the maximum total detector current to about  $10^{-7}$  A to avoid significant over-estimation of bias on the detector. The effect can be corrected in analysis if needed. Applied voltage is kept to a maximum of 2000 V due to the standoff rating of components contained in the filter boxes.

The detector itself is an important part of the circuit. It can be modeled as a variable capacitor and current source in parallel, with capacitance and current determined by applied bias.

Since we have two separate electrodes at the top contact, it is modeled as two separate sets with a capacitance between. The capacitors are variable only when the detector has some undepleted material, the amount of which changes with applied bias. However, once the detector is fully depleted, capacitance is determined by geometry. The current sources continue to vary according to the contact current injection behavior.

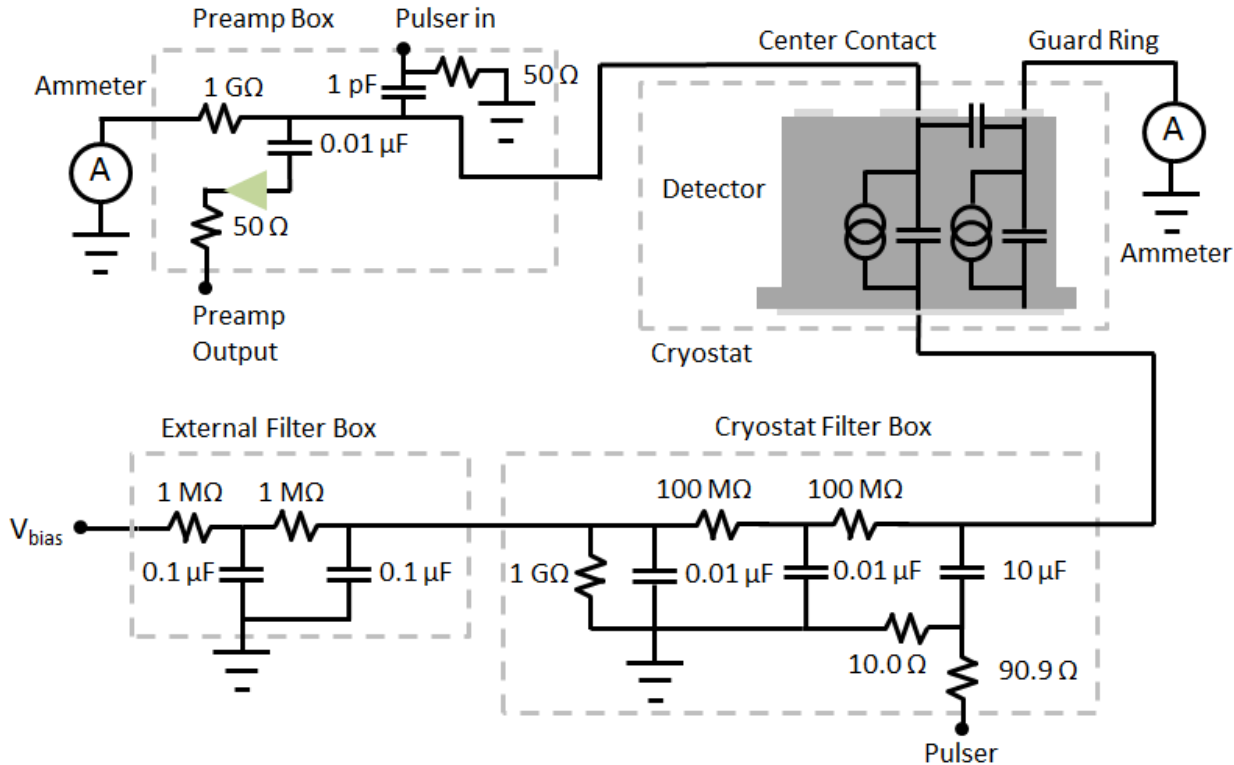


**Figure B.7.** Circuit diagram of the current-voltage measurement system in the single-detector variable-temperature cryostat. The high-voltage power supply is connected through two low-pass filters to the bottom electrode of the detector. The center contact at the top has DC current readout and a pulse height measurement system, while the guard ring goes to a picoammeter. The detector is modeled as a collection of capacitors and current sources.

The center contact is connected to a readout box where the signal is split into AC and DC components. Figure B.8 shows a photograph of the inside of the box. A preamplifier is capacitively coupled to the signal wire, which continues through a high-impedance path to ammeter readout. The pulse height measurement system allows measurement of a test pulse through the detector so the detector capacitance can be measured. The preamp also has its own test pulser input so it can be calibrated apart from the detector and cryostat wiring capacitance. When the high-value resistor is in place for this measurement, the center contact current must remain low to avoid significant voltage drop across this resistor and development of a potential difference between the center contact and guard ring. In practice, the circuit is used as described only when testing a new crystal to confirm depletion voltage by examining when the capacitance stops changing with voltage. For most current-voltage measurements, all series resistance

between the detector and ammeters is eliminated to avoid a potential difference between the center contact and guard ring.

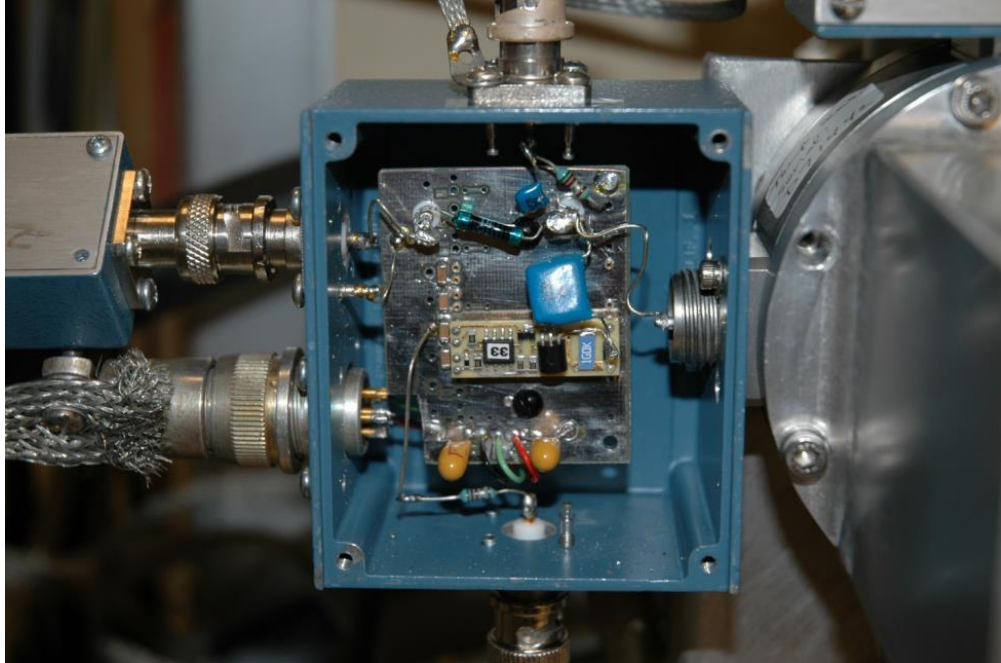


**Figure B.8. Photograph of the center contact readout box for the single-detector variable-temperature cryostat. The box contains a circuit for both DC current measurement and pulse height measurement of signals from the center contact.**

External electronics modules are nearby in a NIM bin. Figure B.9 shows the modules, including a custom preamplifier power supply, the Canberra 3125 high-voltage power supply used for automated current-voltage testing, the custom high-voltage power supply used for manual testing, a Tennelec pulse generator, and a Tennelec shaping amplifier for examining preamp output signals. When detector capacitance is measured, the pulser is used at the input to the filter box to step a small voltage across the detector capacitance, injecting a packet of charge that is then collected at the preamplifier and examined through the shaping amplifier. Typical use is checking for the voltage at which the pulse reaches a minimum, indicating full depletion voltage. The Canberra 3125 HVPS provides detector bias, with automated output provided by the remote 0-5 V input. The low-voltage set level is provided by an analog DC level from a National Instruments 6229 I/O card attached to a nearby computer.

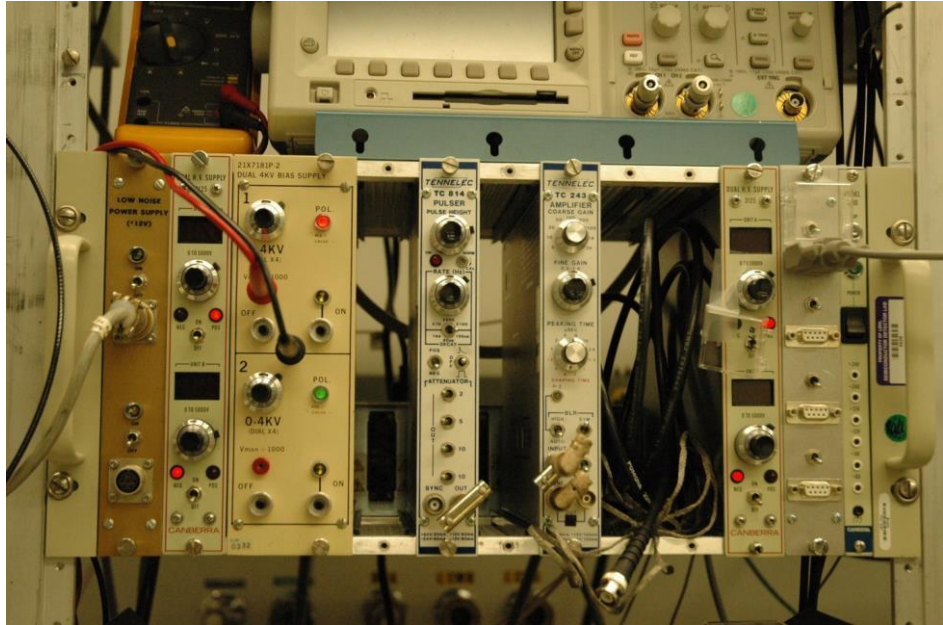


**Figure B.9.** Photograph of the NIM bin containing external electronics modules used in guard ring detector testing.

The guard ring has a separate readout box with a connection that can be switched between the ammeter input and a voltage source. Figure B.10 shows the interior of the guard ring readout box.

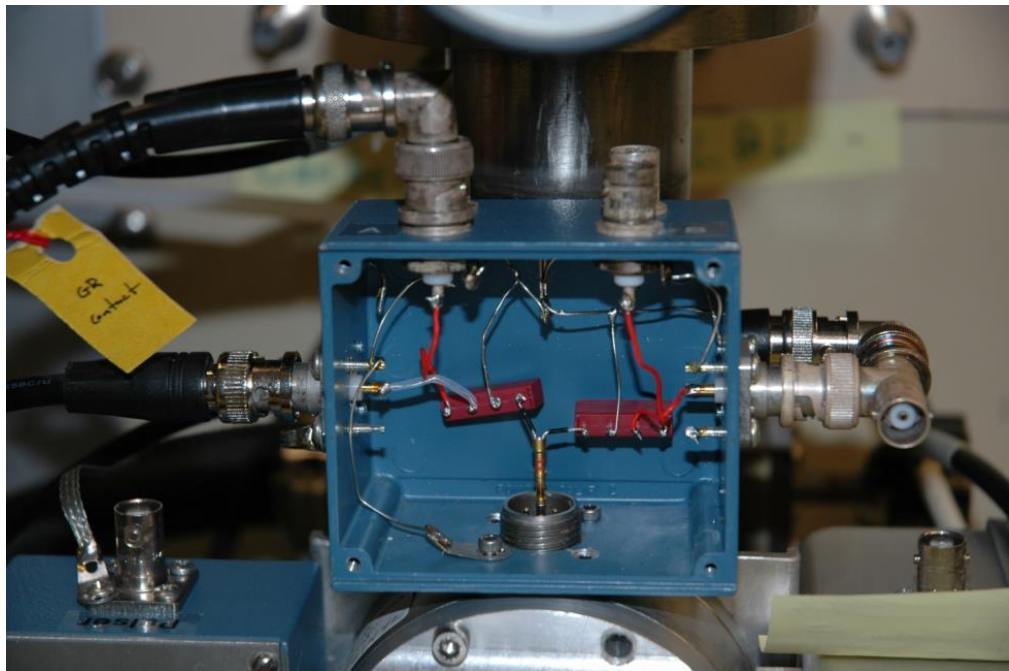


**Figure B.10.** Photograph of the guard ring readout box on the single-detector variable-temperature cryostat. The guard ring electrode can be switched between the ammeter input and a voltage source by the relays (red rectangular components).

During current-voltage measurement, the guard ring is connected directly to the ammeter input. However, for determining resistance between the guard ring and center contact, a voltage source is attached to the guard ring. This switch is done by relays so that the process can be automated.

The current through the detector electrodes must be read precisely. The values at low temperatures are less than  $10^{-12}$  A. Keithley 6485 and 6487 picoammeters provide  $10^{-15}$  A resolution, although the overall system is only capable of  $\sim 5 \times 10^{-13}$  A precision. Figure B.11 shows the picoammeters. The 6485 is an ammeter only and is used for measurement of the center contact current. The 6487 is used for measurement of guard ring current and also has a precision low-voltage power supply used for supplying guard ring bias during inter-electrode resistance measurement. The 6487 has a triaxial input, but the rest of the system was not conducive to using the double shielding, so a converter box connected the coaxial shield to both triaxial shields.

Temperature readout and control is handled through a temperature sensor, heater, and closed PID loop. A LakeShore DT-471-BO Silicon diode temperature sensor affixed to the bottom of the variable-temperature stage gives an indication of the stage temperature and is sent to the input of a LakeShore 335 temperature controller, seen in Figure B.12. The controller also has a current source attached to a power resistor fixed to the cryostat variable-temperature stage. Power dissipated in the resistor heats the stage as necessary. PID loop control is used to reduce time to desired temperature and prevent constant oscillation present in a more simple heat until setpoint algorithm. After a temperature set, the detector is allowed to stabilize 2 hours before testing to ensure thermal equilibrium.



Figure B.11. Photograph of Keithley 6485 (left) and 6487 (right) picoammeters used for precision current measurement.



Figure B.12. Photograph of LakeShore 335 temperature controllers used for temperature readout and heater control of variable-temperature cryostat stages.

## B.4 Current-Voltage Testing Procedure

The test procedure for guard ring devices is outlined below. This is how barrier height and temperature cycling information is obtained.

### Acquiring the current-voltage data

1. Fabricate guard ring device as described in III.B.
2. Store in dry nitrogen purge box until single-detector variable-temperature cryostat is available.
3. Load in single-detector variable-temperature cryostat and pump to  $10^{-7}$  Torr. If desired, turn on ion pump while still warm and allow return to base pressure.
4. Add liquid nitrogen and allow to cool to base temperature of about 79 K.
5. Manual test to ensure the detector can hold high voltage without breakdown. Use custom high-voltage power supply and Keithly picoammeters in manual readout mode.
  - a. Take a few measurements of center contact and guard ring current at different applied bias up to 2000 V or  $\sim$ 1000 V above full depletion, whichever is lower. Be sure to include multiple points above and below full depletion.
  - b. If this is the first time the crystal sample has been tested, attach preamplifier to center contact readout with high-impedance DC out. Pulse at HV filter box across detector and monitor pulse height as a function of applied bias.
  - c. If breakdown, power off and remove liquid nitrogen. Discontinue testing.
6. At zero bias, power off preamp and bypass high-value resistor on DC out. Stop pulser. Change to automated Canberra HVPS and begin automated testing.
  - a. At each temperature, automated LabView procedure takes I-V data to include at least a few hundred volts above full depletion.
  - b. Guard ring connection is switched via relay to low-voltage power source and guard ring-center contact resistance is measured.
  - c. Heater set to next temperature set point and allow 2 hours to settle.
  - d. Continue until at least 3 data sets at different temperatures have significant current (greater than a few pA). Keep total current below about  $10^{-7}$  A.

7. Power off equipment and remove liquid nitrogen. Use heater to slowly bring to 295 K. If detector will be temperature cycled, keep under vacuum.
8. After at least 24 hours, add liquid nitrogen. Perform steps 6-7.
9. Repeat steps 6-8 as desired.

#### Data analysis

The data are analyzed in Matlab using a series of scripts, functions, and structs written for this purpose. The procedure is outlined below. The following section describes the analysis steps in detail, follows through an example analysis procedure with real data, and connects the steps with theory presented in Chapter 3.

1. Examine I-V data for center contact and guard ring at all temperatures for anomalies. Remove any data that is obviously affected by a testing error.
2. Normalize center contact data by contact area.
3. Determine usable temperature range. Some temperatures are too low and do not have current high enough to be precisely measured. Other temperatures are too high and have excessive voltage drop in the HV filters or possibly non-permanent breakdown.
4. Determine usable voltage range. At the lowest bias values, poor separation between the two top contacts causes an inaccurate center contact current reading. Lower bias values can also be affected by a ghost current from the ammeter reset since they are taken first. High bias values are more likely to be affected by breakdown, but the data at lower bias may still be used. The range right around full depletion is also avoided.
  - a. Determine usable voltage range below full depletion for top contact contribution.
  - b. Determine usable voltage range above full depletion for bottom contact contribution.
5. Fit chosen voltage range below full depletion to estimate top contact current.
6. Subtract top contact current at all bias values.
7. Fit chosen voltage range above full depletion to estimate bottom contact barrier lowering term.
8. Repeat steps 4-7 for all data sets in usable temperature range.
9. Choose a bias value (usually highest available) and do current-temperature fit to determine barrier height and pre-factor.

## Appendix C Strip Detector Testing

This appendix describes the details of the double-sided strip detector (DSSD) testing that was used to give the results presented for inter-electrode charge collection in Chapter 7.

### C.1 Cryostat

The strip detectors were tested in another cryostat set up specifically for the purpose. Due to parts availability, the general design has a vertical coldfinger rather than a horizontal one, as the current-voltage testing cryostats do. Figure C.1 shows the outside of the cryostat. Liquid

nitrogen drops into the coldfinger from the top of the photo and extends toward the detector in the “can” at the bottom. Mounted to the top surface of the vacuum chamber are a high-voltage filter box and the preamplifier box.

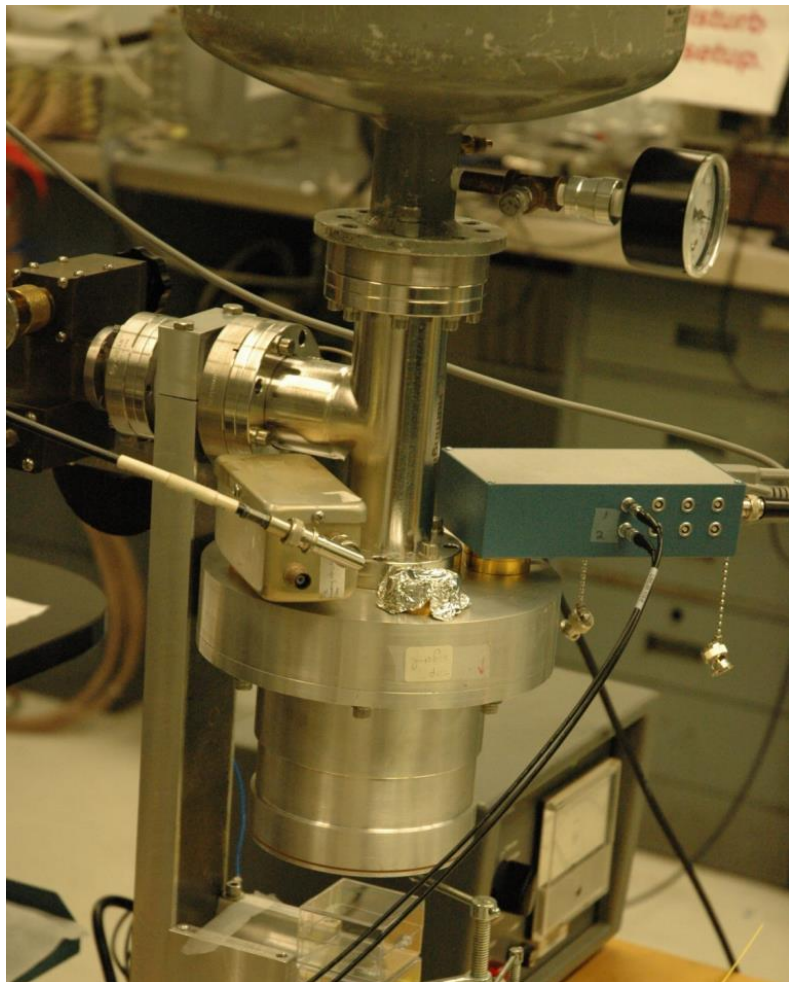


**Figure C.1. Photograph of the outside of the strip detector testing cryostat.**

Inside the vacuum compartment is a baseplate directly attached to the end of the coldfinger. The detector mount rests on this plate, which also includes many feedthroughs for electrical connections. A second “can” over this baseplate completes an infrared shield. Figure C.2 shows an inside view of the baseplate. The infrared shield would be placed around the outside lip of the baseplate and extend over the top and sides of the mounted detector. Electrical connections from the outside feedthroughs can be seen coming from the bottom, passing through a thin stainless steel wire section for a thermal break, and reaching the baseplate feedthroughs (nylon or Teflon screws with wire down the center). The resistors and capacitors of the AC-coupling circuit are near the detector and kept cold during measurements.

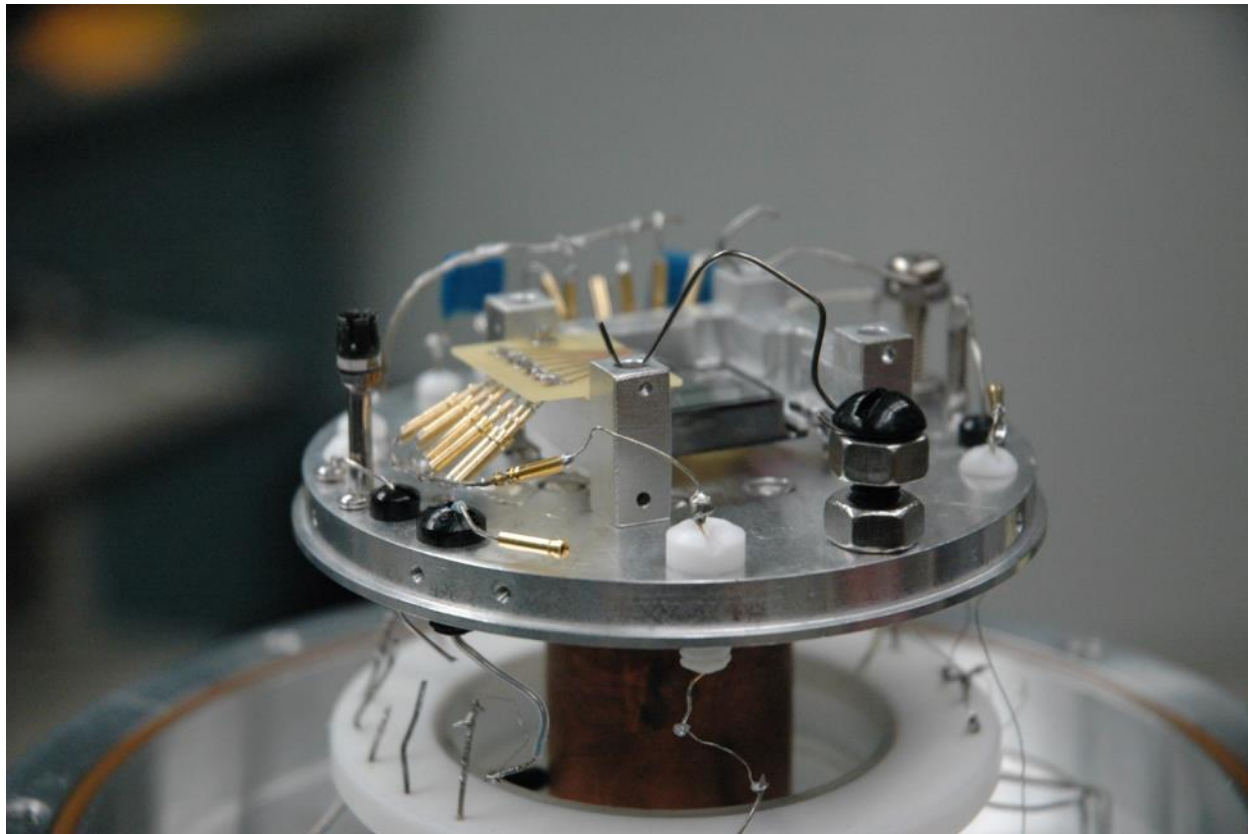


**Figure C.2.** A photograph of the baseplate inside the cryostat with a mounted and wired detector. The cryostat wall and infrared shield are removed.

The baseplate has a strong thermal connection to the liquid nitrogen compared with a variable-temperature cryostat, where the connection is deliberately made weak. However, the detector has additional mounting structures that give thermal weak points. The mount rests on the baseplate on four posts and the detector is connected to the mount only through its wings. An intervening layer of boron nitride keeps the wings electrically separated from the mount, but also gives two additional interfaces that could create thermal weak points. A thermal test was conducted to estimate the final detector temperature before any detector measurements were made. A brass model of the detector geometry was placed in the mount and a temperature sensor was anchored in the center of the brass dummy. Brass was chosen because it has similar thermal conductivity to germanium. The sensor showed an equilibrium temperature of about 78 K.

The cryostat has similar requirements to those described for the current-voltage testing cryostat in B.1. Similar vacuum and thermal considerations are important, but microphonic noise is an additional concern that must be addressed. This type of noise results from physical movement of components in the circuit (usually rattling in a periodic fashion) which changes the overall capacitance of the preamplifier input to ground. Charge moves to keep the voltage unchanged, giving a signal on the preamplifier output. Tapping the cryostat (or anything attached to it) or, in severe cases, speaking nearby, causes vibration and can be observed at the

preamplifier output. The effect derives its name because a microphone works on the same principle.

Microphonic noise is relatively low frequency (period  $\sim 10^{-3}$  s) compared with other time constants like preamplifier decay ( $10^{-5}$  s) and detector charge collection ( $10^{-7}$  s). The filters normally used, whether analog or digital, are effective in removing most microphonic noise. However, since filters are not perfect, energy resolution is negatively impacted by the presence of this noise. Therefore it is good practice to minimize microphonics in any cryostat where spectroscopic measurements are performed. The current-voltage testing cryostats described earlier are only immune to this because measurements are generally DC only.

Microphonics can be reduced in two primary ways. The first is to reduce the stray capacitance in order to reduce the charge fluctuation caused by vibrations. According to the relationship  $Q=CV$ , lowering capacitance will reduce the amount of charge fluctuation. The best practice is keeping the entirety of the signal wire between the detector electrode and the preamplifier well away from other metal surfaces. Maximizing the distance to grounded surfaces minimizes stray capacitance. The second way to reduce microphonics is reducing physical movement of signal wires. Using rigid wires and anchoring them often via insulators is best practice for keeping vibrations low.

## C.2 Measurement Equipment

The data are acquired using standard pulse height measurement techniques with modern digital readout. The detector is biased with either a custom high-voltage power supply or a Canberra 3125 high-voltage power supply and some strips are AC-coupled to preamplifiers for readout. The high-voltage input has a filter of the same RC low-pass design as the filters described for the current-voltage measurement systems. A preamplifier box attached to the cryostat houses the preamplifiers for strip pulse height measurement. The DC component of the two readout strips is tied to the remaining three strips on the bottom surface and goes to a DC readout connection for current measurement during initial testing. The guard ring is directly connected to another output for current measurement.

The preamplifiers are MaFaYa v2 charge-sensitive preamplifiers [129]. Electronic noise is less than 1 keV FWHM with no input. Preamplifier power is provided by a NIM crate via two sets of filters. A custom power module uses two series 10 mH inductors to independently filter two separate +12 V lines and a -12 V line. At the preamp box, an RC filter provides final filtering for the three lines. This design is especially sensitive to noise on the +12 V power, so two independently filtered supplies are provided so that noise is not correlated on the two lines.

The preamplifier outputs are digitized by a Struck Innovative Systems SIS3302 VME board. It has 8 channels operating at 100 MHz sampling frequency with 16-bit resolution. Though the onboard FPGA has real-time trapezoidal filter capability, this is used for quick diagnostics only. For detailed analysis, the waveforms are saved to a file and analyzed later. Figure C.3 shows the VME crate with the SIS3302 and the SIS3150 interface card at the left.

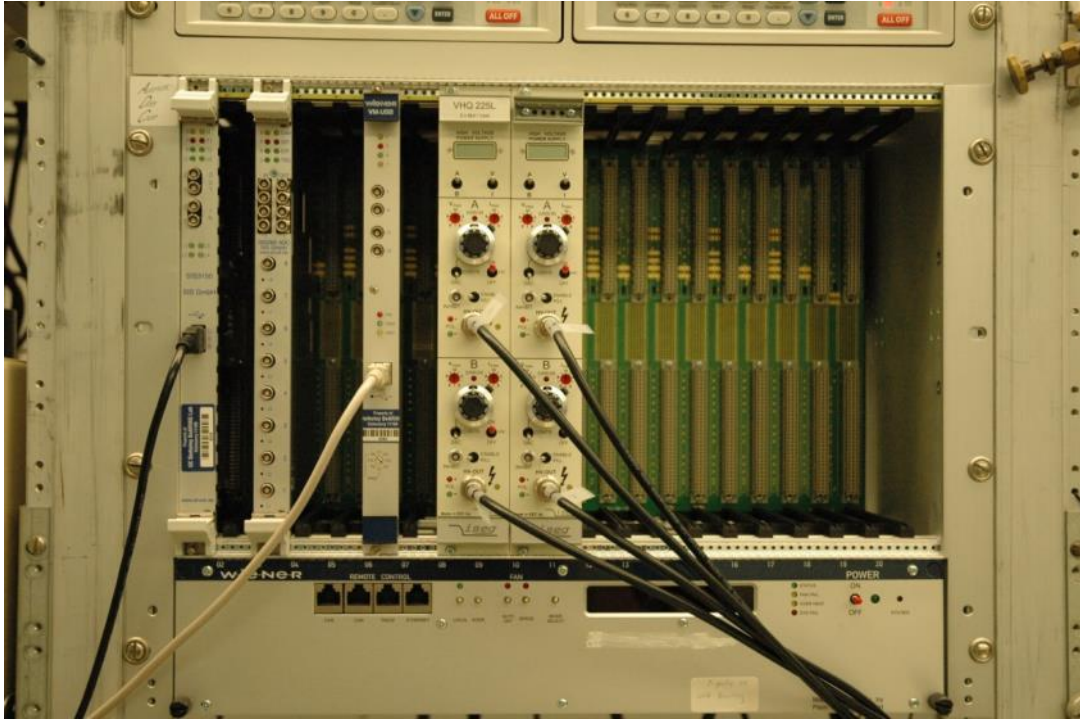


**Figure C.3. Photograph of the VME crate with Struck Innovative Systems modules used for strip detector testing (left 2 modules).**

The nearest-neighbor triggering function was used for both channels on the SIS3302 card, so a signal over threshold on either channel would cause readout of both channels.

### C.3 Miscellaneous Effects

A few other miscellaneous effects were tested on some strip detectors but do not fit into a single significant area for discussion. This section presents findings from some of these minor effects.

The energy of incident gamma-rays affects the size of the charge cloud created in the detector. In principle, this could change the inter-electrode charge collection properties, although the most precise measurement should be the smallest available charge cloud so that all charge could possibly be collected to the gap. Gamma-rays with high energy could not be efficiently stopped in the small detectors used in this study, so only limited tests were conducted with Ba-133 and Cs-137, giving gamma-rays with 356 keV and 662 keV respectively. A Cd-109 source with 88 keV gamma-rays was also used for some tests, but the weak source activity limited its usefulness. All detectors were tested with a Co-57 source, giving 122 and 136 keV gamma-rays in addition to the 59.5 keV gamma-rays from Am-241. The Co-57 data are generally not presented because no significant differences were found between the behavior at 122 keV or 59.5 keV.

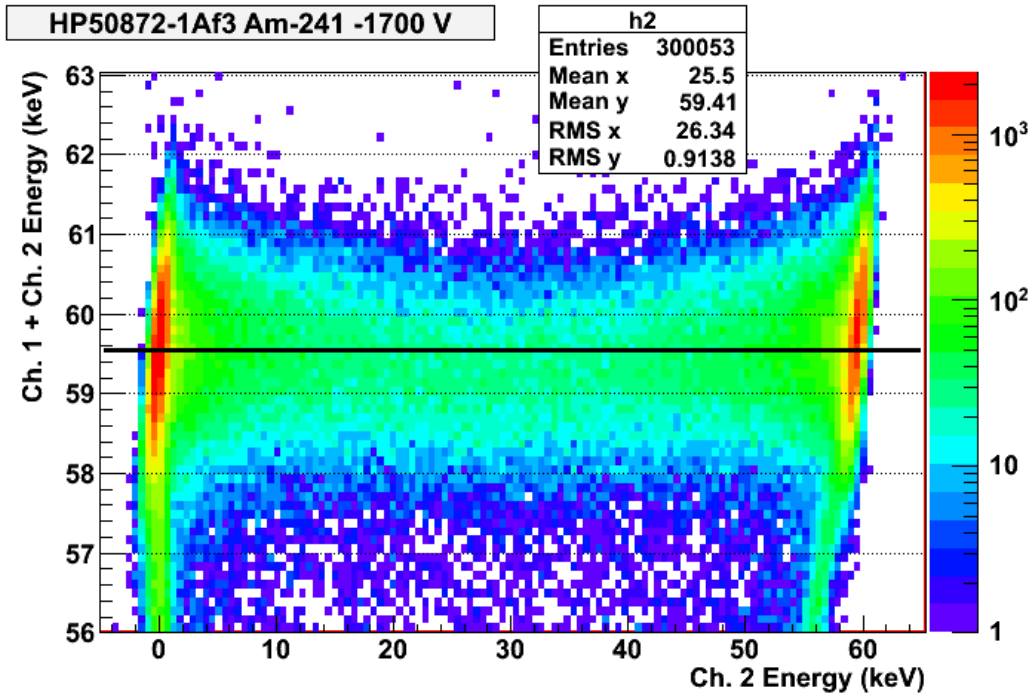


Figure C.4. Charge sharing plot for one detector bottom contact created by sputtering a-Ge in 15 mTorr Ar (7% H<sub>2</sub>) gas. The Am-241 source provided 59.5 keV gamma-rays.

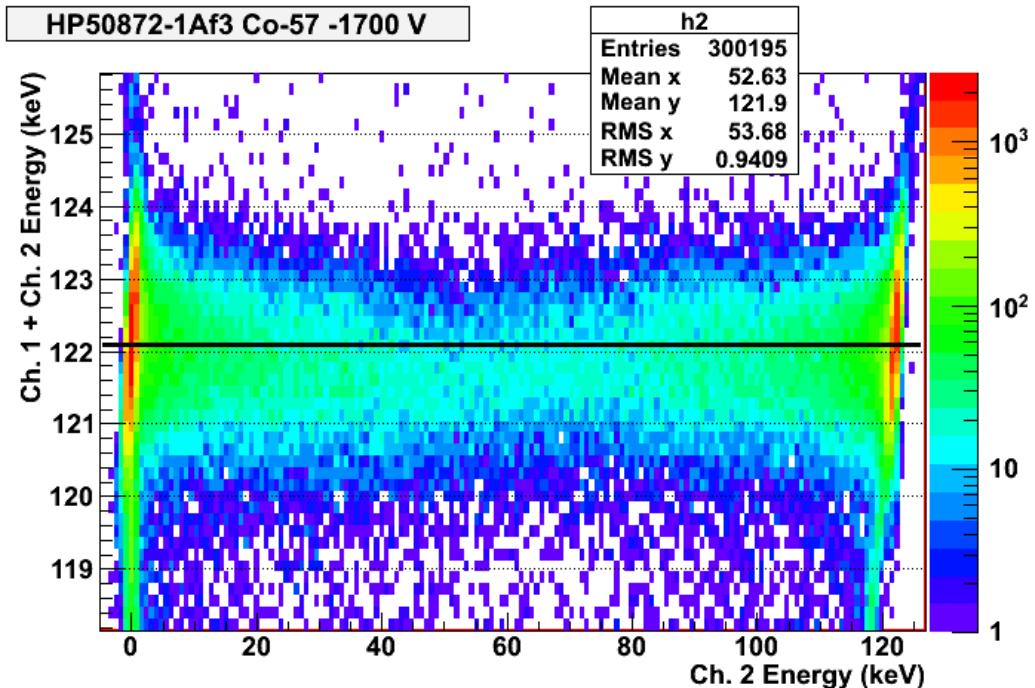


Figure C.5. Charge sharing plot for one detector bottom contact created by sputtering a-Ge in 15 mTorr Ar (7% H<sub>2</sub>) gas. The Co-57 source provided 122 keV gamma-rays.

The data shown in Figure C.4 and Figure C.5 were taken on the same detector with the same bias applied. There is no significant difference in the inter-electrode charge collection behavior.

Some detectors were tested while not fully depleted. One test was conducted where the strips were in the undepleted material. Figure C.6 shows the signal from one strip vs. the signal from an adjacent strip, indicating the strips were not electrically separated. It was not possible to perform an accurate energy calibration or construct the ordinary charge sharing plot.

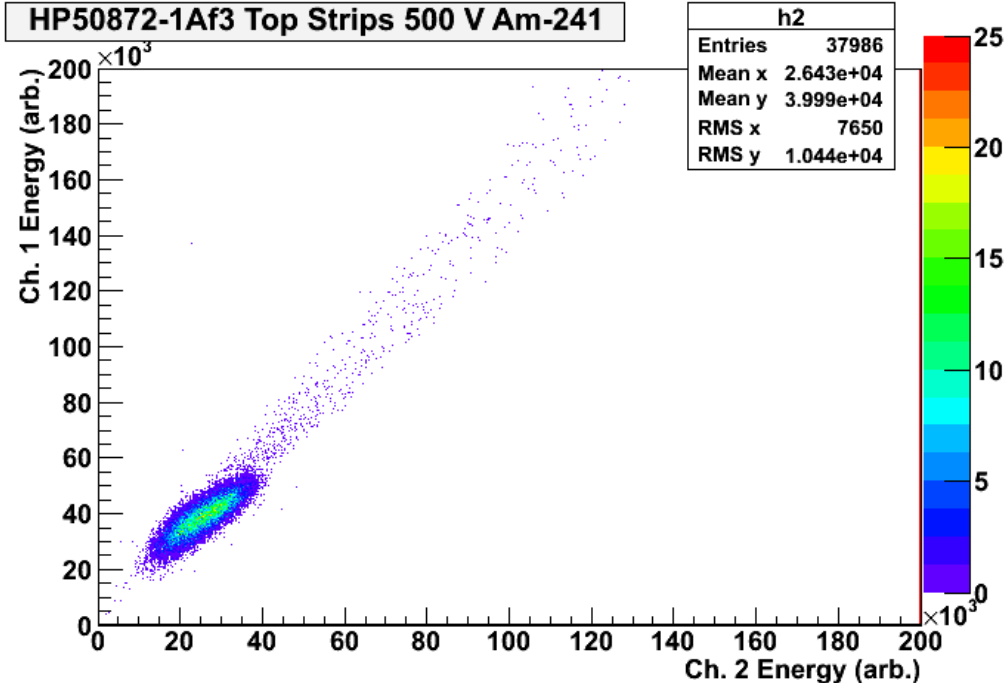


Figure C.6. Signal from one strip vs. signal from the neighboring strip for a detector that was not fully depleted. The strips examined were in undepleted material.

Another detector was tested while not fully depleted, but the strips were in the depletion region. The source illuminated the detector from the opposite side of the readout strips and on the same side as the undepleted material. Some gamma-rays penetrated the undepleted material, giving normal charge sharing behavior, seen in the upper left panel of Figure C.7. Examining the waveforms revealed some events originating from the undepleted region. A subset of events with the full source energy showed typical waveforms for the two strips, while subsets of events with lower energy showed some waveforms with a slow rise time. Presumably this is the sort of behavior described in previous work on a P-type Point Contact (PPC) detector [83], where the charge cloud is created in a region of low or zero electric field, and moves into the depleted region by diffusion. The result is a longer rise-time for the associated pulses and lower measured energy.

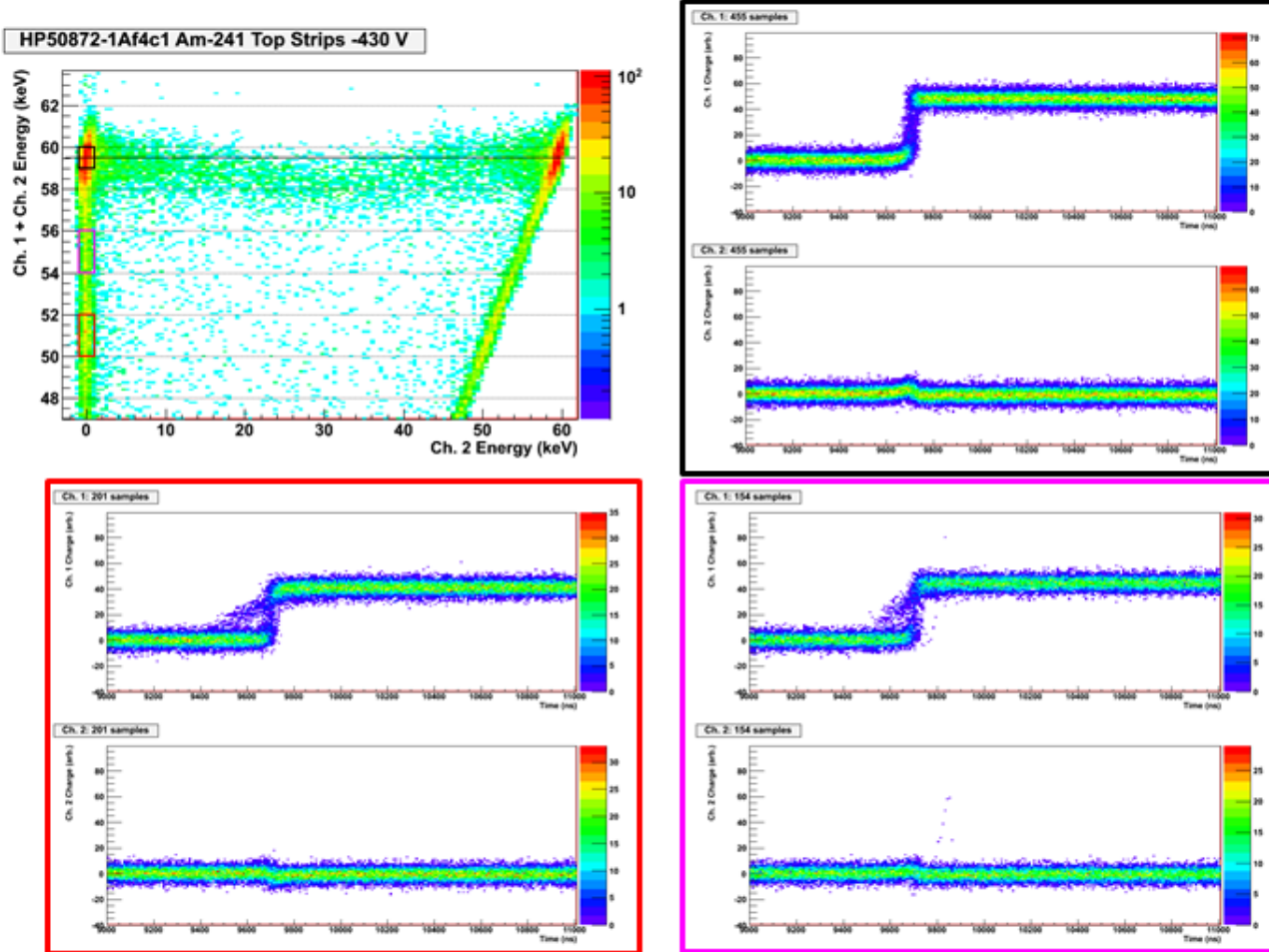


Figure C.7. Charge sharing plot and waveforms for a detector not fully depleted, but with strips in the depletion region. The upper left panel is the charge sharing plot. Three boxes of different color show three different cuts based on the sum energy and ch. 2 energy. The stacked waveforms for each of the three data sets created by the three cuts are shown in the panels with colored outlines, with colors corresponding to the box that defines the subset on the upper left panel.

In general, it was observed that if strips were in the depletion region, regardless of the overall electric field strength, the charge sharing behavior was the same. No unusual behavior was found in the waveforms originating from different portions of the charge sharing plot except as noted above.

## Appendix D Schockley-Ramo Theorem

The signal observed in a radiation detector is created by drift of charges in a volume with applied electric field. The theorem describing signal behavior is named after two authors who independently developed the idea [34] [35]. When radiation causes ionization in a semiconductor detector, a cloud of mobile charge is created, whose drift due to the electric field causes an induced signal on any electrodes on the device. The time-dependent signal can be difficult to calculate without the Shockley-Ramo theorem as one must calculate the electric field distribution in the detector, move the charge by an appropriately small step, then calculate the electric field distribution again, continuing this over many small steps of the mobile charge. This rather tedious process may be avoided by taking advantage of the method developed by Shockley and Ramo, requiring a single calculation dependent only on geometry and a single calculation to determine the drift path of moving charge.

The Shockley-Ramo theorem states that the current sensed by an electrode due to a moving point charge is given by

$$I = q \vec{v} \cdot \overrightarrow{E}_0(\vec{x}), \quad (46)$$

where  $q$  is the moving charge magnitude,  $\vec{v}$  is the velocity of the moving charge,  $\overrightarrow{E}_0$  is the "weighting field," and  $\vec{x}$  is the instantaneous position vector. The velocity vector is determined by the actual electric field as dictated by applied bias to electrodes and space charge from ionized impurities. The weighting field is the electric field that would exist if the electrode of interest had a unit potential, all other surfaces had 0 potential, and no charge existed in the system. This charge induced at an electrode as a function of position is

$$Q = -q\varphi_0(\vec{x}). \quad (47)$$

The quantity  $\varphi_0$  is called the "weighting potential," a unitless quantity derived from the weighting field.

The advantage to this approach is that the real electric field distribution in the device, considering all charge and potentials, must be calculated only once, giving the travel path as a velocity vector. For example, the electric field vectors are shown for a single-sided strip detector in Figure D.1, where the five strips and guard ring on the top are positively biased. The p-type material has a constant space charge density and the bottom electrode is at ground potential. These electric field vectors represent the drift path for moving charge in the detector.

The weighting potential depends only on geometry and is found by a single calculation where the electrode examined has unit potential, all other electrodes have zero potential, and all other charge is removed. Figure D.2 shows the weighting potential for a strip from the example geometry in Figure D.1. While the previous calculation of actual electric field dictated the drift path for moving charge, this calculation reveals the charge induction efficiency for moving charge on this electrode as a function of position in the detector. This calculation would need to be performed for each electrode of interest.

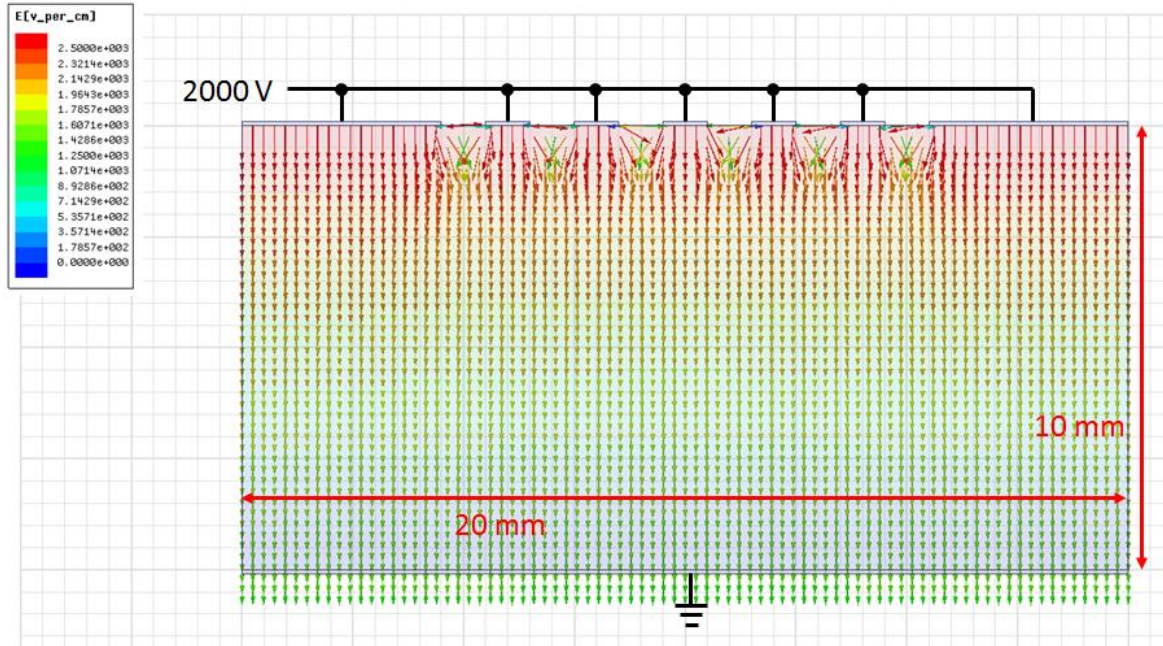


Figure D.1. Electric field for a single-sided strip detector.

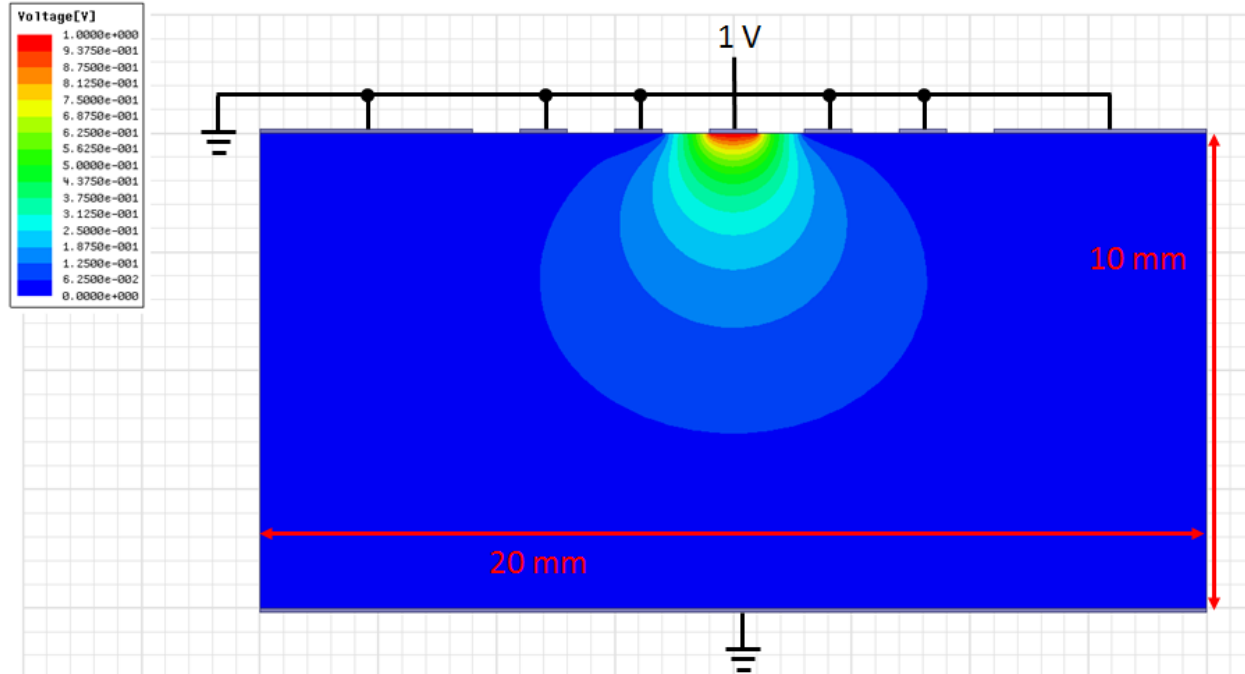
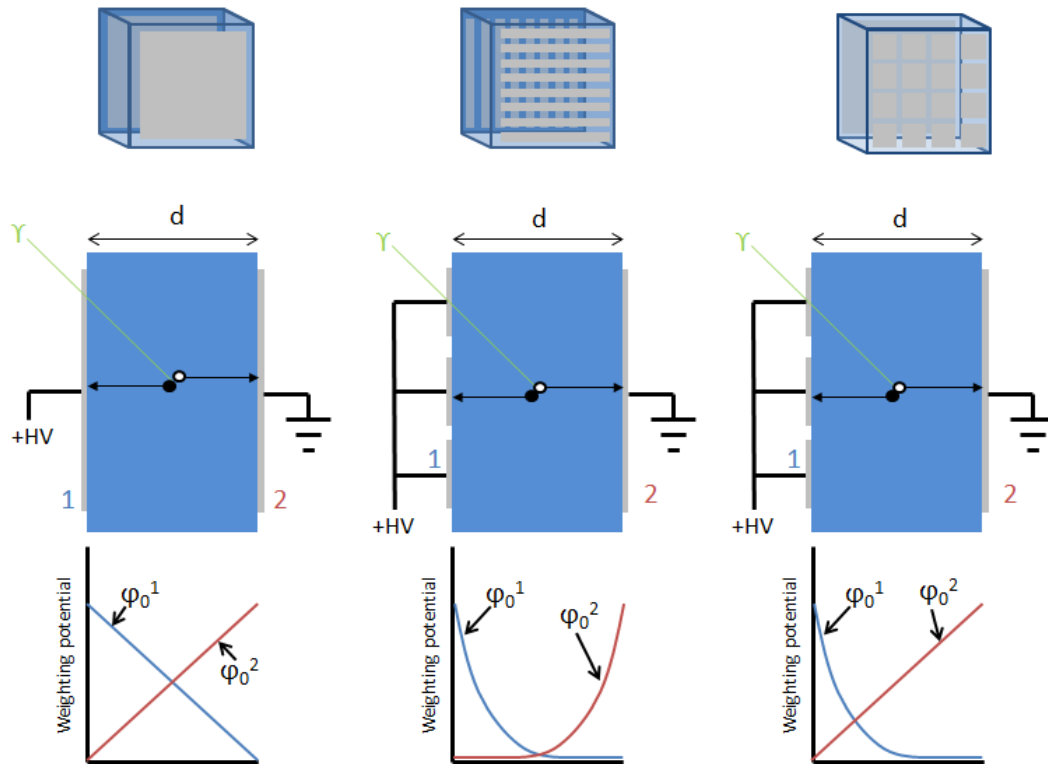


Figure D.2. Weighting potential for one strip on a single-sided strip detector.

The weighting potential can be used to describe unique characteristics of various detector geometries. The simplest example is that of a planar detector, illustrated in the left column of Figure D.3, which has a linear weighting potential for each electrode. In a germanium detector, the  $\mu\tau$  product is high enough that the drift distance is usually much greater than the detector

thickness, so nearly all holes and electrons reach their destination electrode. The consequence is that both types of charge carriers contribute to the signal from every electrode, so in a planar germanium detector, the signal amplitude is largely independent of interaction position. This is contrasted with other materials such as CZT that have a much lower  $\mu\tau$  product for holes. A planar detector constructed of such material will experience severe signal degradation as hole drift distance increases, causing a depth dependence on signal amplitude [36] [2]. The planar detector is the simplest to fabricate, yet provides no position information on the radiation interactions.



**Figure D.3. Schematic of weighting potential for selected electrodes in common detector geometries.** The top row shows electrode geometries for a planar detector, orthogonal strip detector, and single-sided pixel detector. The middle row shows a cross-section view with charge drift and biasing scheme, while the bottom row shows the weighting potential for two electrodes on opposite faces of each detector.

For a double-sided strip detector, the weighting potential decreases more rapidly as a function of distance from the electrode, with a characteristic distance approximately equal to the strip pitch. This profile is extruded in the direction of the strip. This electrode readout scheme is popular with silicon and high-purity germanium because it provides two-dimensional position information with a reduced number of readout channels when compared with an equivalent pixel detector. This requires efficient drift of both charge carrier types. It is possible to extract interaction depth by instrumenting both electrodes and measuring the difference in arrival times [66]. The weighting potential for this electrode configuration is shown in the middle column of Figure D.3.

A third successful readout scheme is a single-sided pixel detector, with weighting potential shown in the right column of Figure D.3. In a material like CZT that has low  $\mu\tau$  product for holes, this method is useful in recovering energy resolution otherwise lost by depth-dependent signal amplitude [130]. The hole-collecting cathode is applied as a planar electrode. Its linear weighting potential gives a depth-dependent signal amplitude so that interaction depth can be determined by comparison with the anode signal. The electron-collecting anode is segmented into pixels with pitch much smaller than the detector thickness so that their weighting potential does not extend significantly into the volume. In this way, each anode's signal is determined by electron drift only in the nearby vicinity, and amplitude may be corrected for charge trapping losses by the depth information.